SPH Simulation

of the

Formation and Evolution

of

Protoplanetary Disks

Annabel Cartwright

A thesis submitted to
Cardiff University,
for the degree of

Doctor of Philosophy

September 2006

UMI Number: U584879

UMI

Dissertation Publishing

ProQuest

Acknowledgements

Abstract

The formation and evolution of protoplanetary disks is simulated by computer modelling, using the Smoothed Particle Hydrodynamics (SPH) method. The suitability of SPH for modelling disks is investigated, and problems are identified with the SPH implementation of Artificial Viscosity in disks with Keplerian velocity profiles.

Analytical and experimental results reveal that the resultant viscous force for a simulated Keplerian disk is in the opposite direction to that produced by linear shear. Applying Artificial Viscosity only to approaching particles results in a radial force four times larger than the force in the direction of the orbit. The viscous force can change direction if temperature, and therefore sound speed, decreases.

Techniques for activating Artificial Viscosity only when convergence is detected are found to fail in differentially rotating disks. Both the Balsara Switch and Time Dependent Artificial Viscosity use the SPH estimate of $\nabla \cdot v \mid_{SPH}$, which has a low freqency time varying component which is independent of h, and so cannot be removed by increasing the number of SPH particles. An alternative method, based on pattern recognition, is shown to reduce the viscous spread of a differentially rotating ring by an order of magnitude.

We also identify problems associated with the gravitational field of disks. The use of an annulus to represent a portion of a much larger, continuous disk, may yield unrepresentative results. The edge effects can cause preferential accretion zones, where the Toomre Q parameter is not the same as it would be for the same region of an extended disk.

SPH simulations of Protoplanetary disks produce condensations which do not persist long enough to collapse. The high tidal shearing forces in a Keplerian accretion disk disrupt the condensations before they accumulate enough mass to collapse. Including a more realistic treatment of the thermal physics, and reducing the effective shear viscosity, makes the situation worse.

Contents

List of Figures

.

List of Tables

Chapter 1

Introduction

1.1 Introduction and Thesis Plan

Planets are believed to evolve from circumstellar disks around young stars. Our own solar system has characteristics which indicate that it originated from a circumsolar disk. The planets are very closely confined to the equatorial plane of the Sun. They all follow nearly circular orbits in the same direction as the Sun's rotation, and indeed their own rotations, the orbits of their satellites and the satellites' rotations nearly all conform to the direction of the Sun's rotation. The theory that all these bodies formed from a disk around the Sun is a plausible explanation for all these features.

Beyond our own solar system, disks and planets can now be observed around other stars. The observational evidence is increasingly persuasive that most newly formed stars have disks which are lost over periods no longer than a few million years. In a systematic survey, Haisch, Lada & Lada(2001) examined the stellar population in clusters raging in age from 2.5 to 30 million years, and found that 80% of the stars in the youngest clusters had disks, this proportion falling monotonically with the age of the cluster. (Haisch et al 2001, lo Curto et al 2006). Since 1995 more than 160 exo-planets have also been found around more mature stars, and current estimates are that 10% of solar type stars have planets (Marcy et al 2005). This may be a conservative figure.

While the solar system contained the only known planets, there was always the small chance that its evolution could be a freak occurrence, perhaps the only planets ever to have formed. However, the evidence of other, extra-solar planets, and their apparent abundance, now indicates that planet formation is not rare. The challenge for Astrophysical theorists, therefore, is to explain how circumstellar disks can evolve, over quite short timescales, into planets. Observations constrain the sizes, masses and temperatures of the disks and the planet formation timescale. We also have increasing evidence about the

sizes and orbital characteristics of exo-planets.

The increasing sophistication of simulation techniques and an explosion in computing power and speed make high resolution computer simulation a practical tool for investigation of this phenomenon. Taking as input parameters the observational evidence for the characteristics of protoplanetary disks, and simulating the physics which must apply in the environment around the stars, it should be possible to follow the evolution of the disks and observe the formation of planets. If the simulated planets look like the observed planets, that is then persuasive evidence that our models for the formation of planets from protoplanetary disks are sound. However, despite concerted efforts (eg Bate et al. 2003; Rice et al 2004; Boss 2001; Gammie 2001; Mayer et al 2004), this approach is not yielding consistent results. For example, Gammie (2001) found that if the cooling time of the disk was below a finite limit, related to the orbital period at each radius, gravitational instabilities could occur. Pickett (2000), however, found that cooling had to be instantaneous for gravitational instability, while Rafikov (2004) pointed out that neither case can be reconciled with the observational evidence, as such rapid cooling would require much more massive, hotter disks, and result in more massive planets, than are observed. Either our understanding of the physics involved, or the faithfulness with which the simulation method reproduces the physics, or indeed both, is suspect.

The objective of this thesis is therefore to investigate the evolution of protoplanetary disks by means of computer simulations, in particular using the Smoothed Particle Hydrodynamics technique. Particular attention will be paid to the handling of viscosity in the simulations. Artificial Viscosity, as used in SPH to capture shocks, is known to cause problems in the modelling of disks, where excessive shear forces may arise in steady Keplerian flow (Bate 2003), which could introduce artefacts into the simulations. Excessive shear could result not only in unrealistically rapid transfer of angular momentum, but also rapid heating of the disks. Both of these could drastically affect the evolution of the disks and the formation of gravitational instabilities. The precise nature and magnitude of excessive shearing forces will be established, and alternative methods to avoid this problem developed.

In the next chapter we review the work done to date in this area, and summarise the observational constraints. In chapter 3 we review the modelling technique Smoothed Particle Hydrodynamics (SPH), assess its suitability for modelling the evolution of disks, and note the details of the code used in Cardiff.

In chapter 4 we explain how disks of SPH particles are initialised to simulate the characteristics of observed disks, and model the gravitational and orbital velocity profiles of disks with various mass distributions. Chapters 5 and 6 look in detail at the handling of

Artificial Viscosity in SPH, a particular problem in SPH simulations of disks. Chapter 7 notes some modifications needed to handle the timing of the calculations, in order to simulate high speed inner orbits accurately, while saving time on the slower outer particles.

Chapter 8 reports and discusses some of the simulations performed using these modifications, and chapter 9 summarises the conclusions of the work in this thesis and plans for future work.

In parallel with the work on the evolution of protoplanetary disks, two papers have been published on the subject of the structural analysis of star clusters and molecular clouds (Cartwright & Whitworth 2004, Cartwright, Whitworth & Nutter 2006). These are attached as Appendices A and B, and also feature in the plans for future work.

1.2 Mathematical Conventions and Definitions and Physical Constants

Throughout this document the following naming conventions are used:

Variable name	Explanation
$\mathbf{v}$	A vector quantity
$\mathbf{v}_i$	Vector quantity associated with the ith particle.
$\hat{\mathbf{v}}_{ij}$	Unit vector in the direction of $\mathbf{v}_{ij}$
$\mathbf{v}_{ij}$	The vector difference $\mathbf{v}_i$ - $\mathbf{v}_j$
r_{ij}	The magnitude of $\mathbf{r}_{ij}$
$|r_{ij}|$	The magnitude of $\mathbf{r}_{ij}$
$\mathbf{v}_{ij} \cdot \mathbf{r}_{ij}$	the scalar or dot product of two vectors
$\mathbf{v}_{ij} \times \mathbf{r}_{ij}$	the vector or cross product of two vectors

Reference is also made to the following physical constants.

Abbreviation	Definition	Magnitude in S.I. Units
1 AU	1 Astronomical Unit	1.496×10^{11} m
1 M$_\odot$	1 solar mass	1.989×10^{30} kg
1 M$_J$	1 Jupiter mass	1.90×10^{27} kg
c	Light speed	2.998×10^8m s^{-1}
G	Gravitational constant	6.673×10^{-11} m^3 kg^{-1} s
k	Boltzman Constant	1.38×10^{-23} J K^{-1}

Chapter 2

The evolution of circumstellar disks.

2.1 Introduction

In this chapter we review previous work of relevance to this study of the evolution of circumstellar disks. This is divided into four sections. First we discuss the observational evidence for protoplanetary disks and extra-solar planets, and the resulting constraints on mass, size, temperature and lifetime of disks and planets. Second we summarise the key results from the analytical work undertaken in the 1960s and 1970s which underpins all subsequent simulation work on disks, and more recent analyses of viscosity in shearing rotational flow. Third, we review the literature on simulations of the evolution of proto-stellar and protoplanetary disks. Finally, we note some published caveats on the use of Smoothed Particle Hydrodynamics (SPH), particularly in the modelling of disks.

2.2 Observational evidence for protoplanetary disks and extra-solar planets.

O'Dell (1995) showed that at least 50% of young stars have disks of dust and gas surrounding them. O'Dell's survey, using the Hubble Space Telescope, produced clear images of disks at different viewing angles, with the stars at the centre. Evidence for disks around more distant stars comes from analysis of the spectral energy distributions (SEDs), where the presence of dust and the kinematics of the disk produce a characteristic SED signature for circumstellar disks. The most recent, comprehensive survey of young clusters using this method (Haisch, Lada & Lada 2001), indicated that 80% of young stars initially have disks. Half of the stars lose their disks in 3 Myr and essentially no disks survive beyond 6 Myr. Disk lifetime appears to be a function of stellar mass, massive stars losing their

5

disks more quickly than lighter stars (Haisch, Lada & Lada 2001a, Oliveira et al. 2002).

Visual images of disks show them to have radii of the order of 0.1-1000AU, (O'Dell & Wong 96, Eisner & Carpenter 2006) and to have dark bands. Side-on images show that they have a flared profile. Some SED's have been interpreted as evidence for disks with gaps, but it has subsequently been shown by Boss & Yorke (1996) that the mid infra-red dips in the SEDs in question can also be explained by the optical properties of the dust in the disks.

The masses of disks are usually taken to be around 0.01-$0.1M_\odot$. This was the range obtained by Weidenschilling (1977) as a lower limit on the original mass of the solar nebula, by projecting backwards in time from the present day mass distribution in the solar system. Subsequent calculations of the mass of dust required to account for the infra red signatures of protoplanetary disks (Beckwith et al. 1990) also indicate disk masses in this range. Eisner & Carpenter (2006) have recently identified hundreds of protoplanetary disks in the Trapezium region with masses in the range 0.13 to 0.39 $M_\odot$, and with radii of the order of 400AU.

Weidenschilling (1977) found that the surface density of the solar nebular was approximately proportional to $r^{-3/2}$, but McCaughrean & O'Dell's (1996) observations found opaque inner disks with exponential edges.

Beckwith et al. (1990) found that the temperatures of protoplanetary disks were of the order of 31K at radius 100AU, assuming that temperature $T(r) \propto r^{-1/2}$, or warmer (Beckwith et al. 1993). Observations of the solar system's asteroid belt (Lecar et al. 2006) indicate that the snow line, where temperature is in the range 145-170K, occurred in the solar nebula at a radius of 2.7AU. Both of these observations would indicate a temperature of around 300K at 1AU in protoplanetary disks.

The first extra-solar planet was reported in 1995 (Mayor & Queloz 1995), and more than 160 have now been discovered. Many of the planets are 'hot Jupiters' ($M \gtrsim 0.25M_{\mathrm{Jupiter}}$, $P \leq 10$ days), however this may be associated with the fact that most detections are made via the Radial Velocity (RV) method, which is less sensitive to light planets on more distant orbits. Recently, a 'Very hot Jupiter' has been discovered (Lo Curto et al. 2006), with a period of only 2.2 days. As new methods for the detection of planets improve the detection rate, it becomes apparent that planetary systems around stars are not rare, and that the planet formation process must be widespread.

2.3 Analytical predictions for protoplanetary disks

Mestel (1963) investigated the gravitational field of disks, which he showed to be fundamentally different from that of spherically symmetric distributions of matter. In a self-gravitating, spherically symmetric distribution of matter, any matter at greater radius than the measurement point contributes nothing to the gravitational acceleration at that point. At any radius within a self-gravitating disk, however, the inward attraction of matter lying within that radius and the outward attraction of the outward matter are both significant quantities, and indeed for an infinitely thin disk both quantities are divergent. Their difference, the radial acceleration, is finite. In particular, Mestel showed that a disk with surface density $\Sigma \propto r^{-1}$ will have an inward radial acceleration which is also proportional to r^{-1}, except in the very central region of the disk. This in turn yields a flat rotation curve, and such a disk is generally known as a Mestel Disk.

Lynden Bell & Pringle (1974) comprehensively described the evolution of a differentially rotating disk as a result of viscous forces, following the earlier work by Goldreich and Lynden-Bell (1964) which described a self-gravitating sheet in uniform rotation. The key result, which we use here, is that viscosity will transport angular momentum from the high velocity inner regions of a Keplerian disk to the lower velocity outer regions. Ultimately, the minimum energy state towards which the disk evolves is a concentration of all mass at the centre of the disk, with all angular momentum transferred to an infinitely small mass particle at infinite distance. A particular prediction is that a differentially rotating ring of matter will spread with time, the e-folding time decreasing with increasing viscosity.

Toomre (1964) investigated the tendency for self gravitating disks to become gravitationally unstable. He showed that pressure forces oppose gravitational collapse on small scales, while the centrifugal forces present in rotating disks oppose gravitational collapse on large scales. It is therefore possible to prescribe a relationship between sound speed, density and rotation speed, which ensures that gravitational collapse is prevented on all scales. We define the Toomre Q parameter as :

$$Q = \frac{\kappa c_s}{\pi G \Sigma},$$
(2.1)

where κ is the epicyclic frequency, c_s the sound speed, Σ the surface density of the disk, and G the gravitational constant. A value of Q greater than about 1.5 (the precise critial value is unknown) is taken to indicate that gravitational fragmentation is impossible.

κ is given by (Binney and Tremaine, 1987) :

$$\kappa^2 = r\frac{d}{dr}\Omega^2 + 4\Omega^2 \tag{2.2}$$

For a Keplerian disk, $\Omega \propto r^{-3/2}$ and therefore $\kappa = \Omega$, while for solid body rotation, Ω is constant, and $\kappa = 2\Omega$.

The evolution of rotating disks as described in Lynden-Bell & Pringle (1974), with matter in the centre losing angular momentum and falling on to a central object, requires viscous forces to transfer angular momentum from inner to outer orbits. There remains some mystery as to what these forces are in real astrophysical objects, and how they work. The analysis of Hayashi & Matsuda (2001) indicated that in circular shear flow, angular momentum moved in the opposite direction to that required by Lynden-Bell & Pringle, from outer orbits to the inner ones. However Clarke & Pringle (2004) used kinetic theory to explain viscous accretion in Keplerian accretion disks, successfully modelling angular momentum flow in the outward direction, and crucially, obtaining no angular momentum flow in a disk in solid body rotation. However, it is interesting to note that both Hayashi & Matsuda and Clarke & Pringle made simplifying, linearising assumptions at various points in their analyses, working in inertial frames, in which all particles move in straight lines, rather than modelling the actual curved trajectories of particles in Keplerian flow.

2.4 Simulations of protoplanetary disks

The observational evidence that protoplanetary disks have only very short lifetimes has led to increasing confidence that planets are formed by gravitational instability in disks, as this is the only mechanism to date which appears to form planets within the observed lifetimes of disks. Boss has used a three dimensional finite-difference hydrodynamics code to investigate the formation of planets, and to argue in favour of gravitational instability as the formation mechanism, as opposed to the other possibility, core accretion. Boss (1993) demonstrated that gravitational instability will result in a measurable wobble of the central star within hundreds of years. Rocky core building followed by gas accretion would take much longer before stellar wobble could be detected. In Boss (2000) simulations yielded planet formation by gravitational instability in a relatively thin disk, 0.091 $M_\odot$ within 20AU. The planets formed with eccentric orbits. In Boss (2001), pseudo magnetic effects were included in the evolution of a protostellar disk, which yielded quadruple star systems, one of which was about $1M_J$ in mass, which was then ejected from the system. This was a possible explanation for the existence of free floating M_J size objects.

Pickett et al. (2000) investigated the evolution of protostellar disks, again using a finite difference code, and found that gravitational instability only occurred in the extreme

case of a locally isothermal disk, that is, instantaneous cooling. With any more realistic cooling treatment, clumps did not form. However Boss (2001a) disagreed with this finding, concluding that with cooling time of the order of an orbit, gravitational instabilities could form. In Boss (2002), locally adiabatic heating and cooling was found to suppress gravitational instability, and the modelling of radiative transfer as a cooling mechanism was found to permit the growth of instabilities. Boss (2003) also looked at the dynamics of a planetary systems and found that it is difficult to explain the formation of outer planets because their relative orbital speeds exceed the excape velocity for the Sun, so they eject each other. Boss suggested that they must form at a radius less than that of Jupiter and then get slung out to larger orbits.

Mayer (2004) used Smoothed Particle Hydrodynamics (SPH) successfully to simulate planet formation by gravitational instability. The inner regions of disks from 4 to 25 AU radius, with mass varying from $0.75 M_\odot$ to $0.125 M_\odot$ were modelled, with temperature and density profiles contrived to give a Toomre Q less than 1.4. Several planets were produced on eccentric orbits. The cooling time was set to be proportional to orbital period, and the cooling rate was found to be crucial for disk fragmentation.

Nelson has used a grid based simulation method to investigate disk evolution. Nelson et al.(1998) reported 2D simulations of massive disks around protostars up to 1 $M_\odot$ in mass. Low mass disks produced filamentary arms, heavier disks larger, grand design spiral arms. The simulation could not be followed beyond hints of clumpiness developing. Nelson (2003) found that it was impossible to form 'hot Jupiters', that is Jupiter mass planets within 1AU of their stars, in situ, so they must form elsewhere and then migrate inwards, a result precisely the opposite of Boss (2003).

Gammie (2001) also found that cooling of the outer regions of an accretion disk caused gravitational instability, the outcome being non-linear. Depending on the cooling time, the result was a steady state with cooling balancing the viscous heating, or fragmentation, or a steady gravito-turbulent state, with density variations at a predictable scale. Gammie performed simulations in a local shearing box, representative of a portion of the disk, with local coordinates rotating with an orbiting particle and periodic boundary conditions. Within the shear box, differential rotation was modelled as linear shear. This representation of Keplerian shear flow is only accurate to first order.

Rice (2003) used SPH to confirm Gammie's finding that disks fragment if cooling time is shorter than $3\Omega^{-1}$, where Ω is the local orbital frequency. Rice successfully obtained gravitationally bound clumps using short cooling times, but for longer cooling times no clumps formed. Rice et al. (2003a) also reported SPH simulations producing many gravitationally bound objects from an initial disk with surface density $\Sigma \propto r^{-1}$ and

temperature $T \propto r^{-1/2}$, the Toomre Q being 2 at 50AU. In Rice (2004) planetisimals were planted in a disk, and their evolution found to be affected by 'drag' forces which caused them to accumulate within the spiral structure.

Rice (2003) and Rice et al.(2003a) were promising starting points for our own simulations, so the disk parameters were calculated and checked against the reported values of the Toomre Q.

Throughout Rice (2003), normalised units of radius and mass are used and the temperature profile of the disk is not spelt out, either in the text or the figures. Instead, parameters are bundled into the value of the Toomre Q parameter for the disk, and we are given the initial surface density profile $\Sigma \propto r^{-1}$ and the information that temperature $T \propto r^{-1/2}$. If we scale to the parameters appropriate for a protoplanetary disk, then at $r_{outer} = 50AU$, in order for Q to fall to ~ 2,

$$c_s(r_{outer}) = M_{disk} \left(\frac{G}{M_* r_{outer}} \right)^{1/2}, \qquad (2.3)$$

and substituting $0.1 M_\odot$ for M_{disk} and $1 M_\odot$ for M_*, we obtain $T \sim 42K$ at $r = r_{outer} = 50AU$ and $T \sim 300K$ at $r \sim 1AU$. These are reasonable initial conditions for the disk.

However, as the simulation progresses, fragmentation occurs in the range $r \sim 20AU$ to $r \sim 40AU$. If we assume that Q must fall below 1 in this region, we require the temperature to fall from 66K to 4K at $r \sim 20AU$ and from 47K to 8K at $r \sim 40AU$. These are very low, compared with the minimum temperature of 56K used in Mayer et al (2004).

Rice et al. (2003a) and Rice et al. (2004) also report results which, if scaled to the parameters appropriate for a protoplanetary disk, require disks to have been allowed to cool to unreasonably cold temperatures. In Rice 2003a, a constant Q disk, mass $0.1 M_\odot$ with temperature $T \propto r^{-1/2}$, radial extent 1-25 AU is allowed to evolve with different cooling times. Graphs show that Q falls to less than unity as the disks cool. Figure 3 in Rice et al. (2003a) shows $Q \sim 0.6$ at $r \sim 21$ AU, which indicates $T \sim 2K$, while Figure 5 in the same paper shows $Q \sim 0.6$ at $r \sim 8$ AU, requiring $T \sim 3K$. These are implausibly low temperatures.

In Rice et al. (2004), a disk is described as having surface density $\Sigma \propto r^{-1}$ and a Q with 'an essentially flat profile, of the order unity'. Assuming Keplerian orbital velocity profile, this requires c_s, and hence T, to increase with radius. The mass of the disk is $M_{disk} = 0.25 M_\odot$, which is distributed only out to radius 25AU, a density corresponding to a 100AU disk of mass $1.0 M_\odot$. Even with a disk an order of magnitude more massive than indicated by observational evidence, very low temperatures are required to achieve $Q \sim 1$. We find that a value of $Q = 1$ at all radii, in combination with the density, mass

and size of the disk, must yield values of T as follows :

Radius (AU)	Temperature(K)
25	160
5	32
1	6.4
0.25	1.6

These temperatures are clearly too low, particularly in the neighbourhood of the star, as observational evidence indicates temperatures in the region of 300K at a distance of 1AU (Beckwith et al.1990, Beckwith et al. 1993, Lecar et al. 2006). The conclusions of papers involving such extreme physical parameters (Rice 2003, Rice et al. 2003a, Rice 2004) must be viewed with caution.

Lodato & Rice (2004) also used SPH to model non-fragmenting, quasi steady-state disks, in which the viscous heating was balanced by parameterised cooling, in order to investigate angular momentum transport. The conclusion was that for light, thin disks $(M < 0.25M_\odot, h < 0.1R)$, angular momentum transport is a local phenomenon, so a viscous treatment may be used for the modelling of the evolution of these disks. More work was required to clarify the situation for heavier disks.

Rafikov (2004) injected a sceptical note, by pointing out that disks must be able to cool very efficiently in order for gravitational instabilities to develop into bound clumps. He noted that for the gravitational instability to form giant planets at 10 AU in a disk cooled by radiation, the gas temperature must exceed 103 K with a minimum disk mass of $0.7M_\odot$ and a luminosity of $40L_\odot$. Masses of bound objects formed as a result of instability were too large, $10M_J$ at 100 AU. Such protoplanetary disks (and planets formed in them) are not confirmed by observation.

Another interesting finding on the subject of disk cooling, is that a planet will have a cooling effect in its locality. Jang-Condell (2003) modelled the radiative transfer of a disk with a planet already in it. The planet was found to create a well causing a shadow, so the disk around the planet was cooler.

The evolution of disks once a planet has formed is dominated by fast (Type I) and slow (Type II) migration of the planet towards the central star (Masset & Papaloizou 2003). Bate (2003) created a stable disk with an embedded planet, and then used SPH to simulate its evolution, allowing the planet to accumulate gas. Planets could accumulate up to a few M_J without migrating too far, but at $10M_J$ were found to migrate quickly into the star. The model ignored disk self gravity and did not allow the central star to move. The shocks predicted by 2D models did not occur. Tanaka (2002) placed a planet in a disk and observed the migration patterns. Migration times of about 10^6 yrs were

found from 5AU in to the star. Schaefer (2004) used SPH to simulate planets embedded in a non self-gravitating, very thin disk, with a fixed central star. Two planets were found to clear the gap between them and get captured into resonant orbits. Papaloizou has studied planet-disk interactions using both a shearing box (Masset & Papaloizou 2003) and a hydrodynamics code as used by Nelson (Papaloizou 2004), and continues to find difficulty in forming large hot-Jupiter type planets which then survive beyond the lifetime of a disk.

The simulations described above all assume that a disk may be treated as isolated in space, evolving under the influence only of its own self-gravity. However, stellar separation within a cluster is of the order of disk size, so star-disk or disk-disk encounters are likely. Boffin et al. (1998) used SPH to model the effect on protostellar disks of close encounters with other stars. These were shown to result in fragmentation of the disk which could lead to formation of low-mass companion stars. Such a disruptive effect would be equally likely on protoplanetary disks.

Watkins et al. (1998) modelled disk-disk encounters and found that they lead to a shock layer which then fragments to form objects, some of which orbit the stars, some are ejected. Larson (2001) proposed that angular momentum is distributed via tidal forces in disks to neighbouring stars, which could cause accretion to be concentrated in short bursts when stars are in eccentric binaries. Accretion would be concentrated in the periods when the stars approach each other.

2.5   Accuracy of the SPH simulation method

Most of the simulations reported above (Boss, Pickett, Nelson, Rice, Bate etc) have used the SPH method, and this method has the advantage of being able to adapt efficiently to handle the wide range of densities and velocities encountered in a Keplerian accretion disk. However, doubts have been cast on the accuracy of SPH simulations.

Imaeda and Inutsuka (2003) suggested that the density formulation is wrong in SPH simulations of shear flows. An array of SPH particles with initially uniform estimated density ρ was allowed to evolve in a shearing environment, and a clumpy structure evolved, variation in the estimated density $\delta\rho$ being of the order of ρ. It was suggested that using a larger kernel, or moving objects with a modified velocity, which ensures that particle separation stays constant, would remove the problem and improve the accuracy of viscous transfer of angular momentum. In trials using various viscosity formulations, it was also noted that use of the Balsara Switch caused the formation of filaments.

Monaghan's (2006) response was that the problems reported in Imaeda & Inutsuka

(2006) were caused by poor selection of initial conditions, which are not in any case sufficiently clearly explained. Batty & Whitworth (in prep) also fail to replicate the very high noise levels obtained by Imaeda & Inutsuka, and conclude that the reported problems with SPH simply do not arise in a properly coded SPH implementation.

The importance of correctly resolving the Jeans Mass was first stipulated in Bate & Burkett (1997), and subsequent workers have taken this precaution in their simulations. Klein, for example Klein, Fisher & McKee (2004), have reported a tendency of SPH to cause multiple fragmentations when there are too few particles to resolve the Jeans mass properly, such fragmentations being artefacts of the simulations. Hubber, Goodwin & Whitworth (2006), however, refute this criticism, and demonstrate that far from causing excessive fragmentation, under-resolved SPH simulations tend to suppress fragmentation or slow it down.

2.6 Conclusion

The short protoplanetary disk lifetimes inferred from observations support the hypothesis that planets are formed by the growth of gravitational instabilities in protoplanetary disks. Although there has been some success in simulating the formation of planets, there are still questions to be answered about the cooling mechanisms necessary to allow planets to form, the transfer and dissipation of angular momentum, and the survival of planets beyond the lifetime of the disk, given the theoretical and experimental findings that they will migrate into the star. The observed preponderence of 'hot Jupiters', that is very large planets in close orbits, is currently difficult to explain.

SPH simulations, particularly by Rice and Mayer, indicate that this is a powerful method for investigation of these problems. However, we note that attention must be given to the initial conditions of the disk, and cooling should not be permitted to unrealistically cold temperatures. It is also important to ensure that sufficient SPH particles are used to resolve the disk properly.

Chapter 3

Smoothed Particle Hydrodynamics

3.1   Introduction

The method adopted for simulating the evolution of protoplanetary disks is Smoothed Particle Hydrodynamics (SPH). This method was introduced in 1977 by Lucy (1977) and independently by Monaghan and Gingold (1983). Over the subsequent decades it has been implemented, refined and improved by many workers in the Astrophysics community, notably in the Cardiff Star Formation group (Whitworth, Goodwin, Kitsionas, Stematellous, Hubber, Gladwin etc), where a robust Fortran SPH code called Dragon is now in its 3rd implementation.

As with other finite-element approaches, SPH simulates the physical behaviour of a fluid by treating the fluid as a defined number of individual elements, whose physical characteristics are repeatedly calculated and updated. Grid based systems have elements whose positions are fixed at a predetermined spacing. They can be thought of as virtual cells, the fluid moving without obstruction between cells. The time-varying physical parameters describing the contents of the cells, such as density and pressure, are calculated exactly for fixed sampling points at the centres of the cells, and interpolated between the sampling points by smoothed interpolation functions.

SPH, by contrast, treats the measurement points as actual physical particles, with the characteristics of mass, position, velocity, acceleration, and temperature. These 'particles' are allowed to interact with one another like real physical entities, moving and accelerating under the influence of their surrounding particles. Physical quantities such as pressure, density and sound speed are calculated as functions of the physical parameters of a particle and its neighbours, using smoothing kernel functions to obtain a statistically weighted average. This method has proved to give very accurate (indeed, surprisingly accurate) results in the modelling of fluids in physically verifiable experiments (Monaghan 2005,

15

Monaghan 2006), possibly because the interaction of the SPH particles so closely imitates the physical interactions of a fluid at the molecular level.

In astrophysics, SPH has the great advantage that widely varying densities can be modelled with more accuracy and greater efficiency than can be achieved using grid based methods. In the formation of planets from circumstellar disks, densities will vary by many orders of magnitude. Setting up a grid which is small enough to follow perturbations at the smallest scale will therefore result in very large numbers of cells. SPH, by contrast, in the mature implementation described here, self-adapts, providing high resolution in both space and time in high density regions, while efficiently processing far less data in areas of low density and low accelerations.

For a full description of the operation of SPH see review articles Monaghan (2005) and Monaghan (1988). Here we describe the operation of the Dragon code, highlighting important features, and noting any adaptations which have been considered, or found necessary, to allow the simulation of the evolution of disks.

3.2 SPH Operation

An overview of the operation of the Dragon code in the treatment of disks is as follows.

3.2.1 Initialisation

An array of SPH particles is created having, at this stage, only the characteristics of mass, position and temperature. The mass of all the particles does not have to be the same, so it is possible to have one particle representing a star, another a planet and many others, usually all the same mass, representing the gas of the disk. Chapter 4 describes how the particles are laid down to achieve the desired initial density profile.

The numerical order of the particles has no correlation with their positions, so the particles are then sorted using a tree code, so that lists are available of particles in various regions of the disk. In particular, a list of some specified minimum number of closest neighbours is calculated for each particle, and the distance h which is half the distance to the furthest neighbour is recorded for each particle. h is now available for use as the 'smoothing length'. Clearly, h is longer in regions of low density and shorter in higher density regions. This variable smoothing length, in contrast with the fixed smoothing lengths used in early implementations of SPH, allows for greater resolution of small high density features.

Using h, the density ρ and sound speed c are calculated. The gravity, pressure and viscous forces may now be calculated for each particle, and this information is used to

calculate an initial velocity **v** which balances the radial forces calculated for each particle. This initialisation process is described in more detail in chapter 4.

To ensure accuracy, a timestep must be calculated which is short enough to resolve the motion of the particles accurately, given the velocities and accelerations they are undergoing. This calculation is described in chapter 7.

3.2.2 Advancing the particles : the equation of motion

The particles are advanced according to an equation of motion which is symmetric between each pair of particles i and j, ensuring that linear and angular momentum are conserved. The acceleration of particle i is calculated as :

$$\frac{d\mathbf{v}_i}{dt} = \sum_j m_j \left(\frac{P_i}{\rho_i^2} + \frac{P_j}{\rho_j^2} + \Pi_{ij} \right) \nabla_i W(r_{ij}, h_{ij}) - \nabla\phi_i, \qquad (3.1)$$

where P_i, P_j and $\rho_i\rho_j$ are the pressure and density at particles i and j, respectively. The term in brackets represents the acceleration due to pressure and viscosity , and the term $-\nabla\phi$ is the gravitational acceleration. These are explained in more detail later in this chapter.

Using this equation, a loop is now entered :

1. recalculate h, ρ and temperature for all particles;

2. calculate gravity, pressure and viscous accelerations;

3. advance particles to new velocities and positions;

4. create 'sink' particles if necessary;

5. repeat.

At specified intervals, the tree and neighbour lists are recalculated, and the length of timestep is adjusted if necessary to resolve the motion of all the particles. Output files are also created regularly so that the progress of the simulation can be monitored and processed offline.

3.2.3 Output

Finally the simulation is halted at some predetermined elapsed time. All of the information about all of the SPH particles at that moment is output to a file. This output file can then be used as an input file for a subsequent simulation, in that case using all the

stored values of parameters, rather than reinitialising them. Thus a simulation can be continued if it is producing interesting results.

3.3   Treebuilding

Dragon uses a tree to shorten the process of finding neighbours of a particle, and also to allow timesaving approximations in the gravity calculation for distant particles. Although the process of building and stocking the tree is time consuming, it saves more time in the neighbour-finding and gravity-calculating routines. This is particularly efficient as the total number of particles increases.

An octal tree is constructed, based on Barnes and Hut (1986). First, a cube precisely large enough to contain all the particles is constructed and then subdivided into eight equal sized cubes. As the disks are created symmetrically about a star placed at the origin of coordinates, the intersection of the top level of cells is also at the origin of coordinates. The star itself is not included in the tree building. If there are 8 or more occupants of the cubes, they are divided again to create sub-cubes and the process is repeated down to the level necessary for each bottom level cell to have no more than 8 occupants. This level is called the leaf level. Every occupied cell is linked to neighbouring cells via careful housekeeping procedures, so that any particle can be identified with the correct cell at every level from top to leaf level.

Figures 3.1(a) and (b) show azimuthal and cross sectional views of the tree cells created by Dragon for a disk of 10000 particles with surface density gradient $\Sigma \propto r^{-7/4}$. Note that the borders of the different sized cells overlap the smaller cells precisely, so the edges of the largest cells (black) are not visible in the azimuthal plot. Table 3.1 lists the number of cells required for this disk at each level.

Given that we are looking at disks, which are almost flat, an octal tree is not the most efficient method to use. After the first 8 cells are created, half of the next level of potential cells are unused, as cells closest to the z=0 plane are always occupied, and those furthest away always empty. This is also true for the third and fourth levels, for which the dimensions of the cells are 1/8 and 1/16 of the diameter of the disk, and so a single layer of cells is sufficient to enclose a disk whose maximum height is one tenth of the disk radius, or one twentieth of the diameter. This can clearly be seen in fig. 3.1b and in table 3.1. Below these levels, the octal tree structure is even less efficient, as the number of cells occupied drops to about 9% of those available in levels 6, 7 and 8. This reflects the radial density gradient, as only the central portion of each layer of cells needs to be subdivided, as is illustrated in fig. 3.1a.

Figure 3.1: Treebuilding for a disk with surface density $\Sigma \propto r^{-7/4}$ (a) azimuthal view of cells, (b) cross sectional view of cells. (c) cells recentred on the centre of mass of contents and resized to their contents, azimuthal view, and (d) cross sectional view.
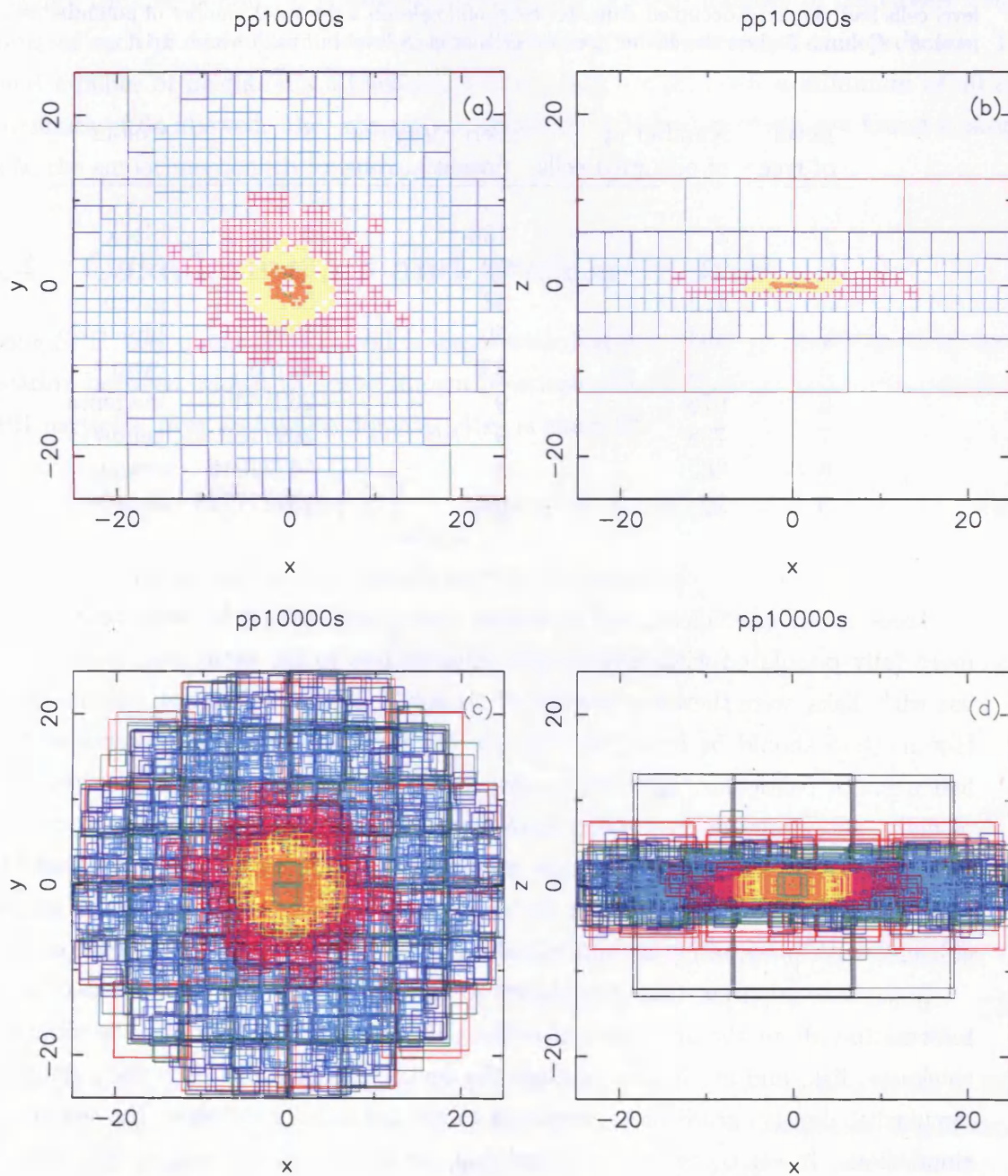
Table 3.1: Numbers of cells of the tree illustrated in fig. 3.1, compared with the potential number of cells available. Column 1 is the level of tree, l, column 2 the number of occupied cells at this level, column 3 the number of cells as a percentage of the potential number of cells at this level if all of the previous level cells had yielded 8 occupied daughter cells, and column 4 the total number of potential cells at this level, 8^l. Column 5 gives the colour used for cells at each level in figs. 3.1 and 3.4.

Level of tree	Number of of occupied cells	Percentage of potential cells	8^l	Colour
1	8	100	8	black
2	32	50	64	red
3	122	48	512	green
4	494	50	4096	blue
5	1294	33	32768	cyan
6	978	9	262144	magenta
7	738	9	2097152	yellow
8	462	8	16777216	orange
9	20	0.5	134217728	lime

Trees are more efficient, and save more time when looking for neighbours, if they are more fully populated with fewer levels. Alternatives to the octal tree, more efficient for use with disks, were therefore considered. However, it was felt that on balance the Barnes Hut method should be retained. First, it was found to have many simple and efficient features. In particular, in order to allocate a particle in a cell to the correct daughter of eight potential sub-cells, only three comparisons need be made. In turn, the x, y and z coordinates of the particle are compared with those of the centre of the cell, and this information is converted into the octal number of the daughter cell. This is highly efficient, with no squaring or multiplication or dividing involved in the comparison.

It was also apparent that alternatives to the octal tree would need to make use of prior information about the arrangement of the particles: the fact that they lie within a finite thickness disk, and are denser towards the centre, for example. Any such assumption of circularity, density gradient or thickness might potentially influence the outcome of the simulations. It was therefore concluded that the absence of any such in-built assumptions is a positive strength of the octal tree, and one less potential source of artefacts. For these reasons, it was decided to retain the octal tree for the disk simulations.

As the final stage in the construction of the tree, each cell is 'populated'. The total mass, centre of mass and the actual extent of the group of particles within the cell, and the quadrupole moments for gravity calculation, are all stored. Figures 3.1(c) and (d)

show the cells, colour coded by level as before, but recentred on their centres of mass and resized according to their contents.

Once the tree is built, it is used to calculate a stipulated number of the closest neighbours of each particle (see Gladwin, 2000, for a full explanation of this process). The usual number of neighbours stipulated in these trials is 50, with a minimum of 40 and maximum of 64 allowed. Half the radius within which 50 neighbours are found is stored as h, the smoothing length for each particle.

3.4 Calculating h,ρ and pressure forces

Using SPH, any quantity $A(\mathbf{r})$ which varies with position can be approximated by interpolation between known values at known positions. At the limit of an infinite density of SPH particles, over an infinite domain, $A(\mathbf{r})$ is given by

$$A(\mathbf{r}) = \int_{allspace} \tilde{A}(\mathbf{r}')W(\mathbf{r} - \mathbf{r}', h)d^3\mathbf{r}' \tag{3.2}$$

where W is the kernel function, which has the characteristics

$$\int W(\mathbf{r} - \mathbf{r}', h)d^3\mathbf{r}' = 1 \tag{3.3}$$

and

$$\lim_{h \to 0} W(\mathbf{r} - \mathbf{r}', h) = \delta(\mathbf{r} - \mathbf{r}'). \tag{3.4}$$

The SPH approximation, where parameter values are calculated and recorded only at particle positions, is

$$A(\mathbf{r}) = \sum_{j=1}^{jtot} A_j \frac{m_j}{\rho_j} W(\mathbf{r} - \mathbf{r}_j, h), \tag{3.5}$$

where A_j, m_j, r_j and ρ_j are the values of A, mass, position and density at particle j. Note that $d^3\mathbf{r}$ in eqn 3.2 is represented by $\frac{m_j}{\rho_j}$ in eqn. 3.5 and that the calculation is performed for the total number of particles in the computational domain, j_{tot}.

An estimate of the gradient of A at position $\mathbf{r}$ can also be made, assuming that the kernel function W is continuous, using

$$\nabla A(\mathbf{r}) = \sum_{j=1}^{jmax} A_j \frac{m_j}{\rho_j} \nabla_i W(\mathbf{r} - \mathbf{r}_j, h), \tag{3.6}$$

where $\nabla W(\mathbf{r} - \mathbf{r}_j, h)$ is the gradient of the kernel function at $\mathbf{r}$.

In particular, the density ρ_i at particle i, position $\mathbf{r}_i$ is obtained, using eqn 3.5,

$$\rho(\mathbf{r}) = \sum_{j=1}^{\mathcal{N}_{neib}} m_j W(\mathbf{r}_{ij}, h), \tag{3.7}$$

where $\mathbf{r}_{ij} = \mathbf{r}_i - \mathbf{r}_j$. Note that we are now only summing over $\mathcal{N}_{neib}$ neighbours. W is so defined that it is zero for any pair of particles i and j for which $r_{ij} > h_i + h_j$, and so any particles which are not on the neighbour list for particle i may be omitted from the calculation. In order to calculate hydrodynamic forces it is necessary to calculate the gradient of the density,

$$\nabla\rho(\mathbf{r}_i) = \sum_{j=1}^{\mathcal{N}_{neib}} m_j \nabla_i W(\mathbf{r}_{ij}, h), \tag{3.8}$$

and the divergence of the velocity, which as

$$\nabla \cdot \mathbf{v} = \frac{1}{\rho}(\nabla(\rho\mathbf{v}) - \mathbf{v} \cdot \nabla\rho), \tag{3.9}$$

is given in SPH by

$$\begin{aligned}(\nabla \cdot \mathbf{v})_i &= \frac{1}{\rho_i}\left(\sum_{j=1}^{\mathcal{N}_{neib}} m_j \mathbf{v}_j \cdot \nabla_i W(\mathbf{r}_{ij}, h) - \mathbf{v}_i \cdot \sum_{j=1}^{\mathcal{N}_{neib}} m_j \nabla_i W(\mathbf{r}_{ij}, h)\right) \\ &= \frac{1}{\rho_i}\sum_{j=1}^{\mathcal{N}_{neib}} m_j \mathbf{v}_{ij} \cdot \nabla_i W(\mathbf{r}_{ij}, h), \end{aligned} \tag{3.10}$$

where $\mathbf{v}_{ij} = \mathbf{v}_i - \mathbf{v}_j$.

From these quantities we can derive the hydrodynamic acceleration and the energy equation. The hydrodynamic acceleration is given by

$$\begin{aligned}\frac{d\mathbf{v}}{dt}\Big|_{hydro} &= -\frac{\nabla p}{\rho} \\ &= -\nabla\left(\frac{p}{\rho}\right) - \frac{p}{\rho^2}\nabla\rho \end{aligned} \tag{3.11}$$

Using the SPH approximation for the gradient of a function, eqn. 3.6, the acceleration

due to pressure forces of particle i is therefore given by

$$\frac{d\mathbf{v}_i}{dt}\bigg|_{\text{hydro}} = -\sum_{j=1}^{\mathcal{N}_{neib}} \frac{p_j}{\rho_j^2} m_j \nabla_i W(\mathbf{r}_{ij}, h_{ij}) - \frac{p_i}{\rho_i^2} \sum_{j=1}^{\mathcal{N}_{neib}} m_j \nabla_i W(\mathbf{r}_{ij}, h_{ij})$$

$$= -\sum_{j=1}^{\mathcal{N}_{neib}} m_j \left(\frac{p_j}{\rho_j^2} + \frac{p_i}{\rho_i^2}\right) \nabla_i W(\mathbf{r}_{ij}, h_{ij}) \quad (3.12)$$

In addition to pressure forces, it is necessary to introduce an Artificial Viscosity which prevents the interpenetration of streams of SPH particles. This is described separately in chapter 5.

3.4.1 The kernel function

The kernel function used throughout these simulations is the M_4 function for 3 dimensions (Monaghan and Lattanzio 1985), which is converted to a dimensionless form, $W(\mathbf{r}, h)$ for use in the Dragon code. $W(\mathbf{r}, h)$ is defined as :

$$W(\mathbf{r}, h) = \frac{1}{\pi h^3} \begin{cases} \left(1 - \frac{3q^2}{2} + \frac{3q^3}{4}\right), & 0 \leq q \leq 1.0; \\ \\ \frac{1}{4}(2-q)^3, & 1 \leq q \leq 2.0; \\ \\ 0, & q > 2.0; \end{cases} \quad (3.13)$$

where the separation factor $q = \frac{|\mathbf{r}|}{h}$. Figure 3.2 shows the value of W plotted against $q/2$.

3.4.2 Energy equation

Two equations of state were used in these simulations. First, a locally isothermal equation of state was used, in which the disk was assumed to be able to radiate any excess energy instantaneously, maintaining a specified temperature profile.

Secondly a more realistic adiabatic equation of state was used. The disk was initialised with a temperature profile $T(r)$. Heating and cooling due to compression and rarefaction were applied to the disk as it evolved, and the disk was allowed to cool (or warm) back to its original temperature profile, with an imposed cooling time set to be a fraction of the orbital period (cf Rice et al. 2003).

In SPH formulation, the rate of change of energy per unit mass for particle i can be
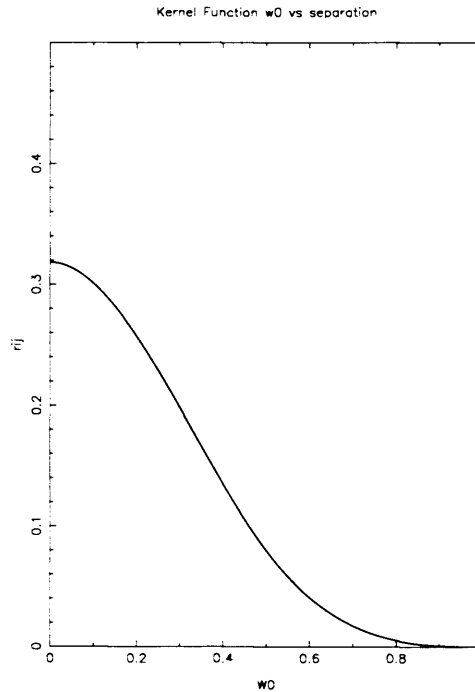
Figure 3.2: $W(\mathbf{r}, h)$, the dimensionless version of the M_4 kernel for three dimensions, plotted against $\frac{|\mathbf{r}|}{2h}$.

shown to be

$$\frac{du_i}{dt} = -\frac{1}{2} \sum_{j=1}^{\mathcal{N}_{neib}} m_j \left(\frac{p_j}{\rho_j^2} + \frac{p_i}{\rho_i^2} \right) \mathbf{v}_{ij} \cdot \nabla_i W(\mathbf{r}_{ij}, h_{ij}). \tag{3.14}$$

At any timestep in the simulation therefore, the value of $\frac{du_i}{dt}$ is calculated using eqn. 3.14, and the temperature T_i updated to become

$$T_i + \frac{2}{3k\bar{m}} \cdot \frac{du_i}{dt} \delta t - (T_i - T_0(r)) \frac{\delta t}{t_{cool}}, \tag{3.15}$$

where k is Boltzman's constant, $\bar{m}$ is the mean gas particle mass for molecular interstellar gas, $T_0(r)$ is the original temperature profile of the disk, δt the length of a timestep and t_{cool} the cooling time, set to be half an orbital period.

3.5   Gravity calculations.

The acceleration of any particle i due to the gravitational attraction of all the other particles j, assuming that the particles are infinitely small with all mass m_j concentrated at the position $\mathbf{r_j}$ of each particle, is given by,

$$a_{ij} = \sum_{i/neqj}^{\mathcal{N}_{tot}} \frac{Gm_j}{r_{ij}^3} \mathbf{r}_{ij}, \tag{3.16}$$

where $r_{ij} = |\mathbf{r_{ij}}|$. In the Dragon implementation of SPH this is modified in two ways.

3.5.1 Gravity Softening

First, gravity is softened for particles approaching within small distances (Hernquist & Katz 1989). The SPH particles are representative of mass which extends over a distance of the order of h for each particle. Therefore it is unrealistic to continue to treat the particles as point masses if they approach within this distance, as very large accelerations will result. The softened gravitational acceleration becomes

$$a_{ij} = \sum_{i \neq j}^{\mathcal{N}_{tot}} \frac{Gm_j}{r_{ij}^3} W^*(r_{ij}, h_{ij}) \mathbf{r}_{ij}. \tag{3.17}$$

The smoothing function W^* is obtained from the kernel function, and represents the fraction of the mass of each particle within the radius r_{ij}. W^* is given by

$$W^*(r_{ij}, h_{ij}) = 4\pi \int_0^q W(r_{ij}, h_{ij}) q^2 dq. \tag{3.18}$$

For the M_4 kernel therefore,

$$W^* = \frac{1}{30} \begin{cases} 40q^3 - 36q^5 + 15q^6, & 0 \leq q \leq 1; \\ 80q^3 - 90q^4 + 36q^5 - 5q^6 - 2, & 1.0 \leq q \leq 2.0; \\ 30, & q > 2.0. \end{cases} \tag{3.19}$$

Figure 3.3 shows the form of this smoothing function plotted against separation. The gravitational attraction of distant particles is unmodified, while the attraction of close particles is reduced as they approach within the distance h.
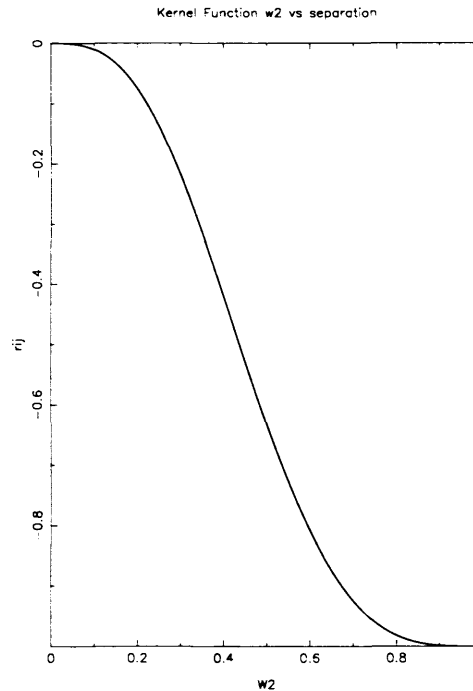
Figure 3.3: The gravity softening kernel function W^* plotted against separation $\frac{r_{ij}}{2h}$.

3.5.2   Tree Gravity

Dragon also modifies gravity calculations for distant particles, by making use of the tree whose construction was explained in section 3.1. A direct calculation using eqn. 3.17 for $\mathcal{N}$ particles will require $\mathcal{N}^2$ calculations. The use of the algorithm developed by Barnes and Hut (1986) reduces the number of calculations so that it scales with $\mathcal{N}log\mathcal{N}$.

The algorithm works as follows. For any particle i, the tree is examined, from the top downwards. For each cell, its angular size, or 'opening angle', as viewed from particle i, is calculated, and compared with a maximum value permitted, θ_{max}. If the opening angle is smaller than θ_{max}, then the whole cell is treated as a single object, with the centre of mass, mass and quadrupolar moments already calculated and stored for this cell. If the cell is too large, it is opened and the next level of cells are examined in the same way.

Fig. 3.4 shows how Tree Gravity works for a disk. Figures 3.4a and b show the azimuthal view and cross section of a disk with 10,000 particles, which has been broken down into cells for the tree-gravity calculation for point 9737, which is situated at the right hand edge of the disk, marked with an asterisk. It can be seen that most of the disk has been treated as cells, some of them coloured red, indicating that they are level 2 cells. It is only in the region very close to particle 9737 that gravity has to be calculated for individual particles, which are indicated by dots. Only 335 calculations are necessary for this Tree Gravity calculation, rather than the 9999 which would be necessary if all
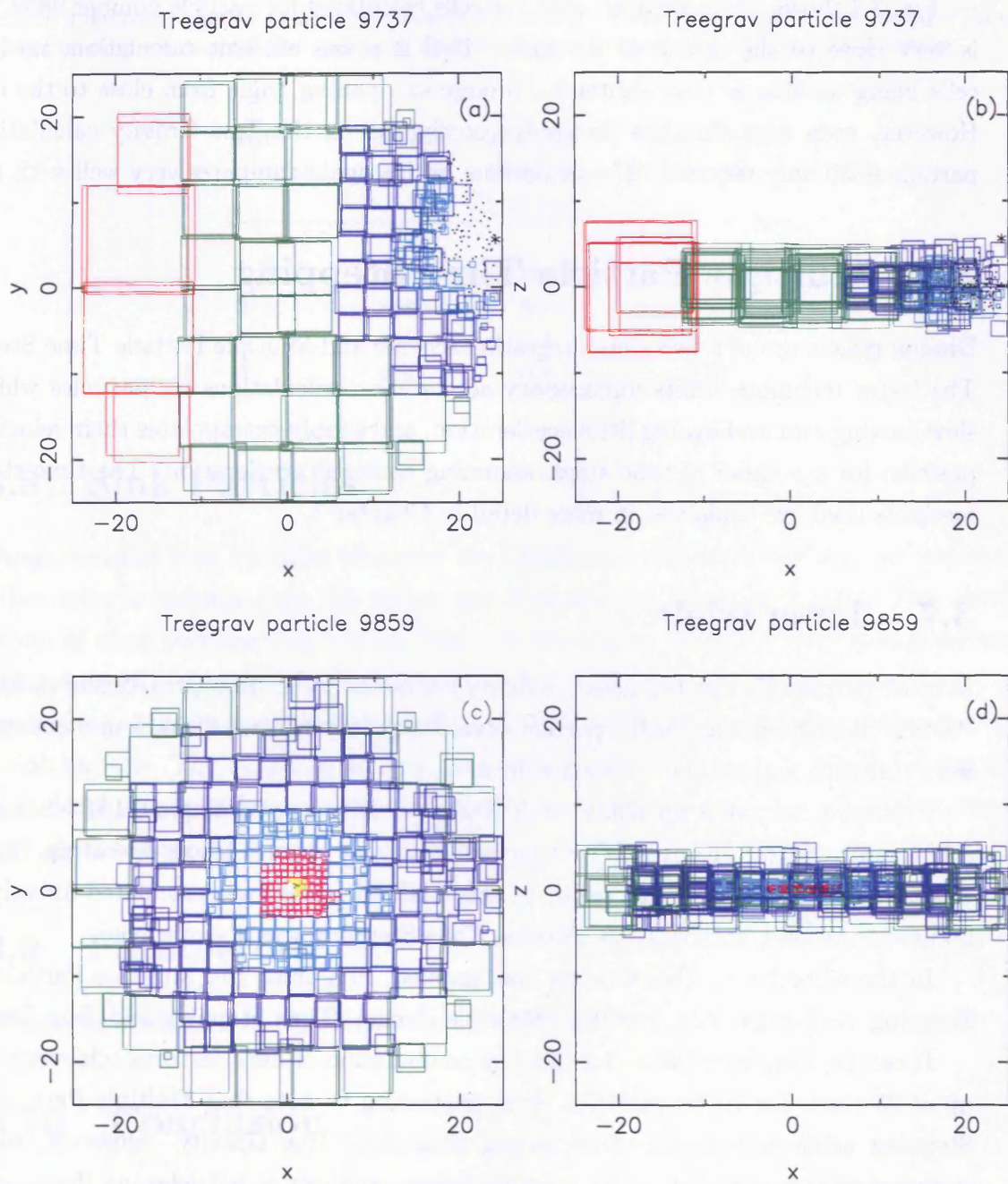
Figure 3.4: The tree cells used for calculation of gravity for (a) particle 9737, located at right hand edge, indicated by an asterisk. Levels of cells within the tree are indicated by the colours listed in Table 3.1, and individual particles are indicated by black dots. A total of 335 particles and cells are visible; (b) cross sectional view of (a); (c) azimuthal view of cells used to calculate gravity for particle 9859, close to the centre of the disk. 727 cells and particles are visible; (d) cross sectional view of (c).

particles were considered individually.

Fig. 3.4 shows the same disk, with the cells calculated for particle number 9859, which is very close to the centre of the disk. This is a less efficient calculation, no level 2 cells being useable as they subtend too large an opening angle from close to the centre. However, even with this less favourable configuration, the Tree Gravity calculation for particle 9859 only requires 727 calculations, which again compares very well with 9999.

3.6   Multiple Particle Time Stepping

Dragon makes use of a two step integration scheme and Multiple Particle Time Stepping. The latter technique omits unnecessary acceleration calculations for particles which are slow moving and undergoing little acceleration, and simply extrapolates their velocity and position for a number of time steps, assuming constant acceleration. The time stepping methods used are explained in more detail in Chapter 7.

3.7   Time trials.

In order to quantify the increases in efficiency achieved by a. Tree Gravity and b. Multiple Particle Time Stepping, for the particular case of protoplanetary disks, four identical trials were run with and without these features.

Protoplanetary disk pp10000s, with 10000 particles representing a $0.1 M_\odot$ disk around a $1 M_\odot$ star was set into Keplerian rotation, with only gravity forces operating. The disk was evolved through 100 time steps. In this trial, all gravity was calculated directly, with no use of the tree, and Multiple Particle Time Stepping was also disabled.

In the second run, Tree Gravity was enabled, in a third run Multiple Particle Time Stepping, and in the final run both Multiple Particle Time Stepping and Tree Gravity.

It can be seen from table 3.2 that the combination of both features achieves a speed-up of 25 times for 10000 particles. It is interesting to note that Multiple Particle Time Stepping achieves a greater time saving than does Tree Gravity. However, the time stepping efficiency will stay the same for larger numbers of particles, as the proportion of particles requiring short timesteps will remain the same, however many particles are used. Tree Gravity, on the other hand, will become more efficient, as more particles are used.

Table 3.2: Time taken to evolve a 10,000 particle disk for 100 timesteps. Column 1, is the run number, column 2 indicates whether or not Tree Gravity was enabled, column 3 whether or not Multiple Particle Time Stepping was enabled and column 4 the time elapsed to evolve the disk for 100 timesteps.

Run number	Tree gravity	Multiple Particle Time Steps	Time elapsed min:sec
1	no	no	55:10
2	yes	no	7:75
3	no	yes	5:48
4	yes	yes	2:22

3.8 Sink Particles

Dragon creates Sink Particles whenever the density in a region exceeds a preset value, and other criteria indicate that the region has become gravitationally bound. The affected group of close particles are deleted from the simulation, all their mass and momentum being assigned to a special sink particle. Sink particles are not included in the tree, and are treated separately in gravity calculations. In disk simulations, the star is initialised as a sink particle. The formation of sink particles prevents Dragon from slowing down when high density regions form, as the high accelerations in such regions will tend to require very short timesteps.

3.9 Parameters

The parameters used in the simulations of disks are listed in table 3.3.

3.10 Conclusion

The Dragon SPH code makes use of Multiple Particle Time Stepping and Tree Gravity to achieve efficiency. This is shown to achieve a 25 times improvement in processing time for a Keplerian disk modelled with 10000 particles.

Table 3.3: Parameter values used in SPH simulations of disks.

Label	Value	Description
N_{tot}	> 10000	Number of SPH particles in simulations
$\mathcal{N}_{neib}$	50	ideal number of neighbours
$\mathcal{N}_{max}$	60	maximum number of neighbours
$\mathcal{N}_{min}$	45	minimum number of neighbours
α	1.0	bulk viscosity term α
β	2.0	shear viscosity term β
η	0.1	viscous soundspeed constant η
θ_{max}	0.44	maximum opening angle
r_{disk}	100AU	maximum radius of disk
M_{star}	$1 M_\odot$	mass of star
M_{disk}	$0.1 M_\odot$	maximum mass of disk
r_{sink}	0.1AU	sink radius
ρ_{sink}	10^{-6}	sink density g/cm^3
α^*	0.1	α^* for time varying viscosity
C1	0.2	Timing constant for time-varying viscosity

Chapter 4

Disk Configuration

4.1   Disk initialisation

Correct initialisation of SPH disk simulations is crucial for the validity of the simulations. There are three stages to this process.

First the SPH particles are generated by a random process to give a disk of the correct dimensions and with the required surface density gradient and total mass. The particles are spaced to avoid very close pairs of particles, which could provide the seeds of gravitational instabilities. At this stage the initial temperature profile is also calculated and the temperature of each particle is assigned.

Next the vertical height of the particles is generated, in order to yield a disk in which hydrostatic forces balance gravitational forces in the vertical direction. This is therefore a function of the temperature and density of the disk.

Finally, the gravitational and pressure forces on all particles are calculated and used to calculate an orbital velocity which will exactly balance the radial components of these forces.

In this chapter we first explain the technique used to obtain disks of randomly positioned particles which conform to a prescribed density profile. The particular characteristics of the gravitational fields are examined.

We then explain how a hard core or inhibition technique (Diggle, 1983) is used to ensure 'anti-clustering' of particles.

Finally the calculation of the vertical height and the equilibrium velocity of each particle is described.

4.2   Self gravitating disks

Disk-shaped sets of particles of varying density gradients may be created using random numbers $\mathcal{R}$ to generate the individual particle positions.

Given a disk with surface density $\Sigma(r)$, we first calculate the function $p(r)$, where

$$p(r) = \frac{\int_0^r \Sigma(r)2\pi r dr}{\int_0^\infty \Sigma(r)2\pi r dr} \tag{4.1}$$

A disk with surface density Σ is then produced by positioning particles according to

$$\left.\begin{aligned}
p(r) &= \mathcal{R}_r\,, \\
\phi &= 2\pi\mathcal{R}_\phi\,, \\
x &= r\cos(\phi)\,, \\
y &= r\sin(\phi)\,,
\end{aligned}\right\} \tag{4.2}$$

where $\mathcal{R}_r$ and $\mathcal{R}_\phi$ are random numbers in the range 0-1.

For example, a disk of type 2Dα with surface density $N \propto r^{-\alpha}$ is created by positioning the particles according to

$$\left.\begin{aligned}
r &= \{(2-\alpha)\mathcal{R}_r/2\}^{1/(2-\alpha)}\,, \\
\phi &= 2\pi\mathcal{R}_\phi\,, \\
x &= r\cos(\phi)\,, \\
y &= r\sin(\phi)\,,
\end{aligned}\right\} \tag{4.3}$$

where $\mathcal{R}_r$ and $\mathcal{R}_\phi$ are random numbers in the range 0-1.

Datasets may be created with any number of particles, however sufficient particles must always be used to ensure the resolution of the Jeans Mass (Bate and Burkett 1997) in high density regions. The Jeans Mass is given by :

$$M_J \simeq \frac{6a^3}{G^{3/2}\rho^{1/2}}. \tag{4.4}$$

For a typical disk with surface density $0.03M_\odot/\text{AU}^2$, temperature 300K and sound speed 1km/sec at 1AU from the central star, we obtain a value of $M_J \simeq 0.0025M_\odot$, and Jeans radius $R_J = 0.4$AU.

All the examples shown here have at least 10,000 particles, which for disks less than $0.1M_\odot$ yields a sufficiently small particle mass to resolve the Jeans Mass with a large safety margin.

Figure 4.1 shows examples of disks produced with α varying from 0 to 1.75, as viewed

by an observer on the axis of the disk. For comparison, a spherical distribution of particles is also shown, an arbitrary projection being used.

4.2.1 The effect of density gradient on the rotation curve

Mestel (1979) showed that the Gravitational field of a disk is very different from that of a sphere. At a radius r from the centre of a sphere, only the mass within the radius needs to be considered, and exerts the same gravitational attraction as if all the matter were concentrated in a point at the centre. This is not the same in a disk, where matter outward of radius r actually exerts an outward force on a particle at r. The total attraction is therefore the difference between the inward attraction of matter inward of radius r and the outward attraction of matter outside radius r.

For each of the disks in fig. 4.1, the sum of the gravitational attraction of all the particles was calculated for 50 equally spaced test-points from the centre of the disk to the outer edge at radius $\mathcal{R}_0$. Note that the particles were assumed to be stationary for the purposes of calculating the distance to the test-points. The gravity of very close particles was softened to avoid singularities. This was done by adding $0.001\mathcal{R}_0^2$ to the square of interparticle distances, so that the value of $\frac{1}{r^2}$ could not be greater than $1000\mathcal{R}_0^{-2}$.

For all radii the resultant force was found to point towards the centre of the disk, with no component in the direction of the orbits of the points. This was as predicted for a stationary, radially symmetrical disk.

The radial component of the resultant force was calculated, and from this, the equilibrium orbital speed of particles at each radius was calculated from the relationship $v^2/r = a$, where v is the orbital speed, r the radius and a the acceleration. Radius was normalised by dividing by the outer radius $\mathcal{R}_0$ of the disk. The speed was normalised by dividing by $\mathcal{V}_0$, the orbital speed of a particle at radius $\mathcal{R}_0$ about a particle of mass $\mathcal{M}$, where $\mathcal{M}$ is the total mass of the disk.

For each type of artificial disk, 100 realisations were analysed, so that means and standard deviations could be obtained for the parameters extracted.

Figure 4.2 shows the rotation curves obtained for the five disks and for comparison, a sphere. All have the same mass and the same radius. It can be seen that the curves are convergent, with small standard deviations about the means for each point. The same curves are obtained when the total number of particles within the disks are changed.

Figure 4.2a shows the rotation curve for a sphere, which as expected is a straight line from zero at the centre of the sphere, to 1 at $r=1$, where the gravitational attraction of the sphere is exactly the same as if all its mass were concentrated at the centre, and therefore $v(r) = \mathcal{V}_0$. It is not a Keplerian curve, with $v(r) \propto r^{-0.5}$, because for any radius,
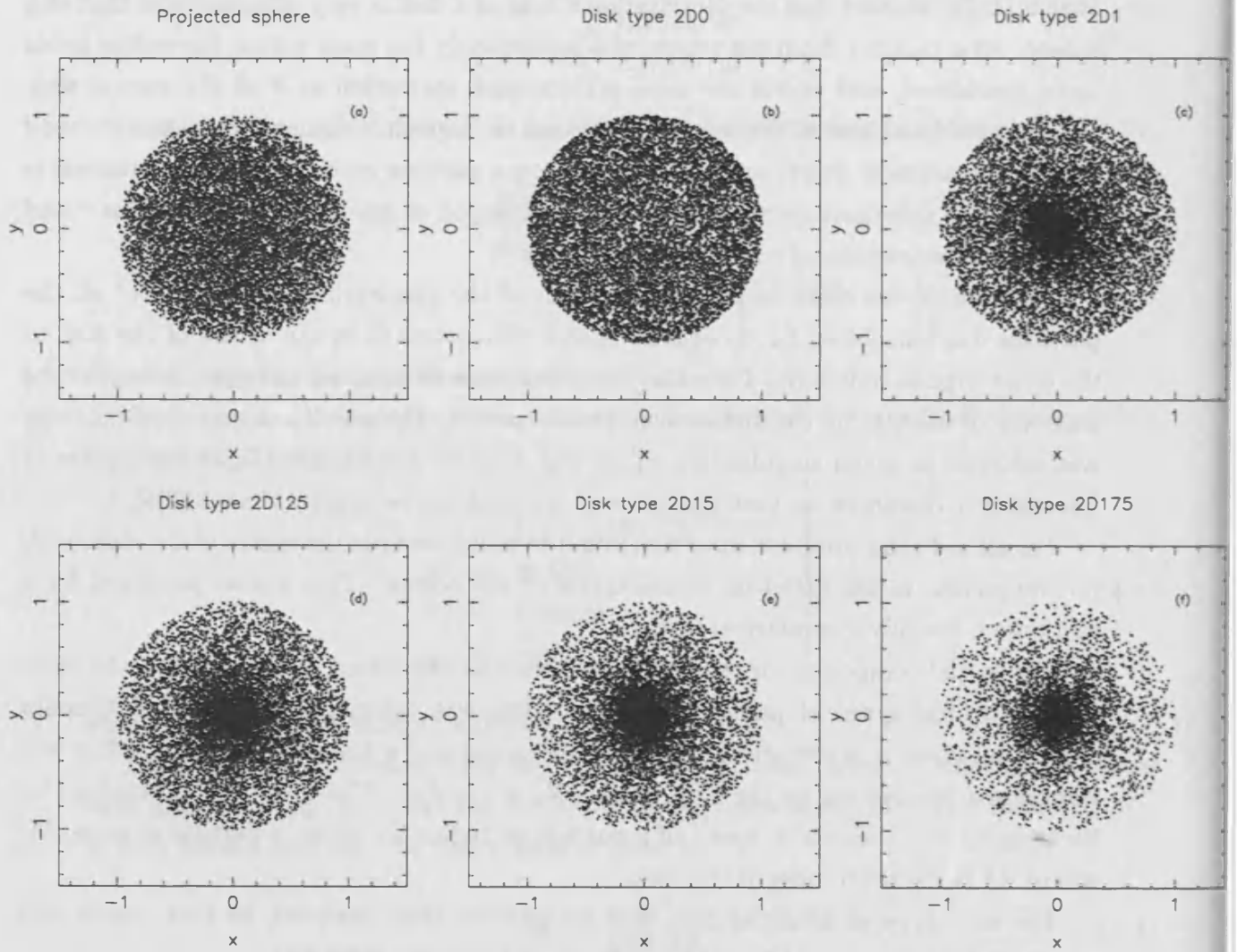
Figure 4.1: Examples of artificial datasets, azimuthal view: (a) 3D0, n constant; (b) 2D0, N constant; (c) 2D1, $N \propto r^{-1}$; (d) 2D1.25, $N \propto r^{-1.25}$; (e) 2D1.5, $N \propto r^{-1.5}$; (f) 2D1.75, $N \propto r^{-1.75}$.
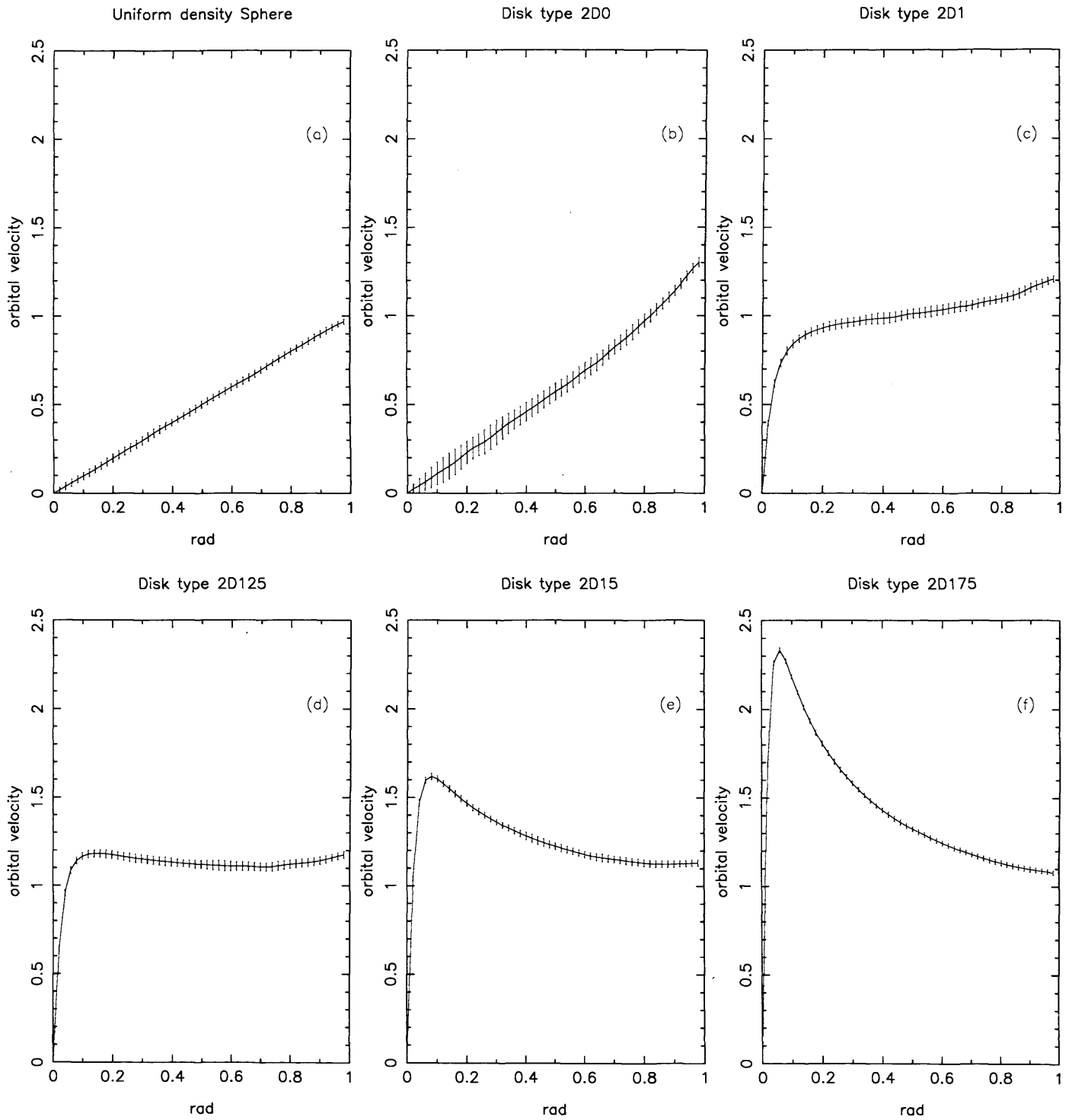
Figure 4.2: Rotation curves for (a) 3D0, n constant; (b) 2D0, N constant; (c) 2D1, $N \propto r^{-1}$; (d) 2D1.25, $N \propto r^{-1.25}$; (e) 2D1.5, $N \propto r^{-1.5}$; (f) 2D1.75, $N \propto r^{-1.75}$. Radius is normalised to the radius of the disk. Velocity is normalised by dividing by the orbital velocity at radius $=1$ about the mass of the disk if placed in a point mass at the centre of the disk.

Table 4.1: Rotation curves for disks of varying density. Column 1 lists the disk type. Column 2 gives the slope of the inner solid body region, $\frac{dv}{dr}(inner)$. Column 3 gives the outer radius of the inner region R_i. Column 4 gives the slope of the outer region, $\frac{dv}{dr}(outer)$. Column 5 is the maximum orbital velocity within the disk V_{max}. Column 6 gives the radius at which maximum orbital velocity is reached. R_{max}.

Cluster type or name	$\frac{dv}{dr}(inner)$	$\mathcal{R}_i$	$\frac{dv}{dr}(outer)$	$\mathcal{V}_{max}$	$\mathcal{R}_{max}$
$2D0(N \propto r^0)$	1.0	1.0	1.0	1.6	1.0
$2D1(N \propto r^{-1})$	11.0	.08	0.3	1.3	1.0
$2D125(N \propto r^{-1.25})$	20.8	.06	0.0	1.25	1.0
$2D15(N \propto r^{-1.5})$	27.8	.06	−0.55	1.7	0.07
$2D175(N \propto r^{-1.75})$	38.9	.06	−0.7	2.4	0.06

the mass inward of the radius is $\propto r^3$. Therefore $v(r) \propto r$.

Figure 4.2b, for a constant surface density disk, shows a similar straight line, but in this case the velocity at the edge of the disk is higher than for the sphere, by a factor of 1.45 ± 0.04. This is close to Mestel's prediction of $\pi/2.0$.

Figure 4.2c shows the velocity curve for disk type 2D1, $N \propto r^{-1}$. This shows an inner steeply sloping section up to r=0.1, at which $v(r) = 0.8V_0$. The region within this radius is one of near solid body rotation. Outside the sharp change of slope at R=0.1, Mestel predicts that the rotation curve should be flat, but we find that the outer part of the curve has a small positive gradient, the maximum velocity at the edge of the disk being $1.3V_0$.

Figure 4.2d shows that it is disk 2D125, $N \propto r^{-1.25}$, that yields a flat outer section. As α is increased, in figures 4.2e and 4.2f, this outer section becomes negatively sloping, and the maximum value of $v(r)$ is actually found within the disk, at the outer edge of the inner region of near solid body rotation.

4.2.2   Outer edge effects

Note that for values of α between 1.00 and 1.5 there is a distinct upwards tilt of the rotation curve at the outer edge of the disk, where the outward pull of the disk suddenly falls to zero. This is a real feature of this type of disk, with a sharp edge, and may be sufficiently steep for v to be proportional to r. That is, a region of solid body rotation forms. In a solid body rotation zone, material on inner and outer orbits does not pass due to differential orbital speeds, so nascent structures have more chance to form without being torn apart by tidal shear. This outermost part of a sharp-edged disk may therefore form

an optimum zone for the formation of structure and, ultimately, gravitational instabilities.

Table 4.1 tabulates the key features of the five disks: the slopes of the inner and outer regions, the maximum orbital velocity and the radius at which maximum orbital velocity is reached.

4.2.3 Inner edge effects

It is a common technique, in SPH treatments of disk dynamics, to omit the central portion of the disk, and to consider only an annulus[1] (eg Mayer et al. 2004, Nelson et al 1998). This has the undoubted benefit of omitting the particles on the very fast, inmost orbits in a Keplerian disk. However, this then creates the problem of inner edges.

As pointed out by Mestel, the self-gravitational force at the inner edge of an annulus is outwards. It is therefore impossible to calculate real orbital velocities for the particles in these regions, so Figure 4.2 cannot be reproduced for disks with the central portion omitted.

The outward force is greatest for annuli which are densest at the inner edge. Figure 4.3 demonstrates this phenomenon. Figure 4.3a shows the inward gravitational force plotted against radius for an annulus with constant surface density N. Figure 4.3b shows the same plot for an annulus with varying surface density $N \propto r^{-1.5}$, and Figure 4.3c shows an annulus with an even denser inner edge, surface density $N \propto r^{-1.75}$. It can be seen that for all three annuli, there is an inner region where the self-gravity of the annulus is directed outward from the centre. The magnitude of this outward force increases with the density of the central region. The maximum value of outward force corresponds precisely with the inner edge for all three annuli.

The outward force diminishes with increasing radius, for radii greater than the inner edge of the annuli. The radius at which the radial force is zero varies between the annuli, being 0.22 for the first disk, 0.13 for the second and 0.12 for the third. Although the annulus with constant surface density has the smallest outward force at the inner edge, this annulus has the largest extent over which the force is directed outwards, and for which, therefore, it is impossible for matter to orbit in centrifugal balance.

The calculation of this inward force is very sensitive to the extent of softening in the gravity calculation. The gravitational acceleration at a position r_i is calculated as

---

[1]An annulus is correctly defined as the portion of a plane bounded by two concentric circles, of any radii, in the plane. Thus a very narrow ring, or a large disk with only a tiny central hole, may equally correctly be described as annuli.
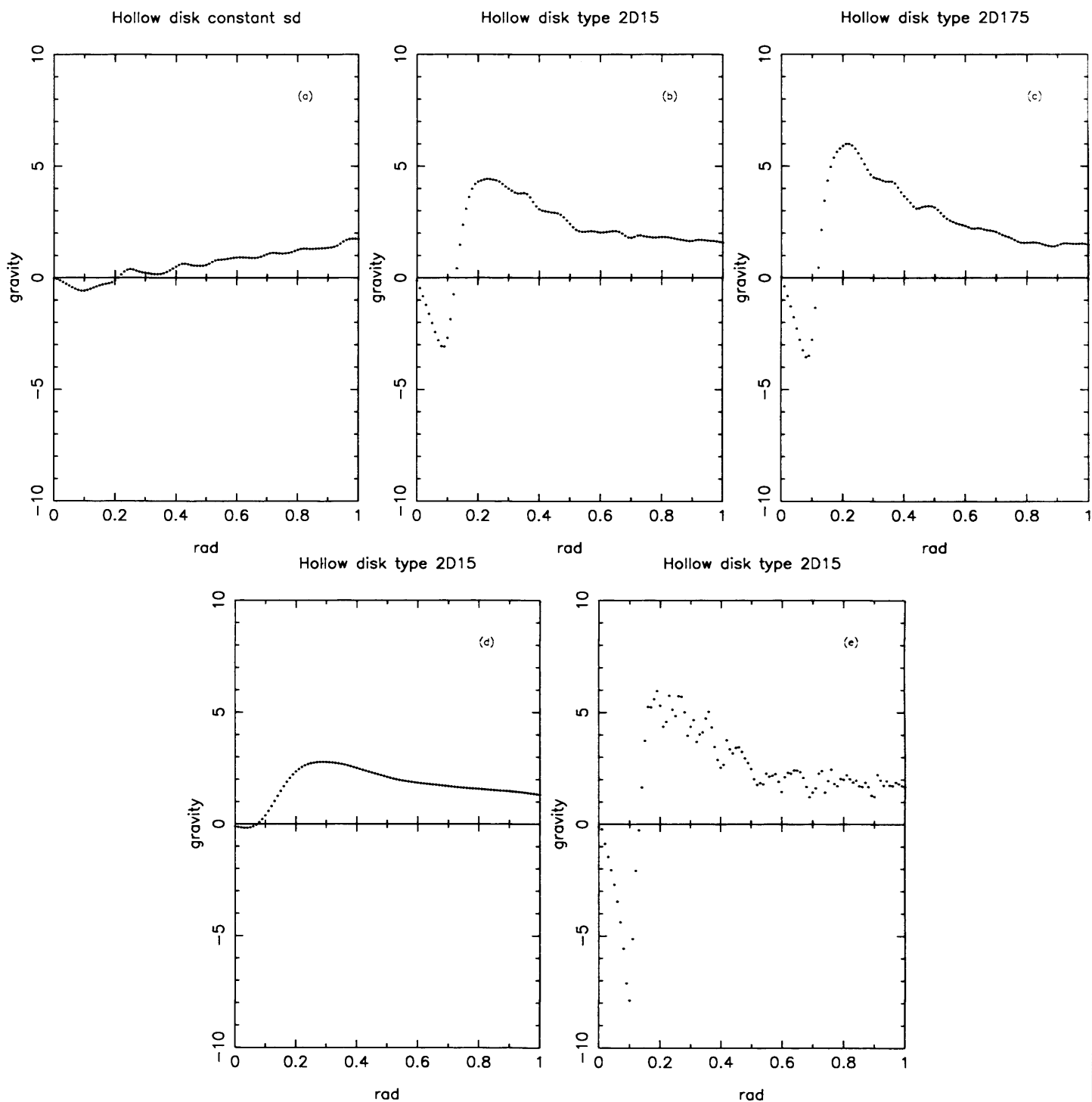
Figure 4.3: Gravity vs radius for annuli. No data points lie within a radius of $0.1\mathcal{R}_0$ of the centre. The masses of all the annuli are 1 unit. Radius is normalised by dividing by the outer radius $\mathcal{R}_0$. Gravity is normalised so that one unit is the gravitational attraction of a point with unit mass at a radius of $\mathcal{R}_0$. A variable smoothing factor ϵ is used in the gravity calculation (egn. 4.5). (a) Annulus, surface density N constant, $\epsilon = 0.03\mathcal{R}_0^2$; (b) Annulus, surface density $N \propto r^{-1.5}$, $\epsilon = 0.03\mathcal{R}_0^2$; (c) Annulus, surface density $N \propto r^{-1.75}$, $\epsilon = 0.03\mathcal{R}_0^2$; (d) same as (b) but $\epsilon = 0.1\mathcal{R}_0^2$; (e) same as (b) but $\epsilon = 0.01\mathcal{R}_0^2$.

$$g_i = -G \sum_j \left(\frac{m_j \mathbf{r}_{ij}}{\left(|\mathbf{r}_{ij}|^2 + \epsilon^2 \right)^{3/2}} \right), \qquad (4.5)$$

where ϵ has the effect of softening the acceleration calculated for particles which are very close to the position $\mathbf{r}_i$.

Figure 4.3d shows the same disk as in Figure 4.3b, but the gravity calculation has smoothed the gravity for close particles more heavily ($\epsilon = 0.03\mathcal{R}_0^2$ for figs. 4.3a,b and c, $\epsilon = 0.03\mathcal{R}_0^2$ for fig. 4.3d). It can be seen that the maxima of the self gravity, either side of the inner edge are much smaller, and the radial force is inward for all radii greater than 0.1. In Figure 4.3e, $\epsilon = 0.01\mathcal{R}_0^2$, and the data is therefore far noisier. In this case, the maximum outward force is three times larger than obtained in Fig. 4.3a, and there is once more a region between r=0.1 and r=0.13 for which the radial force is outward and no stable orbits are possible. Gravity smoothing must be used with care in the analysis of disks.

An annulus of matter can only be stably set into orbit if it has at its centre a large mass, such that the gravitational attraction of the central mass is larger than the outward attraction of the annulus at the inner edge of the annulus.

This creates an interesting problem for the early stages of molecular cloud collapse and disk formation. Any gap at the centre of an accretion disk will be uncrossable until the central object is massive enough to provide enough inward force to outweigh the outward force of the accretion disk. Accretion will not be possible from the disk until enough material has accreted from elsewhere onto the central object.

4.2.4 Combining disks and central point masses

The experiment which produced Fig. 4.2 was repeated, but this time an annulus was created with mass $0.1m$ with values of r from 0.1 to 1.0, and a single object of mass $1m$ placed at the centre. The orbital velocities for points orbiting at radii from 0 to 1 distance units were calculated, again, normalised to the velocity at distance 1 unit from the $1m$ point by itself. The result for a disk with radial density profile r^{-1} is shown in Fig. 4.4a, and for comparison, the rotation curve for the point mass m by itself, is included, as the red dotted line. Clearly there is little difference in the rotation curves for the central object on its own, and the central object plus disk. However, if the annulus is made heavier, or compressed into a narrow radial extent, a difference may be seen. Figure 4.4b shows the result for a $0.1M$ annulus from radius 0.04 to 0.2 units, as used in Mayer (2004), while Figure 4.4c is a $1M$ annulus from 0.06 to 0.5 units, as used in Nelson (1998). Both curves show a divergence above the red rotation curve, noticeably in

the region of the annulus, where the slope of the velocity curve is much shallower, and in the case of Fig. 4.4c, the value of $\frac{dv}{dr}$ is positive in the region of the annulus, rather than negative. This will result in much lower relative velocities between neighbouring particles on different orbital tracks.

4.2.5   The effect of density gradients on the Toomre Q parameter

The Toomre Q stability parameter may be used to predict the unstable areas of rotating disks (Binney and Tremaine, 1987). Q is calculated as

$$Q = \frac{\kappa c_s}{\pi G \Sigma}.$$
(4.6)

Here κ is the epicyclic frequency, c_s the sound speed, Σ the surface density of the disk, and G the gravitational constant. A value of Q greater than about 1.5 (the precise critial value is unknown) is taken to indicate that gravitational fragmentation is impossible. as collapse of a fragment will be opposed by outward forces due to pressure and rotation.

κ is given by (Binney and Tremaine,1987) :

$$\kappa^2 = r\frac{d}{dr}\Omega^2 + 4\Omega^2$$
(4.7)

For a Keplerian disk, $\Omega \propto r^{-3/2}$ and therefore $\kappa = \Omega$, while for solid body rotation. Ω is constant, and $\kappa = 2\Omega$.

The original derivation of the Toomre Q parameter is valid for an infinite rotating sheet. However, Q is used as an indicator of stability against gravitational collapse in simulations of disks, or rather annuli, which are finite in extent (eg Nelson (1998), Rice et al.(2004), Mayer (2004)). The difference in orbital speed caused by the edge effects of a self-gravitating annulus, as compared with the same sized region of a complete disk, will affect the value of Q calculated in the two cases.

A comparison of Ω and the calculation of κ using Eqn. 4.7 is shown in Fig. 4.5. It has been calculated for the 1m disk from 0.06 to 0.5 distance units, around a 1m star. Compare with the rotation curve shown in fig. 4.4c. The region in which the orbital velocity rises with radius causes an increase in the true value of κ, which is higher than Ω throughout the region of the disk, and particularly toward the outer edge. Because of this, Q calculated using the approximation that $\kappa \simeq \Omega$ will be incorrect (too low). An isolated annulus is therefore not fully representative of the equivalent region in an extended disk.

Disk, sd propto r°−1

Disk, sd propto r°−1

Disk, sd propto r°−1
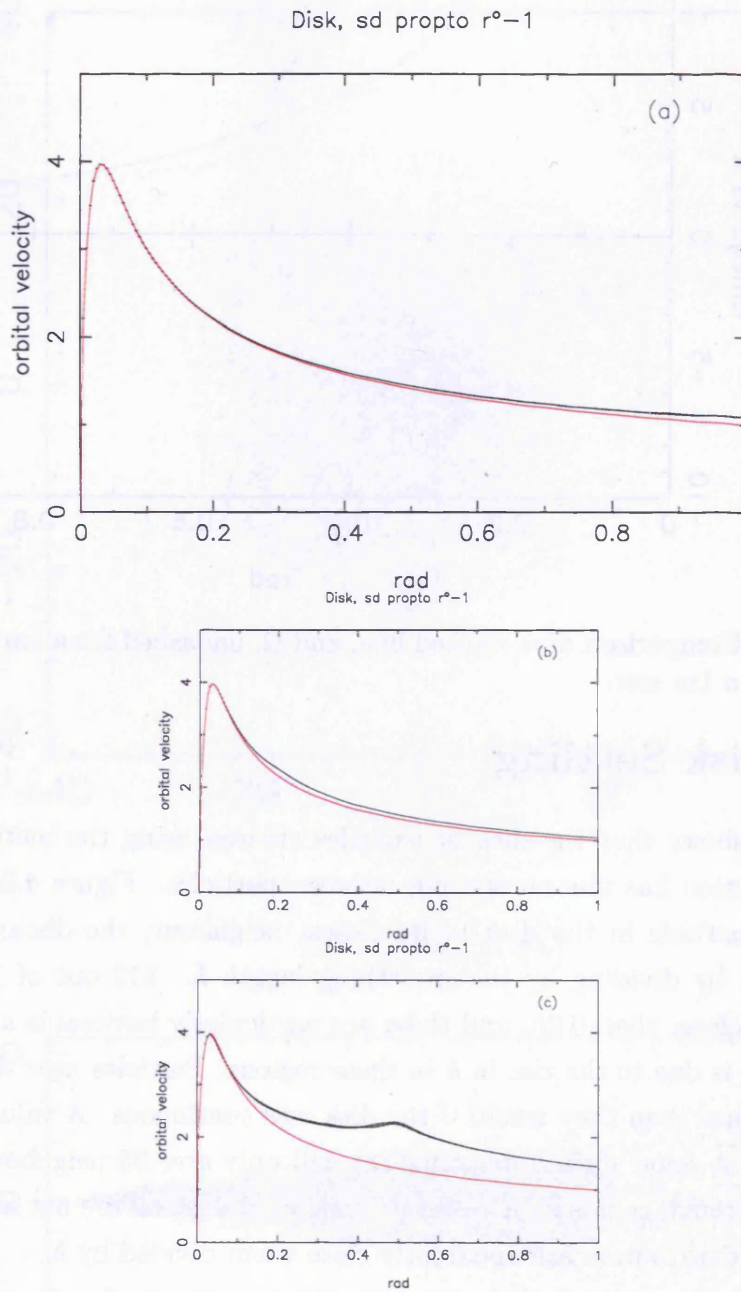
Figure 4.4: Rotation curves for annuli with central objects of mass 1m: (a) annulus has mass 0.1m, $0.1 \leq r \leq 1.0$; (b) annulus mass 0.1m, $0.04 \leq r \leq 0.2$; and (c) annulus mass 1.0m, $0.06 \leq r \leq 0.5$. Black is the rotation curve for central point plus annulus, red the rotation curve for the central point only.
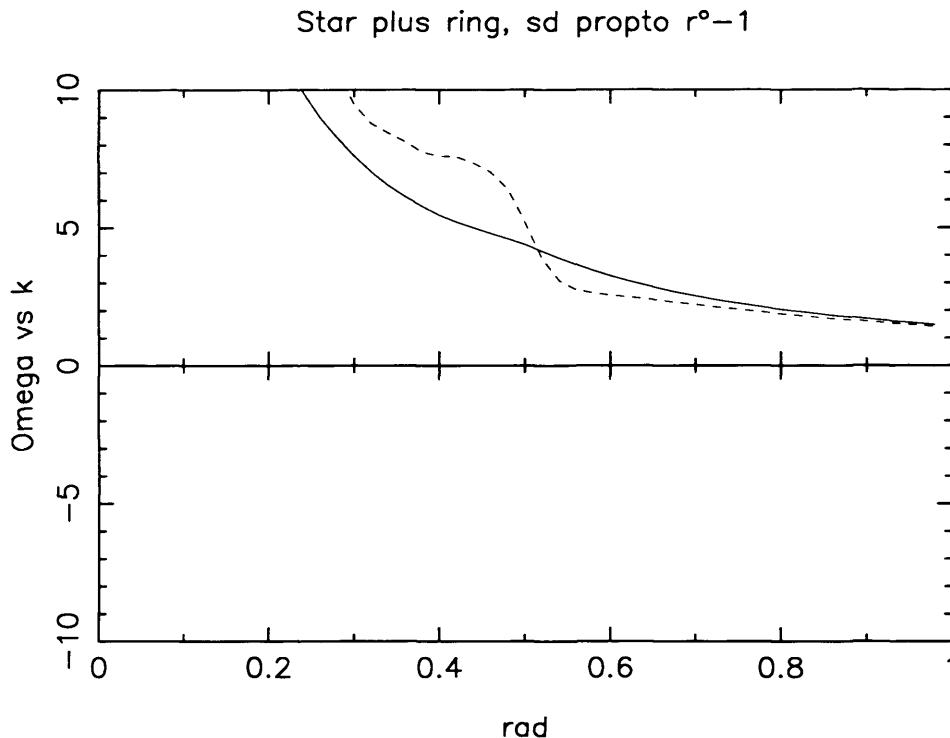
Figure 4.5: Comparison of κ, dashed line, and Ω, undashed for a 1m disk from 0.06 to 0.5 radii about a 1m star.

4.3   Disk Settling

Figure 4.6 shows that the disk of particles created using the method described in the previous section has uneven spacing between particles. Figure 4.8a shows the distance from each particle in the disk to its closest neighbour, the distance being normalised for all radii by dividing by the smoothing length h. 812 out of 10,000 particles have neighbours closer than $0.2h$, and these are particularly noticeable at the inner and outer edges. This is due to the rise in h in these regions. Particles near the edges are assigned larger h values than they would if the disk was continuous. A value of h which gives 50 neighbours at some surface density $\Sigma(r)$ will only give 25 neighbours if the edge of the disk runs through radius r. As a result, neighbours which are not abnormally close given the density distribution are apparently close when divided by h.

This is an important point because gravity and pressure forces are calculated according to the proximity of neighbours measured relative to the value of h for a particle. Particles at the edges will therefore experience a reduced gravitational force but a stronger pressure force than they would with the same distribution of neighbours in a disk which extended beyond the artificially imposed cutoff radii. This will exacerbate the tendency of an annulus to spread due to pressure forces, and require adjustment of the initial orbital

pp10000b.ptt

pp10000b.ptt
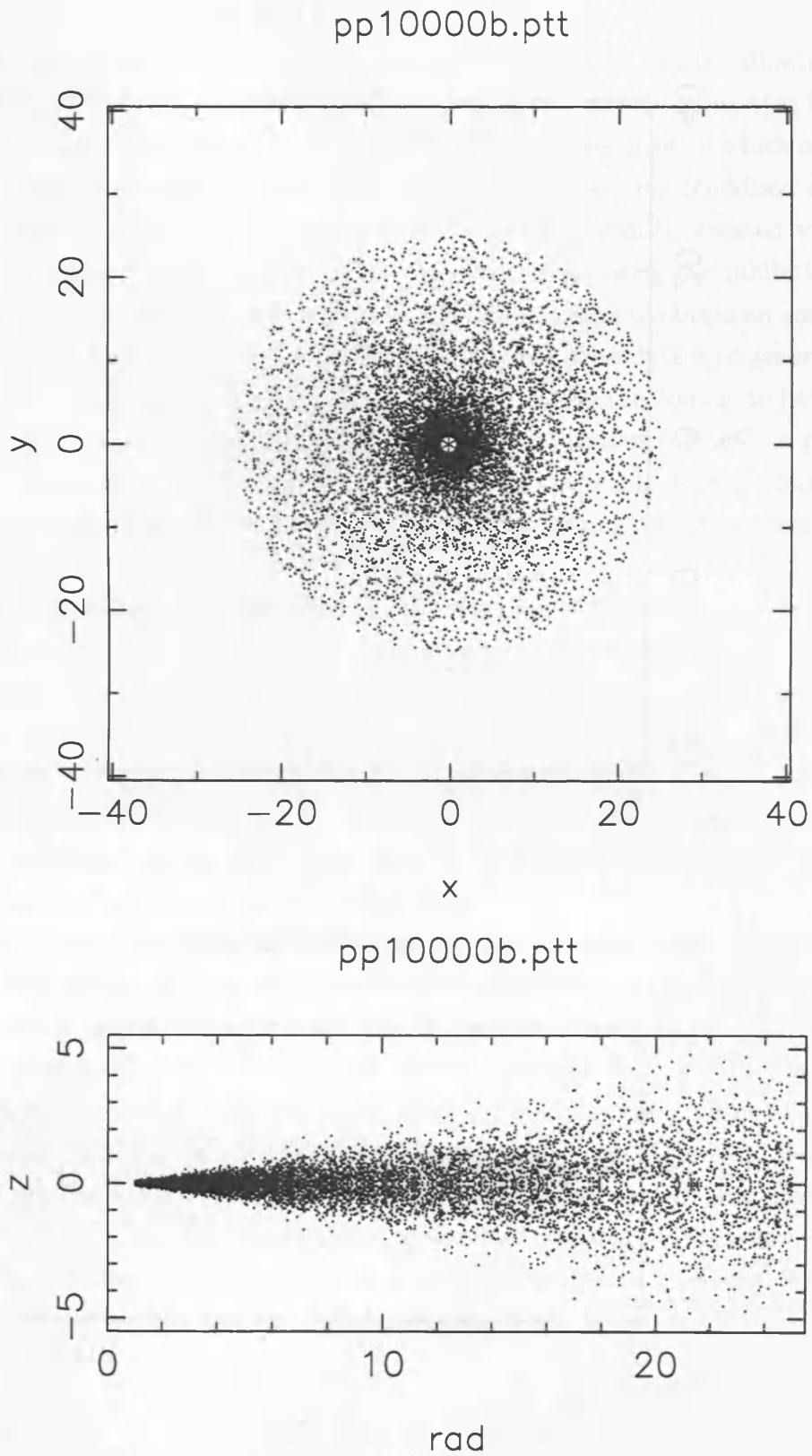
Figure 4.6: Azimuthal and cross sectional views of a disk with surface density profile $\Sigma(r) \propto r^{-7/4}$ and temperature $T(r) = 300(r/AU)^{-1/2}$, purely random positioning of particles.

pp10000s.ptt

pp10000s.ptt
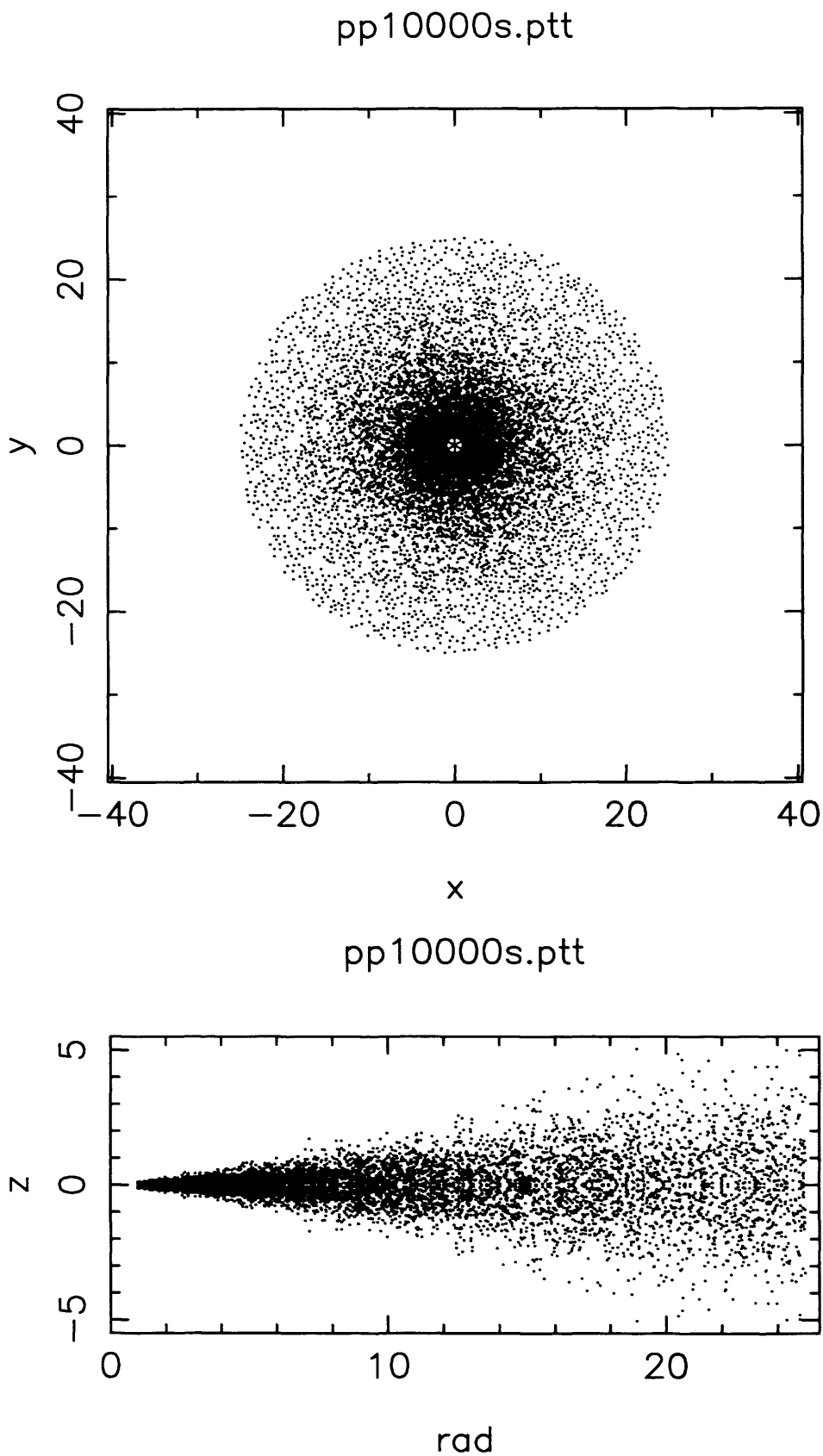
Figure 4.7: Azimuthal and cross sectional views of a disk with surface density profile $\Sigma(r) \propto r^{-7/4}$ and temperature $T(r) = 300(r/AU)^{-1/2}$, particles positioned with anti-clustering to avoid very close neighbours.

velocity profile.

In SPH simulations of disks, the disks are usually allowed to 'settle', allowing pressure forces to move close particles apart, before the simulation starts in earnest(eg Mayer et al 2004). Alternatively, they may be set up on uniformly spaced rings, in which case density gradients must be imposed by giving particles different masses (eg Maddison et al 1996).

An alternative method is used here. Disks of particles can be created without any close pairs by imposing mutual spacing or 'anti-clustering', using the inhibition method of Diggle (1983). This method can be used in 2 or 3 dimensions to obtain an anti-clustered but otherwise random array of coordinates. Normally the procedure is to generate a series of random coordinate pairs (for a 2 dimensional array) within the domain to be populated, but to discard any points which fall within a preset inhibition radius of a pre-existing point. This radius is usually defined and constant over the whole domain. Increasing the inhibition radius results in the array of coordinates approaching a semi-regular, lattice-like appearance.

This procedure had to be modified in two ways for the purposes of populating our disks. First, the inhibition radius was not the same at all locations in the disk but had to be calculated for each point as a function of the radius and surface density profile. Second, if a particle fell within the inhibition zone of another particle it could not simply be discarded, as this could interfere with the generation of the correct surface density profile. The particle was therefore relocated in a new position at the same radius, where the closest neighbour was no longer too close. If, after 20 attempts, no such location was found, the particle was placed in its original spot.

Figure 4.7 shows the azimuthal and cross sectional views of a disk created using this mutual spacing technique, with otherwise identical parameters to the disk shown in fig. 4.6. The difference is apparent to the naked eye. Figure 4.8 shows the comparisons between distance to nearest neighbour for the disks created with and without anti-clustering. The difference is clearly visible, only 100 out of 10000 points lying within $0.2h$ of a neighbour in the anti-clustered disk, most of these being at the inner edge of the disk. Note that the number of very large nearest neighbour distances is also reduced by anti-clustering. By increasing the inhibition zone of particles, the standard deviation of the nearest neighbour distances can be reduced, tending towards, although never reaching because of the random element of the process, the perfect uniform spacing of a lattice.
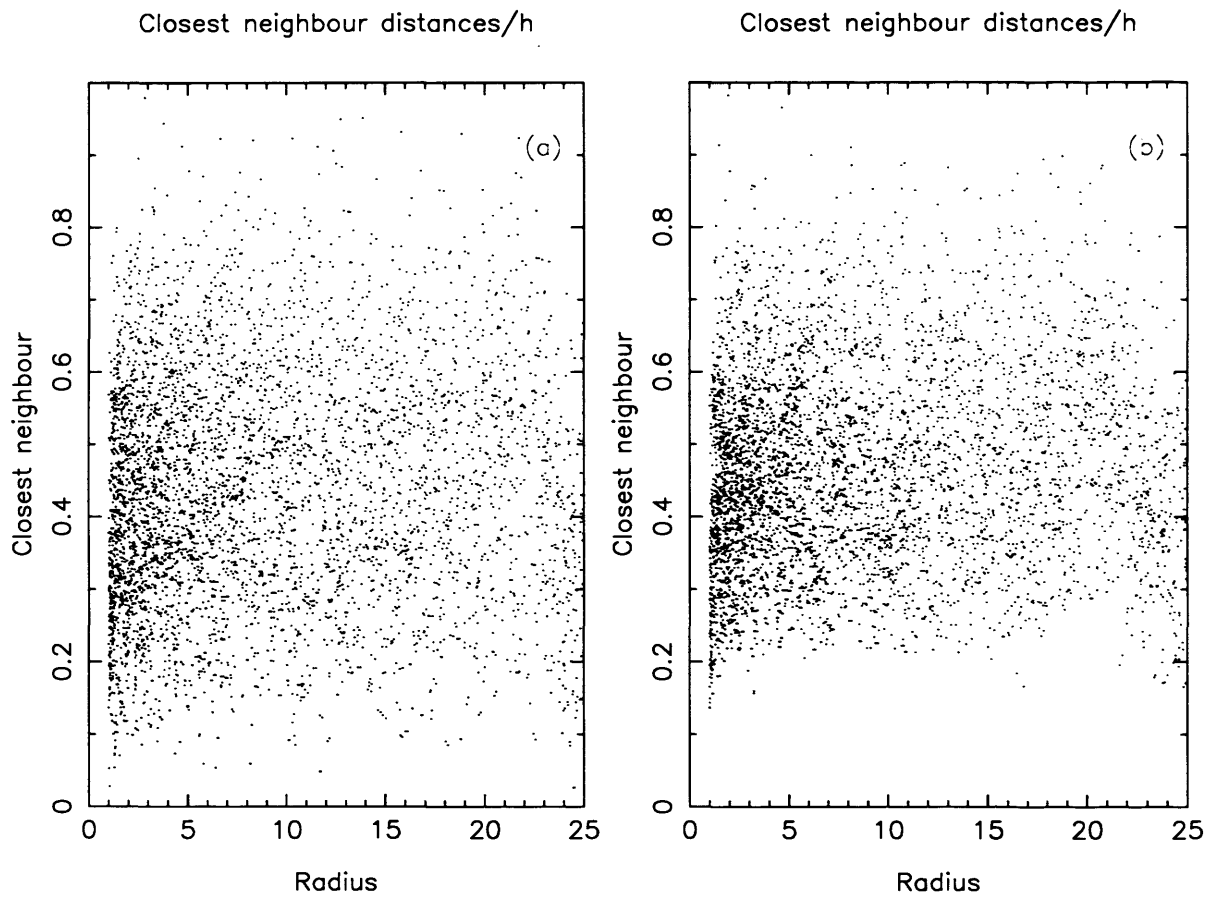
Figure 4.8: Distance from each particle to its closest neighbour, expressed as a frac-
tion of h, (a) random particle spacing; (b) particles mutually spaced to avoid very close
neighbours.

4.4 Setting the height of particles

The thickness of the disk at any radius is set so that pressure support balances the gravitional attraction of both central star and disk, in the vertical direction.

At any radius r we impose an initial temperature $T(r)$, and from this can calculate the sound speed a from :

$$a^2(r) = \frac{kT(r)}{\bar{m}}$$ (4.8)

where k is the Boltzman constant and $\bar{m} \simeq 4 \times 10^{-27}$ kg the mean gas particle mass for molecular interstellar gas.

Setting the hydrostatic pressure equal to the vertical component of gravity at radius r, assuming disk height $z(r)$ we have:

$$\frac{a^2(r)}{z(r)} \simeq \frac{GM_{\star}z(r)}{r^3} + \pi G\Sigma(r)$$ (4.9)

Here the left hand term is the hydrostatic pressure. The first term on the right hand side is the vertical component of the gravitational attraction of the central object, mass $M_{\star}$, and the second term is the vertical component of the self gravity of the disk.

If we assume that the disk is much lighter than the central object (which is the case for our simulations) we can ignore the second term and we have therefore,

$$z(r) = a(r) \left(\frac{r^3}{GM_{\star}} \right)^{1/2}$$ (4.10)

Given initial surface density and temperature profiles $\Sigma(r)$ and $T(r)$ we can therefore obtain a vertical height for the disk at all radii, $z(r)$, which achieves hydrostatic balance. The z height of an individual particle is obtained by calculating a random value within the range $-z(r)$ to $z(r)$, using an algorithm which yields a Gaussian frequency distribution within these limits. We used the Box-Muller algorithm (Press et al 1992).

Figure 4.6 shows the azimuthal and cross sectional view of a disk constructed using the procedures outlined in this and the previous section. A $0.1M_{\odot}$ disk was represented by 10,000 SPH particles, placed in orbit from 1 to 25 AU about a $1M_{\odot}$ star. The surface density and temperature gradients were :

$$\Sigma(r) = \Sigma_0 r^{-7/4},$$
$$T(r) = 300K \left(\frac{r}{\text{AU}} \right)^{-1/2},$$ (4.11)

where the surface density at 1AU, $\Sigma_0 = 0.003\text{M}_{\odot}/\text{AU}^2$.

Orbital Velocity vs radius
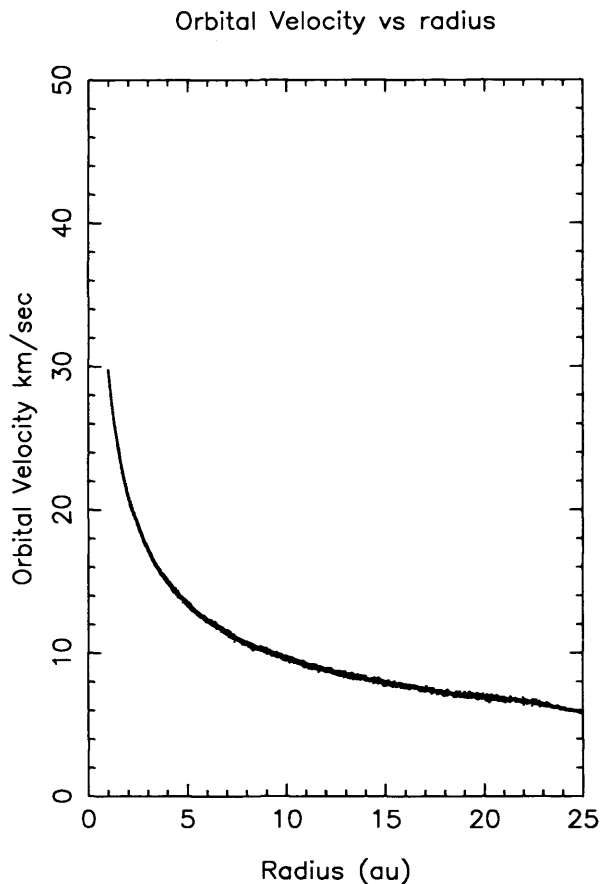
Figure 4.9: Equilibrium velocity versus radius.

4.5   Setting the disk rotating

The final stage in the initialisation of the disk is to set every particle into a stable orbit around the central star.

The radial component of the gravitational and pressure forces, a_{rad} is calculated, and then a velocity v_{kep} calculated, for which

$$\frac{v_{kep}^2}{r} = -a_{rad} \tag{4.12}$$

Figure 4.9 shows the variation of v_{kep} with radius for the disk shown in fig. 4.7.

4.6   Conclusion

Modelling the behaviour of selected regions of disks must be done with care. In particular, an annulus of a disk will have regions at the inner and outer edges where the self gravity of the annulus changes the equlibrium orbital velocity necessary for stable rotation. This is

particularly important for the calculation of the Toomre parameter, where the assumption that the epicyclic frequency κ is equal to the angular velocity Ω, is incorrect in regions where the orbital velocity is not precisely Keplerian.

An adapted anticlustering algorithm has been developed to ensure mutual spacing of SPH particles prior to the start of simulation runs. This is potentially an elegant way of preparing disks of SPH particles with any variable density profile, without the need for varying the masses of the particles. It is intended to elaborate this work and publish it in a technical note.

Chapter 5

Artificial Viscosity

A particular concern in attempting to simulate rotating gaseous disks, using SPH, is the issue of Artificial Viscosity.

Artificial Viscosity was developed for use in SPH simulations of collapsing or colliding turbulent clouds (Monaghan & Gingold 1983). It causes close, approaching SPH particles to repel each other, with a force which increases with approach velocity and proximity. The result is that particles in colliding streams are rapidly decelerated and the streams do not pass through each other. Such particle interpenetration would be an unphysical situation which cannot be allowed in a simulation.

5.1 Artificial Viscosity in SPH

To determine whether Artificial Viscosity should be applied between an SPH particle i with position r_i and velocity v_i and a neighbouring particle with position r_j and velocity v_j, the scalar product of $v_{ij} \cdot r_{ij}$, is calculated. If negative, the particles are approaching and Artificial Viscosity is included in the calculation of hydrostatic acceleration:

$$\frac{d\mathbf{v}_i}{dt} = \sum_j \left\{ m_j \left[\frac{P_i}{\rho_i^2} + \frac{P_j}{\rho_j^2} + \Pi_{ij} \right] \frac{1}{\bar{h}_{ij}^4} W'(r_{ij}, \bar{h}_{ij}).\hat{\mathbf{r}}_{ij} \right\}. \tag{5.1}$$

Here the first two terms give the symmetrical pressure forces between pairs of particles, and the Artificial Viscosity term, Π_{ij} is calculated as

$$\Pi_{ij} = \begin{cases} (-\alpha_\nu c_{ij}\mu_{ij} + \beta_\nu \mu_{ij}^2))/\rho_{ij}, , & \mathbf{v}_{ij} \cdot \mathbf{r}_{ij} \leq 0; \\ \\ 0, & \mathbf{v}_{ij} \cdot \mathbf{r}_{ij} > 0, \end{cases} \tag{5.2}$$

where $\rho_{ij} = (\rho_i + \rho_j)/2$ is the mean density, $c_{ij} = (c_i + c_j)/2$ is the mean sound speed, α and β are constants (1.0 and 2.0 are typical values) and

$$\mu_{ij} = h_{ij}\mathbf{v}_{ij} \cdot \mathbf{r}_{ij}/(r_{ij}^2 + \eta). \tag{5.3}$$

The scalar quantities μ_{ij} and Π_{ij} are calculated for each approaching neighbour, but Eqn. 5.2 is a vector summation. The viscous acceleration from particle j, calculated using eqn. 5.2, acts in the direction $\mathbf{r}_{ij}$, with the gradient of the kernel function $W'(r_{ij}, \bar{h}_{ij})$ reducing the contributions of the more distant neighbours.

This formulation is known to result in high shear viscosity when used in the modelling of accretion disks (Bate 2000).

5.2 Velocity variation in linear and Keplerian shear flow

In a light, cool protoplanetary disk of mass $M_d \sim 0.1M_\odot$ orbiting a star of $1M_\odot$, the self gravity and pressure forces are small enough for the orbiting SPH particles to be considered to be in Keplerian orbits about the central star. Orbital speeds are therefore $\propto r^{-0.5}$, decreasing with increasing radius.

Figure 5.1a shows an azimuthal view of a small portion of an SPH model of a protoplanetary disk, with arrows to show the direction of the orbital paths of the SPH particles around a central star, which is below and to the left of the selected portion of the disk. Figure 5.1b shows the same points, this time with all velocities calculated relative to that of a central particle, P, which is indicated by a cross. All of the black arrows are converging particles, $\mathbf{v}_{ij} \cdot \mathbf{r}_{ij} \le 0$, and all the red arrows are diverging particles, $\mathbf{v}_{ij} \cdot \mathbf{r}_{ij} \ge 0$. They are not randomly distributed in the field of view, but fall distinctly into four quadrants. This is characteristic for disks of particles in Keplerian rotation. Using the Monaghan formulation for Artificial Viscosity, above, all of the black points are decelerated by a repulsive force from P, while the red ones are ignored. P is accelerated by the sum of the viscous forces from all black points.

The relative velocities of particles on inner radii are systematically larger than those of the particles on the outer radii, because orbital speed $\mathbf{v} \propto r^{-0.5}$. When the reaction forces of all neighbours on the central point are added together, the inner particles are predicted to outweigh the outer ones, resulting in a net force on P. This force is predicted to have both a radial component, tending to push point P outwards, and a tangential component, speeding up P and again, causing it to move outwards.
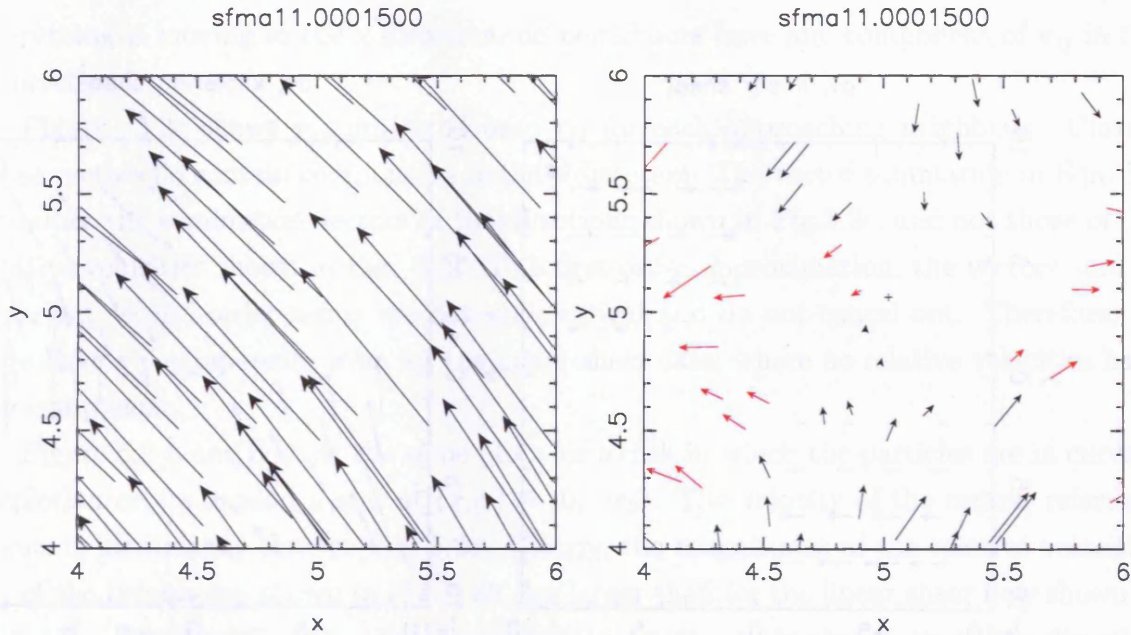
Figure 5.1: Azimuthal view of a portion of a Keplerian disk, the centre of rotation being below and to the left of the imaged portion. (a) arrows show magnitude and direction of orbital velocity. (b) arrows show magnitude and direction of velocity relative to the central point marked with a cross. Red arrows are diverging points, black arrows are converging. The length of the vectors has been doubled in (b) for clarity.

Given that no large shocks are occurring, the first term in Eqn. 5.2 is assumed to dominate the calculation of viscosity in a smoothly rotating Keplerian disk. Assuming that other parameters, in particular density (and hence h_{ij}) and temperature (and hence c_{ij}) are constant for all neighbours j of a point i, the key component in the calculation of μ_{ij} for each neighbour is $\mathbf{v}_{ij} \cdot \mathbf{r}_{ij}/|\mathbf{r}_{ij}|^2$. This is the magnitude of the component of the relative velocity $\mathbf{v}_{ij}$ in the direction $\mathbf{r}_{ij}$. The force between particles is then applied in the direction $\mathbf{r}_{ij}$. This vector sum can be expressed as

$$\mathcal{F}_i = \sum_j \mathcal{F}_{ij} = \sum_j \frac{\mathbf{v}_{ij} \cdot \mathbf{r}_{ij}}{|\mathbf{r}_{ij}|^2} \hat{\mathbf{r}}_{ij} \tag{5.4}$$

It is this vector summation which will dominate the calculation of the viscous force on the central point, in particular defining its direction.

In Fig. 5.2a, a square array of 81 particles has been set in linear shear flow in the x direction and the direction and magnitude of relative velocity with respect to the centre point is shown. For each point, the x component of velocity $v_x = k(r_0 + y)^{-0.5}$, where k is constant. The y component of velocity, v_y, is zero for all points. Only neighbours which are approaching the centre point, that is neighbours for which $\mathbf{v}_{ij} \cdot \mathbf{r}_{ij} \leq 0$, are shown. As
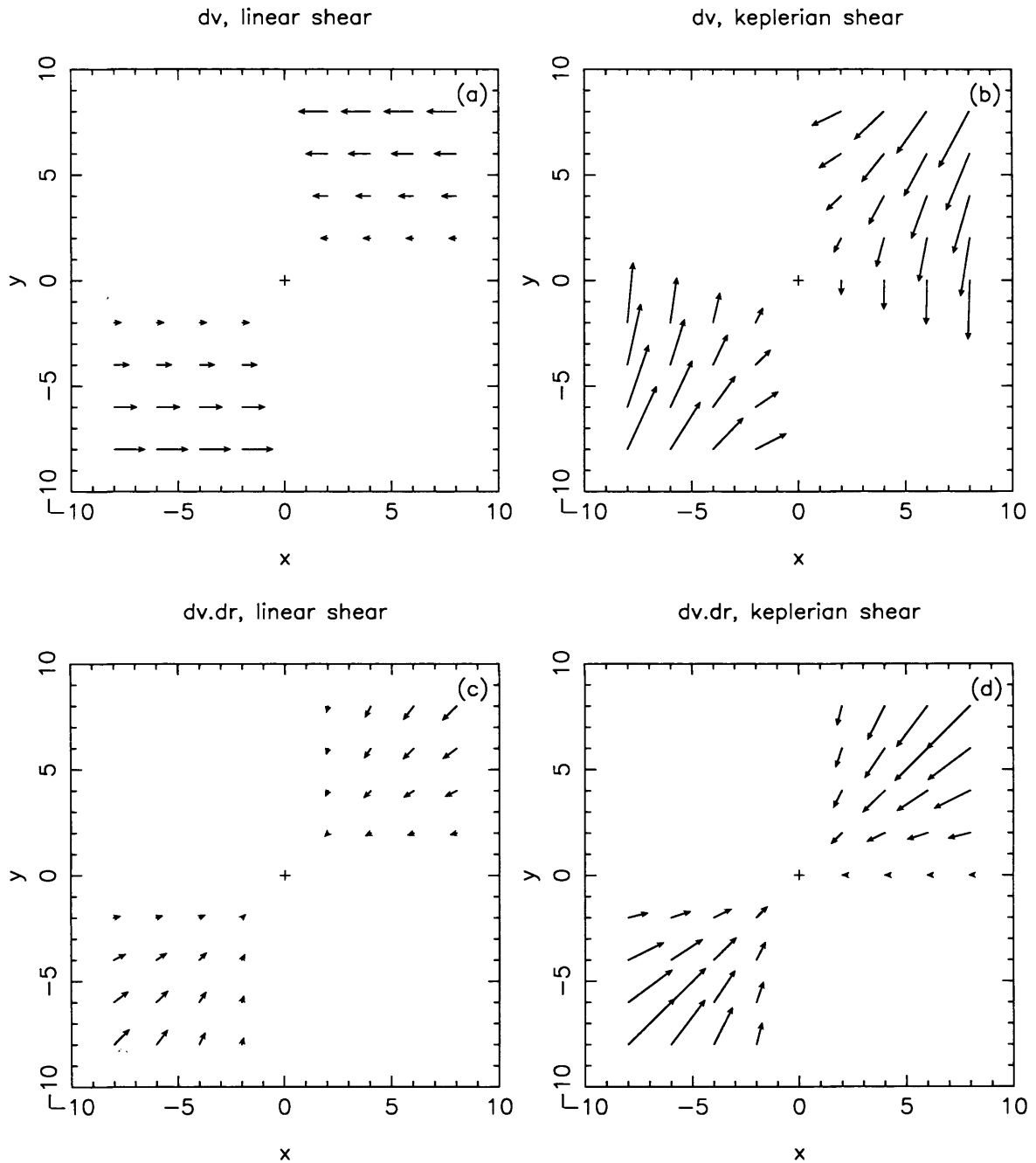
Figure 5.2: Relative velocities of neighbouring particles. (a) the relative velocities of particles in linear shear flow, relative to the central particle marked with a cross, which is moving in the positive x direction. The centre of rotation is distance r away in the negative y direction; (b) the same but for Keplerian shear flow, velocity proportional to $y^{-1/2}$; (c) the component of $\mathbf{v}_{ij}$ in the direction $\mathbf{r}_{ij}$ for linear shear; (d)the the component of $\mathbf{v}_{ij}$ in direction $\mathbf{r}_{ij}$ for Keplerian shear.

everything is moving in the x direction, no neighbours have any component of $\mathbf{v}_{ij}$ in the y direction.

Figure 5.2c shows $\mathbf{v}_{ij}$ projected onto $\mathbf{r}_{ij}$ for each approaching neighbour. Clearly these vectors do contain components in the y direction. The vector summation in Eqn. 5.4 describes the summation vectors in the directions shown in Fig.5.2c, and not those of the relative velocities shown in Fig. 5.2a. To a first order approximation, the vectors sum to zero, but second order terms are not symmetrical and do not cancel out. Therefore, $\mathcal{F}_i$ does have a y component, even for the linear shear case, where no relative velocities have a y component.

Figure 5.2 b and d show the same plots for a disk in which the particles are in curved, Keplerian orbits around a star at $(x, y) = (0, -r_0)$. The velocity of the centre, reference point, is identical to that in Fig. 5.2a. Clearly, the magnitudes of the relative velocities $\mathbf{v}_{ij}$ of the neighbours,shown in Fig. 5.2b, are larger than for the linear shear flow shown in Fig. 5.2a. The direction of each relative velocity vector $\mathbf{v}_{ij}$ is also closer to the direction of $\mathbf{r}_{ij}$. The resultant components of $\mathbf{v}_{ij}$ in direction $\mathbf{r}_{ij}$ for Keplerian shear, shown in Fig. 5.2d, are much larger than for the linear shear flow shown in Fig. 5.2c.

The very marked difference between linear and Keplerian shear flows illustrated in Fig. 5.2 is at first surprising. However, it can simply be proved that the rate of change of radial velocity with distance along the orbit, $\frac{dv_y}{dx}$ in our coordinate system, is twice as large as the rate of change of orbital velocity with radius, $\frac{dv_x}{dy}$.

Consider the array of points shown in Fig. 5.2b. The central point with coordinates $(0,0)$ has velocity components $(kr_0^{-1/2}, 0)$. Any other point with coordinates (x, y) has velocity components $(kr^{-1/2} \cos \phi, kr^{-1/2} \sin \phi)$, where

$$
\begin{aligned}
r^2 &= (r_0 + y)^2 + x^2 \\
\sin \phi &= \frac{-x}{r} \\
\cos \phi &= \frac{y + r_0}{r}
\end{aligned}
\tag{5.5}
$$

If we redefine the local cartesian coordinates as centred on point (0,0) and also moving with that point, the velocity components of any point become (assuming x and y are small compared with r_0)

$$
\begin{aligned}
v_x &= k(y + r_0)((y + r_0)^2 + x^2)^{-3/4} - kr_0^{-1/2} \\
&= \frac{k}{r_0^{1/2}} \left(\left(1 + \frac{y}{r_0}\right) \left(1 + \frac{2y}{r_0} + \frac{(x^2 + y^2)}{r_0^2}\right)^{-3/4} - 1 \right)
\end{aligned}
$$

$$= \frac{k}{r_0^{1/2}} \left(-\frac{1}{2}\frac{y}{r_0} + \frac{3}{8}\frac{y^2}{r_0^2} - \frac{6}{8}\frac{x^2}{r_0^2} + \mathcal{O}\left(\frac{x^2 y}{r_0^3}, \frac{y^3}{r_0^3}\right) \right)$$

$$v_y = \frac{-k}{r_0^{1/2}} \left(\frac{x}{r_0}\right) \left(1 + \frac{2y}{r_0} + \frac{(x^2 + y^2)}{r_0^2}\right)^{-3/4}$$

$$= \frac{-k}{r_0^{1/2}} \left(\frac{x}{r_0} - \frac{3}{2}\frac{xy}{r_0^2} + \mathcal{O}\left(\frac{x^3}{r_0^3}, \frac{xy^2}{r_0^3}\right) \right) \tag{5.6}$$

Differentiating v_x with respect to y, and v_y with respect to x,

$$\frac{dv_x}{dy} = -\frac{k}{2r_0^{3/2}} + \mathcal{O}\left(\frac{x}{r_0^{5/2}}, \frac{y}{r_0^{5/2}}\right)$$

$$\frac{dv_y}{dx} = -\frac{k}{r_0^{3/2}} + \mathcal{O}\left(\frac{x}{r_0^{5/2}}, \frac{y}{r_0^{5/2}}\right) \tag{5.7}$$

Ignoring the smaller terms, therefore, the magnitude of the relative velocity of a particle distance r_{ij} from our reference particle is twice as large for a neighbour further ahead on the orbital path, as it is for an equidistant neighbour on a parallel orbital track. This applies for any radius. Keplerian shear flow in a disc cannot be approximated to be linear shear, even at the smallest, or largest, scales.

5.3 Artificial Viscosity: Keplerian shear flow

Using the values of v_x and v_y in Eqn. 5.6, we can now calculate the radial and tangential components of $\mathcal{F}$. From Eqn. 5.4, $\mathcal{F}$ is given by

$$|\mathcal{F}| = \frac{xv_x + yv_y}{(x^2 + y^2)} \tag{5.8}$$

The components of $\mathcal{F}$ are therefore

$$\mathcal{F}_x = \frac{x(xv_x + yv_y)}{(x^2 + y^2)^{3/2}}$$

$$\mathcal{F}_y = \frac{y(xv_x + yv_y)}{(x^2 + y^2)^{3/2}} \tag{5.9}$$

Substituting for v_x and v_y from Eqn. 5.6,

$$
\begin{aligned}
\mathcal{F}_x &= \frac{k}{r_0^{1/2}} \left(\frac{x^2}{(x^2+y^2)^{3/2}} \left(-\frac{1}{2}\frac{y}{r_0} + \frac{3}{8}\frac{y^2}{r_0^2} - \frac{6}{8}\frac{x^2}{r_0^2} \right) - \frac{xy}{(x^2+y^2)^{3/2}} \left(\frac{x}{r_0} - \frac{3}{2}\frac{xy}{r_0^2} \right) \right) \\
&= \frac{k}{r_0^{1/2}} \left(\frac{1}{(x^2+y^2)^{3/2}} \left(-\frac{3}{2}\frac{x^2 y}{r_0} + \frac{15}{8}\frac{x^2 y^2}{r_0^2} - \frac{6}{8}\frac{x^4}{r_0^2} \right) \right) \\
\mathcal{F}_y &= \frac{k}{r_0^{1/2}} \left(\frac{xy}{(x^2+y^2)^{3/2}} \left(-\frac{1}{2}\frac{y}{r_0} + \frac{3}{8}\frac{y^2}{r_0^2} - \frac{6}{8}\frac{x^2}{r_0^2} \right) - \frac{y^2}{(x^2+y^2)^{3/2}} \left(\frac{x}{r_0} - \frac{3}{2}\frac{xy}{r_0^2} \right) \right) \\
&= \frac{k}{r_0^{1/2}} \left(\frac{1}{(x^2+y^2)^{3/2}} \left(-\frac{3}{2}\frac{xy^2}{r_0} + \frac{15}{8}\frac{xy^3}{r_0^2} - \frac{6}{8}\frac{x^3 y}{r_0^2} \right) \right) \qquad (5.10)
\end{aligned}
$$

We now transform the cartesian coordinates x, y into polar coordinates r, θ centred on the same origin, so that $x = r\cos\theta$ and $y = r\sin\theta$. Substituting in Eqn. 5.10

$$
\begin{aligned}
\mathcal{F}_x &= kr_0^{-1/2} \left(-\frac{3}{2r_0}\sin\theta\cos^2\theta + \frac{15r}{8r_0^2}\sin^2\theta\cos^2\theta - \frac{6r}{8r_0^2}\cos^4\theta \right) \\
\mathcal{F}_y &= kr_0^{-1/2} \left(-\frac{3}{2r_0}\sin^2\theta\cos\theta + \frac{15r}{8r_0^2}\sin^3\theta\cos\theta - \frac{6r}{8r_0^2}\sin\theta\cos^3\theta \right) \qquad (5.11)
\end{aligned}
$$

The total viscous force due to all approaching neighbours within a circle of radius h may now be calculated by integrating over the first and third quadrants of a circle of radius h. We first compute the following integrals:

$$
\int_0^{\frac{\pi}{2}} \sin\theta\cos^2\theta\, d\theta + \int_\pi^{\frac{3\pi}{2}} \sin\theta\cos^2\theta\, d\theta = 0
$$

$$
\int_0^{\frac{\pi}{2}} \sin^2\theta\cos\theta\, d\theta + \int_\pi^{\frac{3\pi}{2}} \sin^2\theta\cos\theta\, d\theta = 0
$$

$$
\int_0^{\frac{\pi}{2}} \cos^4\theta\, d\theta + \int_\pi^{\frac{3\pi}{2}} \cos^4\theta\, d\theta = 3\pi/8
$$

$$
\int_0^{\frac{\pi}{2}} \sin\theta\cos^3\theta\, d\theta + \int_\pi^{\frac{3\pi}{2}} \sin\theta\cos^3\theta\, d\theta = 1/2
$$

$$
\int_0^{\frac{\pi}{2}} \sin^2\theta\cos^2\theta\, d\theta + \int_\pi^{\frac{3\pi}{2}} \sin^2\theta\cos^2\theta\, d\theta = \pi/8
$$

$$
\int_0^{\frac{\pi}{2}} \sin^3\theta\cos\theta\, d\theta + \int_\pi^{\frac{3\pi}{2}} \sin^3\theta\cos\theta\, d\theta = 1/2 \qquad (5.12)
$$

Substituting these identities into Eqn. 5.11

$$
\mathcal{F}_x = kr_0^{-1/2} \int_0^h \int_{1,3} \left(-\frac{3}{2r_0}\sin\theta\cos^2\theta + \frac{15r}{8r_0^2}\sin^2\theta\cos^2\theta - \frac{6r}{8r_0^2}\cos^4\theta \right) r\, dr\, d\theta
$$

$$\begin{aligned}
&= kr_0^{-1/2} \int_0^h \left(\frac{15r^2}{8r_0^2} \frac{\pi}{8} - \frac{6r^2}{8r_0^2} \frac{3\pi}{8} \right) dr \\
&= \frac{3k\pi}{64r_0^{5/2}} \int_0^h -r^2 dr \\
&= -\frac{k\pi h^3}{64r_0^{5/2}}
\end{aligned}$$

$$\begin{aligned}
\mathcal{F}_y &= kr_0^{-1/2} \int_0^h \int_{1,3} \left(-\frac{3}{2r_0} \sin^2\theta \cos\theta + \frac{15r}{8r_0^2} \sin^3\theta \cos\theta - \frac{6r}{8r_0^2} \sin\theta \cos^3\theta \right) r \, dr \, d\theta \\
&= kr_0^{-1/2} \int_0^h \left(\frac{15r^2}{8r_0^2} \frac{1}{2} - \frac{6r^2}{8r_0^2} \frac{1}{2} \right) dr \\
&= \frac{9k}{16r_0^{5/2}} \int_0^h r^2 dr \\
&= \frac{3kh^3}{16r_0^{5/2}}
\end{aligned} \tag{5.13}$$

Therefore, for Keplerian orbits $\mathcal{F}_y$ is $\frac{12}{\pi} \simeq 4$ times larger than $\mathcal{F}_x$. $\mathcal{F}_x$ is in the negative x direction, opposing the direction of the orbit, while $\mathcal{F}_y$ is in the positive y direction, pushing the particle outward from the centre of rotation.

Note, however, that eqn. 5.2 requires a negative coefficient, $-\alpha$ to be applied to this term. The viscosity acts therefore in the expected direction, speeding up particles in their orbits, as a result of the faster inward particles. However, there is also a radial force four times larger, tending to push particles inwards.

Consider again Eqn. 5.11. The expressions for $\mathcal{F}_x$ and $\mathcal{F}_y$ contain odd terms in xy^2 and in $x^2 y$ which cancel out when integrated over the first and third quadrants. These terms can be traced back to the first order terms in the expressions for v_x and v_y in Eqn. 5.6. Clearly these first order terms contribute nothing to the calculation of $\mathcal{F}_x$. If we omit these first order terms, we are left with only the second order terms

$$\begin{aligned}
v'_x &= \frac{k}{r_0^{1/2}} \left(\frac{3y^2}{8r_0^2} - \frac{6x^2}{8r_0^2} \right) \\
v'_y &= \frac{k}{r_0^{1/2}} \left(\frac{3xy}{2r_0^2} \right)
\end{aligned} \tag{5.14}$$

Figure 5.3 shows the magnitude and direction of the second order terms for relative velocity, which actually contribute to the calculation of $\mathcal{F}_x$ and $\mathcal{F}_y$. All values of v'_y are positive, but v'_x is negative for points where $3y^2 - 6x^2 < 0$, that is points lying within 55 degrees of the x axis.
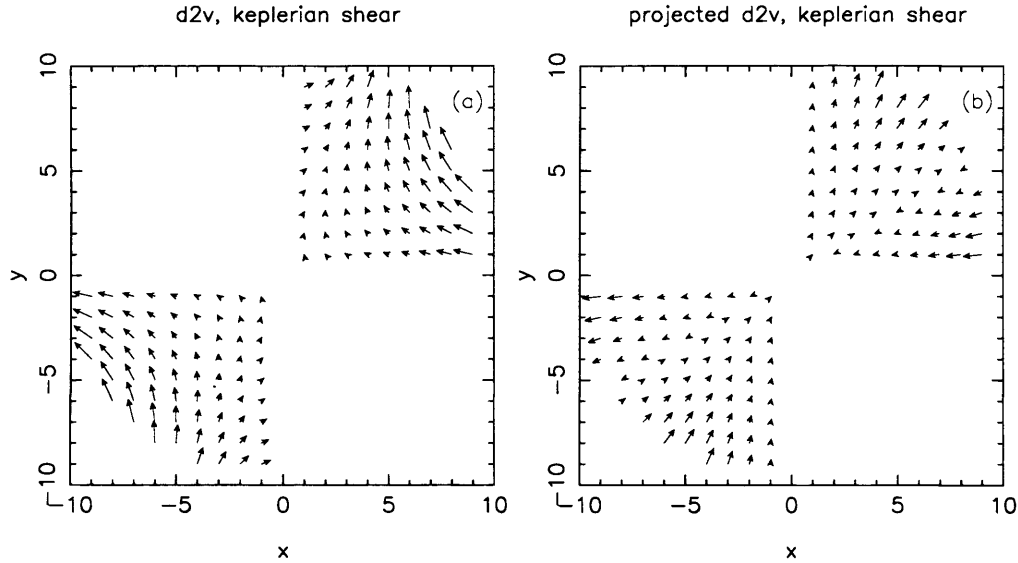
Figure 5.3: Relative velocities of neighbouring particles for Keplerian flow. (a) First order terms for velocity have been subtracted, leaving only the second order terms. Note that v_y is everywhere positive, while v_x is negative for values of $|y| < \sqrt{2}x$. (b) The same as (a) but now projected onto the relative position vector for each particle. These vectors are added to calculate $\mathcal{F}$.

The calculation of $\mathcal{F}$ requires these vectors to be projected into the direction of each particle's position vector. Fig. 5.3 shows these projected vectors. From Eqn. 5.10, we expect the direction of these second order vectors to switch when $15y^2 = 6x^2$, which is a line at 32 degrees to the x axis. Fig. 5.3b shows this clearly.

5.4 Artificial Viscosity: Linear shear flow

For completeness, we can also obtain the viscous force for linear shear flow, set up to mimic the Keplerian flow, as illustrated in Fig. 5.2. The velocity of any point $(x, y + r)$ is simply $(k(r + y)^{-1/2}, 0)$. Moving to our comoving coordinate system, therefore,

$$
\begin{aligned}
v_x &= k(y + r_0)^{-1/2} - kr_0^{-1/2} \\
&= \frac{k}{r_0^{1/2}} \left((1 + \frac{y}{r_0})^{-1/2} - 1 \right) \\
&= \frac{k}{r_0^{1/2}} \left(-\frac{1}{2}\frac{y}{r_0} + \frac{3}{8}\frac{y^2}{r_0^2} \right) \\
v_y &= 0
\end{aligned}
\tag{5.15}
$$

From Eqn. 5.4, as before, the components of the viscosity force contributed by an approaching neighbour, are

$$\mathcal{F}_x = \frac{x(xv_x + yv_y)}{(x^2 + y^2)^{3/2}}$$

$$\mathcal{F}_y = \frac{y(xv_x + yv_y)}{(x^2 + y^2)^{3/2}} \tag{5.16}$$

Substituting for v_x and v_y from Eqn. 5.6,

$$\mathcal{F}_x = \frac{k}{r_0^{1/2}} \left(\frac{x^2}{(x^2 + y^2)^{3/2}} \left(-\frac{1}{2} \frac{y}{r_0} + \frac{3}{8} \frac{y^2}{r_0^2} \right) \right)$$

$$\mathcal{F}_y = \frac{k}{r_0^{1/2}} \left(\frac{xy}{(x^2 + y^2)^{3/2}} \left(-\frac{1}{2} \frac{y}{r_0} + \frac{3}{8} \frac{y^2}{r_0^2} \right) \right) \tag{5.17}$$

We now transform the cartesian coordinates x, y into polar coordinates r, θ centred on the same origin, so that $x = r\cos\theta$ and $y = r\sin\theta$. Substituting in Eqn. 5.17

$$\mathcal{F}_x = kr_0^{-1/2} \left(-\frac{1}{2r_0} \sin\theta \cos^2\theta + \frac{3r}{8r_0^2} \sin^2\theta \cos^2\theta \right)$$

$$\mathcal{F}_y = kr_0^{-1/2} \left(-\frac{1}{2r_0} \sin^2\theta \cos\theta + \frac{3r}{8r_0^2} \sin^3\theta \cos\theta \right) \tag{5.18}$$

The total viscous force due to all neighbours within a circle of radius h may now be calculated, by integrating over the first and third quadrants of a circle of radius h. Substituting the integrals of trigonometrical functions from Eqn. 5.12

$$\mathcal{F}_x = kr_0^{-1/2} \int_0^h \int_{1,3} \left(-\frac{1}{2r_0} \sin\theta \cos^2\theta + \frac{3r}{8r_0^2} \sin^2\theta \cos^2\theta \right) r\, dr\, d\theta$$

$$= kr_0^{-1/2} \int_0^h \left(\frac{3r^2}{8r_0^2} \right) \frac{\pi}{8} dr$$

$$= \frac{3k\pi}{64r_0^{5/2}} \int_0^h r^2 dr$$

$$= \frac{k\pi h^3}{64r_0^{5/2}}$$

$$\mathcal{F}_y = kr_0^{-1/2} \int_0^h \int_{1,3} \left(-\frac{1}{2r_0} \sin^2\theta \cos\theta + \frac{3r}{8r_0^2} \sin^3\theta \cos\theta \right) r\, dr\, d\theta$$

$$= kr_0^{-1/2} \int_0^h \left(\frac{3r^2}{8r_0^2} \right) \frac{1}{2} dr$$
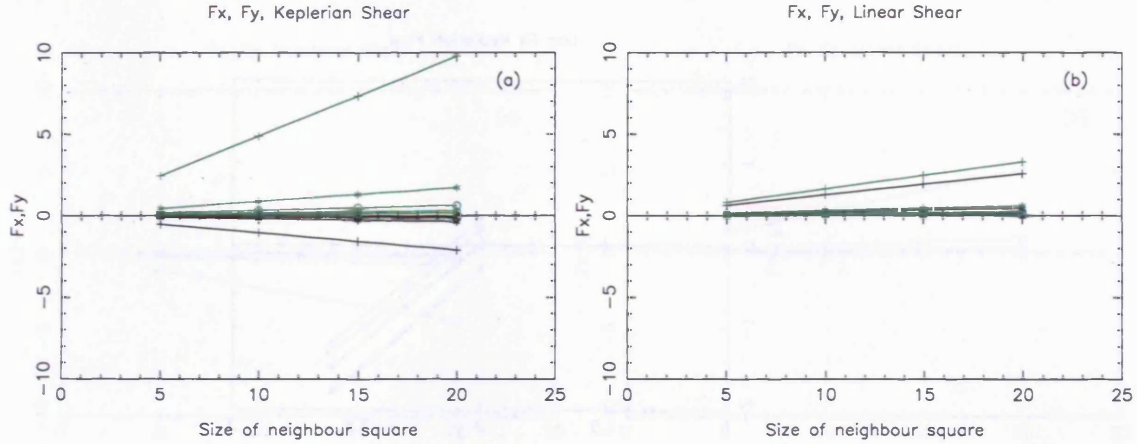
Figure 5.4: Tangential $\mathcal{F}_x$ (black) and radial $\mathcal{F}_y$ (green) for a group of neighbouring particles in (a) Keplerian orbits and (b) linear shear. The size of neighbour box is varied from 5 to 20 units, and five orbital radii are shown, varying from 100 (crosses) to 500 (boxes) units. The straight lines indicate that the magnitude of $\mathcal{F}$ is proportional to the size of the neighbour box.

$$= \frac{3k}{16r_0^{5/2}} \int_0^h r^2 dr$$

$$= \frac{kh^3}{16r_0^{5/2}} \tag{5.19}$$

Note that $\mathcal{F}_x$ is positive for linear shear flow, so once a negative coefficient α is applied, the particle is decelerated in its path, an unexpected result. The magnitude of $\mathcal{F}_x$ is in fact equal and opposite to that obtained in the more complicated situation of Keplerian flow. For linear shear flow $\mathcal{F}_y$ is positive, and $\frac{4}{\pi}$ times larger than $\mathcal{F}_x$.

5.5 Numerical simulations of Artificial Viscosity in Linear and Keplerian Shear flow

To check the above results, a numerical calculation was performed for a neighbour box of 360 particles, in the same configuration as illustrated in Fig. 5.2 but with increased density, all particles moving in the positive x direction and velocity decreasing with increasing y. First the values of $\mathcal{F}$ were calculated for Keplerian shear flow for varying neighbour box sizes h and for different radii of the central point. The value of $\mathcal{F}$ was normalised to the value of the tangential force at a radius of 100 AU for a neighbour box 5AU wide. Note that although the box size was varied, the same number of neighbours was always used, spread uniformly over the area of the box.

Log Fx Keplerian Flow
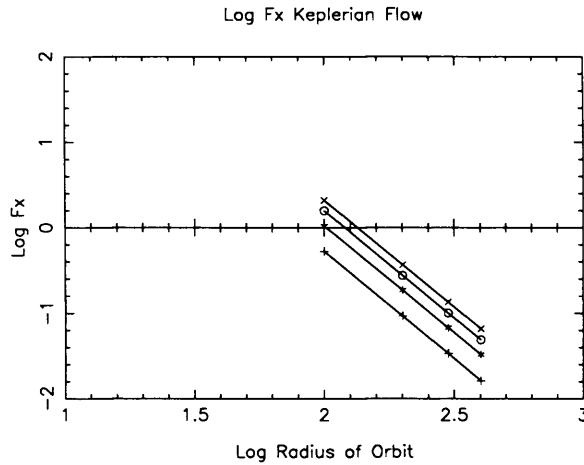
Figure 5.5: Plot of Log $\mathcal{F}_x$ (tangential acceleration) against log of the radius of the test particle's orbit for four different box sizes. Slope of all lines is -5/2. This indicates that $\mathcal{F}_x$ is proportional to $r_0^{-5/2}$. $\mathcal{F}$ calculated for approaching neighbours only, Keplerian orbits.

The results are displayed in Fig. 5.4a. The five different radii of the test particle are indicated by crosses, 100AU; *, 200AU; o, 300AU; ×, 400AU; and squares, 500AU. The black line indicates the tangential forces, which are negative, and the green line indicates the radial forces, which are positive, and about 4 times larger than the radial forces in magnitude, as predicted by the analysis. The plotted lines are straight, which shows that the magnitude of $\mathcal{F}$ is proportional to the size of the neighbour box, and hence to h.

The procedure was repeated for linear shear, and the results are shown in Fig. 5.4b. This time both the tangential (black) and the radial (green) forces are positive, and the magnitude of $\mathcal{F}_y$ is approximately 1.3 times larger than $\mathcal{F}_x$, as predicted by the analysis.

The results from figure 5.4a were replotted on a log log scale against the log of r, the radius of the test particle's orbit. These results are shown in figure 5.5. The slopes of the lines indicate that $\mathcal{F}_x$ is proportional to $r^{-5/2}$.

Our previous analysis (see Eqn. 5.13), indicated that the magnitude of Artificial Viscosity is proportional to $r^{-5/2}$ and h^3. At first sight this appears to contradict the above results. However, the analytical result was obtained by integrating over a circle of radius h around a test particle. This should result in the area of integration, and hence the number of neighbours contributing to the viscosity, increasing with h^2. In the numerical experiment, a fixed number of neighbours was used, and so the results should be a factor h^2 lower than the results from the analysis. The apparent discrepancy is explained.
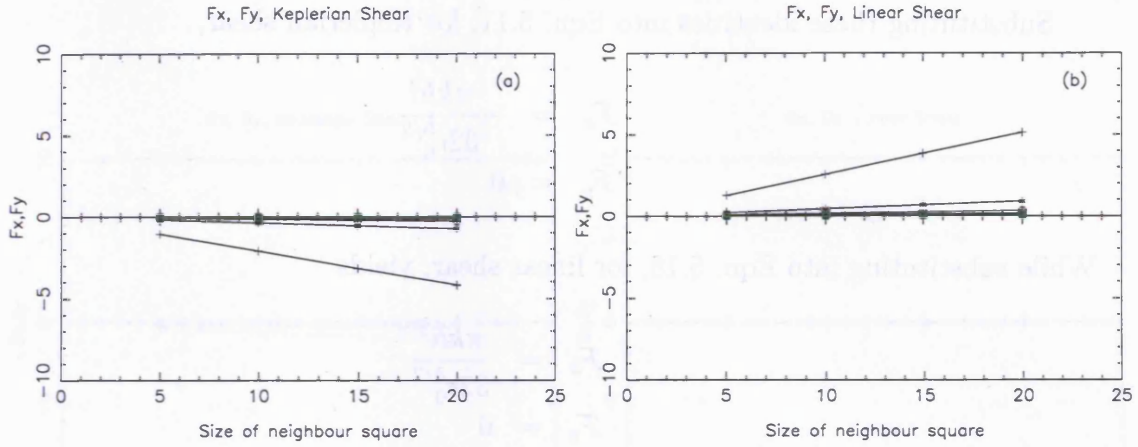
Figure 5.6: Tangential $\mathcal{F}_x$ (black) and radial $\mathcal{F}_y$ (green) for a group of neighbouring particles in (a) Keplerian orbits and (b) linear shear. The size of neighbour box is varied from 5 to 20 units, and five orbital radii are shown, varying from 100 (crosses) to 500 (boxes) units. All neighbouring points have been included in the calculation.

5.6 Including all neighbours in the calculation of Artificial Viscosity

One possible solution to the problem of high viscous forces and hence unwanted transfer of angular momentum was attempted, by including the receding particles in the calculation of Artificial Viscosity. μ_{ij} was calculated using equation 5.3 for all neighbouring particles, which should yield negative values for approaching neighbours and positive values for receding neighbours. We compute again the trigonometric identities in Eqn 5.12, this time over all four quadrants, which yields:

$$\int_0^{2\pi} \sin\theta \cos^2\theta d\theta = 0$$

$$\int_0^{2\pi} \sin^2\theta \cos\theta d\theta = 0$$

$$\int_0^{2\pi} \cos^4\theta d\theta = 6\pi/8$$

$$\int_0^{2\pi} \sin\theta \cos^3\theta d\theta = 0$$

$$\int_0^{2\pi} \sin^2\theta \cos^2\theta d\theta = 2\pi/8$$

$$\int_0^{2\pi} \sin^3\theta \cos\theta d\theta = 0 \qquad (5.20)$$

Substituting these identities into Eqn. 5.11, for Keplerian shear,

$$\mathcal{F}_x = -\frac{\pi k h^3}{32 r_0^{5/2}}$$
$$\mathcal{F}_y = 0$$

While substituting into Eqn. 5.18, for linear shear, yields

$$\mathcal{F}_x = \frac{\pi k h^3}{32 r_0^{5/2}}$$
$$\mathcal{F}_y = 0$$

So, for both linear and Keplerian shear, including all neighbours in the calculation of Artificial Viscosity removes the radial component of the resultant force, but doubles the tangential component, which remains a decelerating force for linear shear flow, and a precisely opposite acceleration for Keplerian shear flow.

This is illustrated in Figure 5.6, which is a repeat of Figure 5.4 but with all neighbouring points included in the calculation of $\mathcal{F}_x$ and $\mathcal{F}_y$. It can be seen that the radial forces $\mathcal{F}_y$ have disappeared, but the forces in the direction of the orbit, $\mathcal{F}_x$ have doubled in magnitude.

A further variation was attempted, this time reversing the polarity of μ_{ij} when calculated for receding particles. In physical terms, this would result in neighbour particles being decelerated as they approached and then accelerated again once they had passed. This was predicted to remove the tangential force while doubling the radial force. Unfortunately when this was tried in practice, it was found to be unstable, as receding particles very rapidly accelerated, increasing both v and r, which further increased the acceleration.

5.7   The inclusion of the term in μ^2

Equation 5.2 includes a second term in μ_{ij}^2, which has been ignored so far in this analysis.

$$\Pi_{ij} = \begin{cases} (-\alpha_\nu c_{ij} \mu_{ij} + \beta_\nu \mu_{ij}^2))/\rho_{ij}, , & \mathbf{v}_{ij} \cdot \mathbf{r}_{ij} \leq 0 \\ \\ 0, & \mathbf{v}_{ij} \cdot \mathbf{r}_{ij} > 0 \end{cases} \qquad (5.21)$$

Again, this term is calculated as a scalar quantity for each neighbouring particle j, and
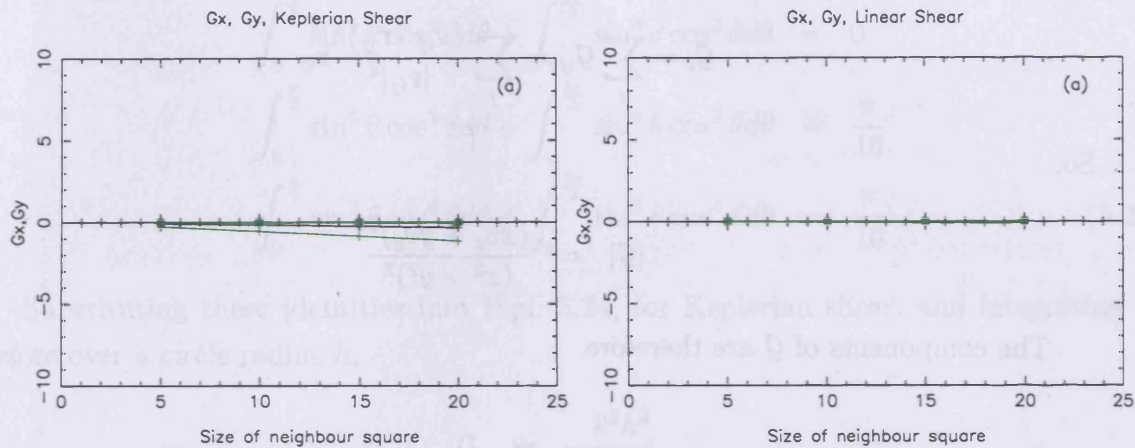
Figure 5.7: Tangential $\mathcal{G}_x$ (black) and radial $\mathcal{G}_y$ (green) for a group of neighbouring particles in (a) Keplerian orbits and (b) linear shear. The size of neighbour box is varied from 5 to 20 units, and five orbital radii are shown, varying from 100 (crosses) to 500 (boxes) units. Only approaching points are included in the calculation.
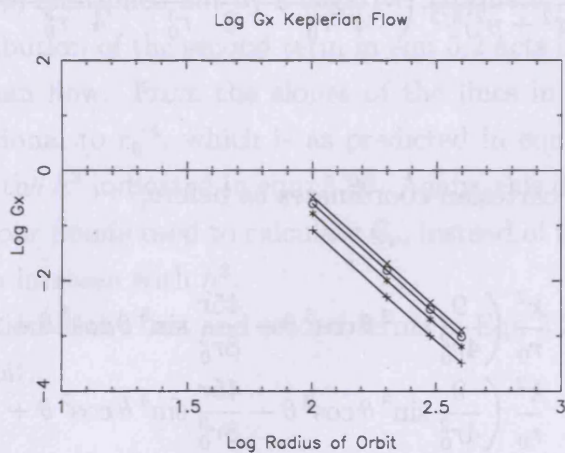
Figure 5.8: Plot of Log $\mathcal{G}_x$ (tangential acceleration) against log of the radius of the test particle's orbit for four different box sizes. Slope of all lines is -4.0, indicating that $\mathcal{G}$ is proportional to r_0^{-4}. $\mathcal{G}_x$ calculated for approaching neighbours only, Keplerian orbits.

then accumulated in a vector summation, each component being added in the direction of $\mathbf{r_{ij}}$ to give the total force on the particle i. This can be expressed as :

$$\mathcal{G}_i = \sum_j \mathcal{G}_{ij} = \sum_j \frac{(\mathbf{v}_{ij} \cdot \mathbf{r}_{ij})^2}{|\mathbf{r}_{ij}|^4} \hat{\mathbf{r}}_{ij} \tag{5.22}$$

So,

$$|\mathcal{G}| = \frac{(xv_x + yv_y)^2}{(x^2 + y^2)^2}$$

The components of $\mathcal{G}$ are therefore

$$\mathcal{G}_x = \frac{x(xv_x + yv_y)^2}{(x^2 + y^2)^{5/2}}$$

$$\mathcal{G}_y = \frac{y(xv_x + yv_y)^2}{(x^2 + y^2)^{5/2}} \tag{5.23}$$

Substituting for v_x and v_y

$$\mathcal{G}_x = \frac{k^2}{r_0} \left(\frac{1}{(x^2 + y^2)^{5/2}} \left(-\frac{9}{4} \frac{x^3 y^2}{r_0^2} - \frac{45}{8} \frac{x^3 y^3}{r_0^3} + \frac{9}{4} \frac{x^5 y}{r_0^3} + \mathcal{O}(\frac{x^3 y^4}{r_0^4}, \frac{x^5 y^2}{r_0^4}, \frac{x^7}{r_0^4}) \right) \right)$$

$$\mathcal{G}_y = \frac{k^2}{r_0} \left(\frac{1}{(x^2 + y^2)^{5/2}} \left(-\frac{9}{4} \frac{x^2 y^3}{r_0^2} - \frac{45}{8} \frac{x^2 y^4}{r_0^3} + \frac{9}{4} \frac{x^4 y^2}{r_0^3} + \mathcal{O}(\frac{x^2 y^5}{r_0^4}, \frac{x^4 y^3}{r_0^4}, \frac{x^6 y}{r_0^4}) \right) \right)$$

Transforming into cartesian coordinates as before,

$$\mathcal{G}_x = \frac{k^2}{r_0} \left(\frac{9}{4r_0^2} \sin^2 \theta \cos^3 \theta - \frac{45r}{8r_0^3} \sin^3 \theta \cos^3 \theta + \frac{9r}{4r_0^3} \cos^5 \theta \sin \theta \right)$$

$$\mathcal{G}_y = \frac{k^2}{r_0} \left(\frac{9}{4r_0^2} \sin^3 \theta \cos^2 \theta - \frac{45r}{8r_0^3} \sin^4 \theta \cos^2 \theta + \frac{9r}{4r_0^3} \cos^4 \theta \sin^2 \theta \right) \tag{5.24}$$

The required trigonometric identities are :

$$\int_0^{\frac{\pi}{2}} \sin^2 \theta \cos^3 \theta d\theta + \int_\pi^{\frac{3\pi}{2}} \sin^2 \theta \cos^3 \theta d\theta = 0$$

$$\int_0^{\frac{\pi}{2}} \sin^3 \theta \cos^3 \theta d\theta + \int_\pi^{\frac{3\pi}{2}} \sin^3 \theta \cos^3 \theta d\theta = \frac{1}{6}$$

$$\int_0^{\frac{\pi}{2}} \sin\theta \cos^5\theta d\theta + \int_\pi^{\frac{3\pi}{2}} \sin\theta \cos^5\theta d\theta = \frac{1}{3}$$

$$\int_0^{\frac{\pi}{2}} \sin^3\theta \cos^2\theta d\theta + \int_\pi^{\frac{3\pi}{2}} \sin^3\theta \cos^2\theta d\theta = 0$$

$$\int_0^{\frac{\pi}{2}} \sin^4\theta \cos^2\theta d\theta + \int_\pi^{\frac{3\pi}{2}} \sin^4\theta \cos^2\theta d\theta = \frac{\pi}{16}$$

$$\int_0^{\frac{\pi}{2}} \sin^2\theta \cos^4\theta d\theta + \int_\pi^{\frac{3\pi}{2}} \sin^2\theta \cos^4\theta d\theta = \frac{\pi}{16} \tag{5.25}$$

Substituting these identities into Eqn. 5.24, for Keplerian shear, and integrating as before over a circle radius h,

$$\mathcal{G}_x = -\frac{k^2 h^3}{16 r_0^4}$$

$$\mathcal{G}_y = -\frac{9\pi k^2 h^3}{128 r_0^4} \tag{5.26}$$

The numerical experiment was repeated, this time calculating $\mathcal{G}$ for approaching neighbours only, varying h, the size of the neighbour box and r, the orbital radius, as before. The results are shown in figures 5.7 and 5.8.

Figures 5.7 and 5.8 show that $\mathcal{G}_x$ and $\mathcal{G}_y$ are zero for linear shear flows, while Keplerian flows produce negative $\mathcal{G}_x$ and $\mathcal{G}_y$. However, referring to Eqn 5.2, we see that this component of viscosity is multiplied not by a negative parameter, $-\alpha$, but a positive one, β. Therefore the contribution of the second term in eqn 5.2 acts in the opposite direction to the first for Keplerian flow. From the slopes of the lines in fig. 5.8, the magnitude of this term is proportional to r_0^{-4}, which is as predicted in eqn 5.26 and h, which is a factor of h^2 lower than the h^3 indicated in eqn. 5.26. Again, this discrepancy is due to the fixed number of neighbour points used to calculate $\mathcal{G}_x$, instead of the number of neighbour points being allowed to increase with h^2.

The opposing direction of the first and second terms in Eqn 5.2 will only be of concern if, in smooth stable orbit,

$$\alpha_\nu c_{ij} \simeq \beta_\nu \mu_{ij},$$

that is, if μ_{ij} is of the order of half the sound speed, if α and β are set to values 1.0 and 2.0 as usual. Figure 5.2 showed that the relative velocity of neighbours and hence μ_{ij} varies in magnitude for different neighbours of a point, increasing with the magnitude of

Maximum Muij and sound speed vs radius
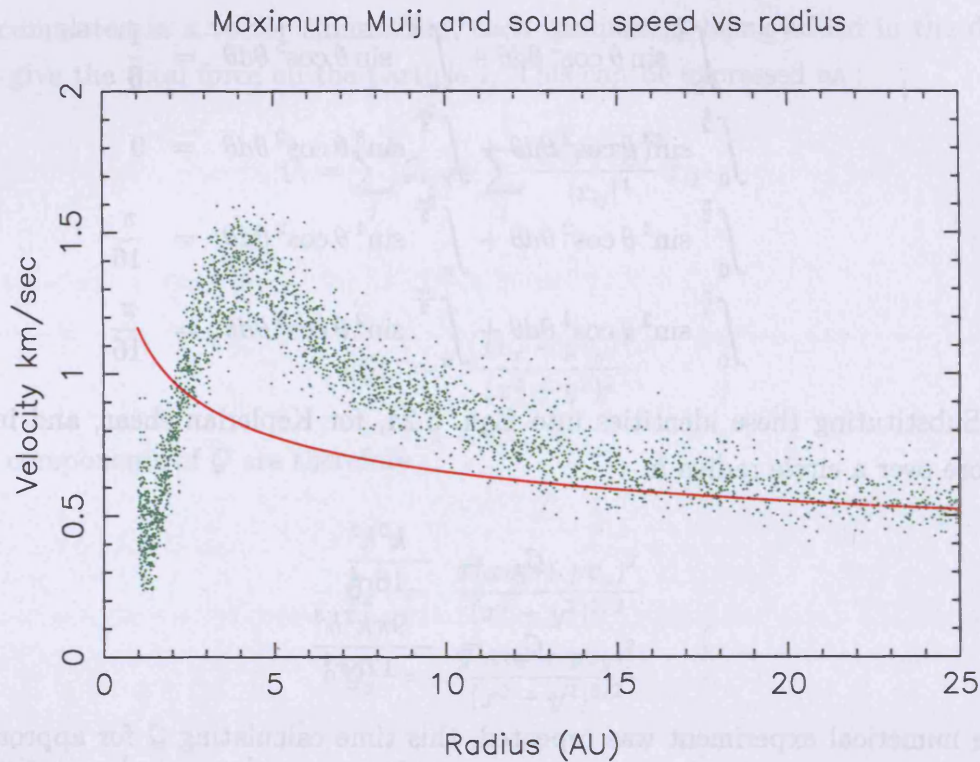
Figure 5.9: Comparison of values of μ_{ij} and c the sound speed. Green points are the maximum magnitude of μ_{ij}, in km.s^{-1}, calculated for each SPH particle in a Keplerian disk with surface density $\Sigma \propto r^{-7/4}$, orbiting a central $1M_\odot$ star, plotted against radius in AU. Red points indicate the sound speed for the same particles, given temperature profile $T \propto r^{-1/2}$.

their separation r_{ij}. Sound speed, however, is likely to vary little over the extent of a particle's neighbours.

Figure 5.9 shows a direct comparison of the values of μ and c for a disk in stable Keplerian rotation about a $1M_\odot$ star. It is clear that the maximum value of μ_{ij} for each particle often exceeds half the sound speed. The value of $\frac{dv}{dr}$ is so high for Keplerian disks, that the relative velocity of neighbours as they pass in other orbits is of the order of the sound speed. Only in the inner regions of the disk is the sound speed clearly greater than the maximum μ_{ij} calculated for all the particles. Sound speed is higher due to the increased temperature in the inner regions. The fall in maximum μ_{ij} with decreasing radius is at first puzzling, given that the orbital velocities, and hence the relative velocities, increase rapidly in central regions. However, the value of h falls with radius as density increases, so the distance to the most distant neighbour of a point gets smaller. The resultant maximum value of μ_{ij} falls with decreasing r, because the effect of reducing h overwhelms the effect of increasing $\frac{dv}{dr}$.

Therefore the two terms in the Viscosity formulation in eqn. 5.2 may accumulate to act in the same, or opposing directions, depending on the temperature of the disk and the distances between pairs of neighbouring particles.

In a simulation of a disk using this formulation of viscosity, therefore, a change in the temperature of the disk, decreasing the sound speed, could result in the resultant acceleration due to Artificial Viscosity changing direction, as the second term in μ^2 becomes larger than the first, and the viscous force acts to slow down, rather than accelerate, the particles in orbit. The precise balance between density gradient, and its effect on h, and the gradient of the velocity profile, is important in trying to predict the effect of Artificial Viscosity in differentially rotating disks.

5.8 Conclusion

The use of Artificial Viscosity to prevent interpenetration of particle streams is known to cause angular momentum transport through high viscous shearing forces, when used in Keplerian accretion disks (Bate 2000). We have demonstrated that, using the standard formulation for Artificial Viscosity with uniform surface density Keplerian disks, angular momentum transport can change direction, depending on the temperature and hence the sound speed, of the disks. This is not a physical effect, but an artifact of the simulation.

The direction of the resultant shear force for Keplerian orbits is in the opposite direction to that obtained for linear shear with the same velocity profile. The curvature of the orbits causes a larger effect than the velocity gradient. Linear shear does not approximate Keplerian shear at any dimension or at any radius of orbit.

This finding is of particular interest because of the use of 'shearing box' approximations to circular shear flow (Gammie 2001, Masset & Papaloizou 2003). Clarke & Pringle (2004) also use a first order approximation to circular shear flow in obtaining the result that angular momentum flows from the centre of a Keplerian disk outwards. Our finding that the direction of angular momentum flow is controlled by the second order terms (eqn 5.14) indicates that first order approximations may yield inaccurate results.

The calculation of the key μ parameter is vulnerable to noise. Some of this is simply Poisson noise, and increasing the density of particles will help to reduce this. Of more concern is the systematic problem that the calculation of μ is highly sensitive to the relative positions and velocities of neighbouring particles.

We also note that Artificial Viscosity when applied to Keplerian disks causes a radial force four times larger than the tangential force, pushing particles inwards. Using all particles, not only the receding particles, in the calculation of Artificial Viscosity, removes

the radial component of force, but doubles the tangential component.

It is apparent that Artificial Viscosity should be switched off as far as possible, when a disk is rotating stably and there is no real convergence, to avoid the unpredictable consequences of these problems.

Chapter 6

Switching off Viscosity

6.1 The Balsara Switch

In the last chapter we demonstrated that the standard implementation of Artificial Viscosity in SPH fails to distinguish between particles overtaking in a smoothly rotating Keplerian accretion disk and particles which approach because of genuine convergence. Clearly it is preferable to discriminate between the two types of approaching particles and apply Artificial Viscosity only in the case of genuine convergence.

A well known tool for enabling the rapid switch-on of Artificial Viscosity in the presence of a shock, is the Balsara Switch (Balsara 1989), which works as follows. The viscosity coefficients α and β in Eqn 5.2 are set to the values required to capture shocks (α =1.0, β=2.0). A multiplicative factor is then calculated for each particle i, being

$$B_i = \frac{\mid \nabla \cdot \mathbf{v} \mid_i}{\mid \nabla \times \mathbf{v} \mid_i + \mid \nabla \cdot \mathbf{v} \mid_i},$$

(6.1)

where $\mathbf{v}$ is the velocity field and the derivatives are evaluated at $\mathbf{r}_i$.

The viscous acceleration between each pair of particles is then multiplied by the mean of the values of B, thus

$$\Pi_{ij} \rightarrow \frac{(B_i + B_j)}{2} \cdot \Pi_{ij}$$

(6.2)

It can be shown that in a Keplerian disk, with all matter orbiting in centrifugal balance about a mass M, $\mid \nabla \times \mathbf{v} \mid$ and $\mid \nabla \cdot \mathbf{v} \mid$ at radius r are given by :

$$\mid \nabla \times \mathbf{v} \mid = \left(\frac{MG}{4r^3}\right)^{1/2}$$
$$\mid \nabla \cdot \mathbf{v} \mid = 0.$$

(6.3)

$| \nabla \times \mathbf{v} |$ is therefore finite while $| \nabla \cdot \mathbf{v} |$ is zero, and hence B is zero for all r. However, if particles start to converge at a particular location, $| \nabla \cdot \mathbf{v} |$ increases, so B increases, approaching a limiting value of 1.0, when $| \nabla \cdot \mathbf{v} | \gg | \nabla \times \mathbf{v} |$. Multiplying the viscosity coefficients by the Balsara factor should effectively switch off the Artificial Viscosity, when a disk is rotating stably with Keplerian velocity profile, but switch it on, selectively, for any points involved in an area of true convergence.

6.2 Noise problems with the SPH implementation of the Balsara Switch

In SPH simulations B is calculated for each particle using eqn. 6.1, substituting numerical estimates $\nabla \cdot \mathbf{v} |_{\text{SPH}}$ and $\nabla \times \mathbf{v} |_{\text{SPH}}$ for the true values of $\nabla \cdot \mathbf{v}$ and $\nabla \times \mathbf{v}$:

$$\nabla \cdot \mathbf{v} |_{\text{SPH}} = \sum_j \frac{m_j}{\rho_j} \frac{\mathbf{v}_{ij} \cdot \mathbf{r}_{ij}}{| \mathbf{r}_{ij} | \bar{h}_{ij}^4} W' \left(| \mathbf{r}_{ij} |, \bar{h}_{ij} \right),$$

$$\nabla \times \mathbf{v} |_{\text{SPH}} = \sum_j \frac{m_j}{\rho_j} \frac{\mathbf{v}_{ij} \times \mathbf{r}_{ij}}{| \mathbf{r}_{ij} | \bar{h}_{ij}^4} W' \left(| \mathbf{r}_{ij} |, \bar{h}_{ij} \right), \tag{6.4}$$

$$\tag{6.5}$$

where W_{ij} is the gradient of the kernel function, $\mathbf{r}_{ij} \equiv \mathbf{r}_i - \mathbf{r}_j$ the position vector of particle i relative to its jth neighbour and $\mathbf{v}_{ij} \equiv \mathbf{v}_i - \mathbf{v}_j$ the relative velocity.

From eqn. 4.12, the value of B should be zero for a stably rotating disk of particles in Keplerian orbits, where there is no convergence. However, as Figs. 6.1a and b demonstrate, this does not happen in practice in SPH simulations.

Figure 6.1a shows the value of B calculated for 10,000 SPH particles in stable Keplerian orbits around a star, plotted against their radius in AU. The disk, mass $0.1 M_\odot$ was set up with randomly positioned particles, such that surface density $\Sigma \propto r^{-7/4}$ and the thickness of the disk was $0.1r$ with an approximately Gaussian density profile in the z direction. Temperature was set to $T = 375 K (r/\text{AU})^{-1/2}$ and a locally isothermal equation of state applied. The particles were set in circular orbits solely under the influence of the gravity of the central star, with no pressure or viscous forces operating. After 20 time steps B was calculated for each point. B can be seen to vary from 0.0 to about 0.6 with some values as high as 0.8, the mean value for this disk being 0.22. Figure 6.1b is a face-on view of the disk, with colour coding indicating the value of B for each particle. Yellow indicates $B < 0.2$, through orange for medium B to red for $B > 0.6$. High B value particles occur

at all radii but are not scattered randomly over the disk, rather they appear to form alignments.

From eqn. 6.1, a non-zero value of B will result from a large positive value of $\nabla \cdot \mathbf{v}$ |$_{\mathbf{SPH}}$, which will occur quite correctly when particles are moving away from each other, not converging. The calculation of B was therefore corrected so that it was only calculated for particles with converging neighbours, giving negative values of $\nabla \cdot \mathbf{v}$ |$_{\mathbf{SPH}}$, and set to 0 otherwise. This resulted in the change shown in fig. 6.1c and d. The colour-coded azimuthal view of the disk fig. 6.1c, shows that the high B value particles are now found at all radii, but the alignments of particles are now predominantly in the 'leading' direction (the disk is rotating in an anti-clockwise direction). For completeness, B was also calculated, incorrectly, for particles with positive $\nabla \cdot \mathbf{v}$ |$_{\mathbf{SPH}}$ and set to zero for negative $\nabla \cdot \mathbf{v}$ |$_{\mathbf{SPH}}$, which yielded fig. 6.1d. Here the high B value particle form 'trailing' strands.

Figure 6.2 shows an enlargement of part of fig. 6.1c, to enable a closer inspection of the alignment features.

Fig. 5.1b in the previous chapter showed that the neighbours of a particle in a Keplerian disk fall into four quadrants of approaching or receding particles. The calculation of $\nabla \cdot \mathbf{v}$ |$_{\mathbf{SPH}}$ will add together positive values of $\mathbf{v}_{ij}.\mathbf{r}_{ij}$ from receding neighbours and negative values from approaching ones. If there are many neighbours and they are evenly distributed, $\nabla \cdot \mathbf{v}$ |$_{\mathbf{SPH}}$ will be small, as the positive and negative components cancel out. However, if there are few neighbours, Poisson noise will cause $\nabla \cdot \mathbf{v}$ |$_{\mathbf{SPH}}$ to increase in magnitude.

In order to quantify the dependence of B on neighbour numbers, the number of neighbouring particles used to calculate B for each particle in the disk used in fig. 6.1 was varied from 16 to 75, which resulted in the mean h increasing from 0.59 to 1.07 AU. The results are tabulated in table. 6.1, and show that increasing the number of neighbours did reduce the mean value of B. However, using more than 60 neighbours had no benefit, as B fell from 0.31 (for 16 neighbours) to 0.20 (for 60 neighbours), and then stayed constant if the number of neighbours was increased further. This was because increasing the radius of the neighbour sphere included neighbours with much larger absolute values of $\mathbf{v}_{ij}.\mathbf{r}_{ij}$. The noise introduced by adding together all these larger positive and negative values was therefore even larger than the noise introduced by adding a small number of small positive and negative values from the nearby neighbours.

Calculating B only for particles with a negative value of $\nabla \cdot v$ |$_{SPH}$ resulted in a smaller mean B value, approximately half that obtained when B was calculated for all particles, the smallest value, 0.08, obtained when 60 or more neighbours were used in the calculation of B.
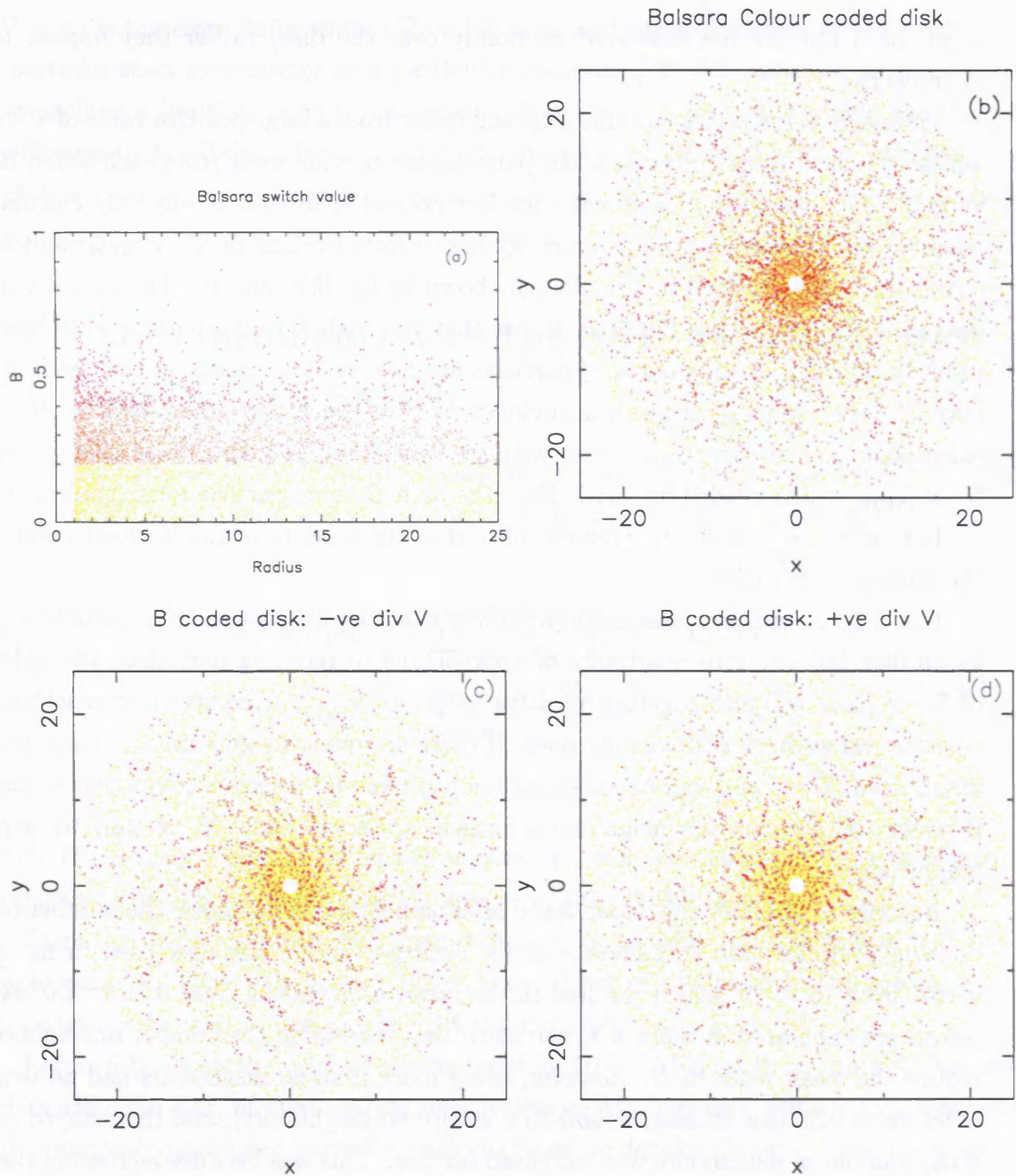
Figure 6.1: Balsara Switch values for a Keplerian disk. B is calculated using 50 neighbours for each point. (a) Values of B plotted against radius for 10,000 points in a disk, colour coded yellow for $B < 0.2$, orange for $0.2 < B < 0.4$ and red for $B > 0.4$; (b) azimuthal view of the actual disk, which is rotating anti-clockwise, each point coloured as before. High B value particles occur at all radii. At intermediate radii, high B particles appear to form strands; (c) as (b) except that B is only calculated for negative values of $\nabla \cdot v \mid_{SPH}$, and set to zero if $\nabla \cdot v \mid_{SPH}$ is positive. Note that the alignments of particles with high B in (c) are predominantly in the 'leading' direction; (d) as (c) except that B is only calculated for positive values of $\nabla \cdot v \mid_{SPH}$, and set to zero if $\nabla \cdot v \mid_{SPH}$ is negative. Alignments of particles with high B are now trailing the anti-clockwise rotation of the disk.
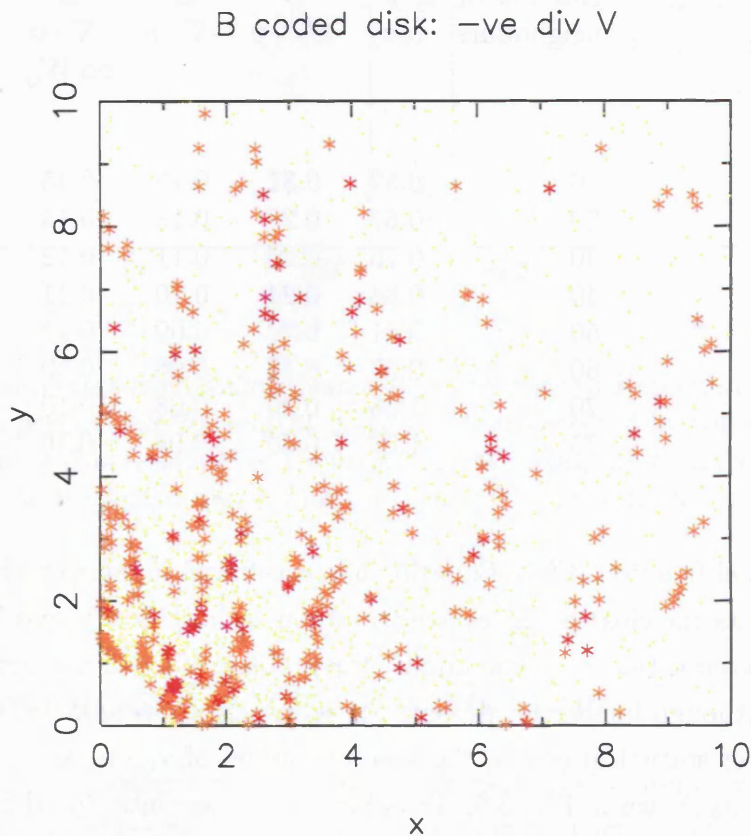
Figure 6.2: An enlargement of a section of the disk in fig. 6.1d. High B value particles
are now indicated with an asterisk, and coloured yellow, orange, red, purple and blue, to
indicate B in the ranges 0 to 0.2, 0.2 to 0.4, 0.4 to 0.6, 0.6 to 0.8 and 0.8 to 1.0. The
disk is rotating anticlockwise, and it can be seen that high B strands occur in the leading
direction (that is, the particles in outer orbits are ahead of those on inner orbits). Where
particles happen to lie in alignments which trail rotation, they have low or zero B values.

Table 6.1: Mean value of B for 10,000 SPH particles orbiting in a Keplerian disk. Column one gives the number of neighbours of each particle included in the Balsara Switch calculation. Column 2 the value of the smoothing length h. Column 3 gives the mean value of B calculated using this value of h, and Column 4 the mean value of B if only negative values of $\nabla \cdot \mathbf{v}$ |$_\mathrm{SPH}$ are allowed to yield non-zero B values, B being set to zero for positive values of $\nabla \cdot \mathbf{v}$ |$_\mathrm{SPH}$. Column 5 omits the kernel function from the calculation of B, and sets B to zero for positive values of $\nabla \cdot \mathbf{v}$ |$_\mathrm{SPH}$.

Number of neighbours	h (au)	B $\pm \nabla \cdot v$	B $-\nabla \cdot v$	B $-\nabla \cdot v$ no W_{ij}
16	0.59	0.31	0.15	0.15
20	0.67	0.29	0.13	0.14
30	0.76	0.26	0.11	0.12
40	0.84	0.24	0.10	0.11
50	0.91	0.22	0.09	0.11
60	0.97	0.20	0.08	0.10
70	1.06	0.20	0.08	0.10
75	1.07	0.20	0.08	0.10

The kernel function W'_{ij} in Equation 6.4, was found to improve the accuracy of B. The kernel weights the close particles' contributions to both $\nabla \times \mathbf{v}$ and $\nabla \cdot \mathbf{v}$ most heavily, so one would assume that it would amplify the problem of small numbers of close neighbours. However, although further neighbours are more numerous and therefore are less prone to small-number statistical errors, the absolute values of $\mathbf{v}_{ij} \cdot \mathbf{r}_{ij}$ are much larger for distant neighbours, as shown in Fig. 5.6. Thus large errors are introduced by distant neighbours, if they are not attenuated by the kernel function. This result is illustrated in Column 5 of Table 6.1. It can be seen that removing the kernel function in the calculation of B does not improve its accuracy, but actually makes it slightly worse.

In order to show that the majority of high B values in fig. 6.1 really are spurious, the disk was also processed using a pattern-matching algorithm, which compared the velocity of each particle's neighbours with the expected velocities, given that all particles are orbiting the central star with a Keplerian velocity profile (the operation of this algorithm is explained in section 6.6). The result is shown in fig. 6.3a. Particles are shown as yellow, if no convergence was detected and red if neighbours were found to be converging. It can be seen that very little real convergence is happening in the disk, only a few random points showing apparent convergence. By contrast in fig. 6.3b, red points indicate a high value of B for many points in the disk, forming clear linear features which are not randomly

Pattern matched disk

B coded disk: −ve div V
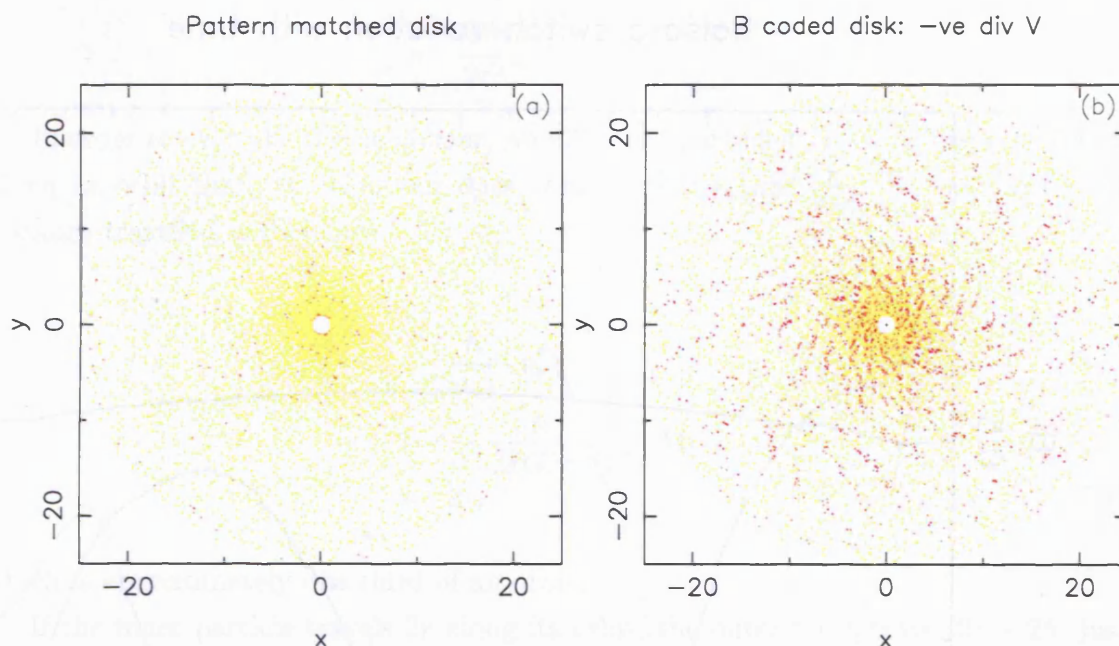
Figure 6.3: (a) Keplerian disk, yellow points indicate smooth Keplerian rotation without convergence, red points have convergent neighbours, as detected by comparing neighbour velocities with those characteristic of Keplerian orbits. Compare with (b), Balsara Switch values for the same Keplerian disk, using the same 50 neighbours for each particle.

oriented.

6.3 Variation of $\nabla \cdot \mathbf{v} \,|_{\mathbf{SPH}}$ with time

In a Keplerian disk, all particles are constantly overtaking their outer neighbours and being overtaken by inner neighbours. As a result, three or more particles often find themselves in alignment. In this case, the closest neighbours of a particle are in opposite quadrants, so they are all positive or all negative. They therefore contribute to a large negative value of $\nabla \cdot \mathbf{v} \,|_{\mathbf{SPH}}$ while they are approaching alignment, and then a high positive value, once they have passed alignment and are spreading out. This explains the orientation of the linear features observed in figs. 6.1b, 6.1d and 6.2. Chance alignments of particles will produce high values of B for any orientation of alignments, if B is calculated for both positive and negative values of $\nabla \cdot \mathbf{v} \,|_{\mathbf{SPH}}$. But if B is set to zero for positive values of $\nabla \cdot \mathbf{v} \,|_{\mathbf{SPH}}$, high B values only occur for points in alignments with outer particles ahead and inner particles behind.

Figure 6.4 shows the value of B for three SPH particles in different orbits within a Keplerian disk. As B is set to zero when $\nabla \cdot \mathbf{v} \,|_{\mathbf{SPH}}$ is positive, we see the positive half of
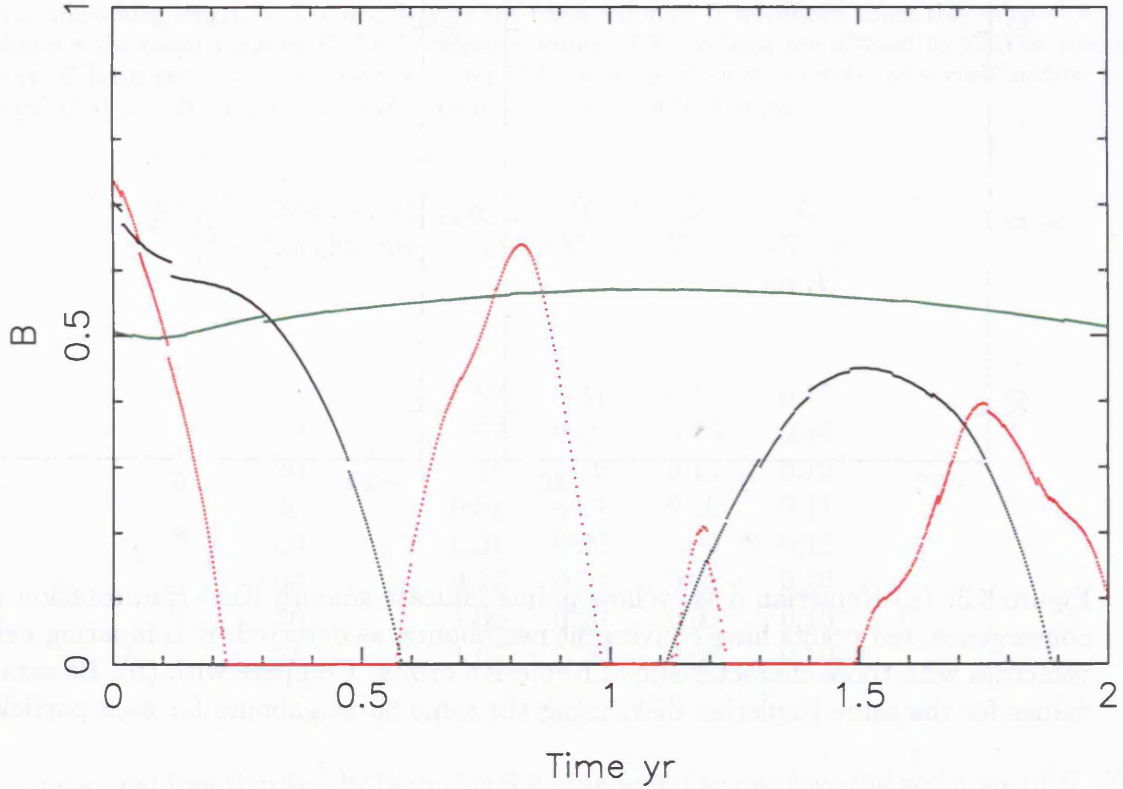
Figure 6.4: Balsara Switch values B plotted against time, for SPH particles at various radii in a Keplerian disk around a $1M_\odot$ star. Red is at radius 1.4AU, black at 3 AU and green at 10au. Orbital periods for these radii are 1.6y, 5y and 30y. Note the discontinuities in B which are due to modifications to the neighbour lists, which affect the calculated values of $\nabla \cdot \mathbf{v} \,|_{\mathbf{SPH}}$ and $\nabla \times \mathbf{v} \,|_{\mathbf{SPH}}$.

three periodical functions. Clearly B is varying periodically, with a frequency decreasing with the radius of the orbit.

This is explained by considering the 'overtaking' speed of a neighbour. Consider a particle orbiting mass M at radius r, and its neighbour orbiting at radius $r + h$. The overtaking orbital speed v_{rel} of the inner particle is :

$$
\begin{aligned}
v_{rel} &= GMr^{-1/2} - MG(r+h)^{-1/2} \\
&\simeq GMr^{-1/2}\left[1 - \left(1 - \frac{h}{2r}\right)\right] \\
&= GMr^{-1/2}\frac{h}{2r}
\end{aligned}
$$

$$= \frac{GMh}{2r^{3/2}} \tag{6.6}$$

In order to overtake the neighbour, we allow the particle to travel a distance h further along its orbit than its neighbour does, which takes a time $\frac{h}{v_{rel}}$. During this time the distance travelled is therefore

$$\frac{h}{v_{rel}} \cdot v_{orb}$$

$$= \frac{h}{0.5MGhr^{-3/2}} \cdot MGr^{-1/2}$$

$$= 2r, \tag{6.7}$$

which is approximately one third of an orbit.

If the inner particle travels $2r$ along its orbit, the outer must travel $2r + 2h$, just to keep its station. So, adding this effect to that calculated in Eqn.6.7, we have the particle moving $3h$ past a neighbour distance h away in the time it takes to travel one third of the way round its orbit. This should be approximately the period of one cycle of the value of B.

The variation of B with time is therefore predicted to be periodic with frequency approximately three times the orbital frequency. A particle orbiting at radius 1.4 AU with an orbital frequency of 1.6 year should show 4 cycles of B in a 2 year period. For 3 AU the period is about 5 years and we expect just over one cycle. For 10 AU, with an orbital period 30 years, we only expect to see about $\frac{1}{5}$ of the cycle. This agrees well with what is seen in Fig.6.4.

There is the possibility that once an alignment structure has formed, all the particles in that structure will have high B values, and will therefore tend to stick to their neighbours more than other particles. The longer such structures exist, the more angular momentum they will transfer. The observation, by Imaeda and Inutsuka (2002), that linear structures are a pronounced feature of SPH simulations of shear flow when the Balsara Switch is used to control Artificial Viscosity, supports this hypothesis. This raises the worrying possibility that the Balsara Switch itself could be enhancing the formation of filaments in disk simulations, which could then lead to misleading results.

6.4   Time Dependent Viscosity

A second method for selectively switching on Artificial Viscosity in shocks while keeping it switched off at other times, was proposed by Morris and Monaghan (1997), and may be referred to as Time Dependent Viscosity.

Each SPH particle is given its own viscosity parameter α, which evolves with time, according to the equation

$$\frac{d\alpha}{dt} = -\frac{\alpha - \alpha^*}{\tau} + S, \tag{6.8}$$

where S is the source term,

$$S = max(-\nabla \cdot \mathbf{v} \mid_{SPH}, 0). \tag{6.9}$$

and τ is the e-folding time, which is set to be

$$\tau = \frac{h}{C_1 \cdot c}, \tag{6.10}$$

where h is the smoothing length for viscous and pressure forces, c is the sound speed and C_1 a parameter chosen to allow α to build up fast enough but not decay too quickly.

Clearly α increases if $\nabla \cdot \mathbf{v} \mid_{SPH}$ is negative, and decays to a minimum value α^* otherwise. This provides a rapidly increasing viscosity around a particle when it encounters shocks, where $\nabla \cdot \mathbf{v} \mid_{SPH}$ is large and negative for a number of successive timesteps. Once the shock is passed, $\nabla \cdot \mathbf{v} \mid_{SPH}$ falls to small or even negative values, and the viscosity dies away again. Morris and Monaghan (1997) suggest that setting C_1 to 0.2 should ensure that the viscosity dies down to the minimum value within about 5 smoothing lengths.

This method is not helpful for preventing spuriously high viscosity in a Keplerian accretion disk, the problem being that once again $\nabla \cdot \mathbf{v} \mid_{SPH}$ is being used as an indicator of convergence. As we have shown, $\nabla \cdot \mathbf{v} \mid_{SPH}$ varies periodically with a frequency dependent on radius, as particles overtake one another, causing alignments to form. It is impossible to tune the Time Dependent Viscosity method to filter out such low frequency noise without making it much too slow to react to shocks.

It is also a problem that the actual value of $\nabla \cdot \mathbf{v} \mid_{SPH}$ is used to increase α for any particle. This will cause viscosity to switch on quickly for particles in the centre of the disk where relative velocities are high, but much more slowly, if at all, in the slower outer reaches of the disk. This is demonstrated in Fig. 6.5. Here a Keplerian disk has been allowed to settle and then the value of α has been calculated for 20 timesteps, using Time Dependent Viscosity (closest particles complete an orbit in 50 timesteps). Values of α can
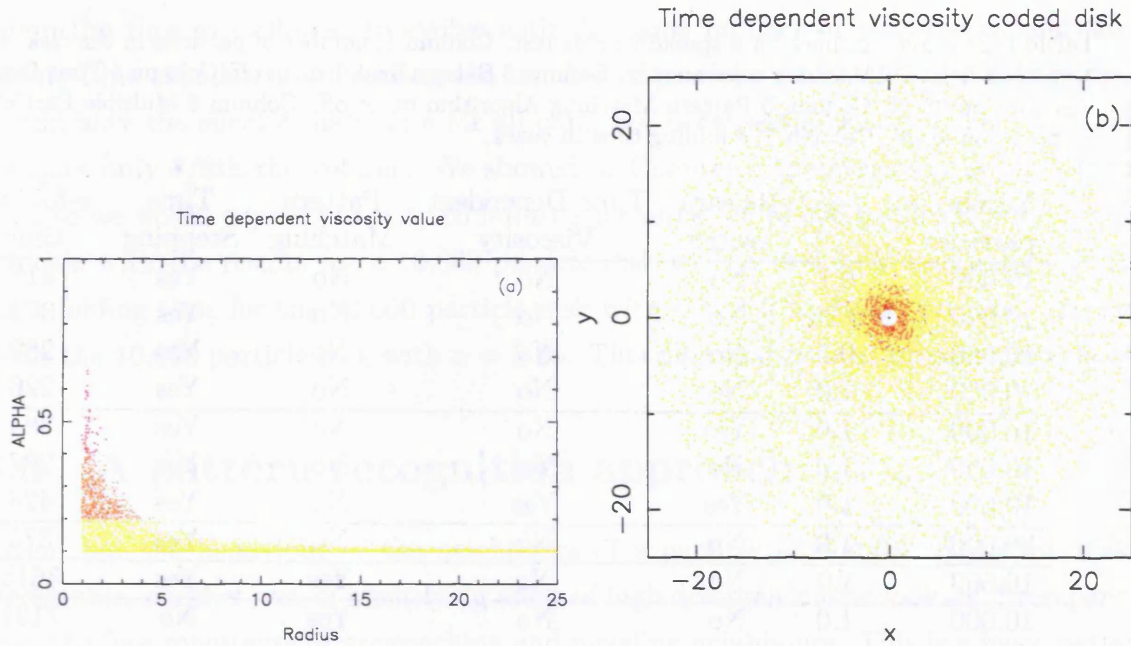
Figure 6.5: Keplerian disk, colour coded with value of Time Dependent Viscosity parameter, α. (a) α plotted against radius, (b) azimuthal view of disk, colour coded as (a). Note high values of α concentrated in the central zone.

be seen to be close to 0.1, the value given to $\alpha^\star$, for radii greater than 4AU, while within that radius α rises sharply with falling radius.

6.5 Spreading ring test

Lynden-Bell and Pringle (1974) predicted that a ring of particles will spread under the influence of viscosity. A ring of 10,000 SPH particles, total mass $0.1M_\odot$ was therefore created, with an approximately Gaussian distribution of surface density about a maximum at 10 AU. This was set in Keplerian orbit about a $1M_\odot$ star, with no self gravity within the ring and no pressure forces, and allowed to evolve only under the influence of the star's gravity and Artificial Viscosity. Multiple Particle Time Stepping was used with a range of 10^4 from the shortest to the longest timesteps. As the ring evolved, all the particles were binned in 100 bins by radius, the mean surface density calculated for each bin, and the maximum value stored as $\Sigma(t)$.

Artificial Viscosity was calculated for 50 neighbours, applied for both positive and negative values of $\nabla \cdot \mathbf{v} \, |_{\mathrm{SPH}}$, in order to avoid the radial forces which arise when only approaching neighbours are used in the Viscosity calculation (see chapter 5). The viscosity parameter α was varied from 0.1 to 1.0, while β was kept constant. This was then

Table 6.2: e-folding times for a spreading ring test. Column 1, number of particles in the disk. Column 2, value of Artificial Viscosity α parameter. Column 3 Balsara Switch on or off, Column 4 Time Dependent Viscosity on or off, Column 5 Pattern Matching Algorithm on or off. Column 6 Multiple Particle Time Stepping on or off. Column 7, e-folding time in years.

Number of particles	α	Balsara switch	Time Dependent Viscosity	Pattern Matching	Time Stepping	e-folding time
10,000	0.1	No	No	No	Yes	418
10,000	0.25	No	No	No	Yes	374
10,000	0.5	No	No	No	Yes	289
10,000	1.0	No	No	No	Yes	226
10,000	1.0	Yes	No	No	Yes	384
10,000	1.0	No	Yes	No	Yes	287
10,000	1.0	Yes	Yes	No	Yes	428
80,000	1.0	No	No	No	Yes	375
10,000	1.0	No	No	Yes	Yes	3615
10,000	1.0	No	No	Yes	No	7191

repeated with the Balsara Switch implemented, as defined in Eqn 6.1 and again with Time Dependent Viscosity. For each trial the e-folding time t_f was calculated, where

$$\Sigma(t) = \Sigma_0 e^{-\frac{t}{t_f}}.$$ (6.11)

Here $\Sigma(t)$ is the maximum density at time t and Σ_0 is the maximum density at time 0.

The first four rows of Table 6.2 show, as expected, that decreasing α increases the e-folding time. Less viscosity transfers angular momentum more slowly and the ring spreads more slowly. A factor of 10 reduction in α from $\alpha = 1.0$ to $\alpha = 0.1$ increases the e-folding time by 85%.

Implementing the Balsara Switch and keeping $\alpha = 1.0$ increases the e-folding time by 70%, which is slightly longer than the increase due to reducing α from 1.0 to =0.25. By comparison, our mean B value for 50 neighbours in Table 6.1 was 0.22. The two results are consistent.

Keeping $\alpha = 1.0$ and adding Time Dependent Viscosity increases the e-folding time by only 27%, equivalent to reducing α to 0.5. This method is less effective at reducing the shearing force than the Balsara Switch, because the value of α does not decay back down to zero between overtaking neighbours.

Using both the Balsara Switch and Time Dependent Viscosity multiplies the two effects, giving an effective α of 0.1.

The ring was then created with the same mass but 80,000 particles instead of 10,000.

Again the ring was allowed to evolve with the same number of neighbours, and the e-folding time calculated. Increasing the number of particles to 80,000, an 8 fold increase, should have the effect of halving h for all particles, because the same number of particles occupies only 1/8th the volume. We showed in Chapter 5 that viscosity is proportional to h, so we would expect viscosity to fall to $\frac{1}{2}$ its value for 10,000 particles, and therefore coincide with the results for a 10,000 particle disk with α of 0.5. We actually find that the e-folding time for the 80,000 particle disk with $\alpha = 1.0$ is almost precisely the same as for the 10,000 particle disk with $\alpha = 0.25$. This discrepancy is at present unexplained.

6.6 A pattern recognition approach

Given that the behaviour of the neighbours of a particle in a stable Keplerian disk is predictable, another way of identifying areas of high divergence is to look for discrepancies from the four quadrants of approaching and receding neighbours. This is a basic pattern-recognition approach, and has already been used to produce the colour coded disk in Fig. 6.3a, picking out only points in a disk with neighbours whose relative velocities differ from those predicted in a Keplerian disk.

A simple algorithm was developed by which each particle's neighbours were examined to determine whether they were approaching or receding. Any approaching neighbours in the quadrants which should have contained receding particles were counted, and that total divided by the total number of particles in those quadrants, to give a scalar factor p in the range $0.0 \leq p \leq 1.0$. p is calculated as follows.

We assume that the particle i is in Keplerian orbit about the origin. Its position vector $\mathbf{r}_i$ describes a line from the centre of rotation to the particle, giving us a radial direction. Its velocity $\mathbf{v}_i$ gives us the direction of the orbit. A neighbour particle j is predicted to be approaching particle i, if it is ahead of particle i and on an outer orbit, or if it is behind particle i and on an inner orbit. Figure 6.6 illustrates this situation for a particle i and its neighbour j, when j is ahead and on an outer orbit. In other words, $\mathbf{r}_{ji} \cdot \mathbf{r}_i$ and $\mathbf{r}_{ji} \cdot \mathbf{v}_i$ are both positive for particles ahead and on an outer orbit, or both negative if behind and on an inner orbit. A negative value of $\mathbf{r}_{ji} \cdot \mathbf{v}_{ji}$ tells us that the neighbour is actually approaching. Note that all of these vector calculations are applied only in the plane of the disk, so vertical velocities are ignored.

Therefore we count how many neighbouring particles have $(\mathbf{r}_{ji} \cdot \mathbf{r}_i)(\mathbf{r}_{ji} \cdot \mathbf{v}_i) < 0$. This gives us a number n_{rec} of neighbours which should be receding if they are in unperturbed Keplerian orbits. For each of these neighbours we test whether they actually are receding by calculating $\mathbf{r}_{ij} \cdot \mathbf{v}_{ij}$. A negative value indicates that they are approaching, and the
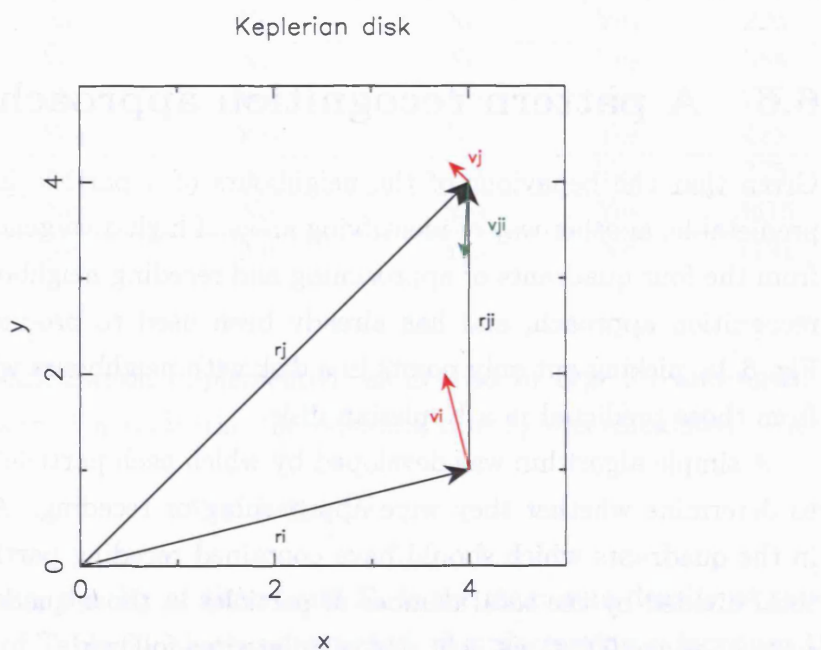
Keplerian disk

Figure 6.6: Two particles i and j in a Keplerian disk, orbiting around the origin in an anticlockwise sense. The position vectors $\mathbf{r}_i$ and $\mathbf{r}_j$ and the relative position $\mathbf{r}_{ji}$ are indicated by black arrows. $\mathbf{r}_i.\mathbf{r}_{ji}$ is positive here because j's orbit lies outside i's. It would be negative for a particle on an inner orbit. Particle velocities $\mathbf{v}_i$ and $\mathbf{v}_j$ are shown in red. $\mathbf{v}_i.\mathbf{r}_{ji}$ is positive for this configuration, because j is ahead of particle i. The relative velocity $\mathbf{v}_{ji}$ is indicated in green. $\mathbf{r}_{ji}.\mathbf{v}_{ji}$ is negative, indicating an approaching pair of neighbours.

number of these anomalous neighbours is accumulated to give us n_{an}. The factor p is then calculated as

$$p = \frac{n_{an}}{n_{rec}} \tag{6.12}$$

Figure 6.3 shows the results obtained using this algorithm, when applied to the stable Keplerian disk of Fig. 6.1. Yellow particles indicate low p, red indicates particles where p is high because convergent neighbours are detected. Very few particles have falsely registered as divergent, and the mean value of p for this disk is 0.023. Compare this with Fig. 6.3b, where the Balsara Switch has been calculated for converging neighbours only. The high B linear features are not truly areas of high convergence, as they are not detected by the pattern matching algorithm. The mean value of B for this disk is 0.114.

Having established that the pattern matching algorithm correctly discards linear arrangements of neighbours, and does not label them as convergent, it was next applied to a disk where structure was developing. Figure 6.7 shows a disk where trailing arms of high density are forming, colour coded as before by (a) the pattern recognition algorithm score, p, and (b) the Balsara Switch value, B. Yellow indicates low values, going through red to blue for very high values.

The mean values for the disk were $\bar{p} = 0.119$ and $\bar{B} = 0.112$. Note that B actually had a lower mean value for this disk with structure forming than it did for the disk with no structure and purely Keplerian orbits in Fig. 6.3b. By contrast, $\bar{p}$ was five times larger for the disk with structure forming than the disk without.

The values for p and B are also shown plotted against radius in Figs. 6.7(c) and (d). p finds convergent neighbours in the central regions of the disk, where matter is infalling onto the central star. By contrast B is low in this region. This is due to the rapid increase in $\nabla \times v \,|_{\text{SPH}}$, which from eqn. 6.4 is proportional to $r^{-3/2}$. As $\nabla \times v \,|_{\text{SPH}}$ is in the denominator of the expression for B, values of B are forced to stay low in the centre of the disk. By contrast, B can be seen to be set to its highest values, (particles coloured purple and blue), not in the areas of the spiral arms where mass is densest and p is high, but in the sparsely populated areas between spiral arms where particles have formed alignments in the 'leading' direction, and because of the low density, h is high, so very distant neighbours are being used to calculate B.

The use of Multiple Particle Time Stepping was a potential complication in the use of the pattern matching algorithm, as the outer neighbours of a particle might have their accelerations calculated less frequently than the inner neighbours. There was a possibility therefore that the quadrant pattern of neighbours might not be as consistent when Multiple Particle Time Stepping was being used. To test this, the pattern matching parameter p was calculated and applied to the viscosity between each pair of particles
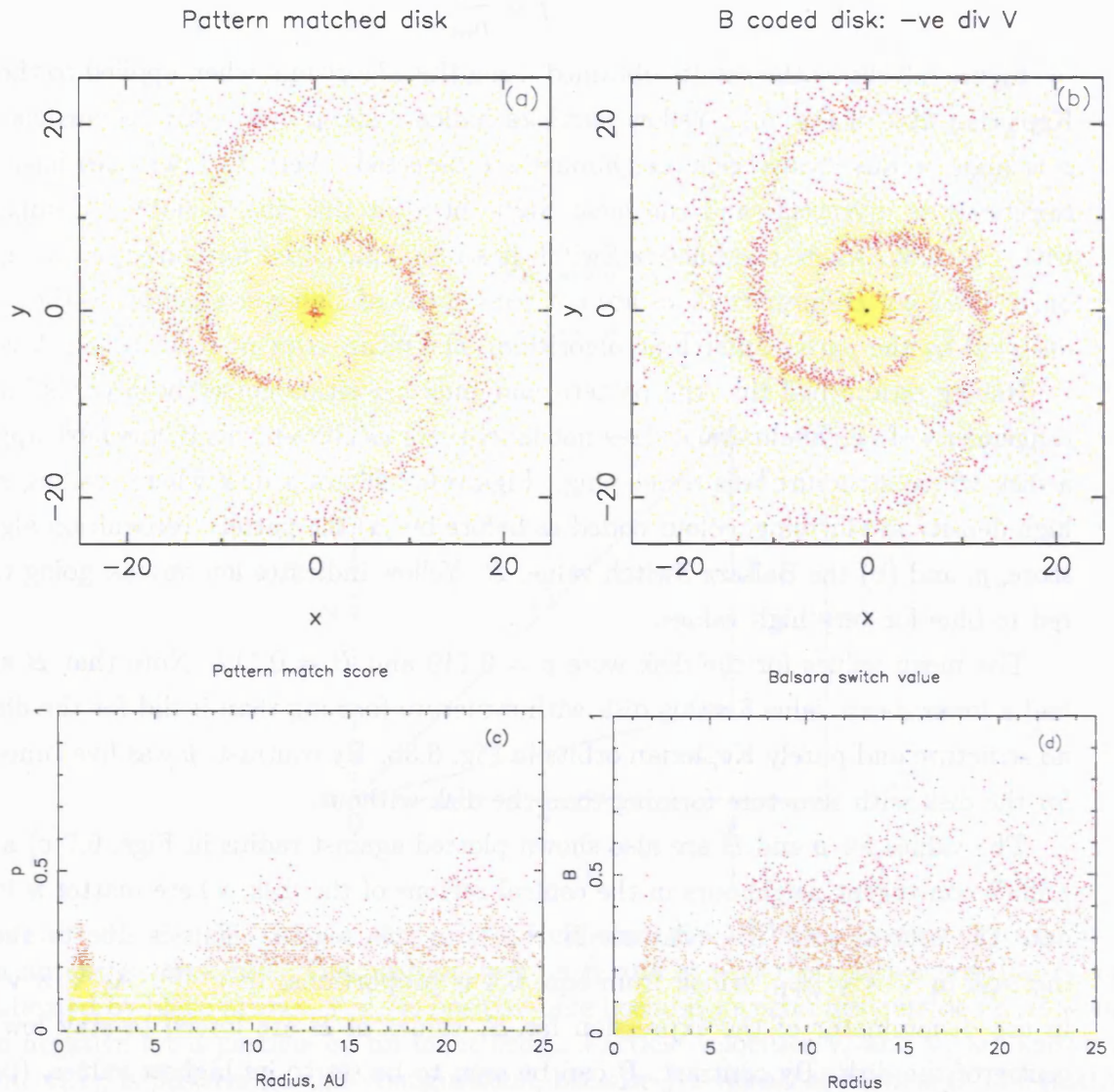
Figure 6.7: Keplerian disk in which structure is developing. In both disks yellow indicates areas where convergence is not detected and viscosity will be kept low. (a) Colour coded with pattern recognition score p, red indicates convergence, mean value of p is 0.119; (b) Balsara Switch value, yellow indicates low B, going through orange to red and purple for high values, mean value of B is 0.112. Note that both techniques identify the high density regions of the spiral arms as convergent; (c) values of p plotted against radius for the same disk. Note high values near the centre; (d) values of B plotted against radius for the same disk. Note that no high values of B occur towards the centre of the disk.

for the ring spreading test, with and without the use of Multiple Particle Time Stepping. As with the Balsara Switch, the viscous acceleration between each pair of particles was multiplied by the mean of the values of p, thus

$$\Pi_{ij} \rightarrow \frac{(p_i + p_j)}{2} \cdot \Pi_{ij} \tag{6.13}$$

The results are shown in Table 6.2. The e-folding time was found to be 3615 yrs when Multiple Particle Time Stepping was implemented and 7191 yrs when it was disabled. Therefore, as predicted, pattern matching was less effective at keeping Artificial Viscosity switched off in Keplerian rotation when Multiple Particle Time Stepping was implemented. However this lower level of effectiveness still represents an order of magnitude improvement over either the Balsara Switch or Time Dependent Viscosity.

6.7 Conclusion

Two well-known techniques for minimising Artificial Viscosity in shear flow, but then switching it on in shocks, have problems dealing with the situation in smoothly rotating Keplerian accretion disks.

The Balsara Switch is prone to an alignment artefact, varying periodically with a frequency $\sim$ 3 times the orbital frequency, which is the overtaking frequency for neighbours. This is independent of h and therefore independent of the number of SPH particles used. It also fails to register high values in the central areas of a Keplerian disk because of the very high values of $\nabla \times \mathbf{v}\ |_{\text{SPH}}$ in these areas, while it tends to register high values in low density regions, because of the higher values of h and therefore the larger relative velocities of neighbours used in the calculation of B.

Time Dependent Viscosity is not suitable for use in Keplerian disks if used with $\nabla \cdot \mathbf{v}\ |_{\text{SPH}}$, as a source term. $\nabla \cdot \mathbf{v}\ |_{\text{SPH}}$, is the source of the low frequency alignment artefact which plagues the Balsara Switch, and applying a low pass filter to it does not remove the effect.

A promising pattern matching algorithm has been developed which correctly identifies areas of high convergence in arrays of orbiting particles, while producing only very small numbers of 'false positives' in disks of particles in Keplerian orbits. It would be possible to produce a much more accurate pattern matching algorithm, which modelled in more detail the expected pattern of relative velocities as a function of relative position for neighbour particles. However, the simple approach outlined above has the advantage of speed, and from the results shown in Figs. 6.7 and 6.3 seems to discriminate effectively

between Keplerian shear and converging flow.

Chapter 7

Time stepping

7.1 Introduction

SPH is used to simulate a physical environment in which forces, velocities and positions vary continuously, but have to be calculated at discrete time intervals. Setting very short time intervals between the calculations will optimise the accuracy of a simulation, but at the cost of increasing computational effort. We therefore seek the best compromise between computational efficiency and accuracy of the simulation.

7.2 Predictor Corrector Algorithm

A two step predictor-corrector algorithm (eg Press et al., 1992) is used to improve the accuracy of the numerical integration scheme.

Given values of $\mathbf{r}$ $\mathbf{v}$ and $\mathbf{a}$ at time t, we predict the values at time $t + \delta t$, where δt is the timestep, as follows. We first calculate the values for $\mathbf{r}$ and $\mathbf{v}$ at the half timestep $t + \frac{\delta t}{2}$:

$$
\begin{aligned}
r(t + \delta t/2) &= r(t) + v(t)\delta t/2 \\
v(t + \delta t/2) &= v(t) + a(t)\delta t/2
\end{aligned}
\tag{7.1}
$$

These values of $\mathbf{r}$ and $\mathbf{v}$ are used to obtain a value of $\mathbf{a}$ for the half timestep. Full step values for $\mathbf{r}$ and $\mathbf{v}$ are then calculated :

$$
\begin{aligned}
r(t + \delta t) &= r(t) + v(t + \frac{\delta t}{2})\delta t \\
v(t + \delta t) &= v(t) + a(t + \frac{\delta t}{2})\delta t
\end{aligned}
\tag{7.2}
$$

7.3   Courant-Friedrich-Levy Condition

It can be seen from eqn. 7.2 that an accurate calculation of $r(t)$ will depend on δt being short enough for $v(t)$ and $a(t)$ not to vary significantly during a timestep. This has been set up in the Dragon SPH code using the following conditions.

For each particle, δt is set to be less than or equal to the following values :

$$t1 \;=\; \frac{h(p)}{v(p) + c(p)}$$

$$t2 \;=\; \left(\frac{h(p)}{a(p)}\right)^{0.5}$$

$$t3 \;=\; \frac{h(p)}{\sigma}$$

where

$$\sigma \;=\; c(p) + 1.2\alpha c(p) + 1.2\beta \mu_{\max} \qquad\qquad (7.3)$$

α and β are the values used in the viscosity calculations, and μ_{max} the largest value of μ found in the viscosity calculations for any particle.The factor 1.2 has been found to be right by experimentation for simulations of turbulent clouds.

These are an adapted version of the Courant-Friedrich-Levy(CFL) condition.

The first condition, $\delta t \leq t1$, is the Velocity Condition, which ensures that δt is shorter than the time necessary for a particle to travel the distance h, the smoothing length for this particle, travelling at its current speed v plus the sound speed. This will be short for high velocity particles, or particles in hot regions with high sound speed.

The second condition $\delta t \leq t2$ ensures that δt is short enough that a stationary particle with acceleration a will travel no further than $2h$ in time δt. This is the Acceleration Condition.

$\delta t \leq t3$ is a modification of the 'Sound Speed Condition' and is intended to set short values of δt in shock conditions. However, as the maximum value of μ found anywhere in the disk is used, this will tend to set short timesteps throughout the disk, even when a shock event is localised. We shall refer to this as the Shock Condition.

Figure 7.1 shows how the three values t1, t2 and t3 vary with radius in a Keplerian accretion disk, which has been allowed to evolve for 100 timesteps. All three conditions increase with radius. Over almost all of the disk, the Acceleration Condition time is consistently the largest and the Velocity and Shock Condition times both are about half that value.
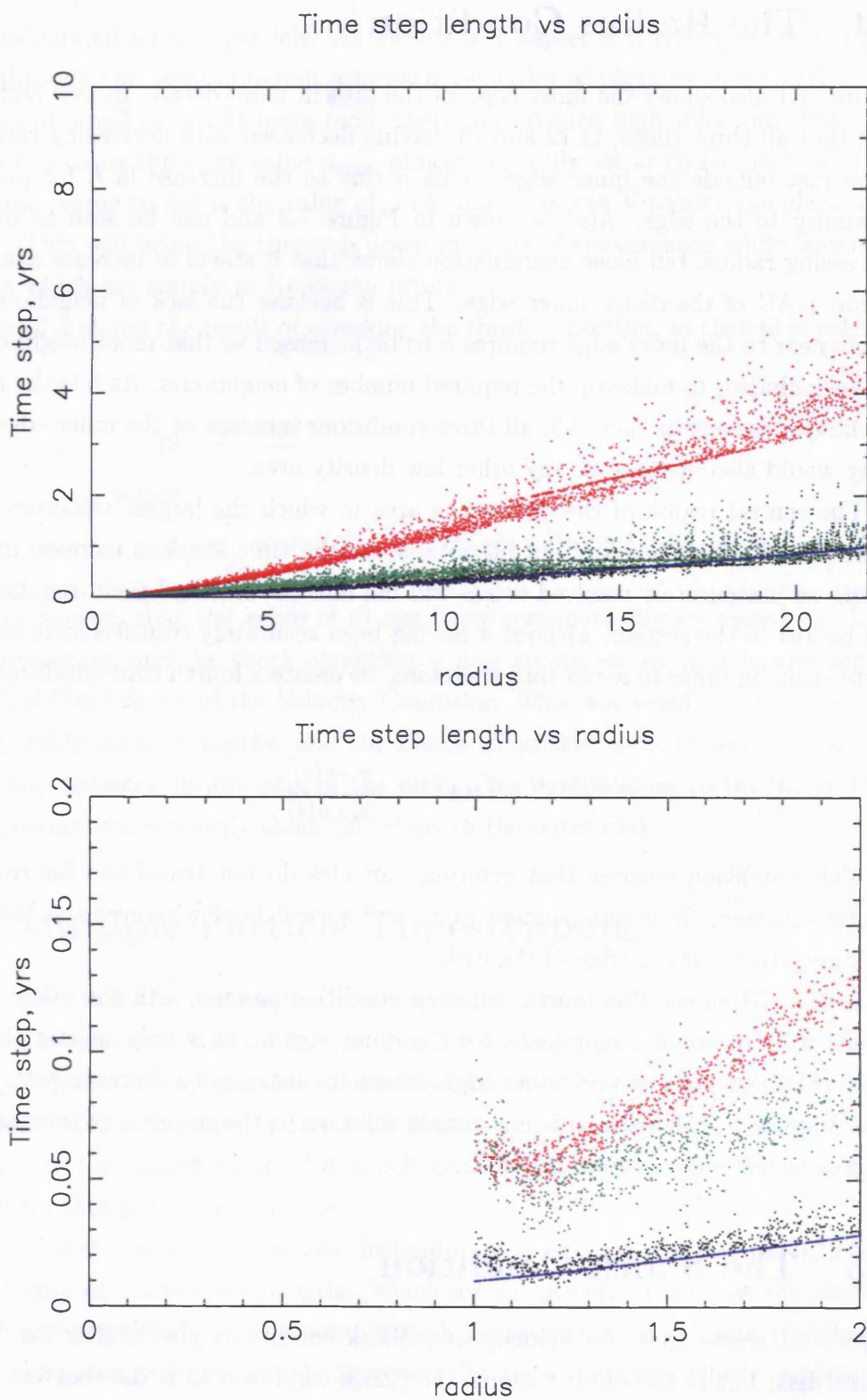
Figure 7.1: Timestep lengths vs radius for a Keplerian disk. Above, whole disk. Below, magnification of the inner edge region. t1 (black) the Velocity Condition, t2 (red) the Acceleration Condition, t3 (green) the Shock Condition and t4 (blue) the Radius condition.

7.4   The Radius Condition

Figure 7.1 also shows the inner edge of the disk in more detail. In this region it can be seen that all three times, t1 t2 and t3, having decreased with decreasing radius, increase again just outside the inner edge. This is due to the increase in h for points in close proximity to the edge. $h(r)$ is shown in Figure 7.3 and can be seen to decrease with decreasing radius, but close examination shows that it starts to increase again for points within 1 AU of the disk's inner edge. This is because the lack of neighbours inward of points near to the inner edge requires h to be increased so that more neighbours outward can be included, to make up the required number of neighbours. As h is the numerator of all the expressions in Eqn. 7.3, all three conditions increase at the inner edge of the disk. They would also increase in any other low density area.

The central region of the disk is the area in which the largest velocities and accelerations occur. It is therefore not acceptable for the time steps to increase in this region. Points on inaccurately resolved orbits will fall into the star and their angular momentum will be lost to the system, without it having been accurately transferred to other particles in the disk. In order to avoid this, therefore, we create a fourth time condition, $t4$, defined as

$$t4 \ = \ \frac{\pi \cdot r(t)}{50 \cdot v(t)}$$

This condition ensures that orbiting particles do not travel too far round an orbit in one timestep. It is independent of h, and so will hold whatever the local density or proximity to the inner edge of the disk.

Figure 7.1 shows this fourth timestep condition plotted with the other three for the whole disk and, on a larger scale, for the inner region. $t4$ is only shorter than the other three conditions at the very inner edge, where it continues to decrease with radius. As it is very quick to calculate, this is a simple solution to the problem of increasing timestep lengths at the inner edge of the disk.

7.5   The Shock Condition

Figure 7.1 shows that the Velocity and Shock conditions give similar results over most of the disk, but in the outer regions, the Shock condition $t3$ is the shortest, shorter even than the Radius Condition. Given that this disk is stably rotating with no shocks, this erroneously short $t3$ in the outer regions will result in unnecessarily short timesteps. It arises from the use of μ_{max} in Eqn. 7.3, which is the largest value of the Shear Viscosity

term μ calculated for any particle. As we saw in Chapter 5, μ can reach very high values simply through the large apparent approach velocities of particles in Keplerian rotation, especially at small radii. At large radii, there are no such high velocities, but the Shock Condition is using the large value μ_{max}, almost certainly set at those inner radii. A more appropriate value to use is the value of μ calculated in the Viscosity calculation for each particle. This will bring the timestep down in areas of convergence while leaving it high for areas which are simply in Keplerian orbits.

Figure 7.2 shows the result of changing the shock condition, so that $t3$ is calculated as

$$t3 = \frac{h(p)}{\sigma}$$

where

$$\sigma = sound(p) + 1.2 \cdot \alpha \cdot sound(p) + 1.2 \cdot \beta \cdot \mu(p) \tag{7.4}$$

It can be seen that the value of $t3$ has been systematically increased by the change in its calculation, and the shock condition is now giving values of $t3$ clearly higher than the Radius Condition and the Velocity Condition. This is a sensible result, as the disk is rotating stably with no shocks, and the Shock Condition should therefore not be giving the shortest timestep in any part of the disk. This modification to the Shock Condition should prevent unnecessarily short timesteps in the outer disk.

7.6 Multiple Particle Timestepping

Having calculated the maximum timestep length permissible for each particle, this information is used to design a Multiple Particle Timestepping scheme. First the shortest timestep required by any particle is identified and used to calculate δt_{min}. Each particle is then allocated a timestep a factor 2^n larger than this minimum timestep, such that $2^n \times \delta t_{min}$ is the largest value of n which gives a timestep smaller than the maximum timestep for that particular particle.

Figure 7.4 shows how this works. Instead of a continuous range of particle timesteps, only an array of discrete steplengths, which are all powers of 2 times the length of the shortest, are permitted. In this way, at each timestep the time-intensive calculation of gravity and pressure forces is only necessary for those particles which require updating of their accleration calculation. All of the other particles may safely be moved using the two-step extrapolation. This achieves a considerable speeding up of the simulation, as was quantified in Chapter 3.

Time step length vs radius
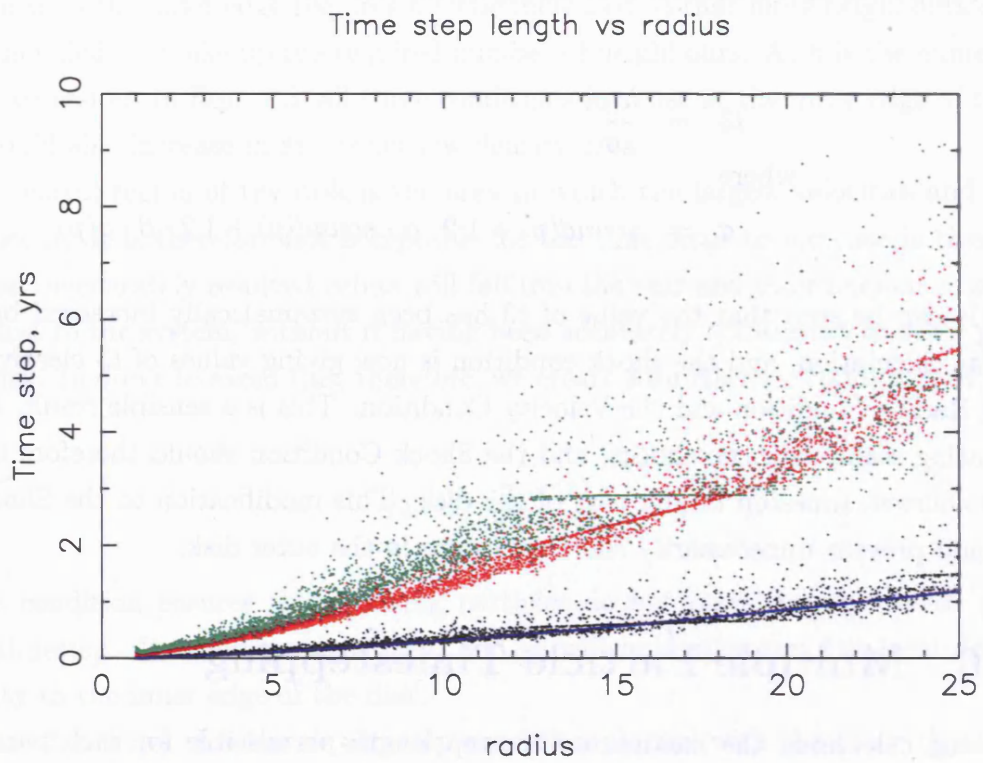
Figure 7.2: Timestep lengths vs radius for a Keplerian disk, with t3 calculated using $\mu(p)$, instead of umax. t1 (black) the Velocity Condition, t2 (red) the Acceleration Condition, t3 (green) the Shock Condition, t4 the Radius Condition.

h (au) vs radius
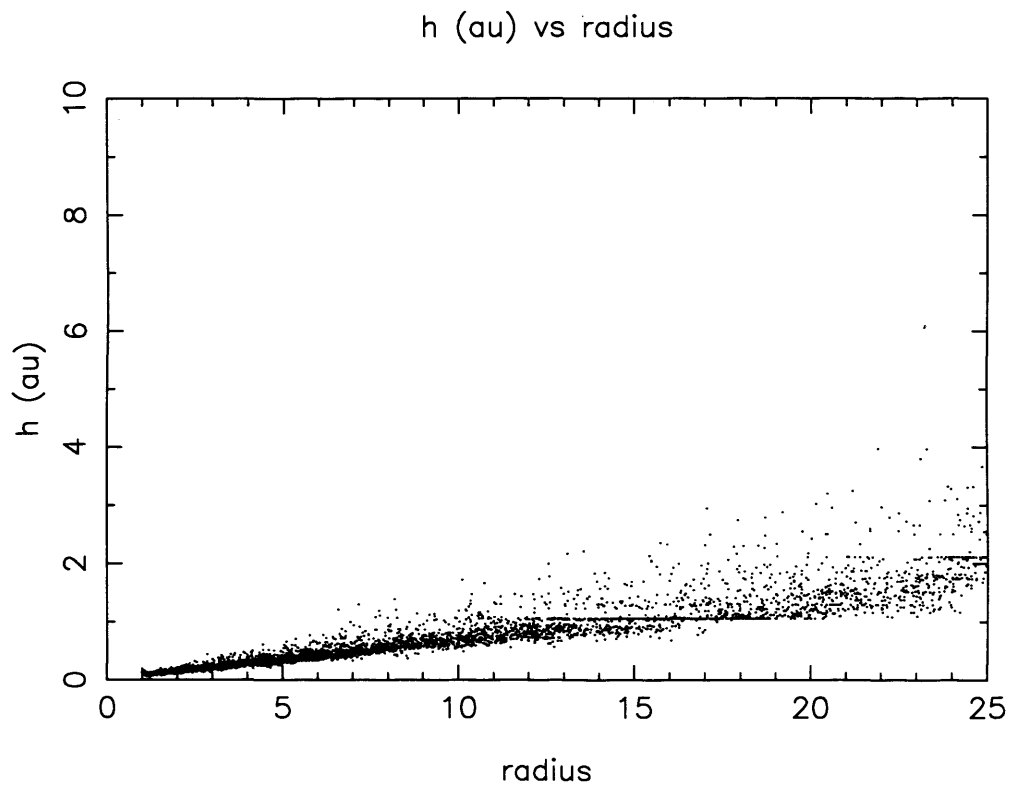
Figure 7.3: h(p) in AU for all points in a keplerian disk, surface density proportional to $R^{-1.75}$, 20 neighbours required.

Time step length vs radius
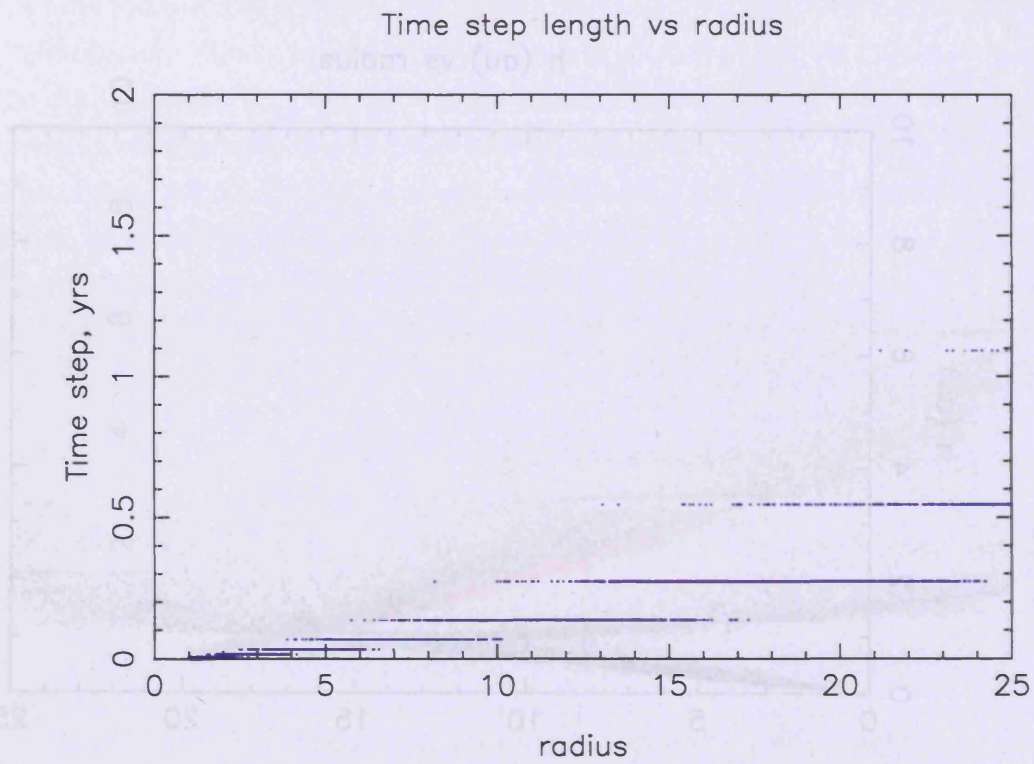
Figure 7.4: Actual timesteps allocated for particles in a disk. Note that all timesteps are a factor 2^n larger than the minimum step, and all are smaller than the four timestep conditions illustrated in Fig. 7.2.

7.7 Angular Momentum Conservation

In order to check that time stepping was giving an accurate simulation, and in particular, that angular momentum was being conserved, the total angular momentum of the system was checked every timestep for each simulation. It was found to be conserved to 97% for 10,000 particle disks and 99% for 100,000 particle disks.

7.8 Conclusion

Modifications were made to the standard Dragon timestepping calculations, in order to cope with two particular features of disks. A Radial Condition ensured that timesteps were short enough to limit the angular distance travelled around one orbit in one timestep, independent of the value of h of a particle. Modification to the Shock Condition set a value dependent on the rate of approach of neighbours of an individual particle, rather than the highest value experienced in the disk, thus avoiding unnecessarily short timesteps in the outer regions of the disk.

Tests indicated that Angular Momentum was conserved to within 97% for 10,000 particle disks and 99% for 100,000 particle disks, and that the timestepping was therefore operating correctly.

Chapter 8

Simulations

8.1 Introduction

Having adapted the Dragon SPH code as described in the previous chapters, simulations of the evolution of protoplanetary disks were run with various input conditions, and with different schemes for handling temperature and viscosity. The results are described here.

Initial experiments exercised the Dragon software with an input dataset which reproduced the initial conditions of a Keplerian accretion disk around a $1M_\odot$ star. Self gravity, pressure and Artificial Viscosity were included. A check was made on the conservation of angular momentum of the system.

A sequence of SPH simulations was then run to investigate whether the effects due to Artificial Viscosity, and the use of the Balsara Switch and Time Dependent Artificial Viscosity, that we predicted in chapters 5 and 6, could be observed in real simulations.

An additional aim was to compare our results with those of Mayer et al.(2004), who found that the value of the Toomre Q parameter was key in predicting whether an accretion disk would be susceptible to gravitational instability. Care was taken to reproduce the parameters used in the Mayer et al (2004) simulations, particularly noting the importance of the values of Q and t_{cool}.

In the interests of keeping computation times down, initial simulations used only 10,000 SPH particles. The last simulations reported here, in which a disk was evolved using the pattern recognition scheme introduced in Chapter 6 and then compared with the same disk evolved using the Balsara switch, were undertaken with the improved resolution of 100,000 SPH particles.

8.2 Methodology

The SPH models of disks were constructed as described in chapter 4. Multiple Particle Time Stepping and Tree Gravity were used in all the simulations. Summary tables of the disk parameters are given in each section below. The range of values for temperature, Q etc are given in the order inner radius to outer radius. Thus Q values of 8.8 to 1.08 indicates that $Q = 8.8$ at the inner edge of the disk (or strictly, annulus) and 1.08 at the outer edge.

All simulations were given a code name which was then attached to all output files. For example, 'sfjn09.000500' indicates the output file for the 500th timestep in experiment labelled sfjn09.

8.3 - Initial experiments: Constant Q disk

8.3.1 Experimental parameters

The input disk pp10000 was used for initial experiments, to check that Dragon, and in particular Multiple Particle Timestepping and Tree Gravity, operated correctly in a large disk. Initial parameters for disk pp10000 were as follows:

Input disk name	pp10000
Disk Mass	$0.1M_\odot$
Surface density profile	$\Sigma(r) = \Sigma_0 r^{-7/4}$
Disk size	1 - 100 AU
Temperature profile	$T(r) = 375K(r/\text{AU})^{-1/2}$
Temperature range	375-37.5K
Toomre Q values	6.76
Number of particles	10000
Output file sfjn17	

The energy equation was solved (see Chapter 3 for details of the SPH calculation), and the disk allowed to cool (or warm) back to its initial temperature with a parameterised radiative cooling term equivalent to

$$\frac{dT}{dt} = \Omega(T(r) - T)). \tag{8.1}$$

Artificial Viscosity was implemented, and calculated for both approaching and receding neighbours to avoid unwanted radial forces (see Chapter 5), and the Balsara switch was used to control the implementation of Artificial Viscosity.
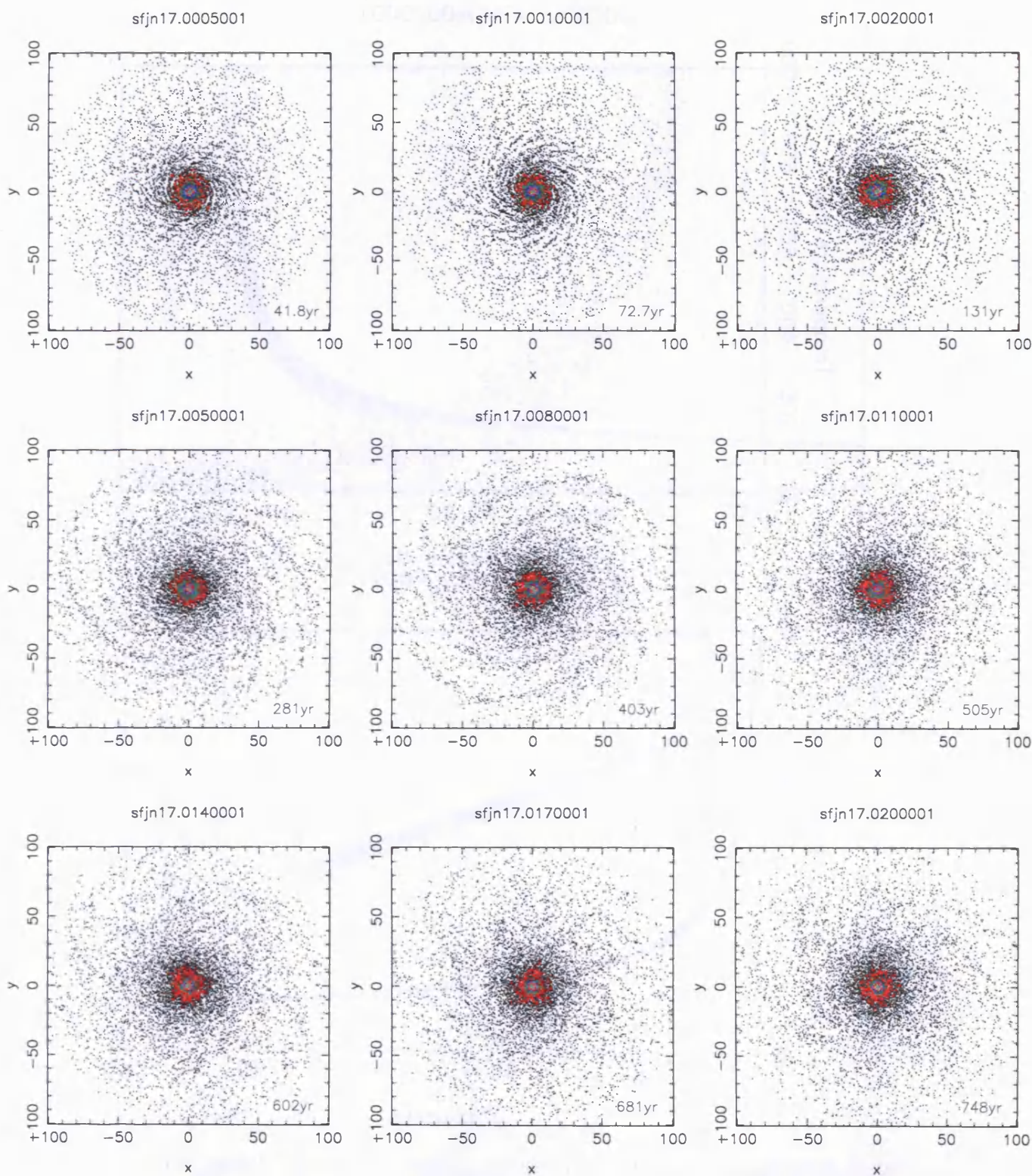
Figure 8.1: sfjn17. pp10000 evolved using parameterised heating and cooling, self gravity, pressure and viscosity forces. Trailing spiral arms form then dissipate. Points are colour coded by logarithmic density increments in the order black, red, green, blue, yellow, cyan, magenta etc. each increment indicating a factor ten increase.

sfjn17.0010001

sfjn17.0010001
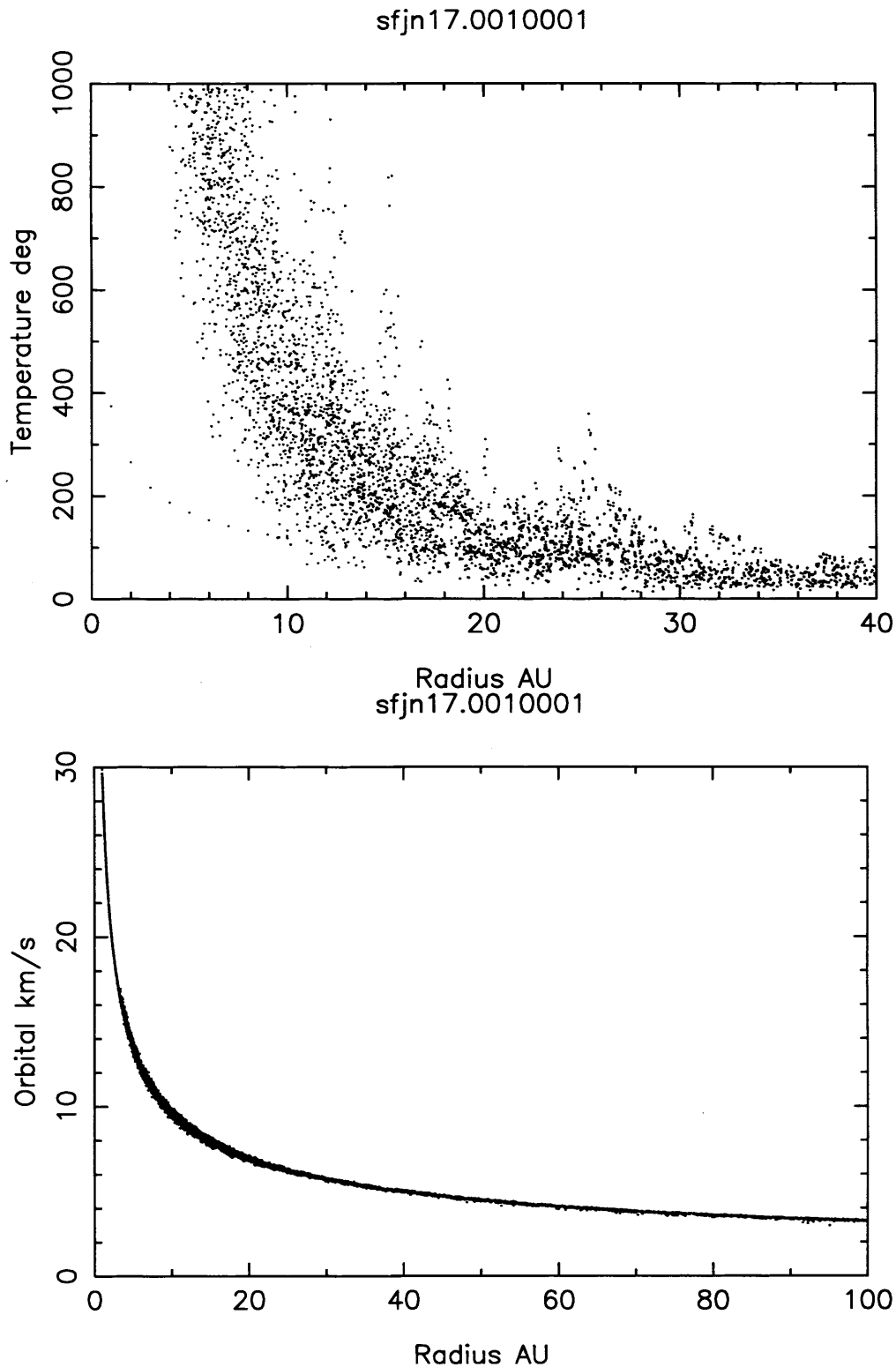
Figure 8.2: sfjn17. Evolution of constant Q disk at 73 years elapsed time. Top, Temperature (K) vs radius(AU). Inner regions are much hotter than the original temperature profile, indicated by the red dots, while outer regions are cooler. Bottom, orbital speed (km/s) vs radius (AU). The rotation curve is smooth, but a spread of values of orbital speed is developing for radii between 5 and 30AU, due to viscous evolution.

sfjn17.0200001

Radius AU
sfjn17.0200001
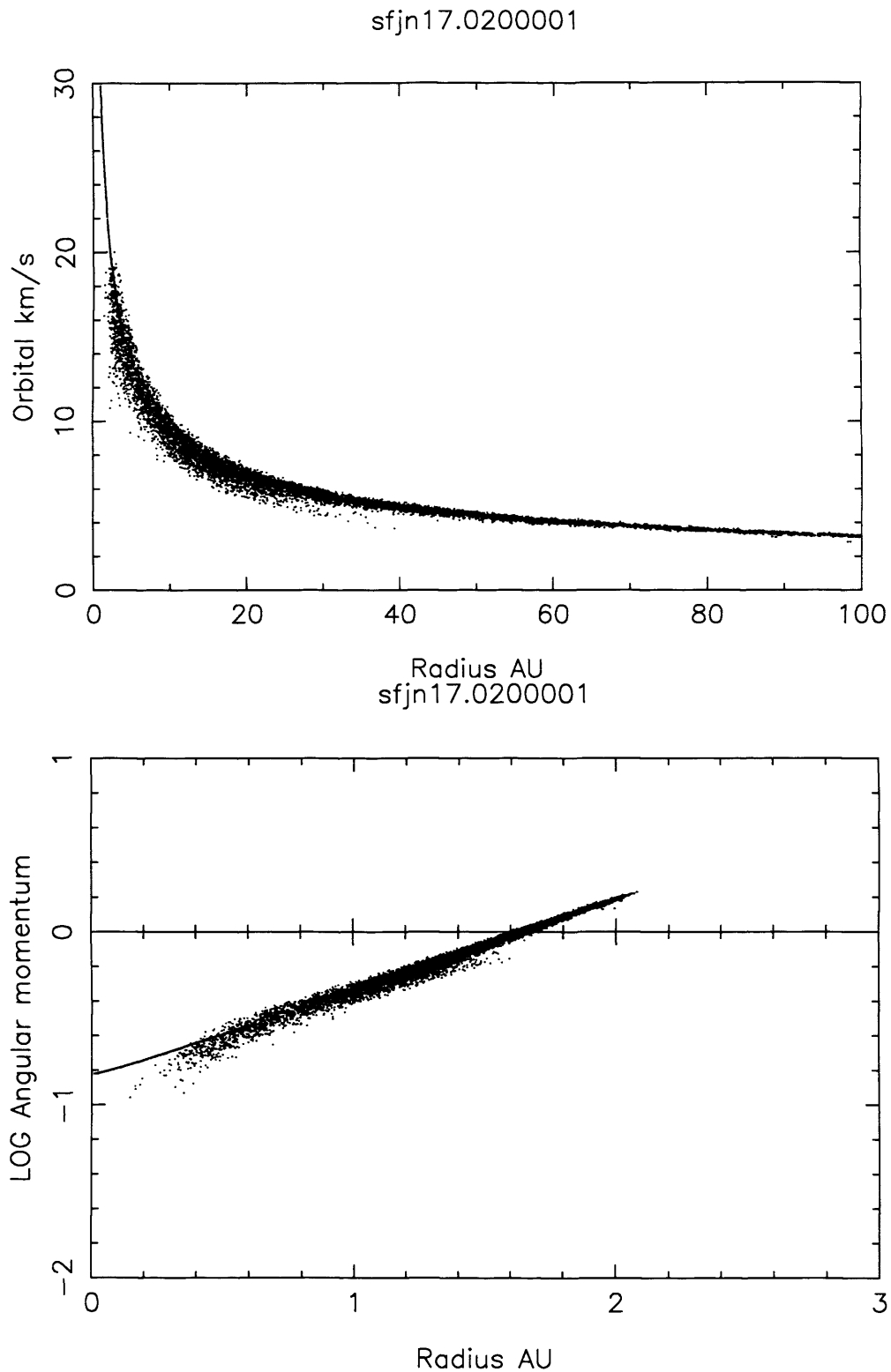
Radius AU

Figure 8.3: sfjn17. Evolution of constant Q disk at 748 years elapsed time. Top, Orbital speed (km/sec) vs radius(AU). There is now a larger spread of orbital speed at radii greater than 5AU. Bottom, log angular momentum vs log radius (AU). The original line with gradient 1/2 for Keplerian rotation is preserved at inner and outer radii. Viscous evolution has resulted in a spread of values between these radii.
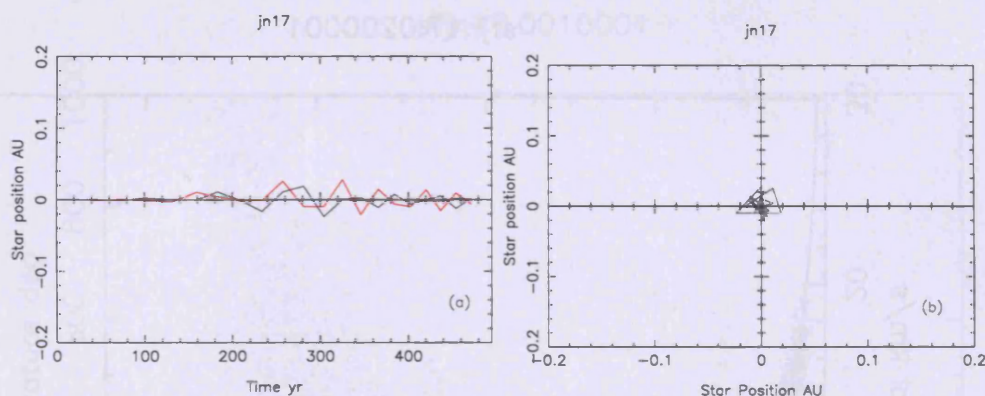
Figure 8.4: Movement of the central star in sfjn17. (a) distance of star from original location (AU) against time in years. Black, red and green signify x,y and z coordinates; (b) the track of the position of the star as it varies with time. x and y are orthogonal axes within the plane of the disk, z the height above the plane. All distances are in AU.

Results obtained using disk pp10000 are illustrated in Figures 8.1, 8.2, 8.3 and 8.4.

8.3.2   Discussion

The combination of mass distribution and temperature in the input disk, pp10000, assuming Keplerian orbital velocities, gave a constant value of the Toomre Q parameter, $Q = \kappa c_s/\pi G\Sigma$. Given that the epicyclic frequency κ is indistinguishable from Ω for Keplerian orbits, $\kappa \propto r^{-3/2}$. The sound speed $c_s \propto T(r)^{-1/2}$ which as $T(r) \propto r^{-1/2}$ gives $c_s \propto r^{-1/4}$. So the factors of r in κ and c_s cancel with the $r^{-7/4}$ in the surface density term, giving a value of $Q = 6.76$ at all radii.

With this high value of Q, gravitational instability was not expected to occur in the disk. The values for disk size, mass and temperature are all consistent with observations (see Chapter 2) so it is interesting to note that the Toomre Q calculated for a circumstellar disk, with physical parameters which are consistent with observations, implies that gravitational instability will not occur in such disks. In order to reduce Q to between 1.0 and 1.5, at which level gravitational instability would be predicted to occur (Mayer et al. 2004), the disk would need to be heavier or colder.

Figure 8.1 shows that in our simulation of the constant Q disk, trailing spiral arms and small mass concentrations formed, but did not persist. This is as predicted, given the high value of Q for the disk.

The temperature profile of the simulated disk at 72.7 years elapsed time is shown in Figure. 8.2. The inner regions of the disk are being heated faster than the disk is permitted to cool, even with cooling time set to $t_{cool} = \Omega^{-1}$, whereas the outer regions

are now cooler than the original temperature profile.

The rotation curve of the disk at 72.7 years is also shown in Figure 8.2. The orbital speed plotted against radius is smooth, but it can be seen that there is a range of orbital speed developing at radii between 5 and 30 AU. This is to be expected in a disk in which Artificial Viscosity is causing the disk to evolve. The absence of any spread in Orbital Speed at radii larger than 30AU is explained by the fact that at 70 years, matter outward of 30AU has not yet completed an orbit, and so there is little variation from the initial Keplerian velocities in the outer regions. There is also no evolution in the very central region. We showed in Chapter 6 that the value of the Balsara coefficient at small radii in a Keplerian disk is very low, (see Fig. 6.7), because of the very high vorticity in this region. This has the effect of keeping Artificial Viscosity switched off in the centre of the Accretion Disk. Artificial Viscosity will also be suppressed in the central region because h is smaller in high density regions. This could explain why the orbital speed in the central regions is failing to evolve.

Figure 8.3 shows the rotation curve after 748 years. The range of orbital speed has increased at radii between 5 and 80 AU. Again, the inner regions are failing to evolve because of the low values of the Balsara Switch at small radii, and the very outermost regions have still not completed an orbit. Also shown in Figure 8.3 is a log log plot of Angular Momentum versus radius. In a Keplerian disk, Angular Momentum is proportional to radius$^{1/2}$, so the gradient of this line should originally have been 1/2. Inner and outer portions of this line are indeed showing the original gradient of 1/2. In between it appears that a steeper slope is developing in the central region, a shallower slope in the outer regions.

As was explained in Chapter 3, Multiple Particle Time Stepping and Tree Gravity are used in the Dragon SPH implementation, in order to speed up simulations. Using these methods compromises the perfect symmetry of interaction between SPH particles. The precise gravitational attraction between pairs of particles is not calculated for every pair, for every timestep, so action and reaction are not precisely equal and opposite, and this leads to the possibility that Angular Momentum will not be precisely conserved.

The Angular Momentum of the disk and central star were calculated throughout the simulation and are tabulated in Table 8.1. It can be seen that angular momentum for the whole system is conserved to within 1.5% for the first 500 years, but that Angular Momentum is then reduced to 97% of its original value by the end of the simulation, at 748 years elapsed time. As no matter has accreted onto the central star, or escaped the system, this angular momentum loss must be due to systematic errors in the simulation.

The angular momentum of the star is very small compared with that of the disk, and

Table 8.1: Angular momentum for sfjn17. All angular momentum values are normalised by dividing by the initial angular momentum of the system. Column one gives the elapsed time of the simulation. Columns two and three give the normalised angular momenta of the disk and star respectively.

Elapsed time (yrs)	Disk Angular Momentum	Star Angular Momentum
41.8	1.000	$1.33.10^{-7}$
72.7	0.999	$1.35.10^{-7}$
131	0.999	$1.45.10^{-7}$
281	0.997	$1.62.10^{-5}$
403	0.991	$7.16.10^{-6}$
505	0.984	$2.27.10^{-5}$
602	0.978	$-2.03.10^{-7}$
681	0.974	$3.80.10^{-6}$
748	0.968	$6.99.10^{-6}$

in table 8.1 it can be seen that the magnitude of the star's angular momentum does not grow monotonically, but varies with time, even, at 602 years elapsed time, going briefly in the opposite direction to the disk. In fig. 8.4, the path of the central star is plotted against time and the maximum excursion of the star can be seen to be 0.02AU. As was shown in Chapter 4, as soon as a central object within an annulus moves away from the centre, it enters the region where the gravitational field of the annulus is directed away from the centre, and this gravitational attraction increases as the star moves towards the inner edge of the annulus. It is interesting, therefore, to see that the excursion of the star is limited in this simulation.

8.3.3 Conclusion

The Dragon SPH code operated satisfactorily for a large (radius 100AU) disk, with angular momentum conserved to within 97%. No condensations formed, as expected in a high Q disk. Artificial Viscosity was observed to cause the transfer of angular momentum at intermediate radii, but viscous effects were not observed in the central region of the disk. The central star was observed to wander erratically about its original location.

8.4 Investigating the effects of Artificial Viscosity.

8.4.1 Experimental Parameters

The initial conditions for the following simulations were:

Disk name	Mayerdisk
Disk Mass	$0.1 M_\odot$
Disk radius	4-20AU
Surface Density profile	$\Sigma_0 \exp\left(-\left(\frac{r_{in}}{r}\right)^2\right) r^{-1} \exp\left(-\left(\frac{r}{r_{out}}\right)^2\right)$
Temperature profile	$T_0 \exp\left(-r/r_{in}\right)^{3/2} + C$
Temperature range	750-56K
Toomre Q values	8.8-1.08
Number of particles	10000
Output filenames	
sfoc11	Balsara switch, locally isothermal eqn of state
sfoc01	Balsara switch, adiabatic heating plus parameterised cooling
sfjb24	As sfoc01 plus Time Dependent Viscosity
sfja24	As sfjb24, but without Balsara switch

This disk was set up to replicate the conditions used in Mayer et al. (2004). T_0 and C were varied to impose a maximum temperature T_0 at the inner radius and a minimum outer temperature C, typical values being $750K$ and $56K$. However, we had difficulty reconciling the explanations in the text of Mayer et al. (2004) with their figures. For example, the temperature profile shown in the figures was not the same as that described in the text, and also was not at all similar to $T^{-1/2}$, as stated. The derived values of Q and of the swing parameter X_m, where $X_m = \Omega^2 R/2m\pi G\Sigma$, m being the order of the unstable mode and R the disk radius, were both found to differ from those plotted in the paper. Q did approach a value of 1.0, indicating that gravitational instability is a possibility, in outer regions of the disk. However, this was only achieved by modelling a small portion of a disk (only the annulus between 4 and 20AU) but giving it a mass of $0.1M_\odot$. A disk of this surface density extending to 100AU would have a mass of $0.6M_\odot$. This increases the value of Σ, which brings the value of Q down to single figures.

Discussions with the author did not clarify the discrepancies between the text and the figures in Mayer et al. (2004). We were also surprised to discover that during the locally isothermal phase of the modelling, particle temperatures were left at their initial values, wherever the particles moved within the disk, so particles with different temperatures mixed together.

Nevertheless, a simulation of the evolution of the disk was attempted, first using a locally isothermal equation of state and then using an adiabatic equation of state with parameterised cooling, the cooling time of the order of one orbital period. The results of these simulations are illustrated in Figures 8.5 and 8.6. Artificial Viscosity, moderated by the Balsara Switch, was used in these simulations, with viscosity applied for both approaching and receding particles.

This simulation was repeated using the Time Dependent Viscosity technique, described in Chapter 6, both in addition to the Balsara Switch and on its own. The results for Time Dependent Viscosity plus Balsara Switchare are shown in Fig. 8.8, and the results for Time Dependent Viscosity on its own are shown in Fig. 8.9 .

8.4.2 Discussion

Figures 8.5 and 8.6 show that more defined spiral arms and potential condensations of particles occur with a locally isothermal equation of state than with parameterised cooling. The results in Fig. 8.5, the locally isothermal run, are strikingly similar in appearance to those in Mayer et al. (2004). However, we found that the promising condensations, for example after 142 and 155 years, did not persist, probably because of lack of resolution. The use of an adiabatic equation of state, and parameterised cooling, as illustrated in Fig. 8.6, resulted in less structure.

In Mayer et al. (2004), Artificial Viscosity is used with $\alpha = 1.0$ and $\beta = 2.0$, and the Balsara switch is used to suppress Artificial Viscosity in regions of high $\nabla \times \mathbf{v}$ and low $\nabla \cdot \mathbf{v}$ (ie shear flows). Exactly the same parameters were used in the simulations reported here. However, given the much higher resolution of the Mayer simulations (250,000 particles used as opposed to our 10,000), the average value of h would be about three times larger in our simulations than the Mayer simulations. One would therefore expect a much higher effective shear viscosity in our Dragon simulation than the Mayer simulation. It is interesting that despite this, our locally isothermal results are so similar in overall appearance to the Mayer results.

The trial using the Balsara Switch, shown in Fig. 8.6 when compared with that using Time Dependent Artificial Viscosity, shown in Fig. 8.9, shows a different pattern of structure formation. Far less material falls into the central star when Time Dependent Viscosity is used. In these simulations, the inclusion of Time Dependent Viscosity seems to cause the disk to evolve towards a ring.

In chapter 6 we showed that the Balsara switch had low values in the central region of an accretion disk, where pattern matching found converging flow (Fig. 6.7). This was due to the very high values of $\nabla \times \mathbf{v} |_{SPH}$ in the central regions. The Balsara switch
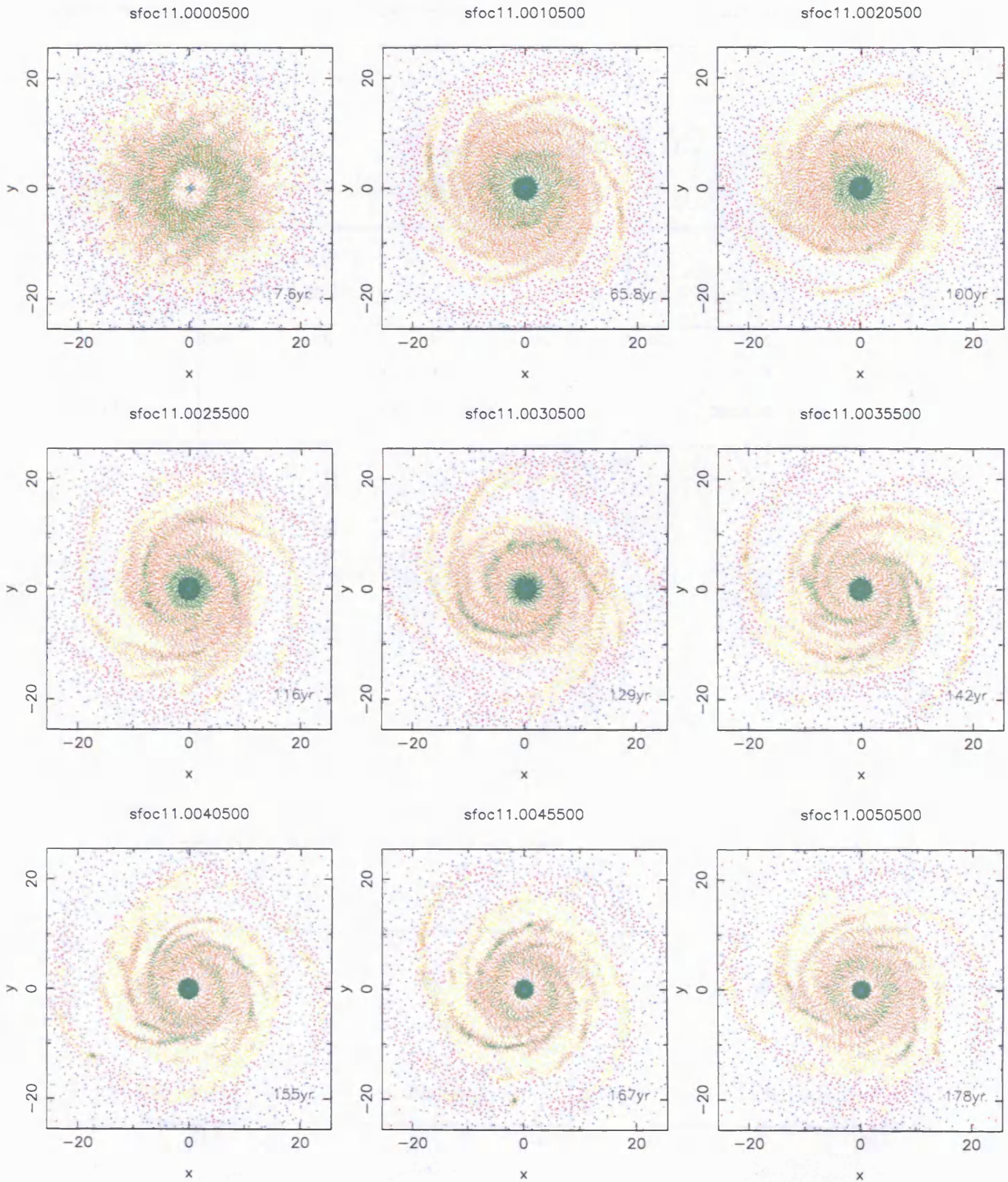
Figure 8.5: sfoc11. Trial using the Mayerdisk, with a locally isothermal equation of state, Artificial Viscosity and the Balsara Switch. Trailing arms and condensations form but do not persist.
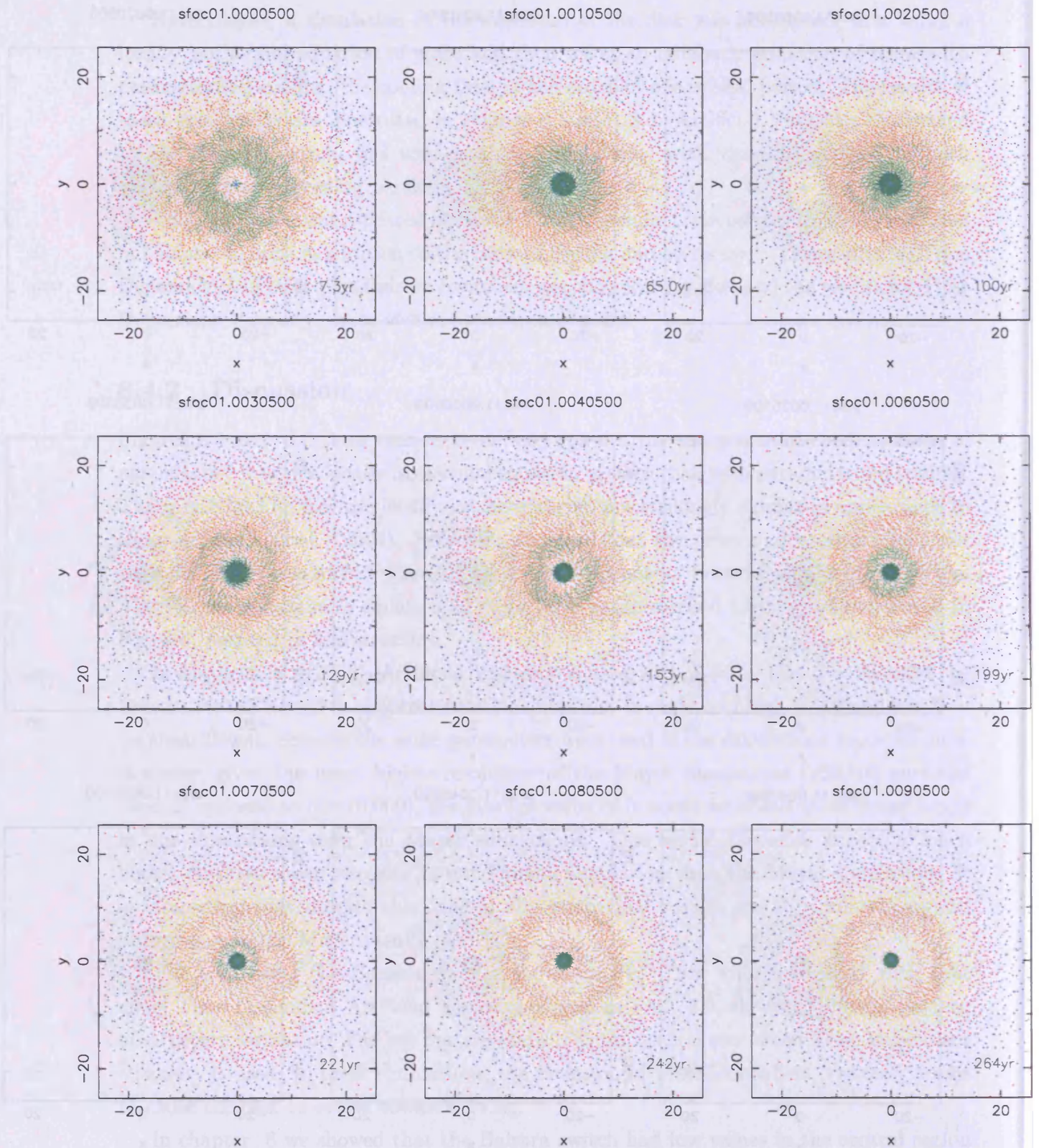
Figure 8.6: sfoc01. Evolution of the Mayer disk using an adiabatic equation of state, Artificial Viscosity and the Balsara Switch. Structure forms but does not persist.
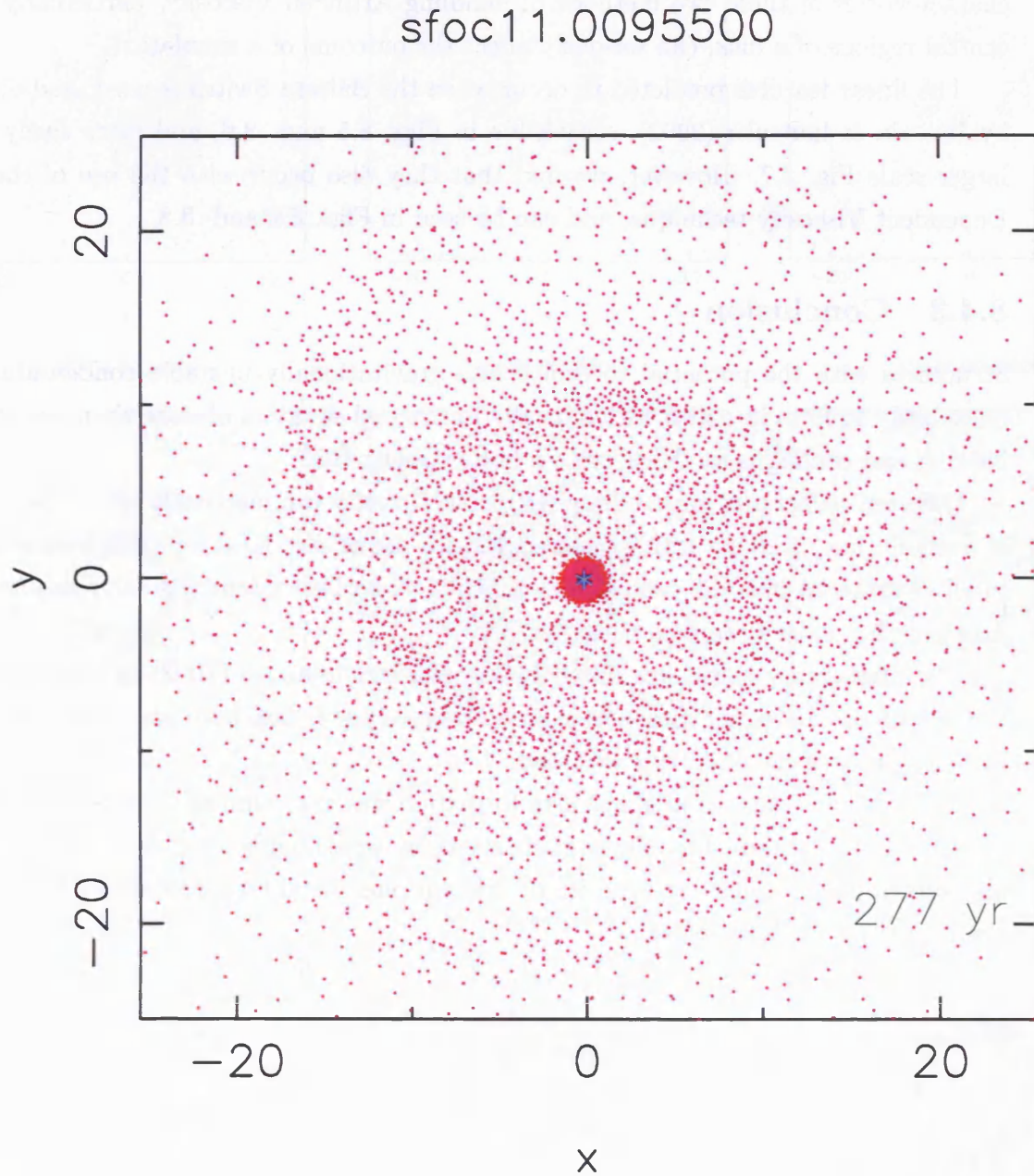
Figure 8.7: sfoc11. Note the linear features associated with the use of the Balsara Switch, in mid- radius regions.

would therefore keep Artificial Viscosity low in this region. Time Dependent Viscosity, by contrast, was found to apply persistently high values of Artificial Viscosity in central areas of a disk (Fig. 6.5). These simulations seem to confirm that the very different characteristics of these two methods of handling Artificial Viscosity, particularly in the central regions of a disk, can seriously affect the outcome of a simulation.

The linear features predicted to occur when the Balsara Switch is used, and observed by Imaeda & Inutsuka (2002), are visible in Figs. 8.5 and 8.6, and more easily in the larger scale Fig. 8.7. However, we find that they also occur with the use of the Time Dependent Viscosity technique, and can be seen in Figs. 8.9 and 8.8.

8.4.3 Conclusion

Structures with the potential to evolve into gravitationally unstable condensations are more likely to form in a disk with a locally isothermal equation of state than one in which heating and cooling is modelled with a finite cooling time.

Different techniques for handling Artificial Viscosity can materially affect the outcome of a simulation. Starting with the same disk, the use of the Balsara Switch results in more infall of material into the central region, while Time Dependent Viscosity results in the disk evolving more towards a ring.

The filamentary structures noted by Imaeda and Inutsuka (2002) as associated with the use of the Balsara Switch, were also observed here, but were also seen when Time Dependent Artificial Viscosity was used.

Although the pattern of spiral arm formation was very similar in our isothermal run (sfoc11) to that obtained by Mayer et al.(2004), we were unable to reproduce their findings and successfully simulate the growth of gravitational instability, probably because of the low resolution of this simulation.
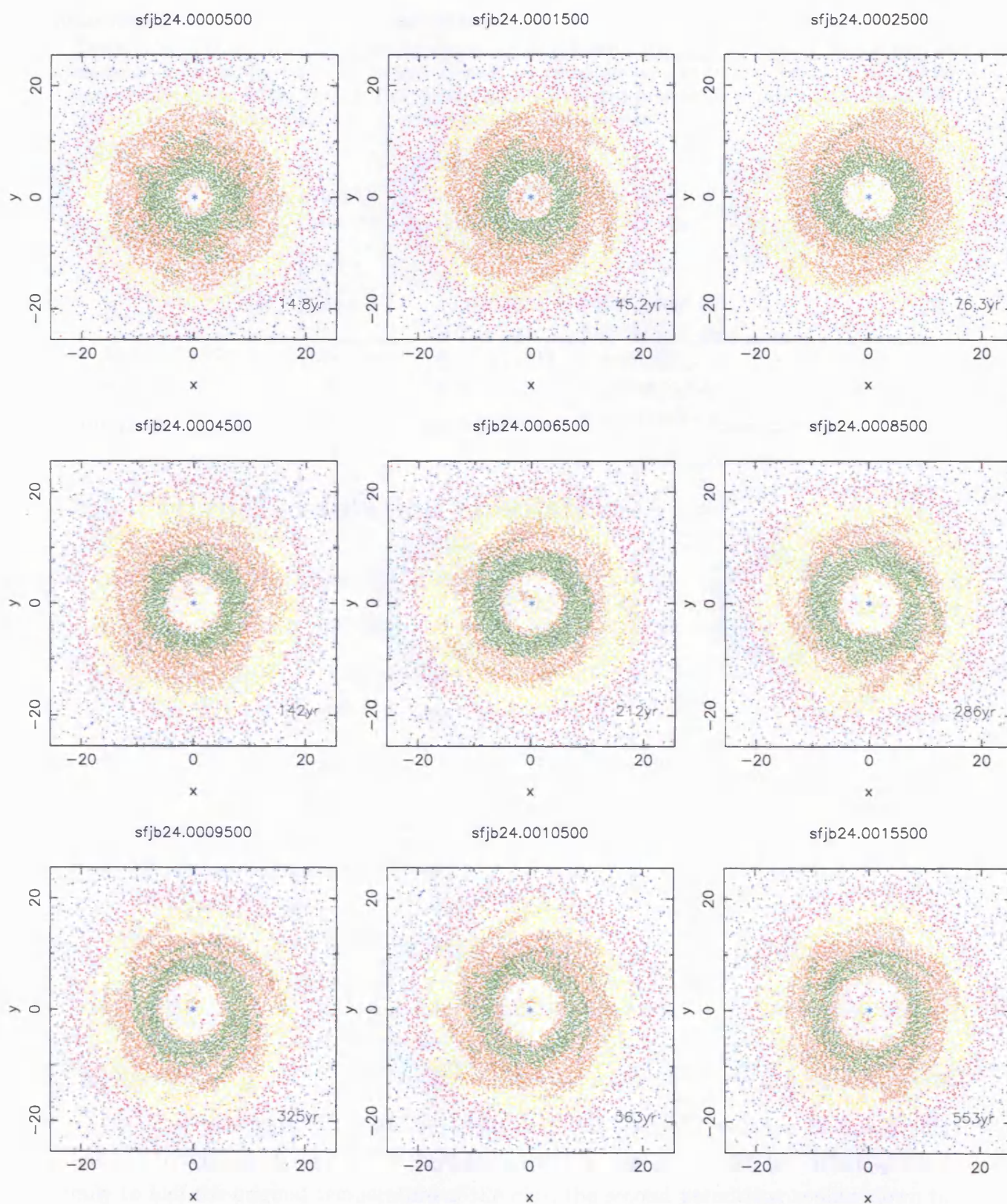
Figure 8.8: sfjb24. Mayerdisk evolved with adiabatic equation of state, both Balsara Switch and Time Dependent Viscosity implemented to control Artificial Viscosity.
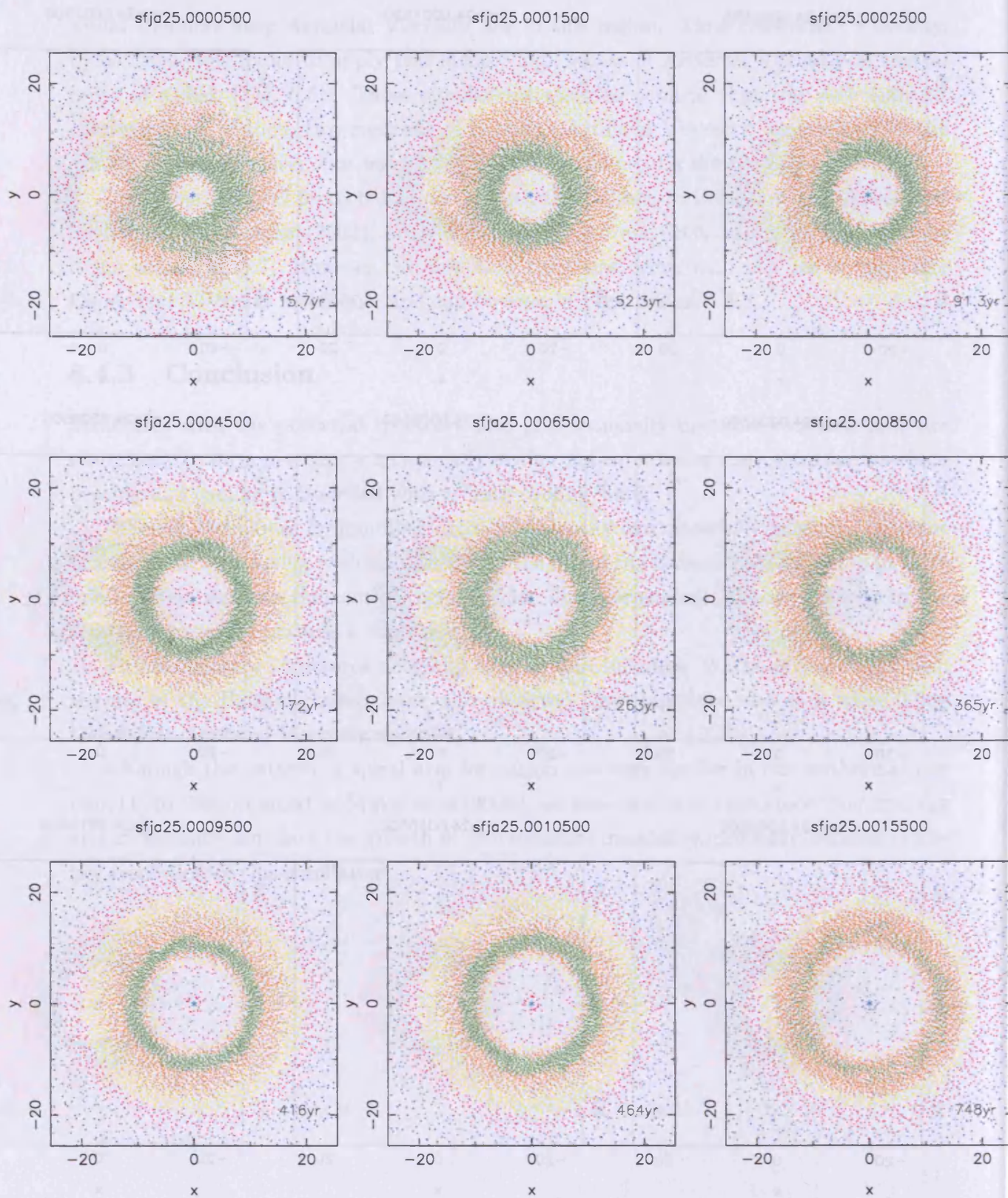
Figure 8.9: sfja25. Mayerdisk evolved using adiabatic equation of state, Artificial Viscosity controlled by Time Dependent Viscosity only.

Table 8.2: Angular momentum for simulation of 100,000 particle disk, with Balsara Switch used to moderate Artificial Viscosity. All angular momentum values are normalised by dividing by the initial angular momentum of the system. Column one gives the elapsed time of the simulation. Columns two and three give the normalised angular momenta of the disk and star.

Elapsed time (yrs)	Disk Angular Momentum	Star Angular Momentum
75	1.0000000	2.2931005E-07
122	0.9999441	7.2671689E-08
151	1.0001141	1.2885495E-08
180	1.0003743	-6.2734875E-09
209	1.0005251	8.8713122E-08

8.5 Higher resolution simulations

8.5.1 Experimental Parameters

A disk was set up with 100,000 particles and the following characteristics.

Disk name	hdisk
Disk Mass	$0.1 M_\odot$
Disk radius	1-50AU
Surface Density profile	$\Sigma_0 \exp\left(-\left(\frac{r_{in}}{r}\right)^2\right) r^{-1} \exp\left(-\left(\frac{r}{r_{out}}\right)^2\right)$
Temperature profile	$T_0 \exp\left(-r/r_{in}\right)^{3/2} + C$
Temperature range	750-56K
Toomre Q values	18.0-8.0
Number of particles	100000
Output filenames	
sfj28a	Balsara switch, adiabatic heating and cooling to 28K
sfj1	Balsara switch, adiabatic heating and cooling to 3K
sfa1	Pattern recognition, adiabatic heating and cooling to 28K

The first two simulations used standard Artificial Viscosity with the Balsara switch and the results are shown in Figs. 8.10 and 8.11, the first simulation permitting cooling only to half the original temperature of the disk, the second permitting cooling down to 3K. Conservation of Angular Momentum was checked for this higher resolution simulation, and the results are tabulated in Table 8.2.

A third simulation, sfa1, was run using the pattern recognition technique for switching on Artificial Viscosity only when convergence was detected, and permitting cooling down to half the original temperature. The results are shown in Figs. 8.13 and 8.14.

8.5.2 Discussion

In Figure 8.10, the disk developed no structure when adiabatic heating and parameterised cooling were implemented, with a cooling time of Ω^{-1}, and temperatures prevented from cooling below half the initial radial temperature profile. The rotation curve for this simulation is included to show that a smooth rotation velocity profile was maintained. By contrast, Fig. 8.11 started with the same heating and cooling regime, but after 160 years the disk was cooled below the original temperature, to 3K. The resulting collapse of the disk in the z direction caused ring structures to evolve in the central region, while in the outer regions, radii greater than 30AU, trailing spiral features are seen. The rings are more clearly shown in Fig. 8.12. It is interesting to speculate that this regional differentiation may be due to the change in direction of viscous acceleration with temperature, as predicted in Chapter 5, causing rings to become narrower, rather than spread. We showed that this would occur if μ_{ij} exceeded half the sound speed. Fig. 8.12 shows that, in this very cold disk, μ_{ij} is only less than the sound speed in the highest density rings.

Angular momentum was calculated to check that it was also conserved for the higher resolution simulations. The results for simulation sfj28 are tabulated in Table 8.2 and show that angular momentum was conserved to better than 99%. Similar results were found for all the simulations in this section. Note that again the path of the central star can actually move in the opposite rotational sense to the disk, giving it a negative angular momentum.

A third simulation, sfa1, was run using the pattern recognition technique for switching on Artificial Viscosity only when convergence was detected. The results are shown in Figs. 8.13 and 8.14. Ring structures developed in the inner regions of the disk after 116 years. For example, there is a green (higher density) ring clearly visible at a radius of 10AU, with lower density orange rings on either side of it. Figure 8.14 shows the temperature and orbital velocity profile at this stage of evolution. This disk has been allowed to cool to half the original temperature profile. It can be seen that there is a temperature bulge at about 10AU, indicating convergence and adiabatic heating. The rotation curve in Fig. 8.14 can be seen to vary from the smooth Keplerian profile in Fig. 8.10, and apparently two straight line segments are developing in the inner regions of the disk. Note that there are apparently radii where a range of orbital velocities coexist, for example between 5 and 7 AU. It appears that in these regions, the velocity is varying with height above
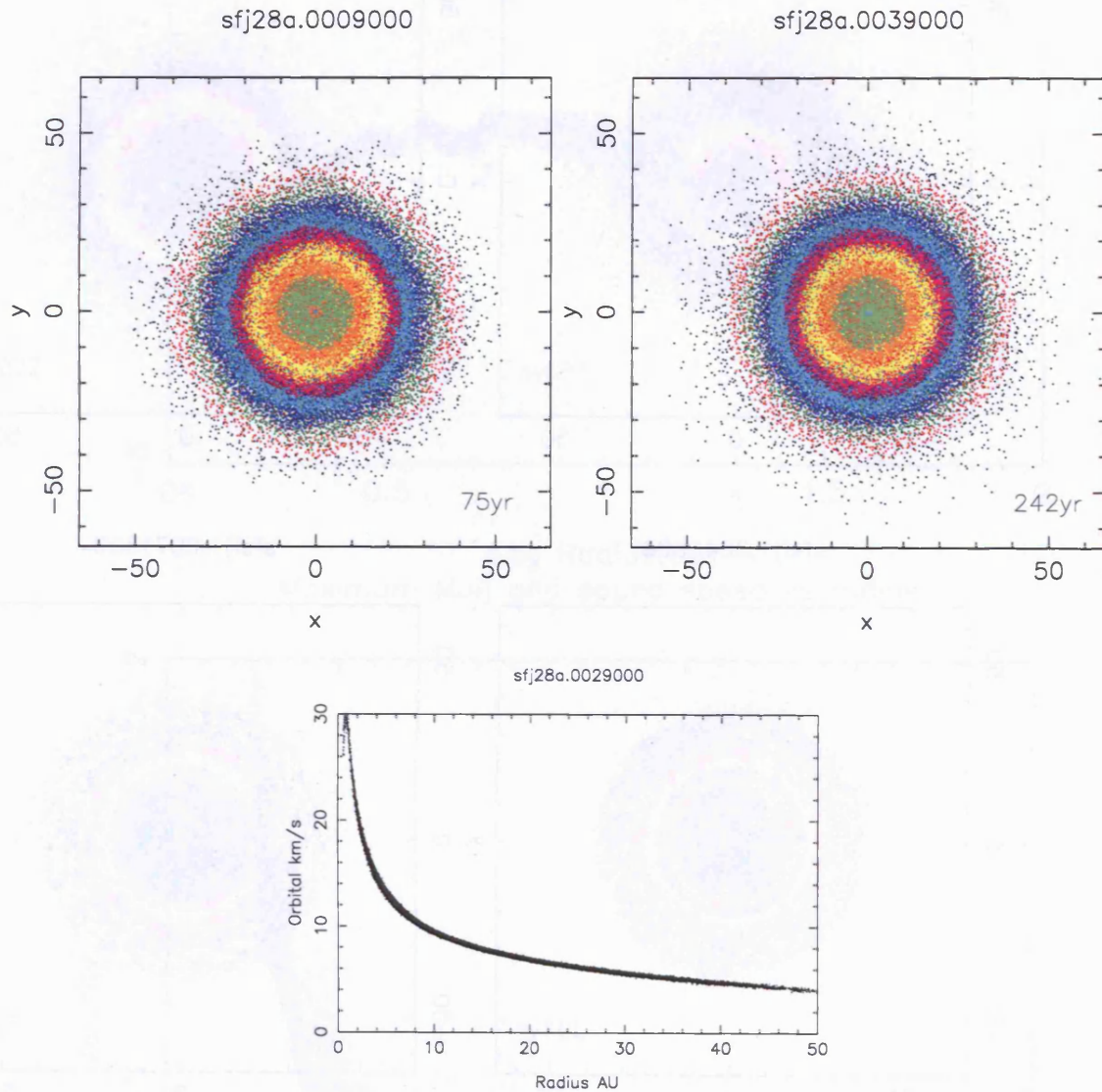
Figure 8.10: sfj28a. Trial using the 100,000 particle disk, with an adiabatic equation of state and parameterised cooling. Artificial Viscosity was moderated by the Balsara Switch. Top, the disk maintained equilibrium for 242 years. Bottom, the rotation curve is smooth.
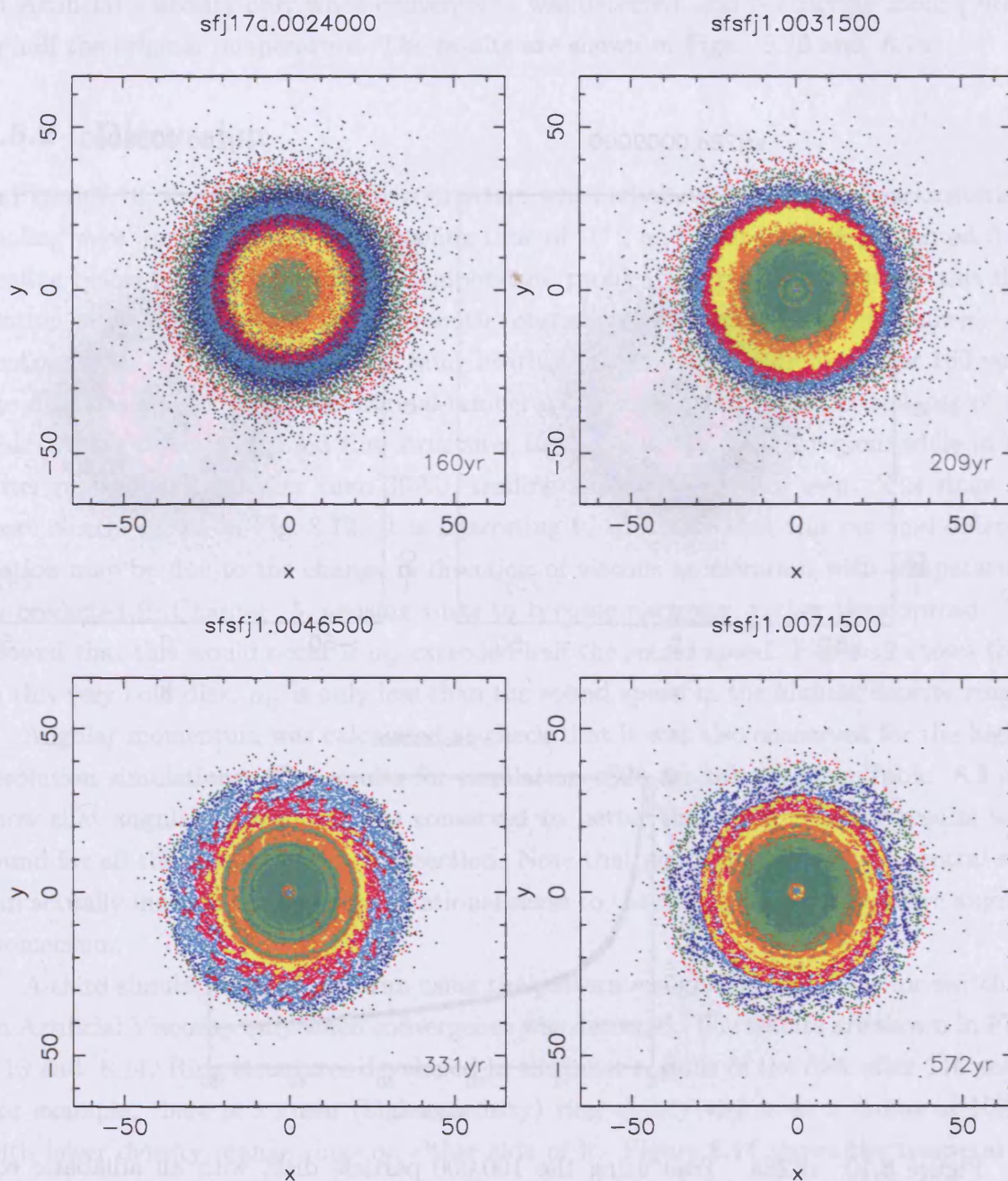
Figure 8.11: sfj1. Trial using the 100,000 particle disk. Up to 160 yrs, adiabatic heating and parameterised cooling were permitted down to half the original temperature profile. After 160 years, cooling was permitted to 3K. Note that the very cool disk developed two different patterns. Inner regions developed concentric rings, while outer regions formed trailing, spiral features.

LOG LOG Density vs radius

Maximum Muij and sound speed vs radius
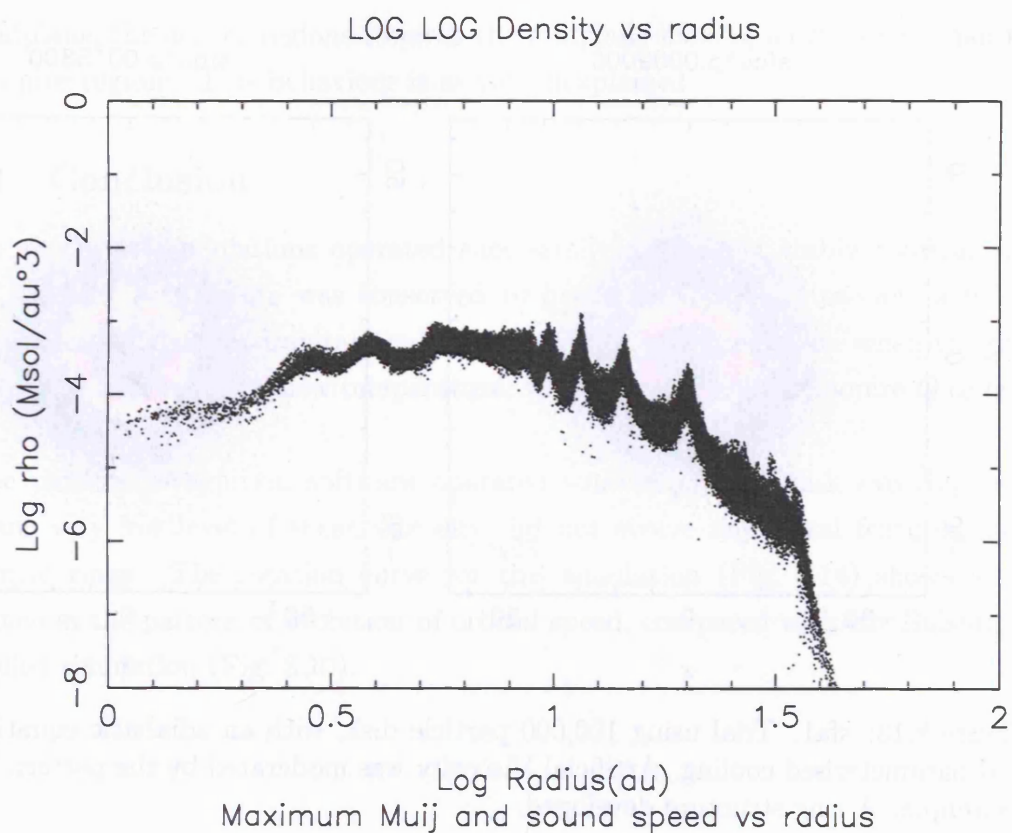
Figure 8.12: sfj1. Top, log log plot of density versus radius, which shows the ring structure more clearly. Bottom, sound speed (red) and maximum μ_{ij} (green) for all points, plotted against radius. In the high density rings, h falls so that μ_{ij} is comparable with the very low sound speed in this cold disk.

sfau1p.0009000   sfau1p.0015800
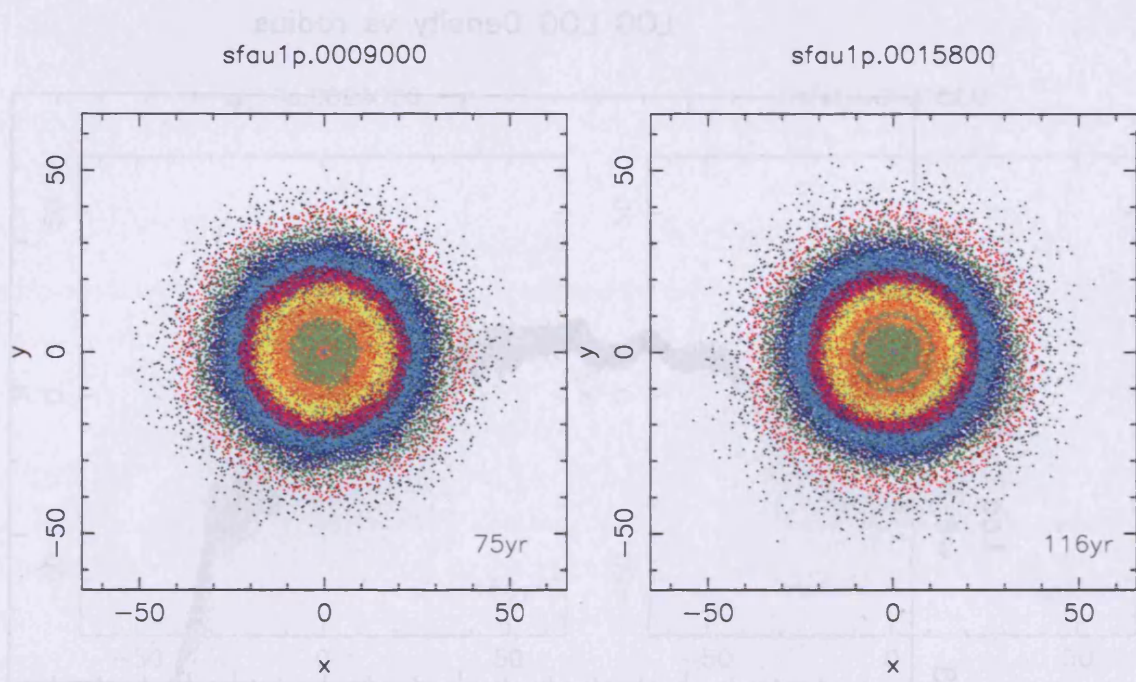
Figure 8.13: sfa1. Trial using 100,000 particle disk, with an adiabatic equation of state and parameterised cooling. Artificial Viscosity was moderated by the pattern recognition technique. A ring structure developed.

sfau1p.0015800   sfau1p.0015800
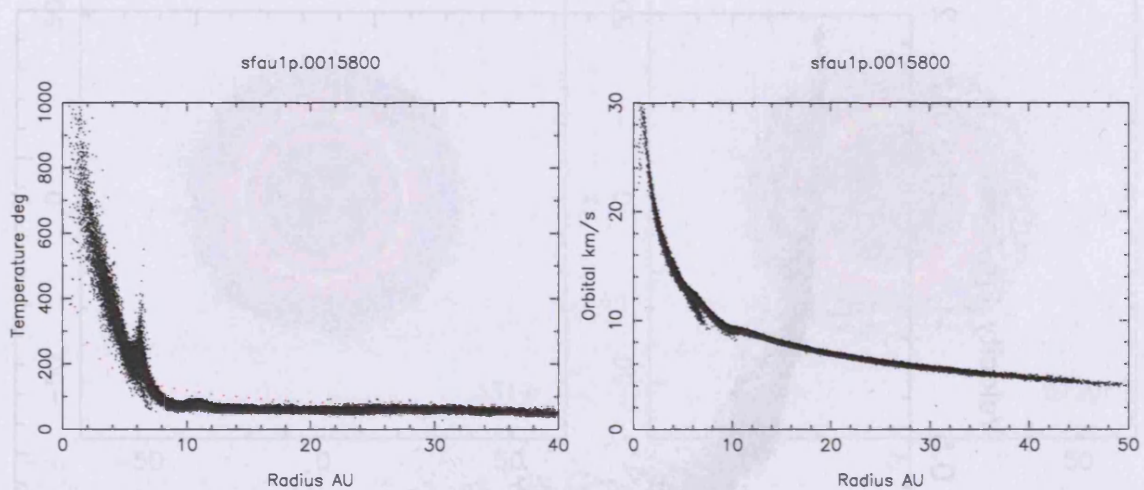
Figure 8.14: sfa1. Trial using 100,000 particle disk, with an adiabatic equation of state and parameterised cooling. Pattern recognition was used to switch on Artificial Viscosity. The disk is allowed to cool to half its original temperature. Left, temperature vs radius at 116 yrs. Note the temperature bulge, coinciding with a region of convergence where a ring structure is developing. This disk is not as hot as that in Figure 8.1. Right orbital speed vs radius at 116 yrs. This rotation curve is not smooth, but has developed straight line segments.

the midplane, the denser regions towards the midplane moving more slowly than the less dense outer regions. This behaviour is as yet unexplained.

8.5.3 Conclusion

Higher resolution simulations operated successfully, producing stably rotating disks in which Angular Momentum was conserved to better than 99%. However, a null result was recorded, in that no gravitational instability was produced, even when the disk was permitted to cool to a very low temperature, which should yield a Toomre Q of less than 1.5.

The pattern recognition software operated successfully. A disk evolving with the resultant very low level of shear viscosity did not evolve any spiral features, but only concentric rings. The rotation curve for this simulation (Fig. 8.14) shows a distinct difference in the pattern of evolution of orbital speed, compared with the Balsara Switch controlled simulation (Fig. 8.10).

8.6 Conclusions

The dragon SPH code was shown to operate accurately in the simulation of disks, conserving angular momentum, and maintaining equilibrium rotation for long periods when used with up to 100,000 particles.

Efforts to reproduce the results of Mayer et al.(2004) were only partially successful. Similar structures were formed, but none of the potential condensations actually collapsed.

The use of the Balsara switch was demonstrated to result in the formation of the linear features reported by Imaeda and Inutsuka (2003), but such structures also evolved when the Time Dependent Artificial Viscosity technique was used.

The use of different techniques to handle Artificial Viscosity resulted in strikingly different results, probably because of the very different behaviour of Time Dependent Viscosity and the Balsara switch in the central regions of an accretion disk, which we reported in chapter 6.

In higher resolution simulations using 100,000 particles, allowing the temperature to fall below its original value caused rings to form in the central region, while allowing the temperature to fall to 3K caused rings to form in the central region and spiral, trailing structures in the outer regions. The pattern recognition software was found to operate satisfactorily, but its effect on the orbital velocity profile will need to be investigated further.

Chapter 9

Conclusions and future work

9.1 The use of SPH for simulation of Keplerian accretion disks

The objective of this thesis was to investigate the computer simulation of the formation of planets from protoplanetary disks. In particular, the variable results reported by other workers (eg Bate et al, 2003; Rice et al 2004; Boss 2001; Gammie 2001; Mayer et al 2004), indicated that there may be problems with the simulation methods, or our understanding of the physics involved.

Investigation of the Smoothed Particle Hydrodynamics method revealed profound problems with the standard techniques for implementing Artificial Viscosity, when these were applied to accretion disks with a Keplerian velocity profile. Analytical and experimental results revealed that the resultant force for a Keplerian disk is in the opposite direction to that experienced in a linear shear situation. Applying Artificial Viscosity only to approaching particles results in a radial force which is four times larger than the force in the direction of the orbit. It is also possible for the force to change direction if temperature, and therefore sound speed, changes. Ensuring that the disk is adequately resolved, by using sufficient SPH particles, and using all particles for the calculation of viscosity, rather than only the approaching neighbours, addresses both of these problems and results in the Artificial Viscosity behaving more like real viscosity.

Familiar techniques for dealing with this problem, and activating Artificial Viscosity only when convergence is detected, were found to fail in the particular situation of a differentially rotating disk. The fundamental problem with both the Balsara Switch and Time Dependent Viscosity is that the SPH estimate of $\nabla \cdot v \mid_{\text{SPH}}$ has a low-freqency time-varying component which is independent of h, and so cannot be reduced by increasing

the number of SPH particles. An alternative method, based on pattern recognition, was found to be resistant to this problem.

Difficulties were also identified with the simulation of the gravitational field of disks. High resolution simulation of a protoplanetary disk requires enormous processing and data storage capacity, and a common approach is to simulate only a small annular portion of the disk. We demonstrate that this may yield unrepresentative results. This is because the edge effects of the annulus can cause preferential accretion zones, where the Toomre Q parameter is not the same as it would be for the same region of an extended disk.

Closer examination of some apparently successful simulations also revealed that very dense disks had been used, which had been allowed to cool to unphysically cold temperatures (Rice et al 2003a,2003b,2004).

We therefore recommend that SPH simulations of disks be undertaken with close attention to :

Resolution: ensuring that sufficient particles are used to resolve the disk;

Artificial viscosity: using all neighbours in the calculation of viscous forces and implementing a more discriminating method for deactivating viscosity during normal non-convergent shear flow;

Edge effects: anomalous rotation curves can result if annuli are used to represent sections of larger disks;

Initial conditions: disks should not be excessively massive;

Excessive cooling: the actual temperature of particles should be tracked and prevented from falling below a sensible minimum.

9.2   SPH simulations of Protoplanetary disks

SPH was found to operate successfully in the simulation of disks, in particular Angular Momentum was found to be conserved to better than 98% and the time stepping and integrations routines successfully resolved particle orbits from 1 to 100AU.

Using several different disk formats, we found that condensations did not persist long enough to collapse. The high tidal shearing forces in a Keplerian accretion disk disrupted the condensations before they could accumulate enough mass to collapse. Including a more realistic treatment of the thermal physics made the situation worse, as did reducing the effective shear viscosity.

The most promising simulations were the earliest, low resolution simulations, in which effective shear viscosity was high. Nelson (2006) has recently reported that identical SPH simulations of disk evolution, changing only the resolution of the simulation, results in

less structure formation as resolution increases. Our findings are consistent with Nelson's results. Increasing resolution decreases h, decreasing effective shear viscosity, and decreasing viscosity prevents the formation of converging structures in Keplerian disks.

9.3 Future work

9.3.1 SPH simulations of disks

It is planned to publish material from this thesis, to cover,

1. Artificial Viscosity in Keplerian shear flow;

2. A pattern matching algorithm as an alternative to the Balsara Switch and Time Dependent Viscosity in Keplerian accretion disks. (It is hoped to adapt this method to be more universally applicable, so that it is automatically applied when disks are detected, whatever their orientation);

3. The modified inhibition zone method for creating disks of mutually spaced equal mass SPH particles with any density profile;

4. Simulations. It is planned to repeat all the simulations in chapter 8, using the new viscosity handling technique developed in chapter 6, but with a much higher number of particles – at least 250,000. This will probably be done using the UKAFF facility, or the new cluster at Cardiff.

9.3.2 Clustering Analysis

Two papers have already been published, Cartwright & Whitworth (2004) and Cartwright, Whitworth & Nutter (2006). Further work in this area is aready in progress at the Astrophysical Institute in Potsdam, where Professor Ralf Klessen, Dr S Schmeja and Dr S Kitsionas are planning to use the 'Q' parameter for large scale analysis of star forming regions. They have already confirmed the usefulness of the work (Schmeja and Klessen, 2006), and in consultation with AC are continuing the effort to apply the same technique to molecular clouds, work begun in Cartwright, Whitworth & Nutter (2006).

Cartwright and Cartwright (2006), in prep, will apply clustering analysis to features on the seabed, related to sea-level change.

I am also interested in relating the fractal dimension of clouds to the Initial Mass Function.

9.3.3 Relativistic Effects: timing

The difficulty in obtaining satisfactory results from simulations of protoplanetary disks with a more realistic viscosity treatment prompts a re-examination of the physical assumptions inherent in the model. In particular, the non-relativistic model assumes that all particles may be treated as stationary for the purposes of the gravity calculation. This is clearly not true. All receding particles will appear closer to an observer, and all approaching particles further away, because of the finite speed of gravity. This will cause the gravitational field of a rotating disk, unlike a stationary disk, to have a component in the direction of rotation.

The Retarded Potentials methods from Electrodynamics theory, (see eg Griffiths, 1983), enables this effect to be quantified. We have previously calculated the gravitational acceleration at a point i by summing the contributions of all other particles at their instantaneous positions, $\mathbf{r}_j$,

$$\mathbf{g}_i = -G \sum_{j} \left(\frac{m_j \mathbf{r}_{ij}}{|\mathbf{r}_{ij}|^3} \right), \tag{9.1}$$

Taking account of the velocities of the particles and the finite speed of gravity, for each particle, position $\mathbf{r}_{ij}$ relative to the test particle location, the time retardation δt is calculated:

$$\delta t = \frac{r_{ij}}{c} \tag{9.2}$$

which yields a retarded position $\mathbf{r}_j^*$ for each particle:

$$\mathbf{r}_j^* = \mathbf{r}_j - \mathbf{v}_j \delta t \tag{9.3}$$

The gravitational attraction of a single particle j is then given given by:

$$\mathbf{g}_j(\mathbf{r}_j^*, t) = -\frac{MG\mathbf{r}_j^*}{(\mathbf{r}_j^* \cdot u_j)^3} \left[\left(c^2 - v_j^2 \right) \mathbf{u_j} + \mathbf{r}_j^* \times (\mathbf{u}_j \times \mathbf{a}_j) \right], \tag{9.4}$$

where $\mathbf{v}_j$ and $\mathbf{a}_j$ are the velocity and acceleration of particle j at the retarded time, and the vector $\mathbf{u}_j$ is defined as $\mathbf{u}_j = c\hat{\mathbf{r}}_j^* - \mathbf{v}_j$.

The first term in Eqn 9.4 is the velocity field, and the second term the acceleration field. Both of these terms contain a non-radial component, and curiously, these act in opposite directions. Fig. 9.1 shows the magnitude of the non-radial components of the two terms as experienced by a test particle moving from the centre of a rotating ring of particles to a position outside the ring. All the elements in the ring of particles are travelling in a circle radius 1 distance unit at speed $v = 0.001c$. It can be seen that the
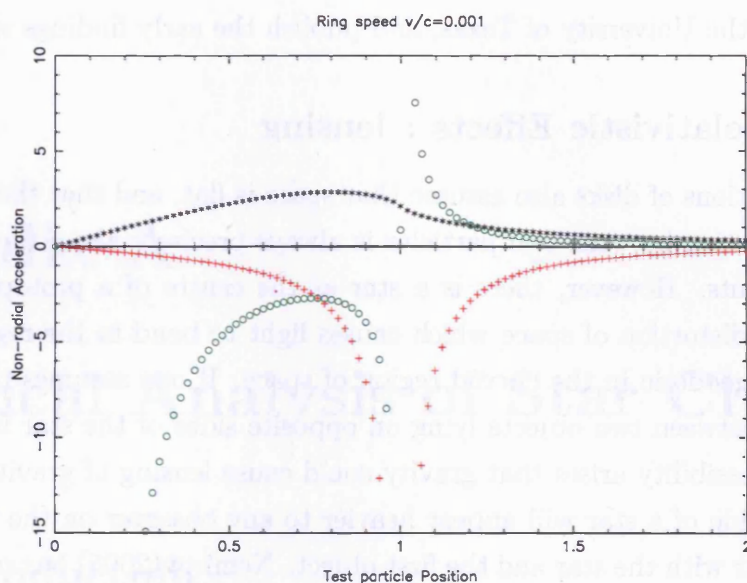
Figure 9.1: Non-radial gravitational acceleration due to a ring of orbiting particles, radius 1 distance unit, plotted against the distance of the test particle from the centre of the ring. * the acceleration field, + the velocity field $\times 10^{-1}$. For comparison, on the same scale, o radial field $\times 10^{-4}$. Note that the radial field changes direction either side of the ring of particles at radius = 1 . Normalised distance and acceleration units.

non-radial component of the velocity field (crosses) acts in the opposite direction to the rotation of the particles in the ring, while the non-radial component of the acceleration field (stars) is a smaller force, acting in the direction of rotation.

The magnitude of these non-radial accelerations varies with the speed of the orbiting particles, but is of the order of 0.1% of the radial force for velocities in the region of 0.001c.

In order for a disk to remain in equilibrium, therefore, it is not sufficient simply to calculate the radial component of gravity and set the orbital speed to achieve centrifugal balance. The total contributions of the off-radial forces, caused by gravitational propagation delay, must also be considered.

If interactions between particles are not instantaneous, Newton's third law is not obeyed, as action and reaction cannot be precisely equal and opposite. As a result the angular momentum of the physical matter in the disk will not be conserved. In order for conservation laws to hold, a post-Newtonian treatment of disks as outlined above will require the angular momentum of the gravitational field itself to be calculated and included in the total to be conserved. This may challenge some of the fundamental theories of viscous disk evolution laid down by Mestel (1963) and Lynden Bell and Pringle (1974).

It is planned to continue this approach to disk evolution in collaboration with Dr Joe

Romano of the University of Texas, and publish the early findings shortly.

9.3.4 Relativistic Effects : lensing

SPH simulations of disks also assume that space is flat, and that the direction of gravitational attraction between two particles is always precisely along the straight line joining the two points. However, there is a star at the centre of a protoplanetary disk, and a star causes distortion of space which causes light to bend in the region of the star, as it follows the geodesic in the curved region of space. If one assumes that the gravitational attraction between two objects lying on opposite sides of the star is also 'bent', like the light, the possibility arises that gravity could cause lensing of gravity. That is, an object on the far side of a star will appear heavier to any observer on the near side of the star, and collinear with the star and the first object. Nemirov(2005) has recently speculated on the possibility of measuring such an effect in the solar system, but points out the difficulty because such effects depend on transient alignments.

In a disk, by contrast, all matter is by definition collinear with the central star and the matter on the other side of the disk. Initial calculations indicate that the result could be, for both galaxies and protoplanetary disks, that the gravitational field of disks is proportional to $1/r$ as $r \to \infty$, rather than $1/r^2$. Lensing will also amplify the non-radial forces due to timing delays.

This work will also be prepared for publication shortly.

Appendix A

Statistical Analysis of Star Clusters

A.1 Introduction

Since most stars are formed in clusters, it would be useful to have quantitative and objective statistical measures of their structure, with a view to comparing clusters formed in different environments, and tracking changes in structure as clusters evolve. This is particularly important for young, embedded clusters, where the structure may yield important clues to the formation process but is changing rapidly. It is also important for comparing observed clusters with numerical simulations.

At present, we do not have sufficiently robust statistical measures for this purpose. Features which are easily identified by the human eye, such as sub-clusters, or linear features, can be strangely elusive to objective statistical analysis. For example, it is difficult to distinguish, statistically, between a degree of fractal or random sub-clustering, and the existence of a density gradient (Bate, Clarke & McCaughrean 1997). This paper explores some possible measures, and evaluates their usefulness. In particular, we find a robust objective measure which both quantifies, and distinguishes between, a smooth large-scale radial density gradient and multi-scale (fractal) sub-clustering.

In Section A.2 we describe our methodology. In Section A.3 we look again at the Mean Surface Density of Companions (MSDC), a tool pioneered by Larson (1995) and subsequently used by several others (e.g. Simon 1995; Bate, Clarke and McCaughrean 1997; Nakajima et al. 1998; Brandner & Köhler 1998; Gladwin et al. 1999; Klessen & Kroupa 2001). We focus on measures which reflect the clustering regime (wide separations) rather than the binary regime (close separations). In Section A.4 we explore the use of the Minimal Spanning Tree (Barrow, Bhavasar & Sonoda 1985) and its derivatives. In Section A.5 we combine the MSDC and the MST to derive a single measure Q which is able both to quantify, and to distinguish between, a smooth radial density gradient and

Table A.1: Sources of positions for cluster members and approximate ages and crossing times for clusters. (Crossing times were calculated using a typical velocity dispersion of 2 km/sec.)

Name	Members	Age Myr	T_{cross} Myr	Sources
IC2391	166	53	2.5	Barrado et al. (2001)
Cham.	136	0.1-40	2.7	Lawson et al. (1996)
				Ghez et al. (1997)
Taurus	215	1.0	10.0	Briceno et al. (1993)
				Ghez et al. (1993)
				Gomez et al. (1992)
				Hartmann et al. (1991)
				Herbig et al. (1988)
				Leinert et al. (1993)
				Simon et al. (1995)
				Walter et al. (1988)
				Luhman et al. (2003)
ρ Oph.	199	0.3 - 2.0	1.35	Bontemps et al. (2001)
IC348	288	2.0	2.0	Luhman et al. (2003)

multi-scale (fractal) sub-clustering.

All the measures are tested and calibrated on multiple realizations of artificial star clusters, and applied to ρ Ophiuchus, Chamaeleon, Taurus, IC348 and IC2391. Our results are discussed in Section A.6, and the main conclusions are summarized in Section A.7.

A.2   Methodology

Three different types of artificial star cluster have been created, using random numbers $\mathcal{R}$ to generate the individual star positions. The first type (2Dα) are circular clusters (i.e. two-dimensional disc-like clusters) with surface density $N \propto r^{-\alpha}$ and $\alpha = 0$ or 1. The second type (3Dα) are spherical clusters (i.e. three-dimensional clusters) having volume density $n \propto r^{-\alpha}$ with $\alpha = 0$, 1, 2, and 2.9. The third type (FD) are fractal star clusters (again three dimensional) with fractal dimension $D = 3.0$, 2.5, 2.0, or 1.5.

The different types are listed in Column 1 of Table A.2. All of the artificial clusters are created with 100 to 300 stars, as the numbers of stars within the five real clusters lie within that range. Table A.1 gives the sources of the positions of stars — or, in the case of ρ Ophiuchus, protostars — used in the analysis of Sections 3 and 4. These positions are plotted on Fig. A.1.
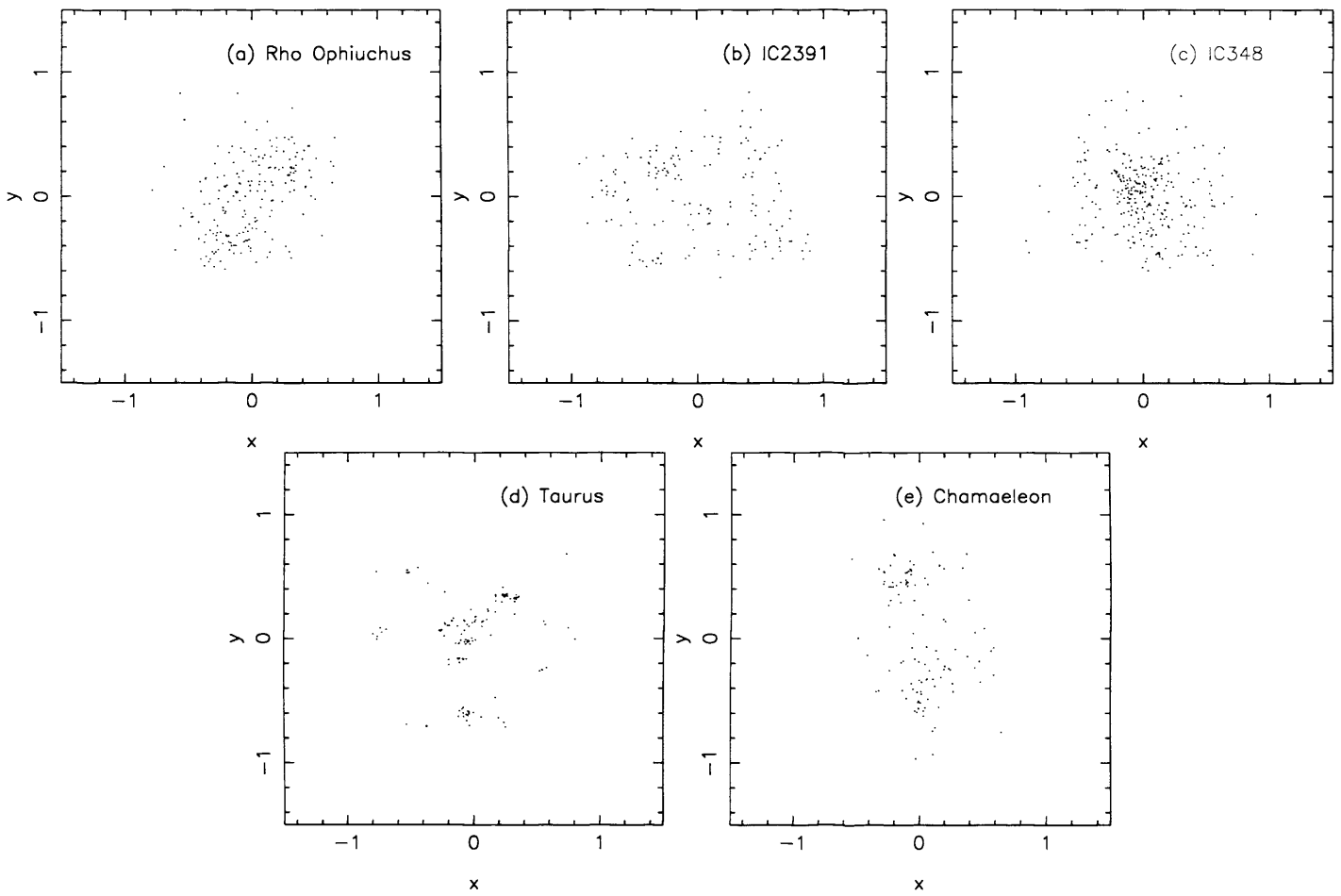
Figure A.1: Raw data for all real star clusters analysed in the paper. The clusters have been centred on the mean position of all stars and scaled so that the distance from the centre to the most distant star is unity.

Table A.2: Clustering measures obtained for artificial and real star clusters. Column 1 lists the cluster type (for artificial clusters) or name (for real clusters). Column 2 gives the Normalized Correlation Length $\bar{s}$ (i.e. the ratio of the mean separation to the cluster radius, see Section 3). Column 3 gives the Normalised Mean Edge Length $\bar{m}$ (see Section 4). Column 4 gives the mean value of the standard deviation of the edge length, $\bar{\sigma}_m$. Column 5 gives $Q = \bar{m}/\bar{s}$. For the artificial star clusters, means and standard deviations are computed from 100 realisations of each type, with $100 \leq \mathcal{N}_{total} \leq 300$.

Cluster type or name	$\bar{s}$	$\bar{m}$	$\bar{\sigma}_m$	Q
$2D0(N \propto r^0)$	$.88 \pm .03$	$.65 \pm 0.02$	$.31 \pm .02$	$.74 \pm .02$
$2D1(N \propto r^{-1})$	$.70 \pm .03$	$.61 \pm .02$	$.38 \pm .02$	$.85 \pm .03$
$3D2.9(n \propto r^{-2.9})$	$.16 \pm .02$	$.24 \pm .05$	$.59 \pm .07$	$1.50 \pm .13$
$3D2(n \propto r^{-2})$	$.60 \pm .03$	$.55 \pm .02$	$.41 \pm .03$	$.93 \pm .03$
$3D1(n \propto r^{-1})$	$.73 \pm .03$	$.61 \pm .02$	$.33 \pm .03$	$.84 \pm .02$
$3D0(n \propto r^0)$	$.80 \pm .02$	$.63 \pm .02$	$.31 \pm .02$	$.79 \pm .02$
$F3.0(D=3.0)$	$.81 \pm .03$	$.64 \pm .02$	$.30 \pm .02$	$.80 \pm .02$
$F2.5(D=2.5)$	$.74 \pm .09$	$.54 \pm .05$	$.28 \pm .03$	$.73 \pm .06$
$F2.0(D=2.0)$	$.67 \pm .13$	$.41 \pm .04$	$.28 \pm .02$	$.61 \pm .08$
$F1.5(D=1.5)$	$.62 \pm .18$	$.27 \pm .07$	$.35 \pm .07$	$.45 \pm .09$
IC2391	0.74	$.49$	$.30$	$.66$
Chamaeleon	0.63	$.42$	$.45$	$.67$
Taurus	0.55	$.26$	$.56$	$.47$
ρ Ophiuchus	0.53	$.45$	$.39$	$.85$
IC348	0.49	$.48$	$.46$	$.98$

A cluster of type 2Dα is created by positioning the stars according to

$$
\left.
\begin{aligned}
r &= \{(2-\alpha)\mathcal{R}_r/2\}^{1/(2-\alpha)}\,, \\
\phi &= 2\pi\mathcal{R}_\phi\,, \\
x &= r\cos(\phi)\,, \\
y &= r\sin(\phi)\,.
\end{aligned}
\right\}
\tag{A.1}
$$

where $\mathcal{R}_r$ and $\mathcal{R}_\phi$ are random numbers in the range 0-1.

A cluster of type 3Dα is created by positioning the stars according to

$$
\left.
\begin{aligned}
r &= \{(3-\alpha)\mathcal{R}_r/3\}^{1/(3-\alpha)}\,, \\
\theta &= \cos^{-1}(2\mathcal{R}_\theta - 1)\,, \\
\phi &= 2\pi\mathcal{R}_\phi\,, \\
x &= r\sin(\theta)\cos(\phi)\,, \\
y &= r\sin(\theta)\sin(\phi)\,, \\
z &= r\cos(\theta)\,.
\end{aligned}
\right\}
\tag{A.2}
$$

where $\mathcal{R}_r$, $\mathcal{R}_\theta$ and $\mathcal{R}_\phi$ are random numbers in the range 0-1. Clearly this method cannot be used for $\alpha = 3$, so to have a cluster type approximating to $\alpha = 3$ we use $\alpha = 2.9$.

A cluster of type FD is created by defining an ur-cube with side 2, and placing an ur-parent at the centre of the ur-cube. Next, the ur-cube is divided into $\mathcal{N}_{\mathrm{div}}^3$ equal sub-cubes, and a child is placed at the centre of each sub-cube (the first generation). Normally we use $\mathcal{N}_{\mathrm{div}} = 2$, in which case there are 8 sub-cubes and 8 first-generation children. The probability that a child matures to become a parent in its own right is $\mathcal{N}_{\mathrm{div}}^{(D-3)}$, where D is the fractal dimension. For lower D, the probability that a child matures to become a parent is lower, and the cluster is more 'porous'. Children who do not mature are deleted, along with the ur-parent. A little noise is then added to the positions of the remaining children, to avoid an obviously regular structure, and they then become the parents of the next generation, each one spawning $\mathcal{N}_{\mathrm{div}}^3$ children (the second generation) at the centres of $\mathcal{N}_{\mathrm{div}}^3$ equal-volume sub-sub-cubes, and with each second-generation child having a probability $\mathcal{N}_{\mathrm{div}}^{(D-3)}$ of maturing to become a parent. This process is repeated recursively until there is a sufficiently large generation that, even after pruning to impose a spherically symmetric envelope of radius 1 within the ur-cube, there are still more children than the required number of stars. Children are then culled randomly until the required number is left, and the surviving children are identified with the stars of the cluster. At each generation, the survival of a child is determined by generating a random number $\mathcal{R}$ in $(0,1)$; survival then requires that $\mathcal{R} < \mathcal{N}_{\mathrm{div}}^{(D-3)}$.

Clusters of type $2D\alpha$ are investigated for two purposes. First, we wish to clarify the effect of a sharply defined circular edge on an otherwise statistically uniform, two-dimensional distribution of stars. Clusters of type 2D0 enable us to isolate this effect. Second, we wish to explore how readily two-dimensional and three-dimensional distributions can be distinguished. This could be important if stars are being formed in layers, for example at a shock front.

For each type of artificial cluster, 100 realisations are analysed, so that means and standard deviations can be obtained for the parameters extracted. Three-dimensional clusters (types $3D\alpha$ and FD) are projected onto an arbitrary plane prior to analysis. Two-dimensional clusters are viewed face-on.

A.3   The Mean Surface Density of Companions

A.3.1   Log-log plots and edge effects

A widely used tool for analysing the structure of star clusters is the log/log plot of the mean surface-density of companions, $\bar{N}$ against separation, s. This tool has been pioneered by Larson (1995), building on earlier work by Gomez et al. (1993), who used the two point correlation function. Several papers have confirmed Larson's finding that a plot of $\ell og[\bar{N}]$ against $\ell og[s]$ — hereafter a Larson Plot — can be fitted with two power law sections, corresponding to two distinct regimes. At the smaller separations, $s < s_{break}$, a star's companions are mainly in binary and higher multiple systems, and the slope of the Larson Plot is $\eta_{binary} \equiv d\ell og[\bar{N}]/d\ell og[s] \simeq -2$. At larger separations, $s > s_{break}$, companions are simply other members of the overall cluster, and may only be close due to projection. The slope here is generally larger (i.e. still negative but smaller in magnitude), $\eta_{cluster} \equiv d\ell og[\bar{N}]/d\ell og[s] \gtrsim -1$. Larson has suggested that $\eta_{cluster}$ might be related to the fractal dimension of the sub-clustering, $D = \eta_{cluster} + 2$. In addition, he has proposed that the break point between the two straight sections, at s_{break}, might correspond to the Jeans length. However, recent analysis has cast some doubt on these interpretations. First, the break point is strongly influenced by the overall surface-density of stars (and hence by the depth of the cluster along the line of sight), as pointed out by Simon (1997) and Bate et al (1997). Second, fitting $\eta_{cluster}$ objectively is difficult, because at the low-s end it is distorted by the switch to the binary regime, and — more importantly — at the high-s end it is distorted by edge effects. Consequently, one is left with at best a range of order $2s_{break}$ to $0.1R_{cluster}$ and the result is sensitive to how the range is actually chosen; if the range is shortened or extended arbitrarily, the slope of the fitted line may
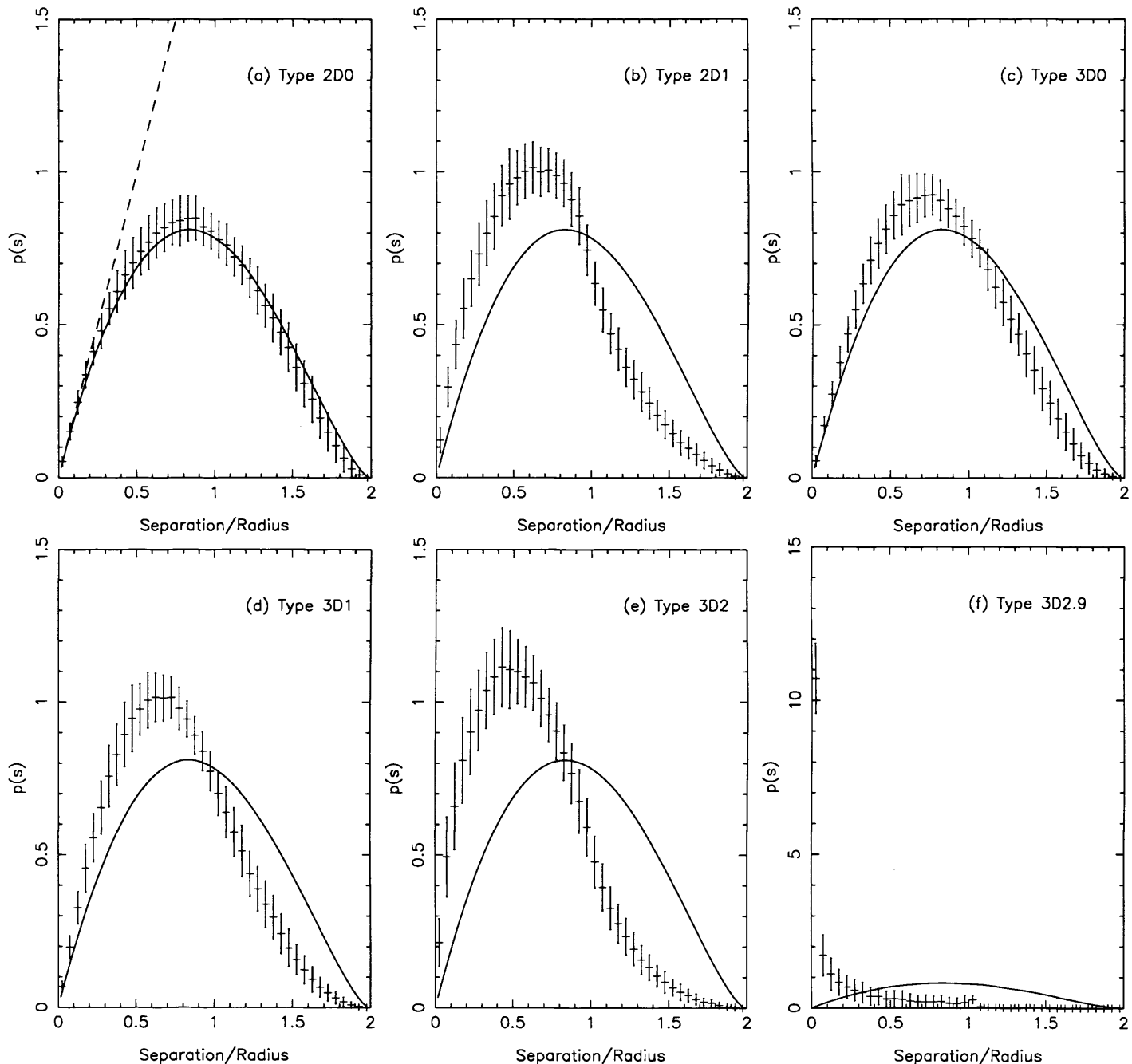
Figure A.2: Distribution function $p(s)$ for separations between randomly chosen stars in artificial (non-fractal) cluster of type (a) 2D0, $N \propto r^0$; (b) 2D1, $N \propto r^{-1}$; (c) 3D0, $n \propto r^0$; (d) 3D1, $n \propto r^{-1}$; (e) 3D2, $n \propto r^{-2}$; and (f) 3D2.9, $n \propto r^{-2.9}$. The solid line is the value of $p(s)$ for a star cluster of type 2D0 having an infinite number of stars (Eqn. A.4), and is included for reference. The dashed line is $p(s) = 2s$ (see text). s is normalized to the overall radius of the cluster, as described in the text.
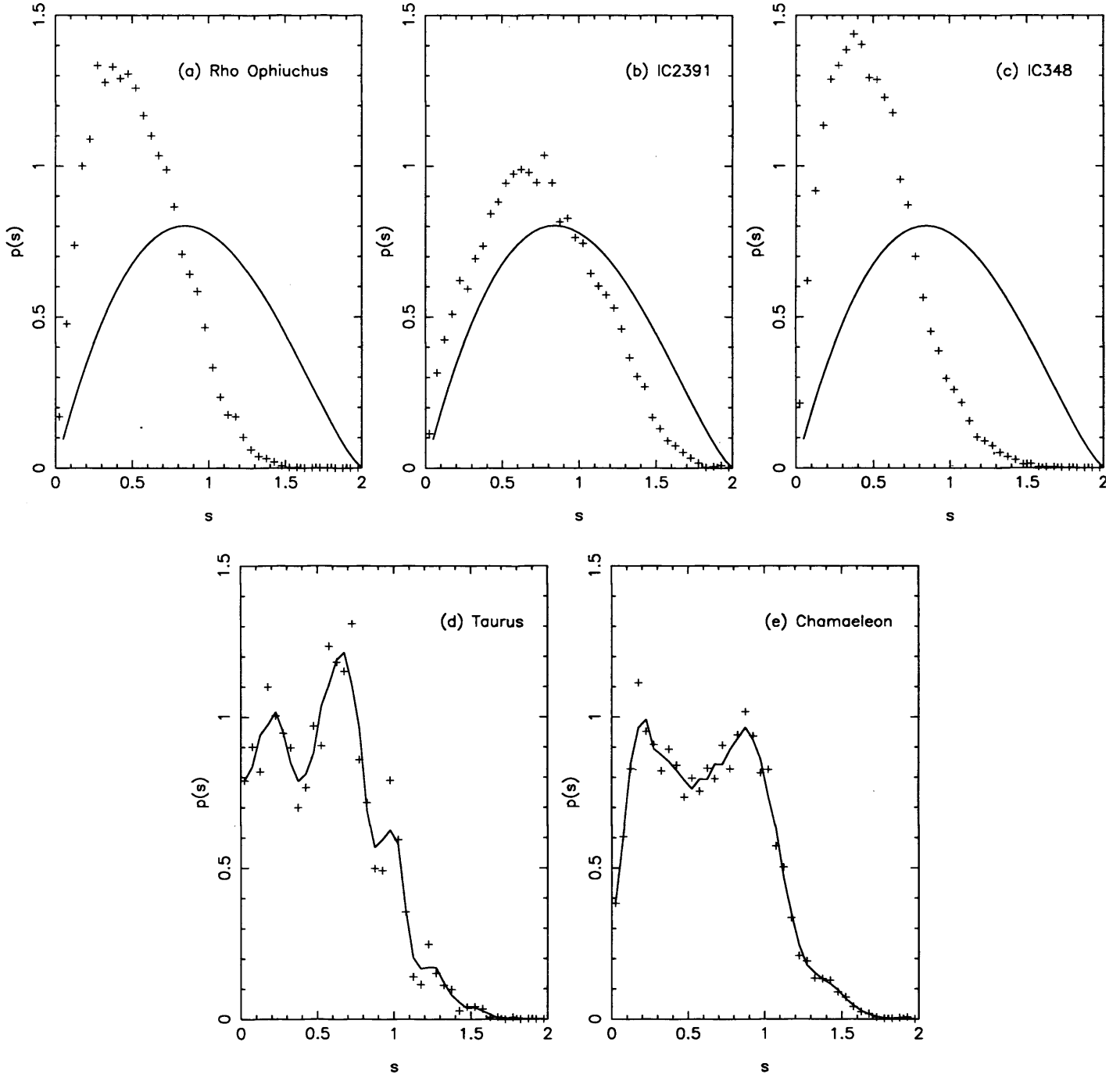
Figure A.3: Distribution functions for separations between randomly chosen stars in five real star clusters. (a) ρ Ophiuchus, (b) IC2391, (c) IC348, (d) Taurus, and (e) Chamaeleon. The solid line is the value of $p(s)$ for a star cluster of type 2D0 having an infinite number of stars (Eqn. A.4), and is included for reference. In (d) and (e), the solid line represents a smoothed version of the raw data, to show the existence of multiple maxima.

change dramatically. Third, η_{cluster} is not necessarily related to the fractal dimension of the clustering. As shown by Bate et al. (1997) and Klessen & Kroupa (2001), it may simply reflect a large-scale density gradient in the cluster.

A.3.2 Linear plots and edge effects

An alternative way of evaluating the data from which Larson plots are derived is to calculate the distribution function $p(s)$, where $p(s)ds$ gives the probability that the projected separation between two cluster stars chosen at random is in the interval $(s, s + ds)$. To do this empirically, we define i_{max} equal s-bins in the range $0 < s < 2R_{\text{cluster}}$, so that all the bins have width $\Delta s = 2R_{\text{cluster}}/i_{\text{max}}$, and the ith bin corresponds to the interval $(i-1)\Delta s < s < i\Delta s$, with mean value $s_i = (i - 1/2)\Delta s$. R_{cluster} is the overall radius of the cluster, and is defined by finding the mean position of all the stars in the cluster and then setting R_{cluster} equal to the distance to the furthest star. Then we count the number of separations $\mathcal{N}_i$ falling in each bin, and put

$$p(s_i) \;=\; \frac{2\mathcal{N}_i}{\mathcal{N}_{\text{total}}\,(\mathcal{N}_{\text{total}} - 1)\,\Delta s}\,, \tag{A.3}$$

where $\mathcal{N}_{\text{total}}$ is the total number of stars in the cluster, and hence $\mathcal{N}_{\text{total}}\,(\mathcal{N}_{\text{total}} - 1)/2$ is the total number of separations.

Figure A.2(a) presents the results obtained from 100 clusters of type 2D0, i.e. a disc having statistically uniform surface-density. The plotted points give the mean $\bar{p}(s_i)$ from the 100 realizations, and the error bars give the width of the bin and the 1σ standard deviation. If there were no edge effects (i.e. if the uniform surface-density extended to infinity in two dimensions), we would have $\bar{p}(s) = 2s$, and this is indeed a good fit to $\bar{p}(s_i)$ at small s_i values, as indicated by the dashed line on Fig. A.2(a). *Departures from this straight line are entirely due to edge effects.*

In fact, $\bar{p}(s)$ can be calculated semi-analytically for a disc having uniform surface-density:

$$\bar{p}(s) \;=\; \begin{cases} 2s(1 - s)^2 + \frac{4s}{\pi}\int_{1-s}^{1}\theta r\,dr\,, & 0 \le s < 1\,; \\[2ex] \frac{4s}{\pi}\int_{s-1}^{1}\theta r\,dr\,, & 1 \le s < 2\,; \\[2ex] 0\,, & s \ge 2\,; \end{cases} \tag{A.4}$$

where

$$\theta = \cos^{-1}\left[\frac{r^2 + s^2 - 1}{2rs}\right] \tag{A.5}$$

The solid line on Fig. A.2(a) shows that this function fits the plotted points well, and it is included on all the other plots for reference, i.e. to emphasize the features which are not due to edge effects.

When derived in this way, the $\bar{p}(s)$ plot contains little information about the distribution of binary separations, since they are all in the first bin. However, it seems to be well established that the distribution of binary separations is approximately scale free over a wide range of separations ($\eta_{\text{binary}} \simeq -2$). The more critical issue — the one with which we are concerned here — is the distribution of separations in the clustering regime and what it tells us about the overall structure of the cluster. This information is well represented by $\bar{p}(s)$, as can be seen from Figs. A.2(b) through A.2(f), which show the results obtained for the other five types of non-fractal artificial star cluster. Figure A.2(b) shows how $\bar{p}(s)$ is slewed towards smaller s values for a disc with a centrally concentrated surface-density, $N \propto r^{-1}$. Figures A.2(c) to A.2(f) show spherical clusters having volume-density gradients $n \propto r^{-\alpha}$ with $\alpha = 0$, 1, 2, and 2.9. Again the distribution slews to smaller s values as the sphere becomes more centrally concentrated (i.e. with increasing α).

A.3.3 The Normalised Correlation Length

One feature which distinguishes the plots is the location of the maximum, i.e. the separation s_{max} at which $\bar{p}(s)$ is largest. As a cluster becomes more centrally condensed, s_{max} moves to smaller values, and the amplitude of the maximum increases. However, for an individual cluster s_{max} will not be well defined, and so it is not a robust measure.

A better measure of this trend is the Normalized Correlation Length for each cluster. The Correlation Length is the mean separation $\bar{s}$ between stars in the cluster, and it is normalized by dividing by R_{cluster}. The second column of Table A.2 gives mean values of $\bar{s}$ and their standard deviations, for the various artificial cluster types. The $\bar{s}$ values for the five real star clusters are also given.

The shapes of the $p(s)$ plots, and hence also the $\bar{s}$ values, are independent of the number of stars in the cluster. In trials with cluster sizes of 100 to 1000 stars, $\bar{s}$ stays within one standard deviation of the mean value for 200 stars. This is at first sight surprising. A 1000-star cluster is so much more dense than a 100-star cluster, that one might expect the mean separation of stars to be smaller. However, although each star has more close neighbours, it also has more distant neighbours, and the value of $\bar{s}$ remains constant. This

is an attractive feature of the Normalised Correlation Length as a statistical descriptor for clusters. From Table A.2, we see that $\bar{s}$ decreases monotonically with increasing α, and can therefore be used to estimate α for star clusters which are presumed *a priori* to have radial density gradients.

Importantly, cluster types 2D1 and 3D2 are easily distinguished by their $\bar{s}$ values and their $\bar{p}(s)$ plots, despite the widespread but fallacious assumption that a three dimensional cluster with volume-density $n \propto r^{-2}$ is, when projected on the sky, similar to a two dimensional cluster with surface-density $N \propto r^{-1}$. In fact it is clusters of types 2D1 and 3D1 (i.e. with the same exponent, $d\ell n[N]/d\ell n[r] \sim -1$, and $d\ell n[n]/d\ell n[r] \sim -1$) which are hard to distinguish.

$p(s)$ plots for the real clusters are shown on Fig. A.3. IC348 and ρ Ophiuchus resemble clusters of type 3D2, both on the basis of their $\bar{s}$ values (Table 1), and the shapes of their $p(s)$ plots (Figs. A.3(a) and A.3(c)). For IC2391 the $\bar{s}$ value and the $p(s)$ plot (Fig. A.3(b)) are most like those for clusters of type 3D1.

A.3.4   The effect of subclusters on $p(s)$ and $\bar{s}$

Chamaeleon and Taurus have correlation lengths intermediate between types 3D1 and 3D2, but their $p(s)$ plots are clearly not generic. This is because they contain sub-clusters, as illustrated in Figs. A.1(d) and A.1(e). Consequently $p(s)$ has multiple maxima. In some cases these maxima can be identified with (i) separations between stars in the same sub-cluster (the maximum at the smallest separations) and (ii) separations between stars in two distinct sub-clusters (maxima at larger separations, corresponding to the separation between the two sub-clusters). If there are $\mathcal{N}_{sub}$ sub-clusters, there can be up to $1 + \mathcal{N}_{sub}(\mathcal{N}_{sub} - 1)/2$ maxima, but fewer if there is degeneracy in the distances between sub-clusters. After smoothing, the $p(s)$ plot for Chamaeleon (Fig. A.3(e)) shows two distinct maxima, suggesting at least two sub-clusters, and Fig. A.1(e) does indeed show two sub-clusters. They are separated by ~ 1, hence giving rise to the maximum in $p(s)$ at $s \sim 1$. However, after smoothing, the $p(s)$ plot for Taurus (Fig. A.3(d)) shows only three well defined maxima, suggesting at most three sub-clusters, whereas Fig. A.1(d) shows at least eight well defined sub-clusters. Evidently the $p(s)$ plot is not a robust diagnostic of sub-clustering.

If we now consider artificial fractal star clusters with the same fractal dimension D, we find that there is so much variance in their individual $\bar{p}(s)$ plots that we cannot sensibly define a mean $\bar{p}(s)$ plot. However, we can still compute the mean Normalised Correlation Length $\bar{s}$ and its variance. The results are given in Table 1. We see that $\bar{s}$ increases monotonically with increasing D and can therefore be used to estimate D for star clusters

which are presumed *a priori* to be fractal.

Moreover, the value of $\bar{s}$ for star clusters of type F3.0 is essentially the same as for clusters of type 3D0, as it should be. The small difference is attributable to the fact that in constructing clusters of type F3.0 the positioning of the individual stars is not completely random, whereas for type 3D0 it is.

However, the range of $\bar{s}$ for D in (1.5,3.0) is almost identical to that for α in (0,2). Therefore $\bar{s}$ is degenerate and cannot on its own be used to distinguish multi-scale (fractal) sub-clustering from a large-scale radial density gradient.

A.4   Minimal Spanning Trees

The Minimal Spanning Tree (MST) is the unique[1] network of straight lines joining a set of points, such that the total length of all the lines – hereafter 'edges' – in the network is minimised. The construction of such a tree is described by Gower and Ross (1969). Starting at any point, an edge is created joining that point to its nearest neighbour. The tree is then extended by always constructing the shortest link between one of its nodes and an unconnected point, until all the points have been connected. Figure A.4 shows the MSTs for the real star clusters ρ Ophiuchus, Taurus, Chamaeleon, IC348 and IC2391.

The use of Minimal Spanning Trees (MSTs) as a probe of cosmological structure was explored by Barrow, Bhavsar and Sonoda (1985), and a further refinement, the self avoiding random walk, was described by Baugh (1993). Although the approach seemed promising as a means of picking out clumps and filaments, the only statistical analysis of the MST for cosmological purposes of which we are aware is due to Graham, Clowes and Campusano (1995), who adopted methods developed by Hoffman and Jain (1983) and Dussert et al(1987) and applied them to the distribution of quasars.

A.5   Detecting randomness and clustering using the Minimal Spanning Tree.

Graham et al (1995) have applied the MST to quasar clustering on very large scales, using a method which was developed by Dussert et al (1987) for characterising biological structures. In Dussert's method, the mean $\bar{m}$ and standard deviation σ_m of the edge lengths of the MST are first computed and normalised by dividing by the factor

---

[1]strictly speaking, if the array of points contains two or more pairs with exactly the same separation, the network may not be unique, as the points may be connected in a different order. However, even if this is the case, the total length of edges and the distribution of edge-lengths is preserved for all solutions.
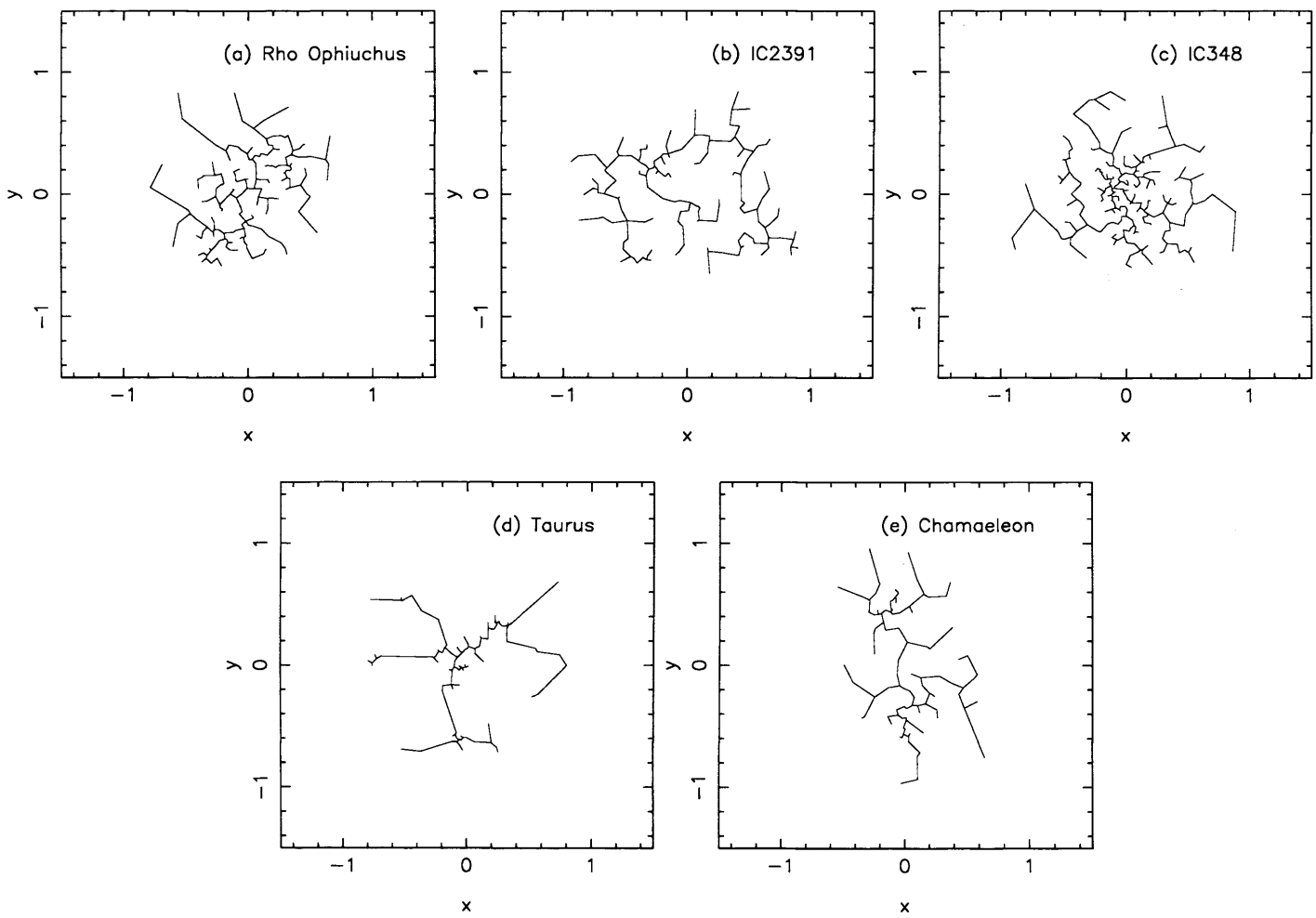
Figure A.4: Minimal Spanning Trees for (a) ρ Ophiuchus, (b) IC2391, (c) IC348, (d) Taurus, and (e) Chamaeleon.

$(\mathcal{N}_{\text{total}}A)^{1/2}/(\mathcal{N}_{\text{total}}-1)$, then plotted on the (m, σ_m)-plane. Fig. A.6(a), reproduced from Dussert et al. (1987), shows the theoretical locations on the (m, σ_m)-plane for different types of clustering in two-dimensions. The region of the (m, σ_m)-plane around the central star represents the locus of a random distribution. The region of the (m, σ_m)-plane around '1' represents the locus of distributions dominated by sub-clustering. The region of the (m, σ_m)-plane around '2' represents the locus of distributions dominated by radial concentration gradients. The region of the (m, σ_m)-plane around '3' represents the locus of distributions dominated by quasi-periodic tilings. And the region of the (m, σ_m)-plane around '4' represents the locus of highly organized distributions (i.e. lattices).

Fig. A.6(b) shows the loci on the (m, σ_m)-plane for the various artificial star cluster types and the five real clusters, and reveals some drawbacks to this plot. The locus for artificial clusters with a radial density gradient do indeed tend towards region 2 with increasing α (i.e. greater degree of central concentration), although only for $\alpha \gtrsim 2$ are they clearly distinguishable from a purely random distribution. Similarly, the locus for artificial clusters with fractal sub-clustering tend towards region 1 with decreasing D (i.e. greater degree of sub-clustering) for $D \gtrsim 2.0$. However, for $D \lesssim 2.0$, this trend is abandoned, and the locus moves towards region 2; in other words, a cluster with a low fractal dimension and hence a high degree of sub-clustering masquerades – on the (m, σ_m)-plane – as a cluster with a strong radial density gradient, albeit it not precisely of the form $n \propto r^{-\alpha}$. Moreover, Taurus, which to the human eye appears to have the most well defined sub-clustering of all five real clusters, masquerades on the (m, σ_m)-plane as a cluster with a strong radial density gradient, $\alpha \simeq 2.7$.

We conclude that the (m, σ_m)-plane is not able to distinguish between a smooth large-scale radial density gradient and multi-scale fractal sub-clustering

A.5.1 The Normalised Mean Edge Length

Once the MST of a cluster has been constructed it is straightforward to compute the Mean Edge Length, $\bar{m}$. Unlike the Normalised Correlation Length $\bar{s}$, $\bar{m}$ is not independent of the number of stars in the cluster, $\mathcal{N}_{\text{total}}$. As $\mathcal{N}_{\text{total}}$ increases, more short edges are created on the MST and $\bar{m}$ decreases. The expected total length of the MST of a random array of $\mathcal{N}_{\text{total}}$ points, uniformly distributed over a two-dimensional area A, is asymptotically proportional to $(\mathcal{N}_{\text{total}}A)^{1/2}$ (Hammersley et al. 1959). As there are $\mathcal{N}_{\text{total}} - 1$ edges, the mean edge length is asymptotically proportional to $(\mathcal{N}_{\text{total}}A)^{1/2}/(\mathcal{N}_{\text{total}} - 1)$, and so this factor should be used to normalise the mean edge length of clusters having different areas A and/or different numbers of stars $\mathcal{N}_{\text{total}}$.

The resulting Normalised Mean Edge Length $\bar{m}$ has been evaluated for 100 realisations

of each type of artificial star cluster, and for the real star clusters, and the results are recorded in Table A.2 (column 3). Also recorded in Table A.2 (column 4) is the mean of the standard deviations of the MST edge lengths, $\bar{\sigma}_m$.

A.5.2 $\mathcal{Q}$

Table A.2 shows that for artificial clusters of type 2Dα, 3Dα and FD, both $\bar{m}$ and $\bar{s}$ decrease monotonically as α increases (i.e. the degree of central concentration becomes more severe) or as D decreases (i.e. the degree of sub-clustering become more severe). However, $\bar{s}$ decreases more quickly than $\bar{m}$ as α is increased, while $\bar{m}$ decreases more quickly than $\bar{s}$ as D is decreased. Thus, the ratio

$$\mathcal{Q} = \frac{\bar{m}}{\bar{s}} \tag{A.6}$$

yields a measure which not only quantifies, but also distinguishes between, a smooth overall radial density gradient and multi-scale fractal sub-clustering.

Mean values of $\mathcal{Q}$ for the various types of artificial star cluster are recorded in Table A.2 (column 5). For artificial clusters with a smooth large-scale radial density gradient (type 3Dα), $\bar{\mathcal{Q}}$ increases from $\bar{\mathcal{Q}} \simeq 0.80$ to $\bar{\mathcal{Q}} \simeq 1.50$ as the degree of central concentration increases from $\alpha = 0$ (statistically uniform number-density) to $\alpha = 2.9$ ($n \propto r^{-2.9}$). For artificial clusters with fractal sub-structure (type FD), $\bar{\mathcal{Q}}$ decreases from $\bar{\mathcal{Q}} \simeq 0.80$ to $\bar{\mathcal{Q}} \simeq 0.45$ as the degree of sub-clustering increases from $D = 3.0$ (uniform number-density, no sub-clustering) to $D = 1.5$ (strong sub-clustering).

We can therefore construct a plot (Figure A.5) of D against $\mathcal{Q}$ for $\mathcal{Q} \leq 0.80$, and α against $\mathcal{Q}$ for $\mathcal{Q} \geq 0.80$. For any real cluster we can compute its $\mathcal{Q}$ value, and then use Figure A.5 to read off its notional fractal dimension D' (if $\mathcal{Q} < 0.80$, implying sub-clustering), or its radial density exponent α (if $\mathcal{Q} > 0.80$, implying a large-scale radial density gradient).

The small kink at $\mathcal{Q} \simeq 0.8$ is due to the fact in constructing a cluster of type F3.0 the stars are positioned regularly (in the sense that at each generation, each subcube of space is occupied) and therefore the number-density is artificially uniform; in contrast, when we construct a cluster of type 3D0 the stars are positioned randomly, so that the density is only uniform in a statistical sense and there are Poisson fluctuations in the local density.

Fractal dimensions obtained from Fig. A.5 in this way are only notional, because $\mathcal{Q}$ (or any other single measure) can reflect sub-clustering, but cannot capture whether the sub-clustering is hierarchically self-similar.

Using Figure A.5, we infer that Taurus, IC2391 and Chamaeleon have substructure
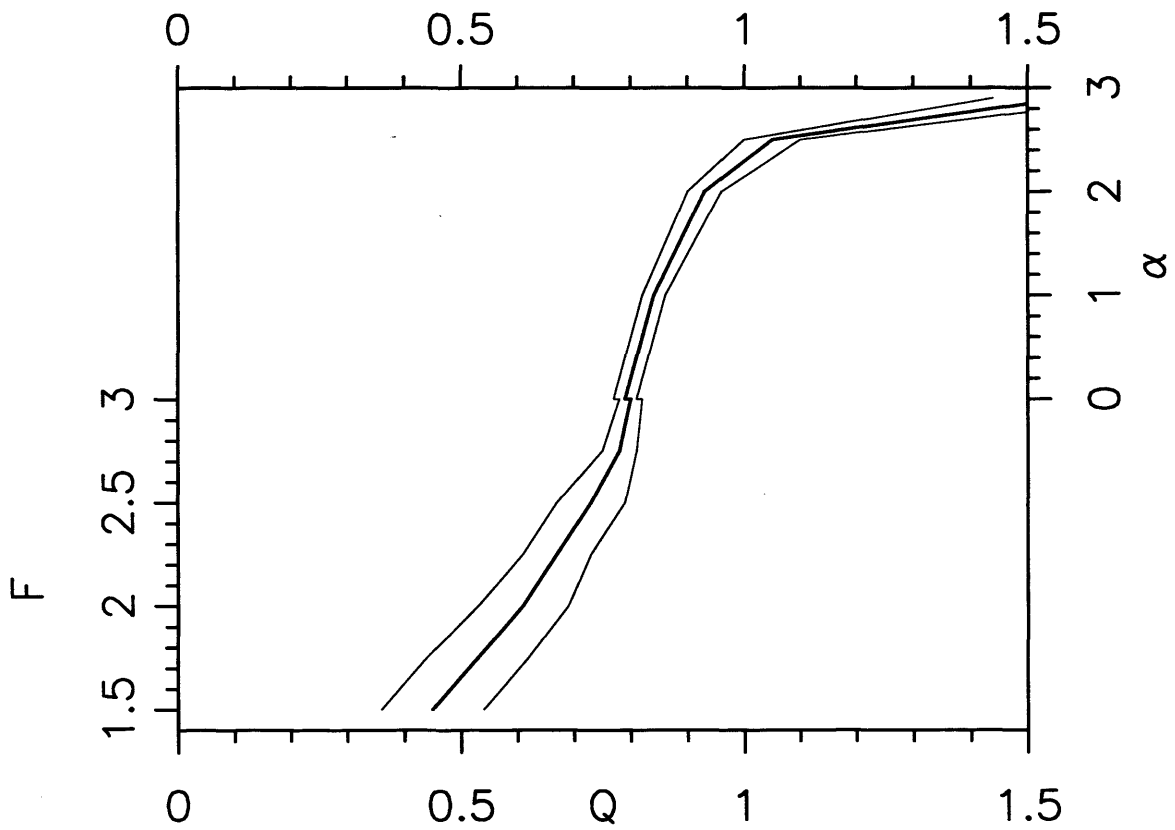
Figure A.5: $\mathcal{Q}$ plot for artificial star clusters. For $\mathcal{Q} \leq 0.80$, the fractal dimension D should be read from the lefthand axis, and for $\mathcal{Q} \geq 0.80$, the radial density exponent α should be read from the righthand axis. The small kink at $\mathcal{Q} \simeq 0.8$ is explained in the text.

with notional fractal dimensions $D = 1.5$, 2.2 and 2.25. In contrast, ρ Ophiuchus and IC348 appear to be centrally concentrated, with radial density exponents $\alpha = 1.2$ and 2.2. These inferences agree well with an intuitive reading of the raw data shown in Fig. A.1.

A.5.3 The effect of binary companions on the MST Edge Length

The MST will normally link a star to its binary companion, as this will usually be the shortest way of adding one or other of the stars to the tree. Binaries create very short edges and therefore a large population of binary stars will cause a noticeable reduction in the mean edge length, $\bar{m}$. Of the five real clusters considered in this paper, Taurus has been subjected to particularly close scrutiny and has a larger identified population of binaries than any of the others. As the binaries are not part of the clustering regime, it is important to establish whether they are distorting the result.

Using the MST, all pairs of stars lying closer together than 10^{-4} of the cluster radius were pruned, leaving single stars. For Chamaeleon, ρ Ophiuchus, IC348 and IC2391, only 3, 0, 1 and 2 such pairs were found; Taurus, however, was pruned from 215 down to only 137 primary stars. For the pruned version of Taurus, $\bar{s}$ increased from 0.55 to 0.57, while $\bar{m}$ increased from 0.26 to 0.33 and $\mathcal{Q}$ increased from 0.47 to 0.58. Removal of the binaries resulted in the notional fractal dimension for Taurus being increased from 1.5 to 1.9. This demonstrates that in a cluster with a large binary population, it is important to prune the close companions before evaluating $\bar{s}$, $\bar{m}$ and $\mathcal{Q}$.

A.6 Discussion

The ratio of the Normalized Mean Edge Length to the Normalized Correlation Length, $\mathcal{Q}$, is effective in distinguishing between a smooth large-scale radial density gradient and multi-scale fractal sub-clustering, because it is sensitive not only to the frequency of small separations between stars, but also to their spatial distribution.

The MST Edge length $\bar{m}$ is a simple average of the distances of stars to their (usually) closest neighbours. If one star is moved very close to another, the change in $\bar{m}$ will be diluted by the total number of stars, $\mathcal{N}_{total}$. However, when calculating the mean distance of companions for all stars, only one star out of $\mathcal{N}_{total}$ in the cluster has had one of its $\mathcal{N}_{total} - 1$ companions moved very close. The change in $\bar{s}$, is therefore diluted by $\mathcal{N}_{total}^2$. Thus, when small separations are scattered all over the cluster, increasing the number of small separations causes both $\bar{m}$ and $\bar{s}$ to decrease, but $\bar{s}$ decreases more slowly than $\bar{m}$. This is the case for decreasing fractal dimension.
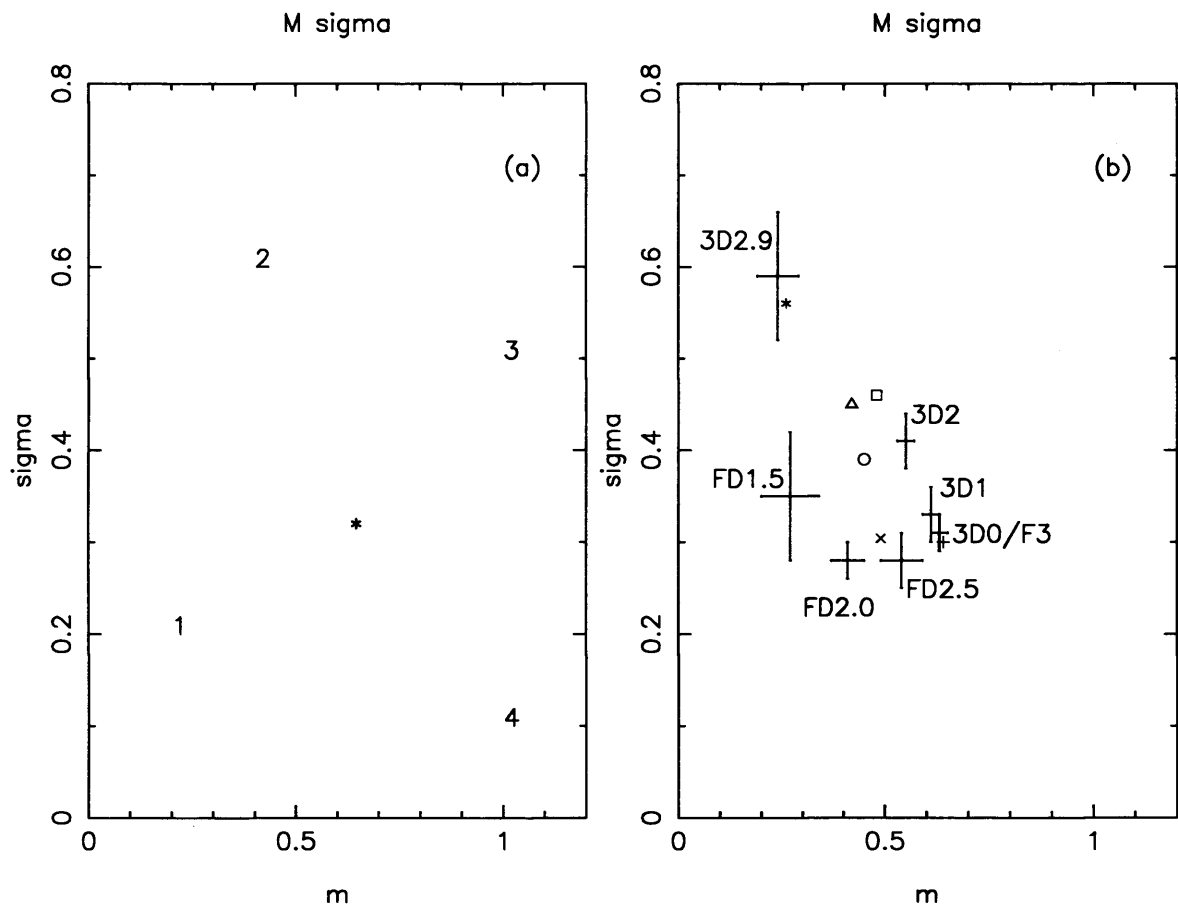
Figure A.6: MST (m, σ_m)-plots. (a) (m, σ_m)-plane, showing the regions of the plane in which well characterised distributions of points converge (from Graham et al). *: random distributions, 1: clustered structures, 2: concentration gradients, 3: quasi periodic tilings, 4: highly organised distributions. (b) (m, σ_m)-plane, with artificial star clusters of types 3D0 to 3D2.9 and F1.5 to F3.0 plotted. The five real clusters are indicated by symbols + : Taurus, o : ρ Ophiuchus, × : IC2391, □ : IC348, △ : Chamaeleon.

For radially concentrated clusters, by contrast, increasing the clustering creates more small separations between stars, but these are all in the central region of the cluster. Moving another star to this area affects $\bar{m}$ in the normal way, the star having a newly short edge length between it and its nearest neighbour, and the change in the mean distance being diluted by $\mathcal{N}_{\text{total}}$. However, the large number of other stars in the centre also gain another close neighbour. The decrease in $\bar{s}$ is therefore compounded and exceeds that in $\bar{m}$.

Consequently, the quotient $\mathcal{Q} = \bar{m}/\bar{s}$ successfully distinguishes between clusters which have a smooth large-scale radial density gradient and clusters which have multi-scale fractal sub-clustering, in a way which agrees with an intuititive analysis but which cannot be accomplished using existing methods such as Larson Plots or Box Dimension Plots. An additional advantage over these methods is that the calculation of $\mathcal{Q}$ is quantitative and objective, as no intervention is required in the normalisation process, in the construction of the MST, or in choosing a range over which to calculate a slope.

We should emphasize that classical methods for evaluating the density profile of a cluster, or its fractal dimension, are not viable for clusters with ~ 200 members, primarily because of low-number statistics. For example, if one attempts to define the projected radial density profile for a real cluster of stars by counting stars in different annuli, the result is very noisy.

Alternatively, if one attempts to determine the mean projected radial density profile for a 200-member artificial cluster having a given radial density profile in three dimensions, using many different realizations and with a view to comparing this with a real cluster, one finds that the standard deviation is very large, and so the diagnostic power of this profile is poor.

In the same spirit one might attempt to construct the Box Dimension Plot (BDP) of a real cluster and compare it with the mean BDP of artificial star clusters having a given fractal dimension. To construct a BDP one divides the projected image of the star cluster into a grid of square cells of side l and counts the number of cells, $\mathcal{N}_{\text{occ}}(l)$ which are occupied by stars. Then, by repeating this for different values of l, one obtains a plot of $log(\mathcal{N}_{\text{occ}}(l))$ against $-log(l)$. For a true fractal this plot is a straight line with slope equal to the fractal dimension. However, for a star cluster with only ~ 200 members, the plot is not linear. By treating many realisations of artificial clusters all having the same fractal dimension *and the same number of stars*, one can define a mean BDP. However, the mean BDP is not very strongly dependent on the fractal dimension and it has a large standard deviation. Therefore the Box Dimension Plot of a real cluster does not give a useful constraint on its fractal dimension.

It is for this reason that we have sought integral measures of cluster structure. The same philosophy informs the use of equivalent width when evaluating noisy spectral lines (for example).

We also note that a cluster cannot have a large-scale radial density gradient, and at the same time be fractally sub-clustered. A cluster could have a large-scale radial density gradient and *non-fractal* sub-clustering – but then it would require more parameters to characterize the structure, and its diagnosis would become correspondingly more difficult (if not impossible for clusters with $\sim$ 200 stars).

In Table A.2 we list estimates for the ages and the crossing times of the clusters we have analyzed. On the basis of simple arguments, we might expect the Q value of a cluster to increase with time, as the substructure dissolves and the overall cluster relaxes to a radially concentrated density profile. However, this is not evident in the small sample treated here. Taurus has an age much less than its crossing time, which is consistent with its small Q value and low fractal dimension. On the other hand, IC2391 and Chamaeleon have ages much greater than their crossing times and yet they are still fractal with relatively low Q values. In contrast, ρ Ophiuchus and IC348, which have ages comparable with their crossing times, are both centrally condensed, with no discernible substructure. We should, however, caution against drawing firm conclusions from such a small sample. We also note that young clusters observed at short wavelengths (i.e. in the optical), may appear to have substructure due to patchy obscuration. therefore long wavelength surveys are preferable for embedded young star clusters.

A.7 Conclusions

We have explored two statistical measures for analysing objectively the observed (i.e. projected) structures of star clusters. These measures are based on the Mean Surface Density of Companions (MSDC), and the Minimal Spanning Tree (MST). The measures are $\bar{s}$, the normalised mean separation between stars, and $\bar{m}$, the normalised mean edge-length of the MST, both of which are independent of the number of stars in the cluster. For artificial star clusters, created with a smooth large-scale radial density profile ($n \propto r^{-\alpha}$), and for artificial star clusters created with sub-structure having fractal dimension D, $\bar{s}$ and $\bar{m}$ both decrease with increasing α and/or decreasing D – but at different rates. Hence a cluster with a radial gradient can be distinguished from one with sub-structure by evaluating $Q = \bar{m}/\bar{s}$. For a cluster of uniform volume-density (i.e. $\alpha = 0$ and $D = 3.0$), $Q \simeq 0.80$. If the cluster is made more centrally condensed by increasing α, Q increases monotonically, reaching $Q \simeq 1.50$ at $\alpha = 2.9$. Conversely, if the cluster is given sub-

structure by reducing D, Q decreases monotonically, reaching $Q \simeq 0.45$ at $D = 1.5$.

On the basis of their Q values, ρ Ophiuchus and IC348 have radial gradients with $\alpha \simeq 1.2 \pm 0.3$, and 2.2 ± 0.2, respectively. Chamaeleon and IC2391 have sub-structure with notional fractal dimension $D' \simeq 2.2 \pm 0.2$. Taurus has even more sub-structure, with $D' \simeq 1.55 \pm 0.25$, and if the binaries in Taurus are treated as single systems, D' increases to 1.9 ± 0.2. D' is only a notional fractal dimension, because the integral measures we have defined do not give any indication of whether the sub-structure is hierarchically self-similar. (Indeed, for clusters having only ~ 200 stars the range of separations is too small to possess hierarchical self-similarity.)

Appendix B

Methods for Analysing the structure of Molecular Clouds

Since most stars are formed in clusters, embedded within gas clouds (Larson 1995), it would be useful to have quantitative and objective statistical measures, which facilitate comparison of the two types of object. Given the wealth of new data available, both real and simulated, this would be a helpful step in characterising and analysing the data, and would assist in comparing observed clusters and gas clouds with numerical simulations.

We have previously reported (Appendix A), a robust, objective measure, $\mathcal{Q}$, which both quantifies, and distinguishes, large-scale radial density gradients and small-scale (fractal) sub-clustering in star clusters. This method has been applied successfully to the analysis of both real observations (Appendix A) and numerical results (Schmeja & Klessen 2005). Here we extend this work to the analysis of clouds of gas, where data is present in the form of grey-scale pixellated two-dimensional images, rather than lists of two-dimensional star co-ordinates.

In Section B.1 we describe our methodology for creating artificial clouds, then in Section B.2 describe the real data used. In Section B.3 we look again at the Normalised Correlation Length, $\bar{s}$, as a measure of the degree of clustering of point data, and in Section B.4 we successfully adapt it for use with grey-scale images. In Section B.5 we explain why the Minimal Spanning Tree cannot be adapted in the same way. In Section B.6 we use the Perimeter-Area method to estimate fractal dimensions of artificial clouds, and compare the results with those obtained using the Normalised Correlation Length and with the values used in the construction of the clouds. All the measures are tested and calibrated on multiple realizations of artificial clouds, and are then applied to real data from the Orion B North molecular cloud. The results are discussed in Section B.7, and the main conclusions are summarized in Section B.8.

B.1 Methodology

As we are investigating, and attempting to quantify, the structures of gas clouds, we first need data with known characteristics on which to test the methods which we develop. Two different types of three-dimensional artificial gas cloud have been created for this purpose, using a random number generator to place unit masses of gas in three-dimensional positions within a unit-radius sphere. The first type ($3D\alpha$) are spherical clouds with volume density $n \propto r^{-\alpha}$ and $\alpha = 0$, 1, 2, or 2.9. The second type (FD_3) are fractal clouds with fractal dimension $D_3 = 3.0$, 2.5, 2.0, or 1.5. The different types are listed in Column 1 of Table B.1. All of the artificial clouds are created with 1000 to 10000 unit masses.

A cloud of type $3D\alpha$ having $\mathcal{N}$ mass units is created by positioning $\mathcal{N}$ unit masses of gas according to

$$\left.\begin{aligned}
r &= \{(3-\alpha)\mathcal{R}_r/3\}^{1/(3-\alpha)}, \\
\theta &= \cos^{-1}(2\mathcal{R}_\theta - 1), \\
\phi &= 2\pi\mathcal{R}_\phi, \\
x &= r\sin(\theta)\cos(\phi), \\
y &= r\sin(\theta)\sin(\phi), \\
z &= r\cos(\theta).
\end{aligned}\right\} \tag{B.1}$$

where $\mathcal{R}_r$, $\mathcal{R}_\theta$ and $\mathcal{R}_\phi$ are random numbers. Clearly this method cannot be used for $\alpha = 3$, as the central mass then diverges, so to have a cloud type approximating to $\alpha = 3$ we use $\alpha = 2.9$.

A cloud of type FD_3 having $\mathcal{N}$ mass units is created by adapting the method used in Appendix A. We define an ur-cube with side 2, and place an ur-parent at the centre of the ur-cube. Next, the ur-cube is divided into eight equal-volume sub-cubes, a child is placed at the centre of each sub-cube, and the ur-parent is culled; these children constitute the first generation. For each of these first-generation children, the probability of maturing to become a first-generation parent is $2^{(D_3-3)}$, where D_3 is the fractal dimension. If a child does not mature, it is deleted. When $D_3 = 3$, all children mature and become parents, so the ur-cube is completely filled with a uniform density of first-generation parents. When D_3 is lower, the probability that a child matures to become a parent is lower, and the resulting distribution of first-generation parents is sparser. Next, the sub-cubes containing the surviving first-generation parents are divided into eight equal-volume sub-sub-cubes, a child is placed at the centre of each of these sub-sub-cubes, and the parents are culled; these children constitute the second generation. The second-generation children also have a probability $2^{(D-3)}$ of maturing to become parents and spawning the third generation of children. The process is repeated recursively until there is a sufficiently large generation

Table B.1: Clustering measures obtained for real and artificial gas clouds and star clusters. Column 1 lists the cloud or cluster type, or the name of a real molecular cloud or star cluster. Column 2 gives the Normalized Correlation Length $\bar{s}$ (i.e. the ratio of the mean separation to the cluster radius) for star clusters, as reported in chapter A, and Column 3 gives the same quantity for gas clouds. For the artificial star clusters, means and standard deviations are computed from 100 realisations of each type, with $100 \leq \mathcal{N}_\star \leq 300$. For the gas clouds, 100 realisations are computed, with the mass of the cloud varying from 1000 to 10000 units, and the pixel size of the grey scale image varying from 0.1 to 0.01 times the image size (comparable with the pixel sizes on the 850μm map of Orion B North; see Section 3). Column 4 gives the slope (plus standard deviation) of a log-log plot of perimeter versus area for features within a cloud; this should be $D_2/2$. For the artificial cloud types, perimeter-area coordinates are accumulated for 20 realisations, and a single regression is then performed on the composite data.

Cluster or cloud type or name	Cluster $\bar{s}$	Cloud $\bar{s}$	Slope of Perim vs area
3D0 $(n \propto r^0)$	0.80 ± 0.02	0.80 ± 0.01	-
3D1 $(n \propto r^{-1})$	0.73 ± 0.03	0.73 ± 0.01	-
3D2 $(n \propto r^{-2})$	0.60 ± 0.03	0.58 ± 0.01	-
3D2.9 $(n \propto r^{-2.9})$	0.16 ± 0.02	0.15 ± 0.02	-
F3.0 $(D_3 = 3.0)$	$0.81 \pm .03$	0.77 ± 0.01	$0.81 \pm .03$
F2.5 $(D_3 = 2.5)$	$0.74 \pm .09$	0.73 ± 0.06	$0.84 \pm .03$
F2.0 $(D_3 = 2.0)$	$0.67 \pm .13$	0.68 ± 0.08	$0.77 \pm .09$
F1.5 $(D_3 = 1.5)$	$0.62 \pm .18$	0.63 ± 0.11	$0.71 \pm .08$
Orion B	-	0.50	$0.56 \pm .07$
Orion B/1	-	0.20	$0.61 \pm .07$
Orion B/2	-	0.52	$0.59 \pm .08$
Orion B/3	-	0.59	$0.60 \pm .08$
IC2391	0.74	-	-
Chamaeleon	0.63	-	-
Taurus	0.55	-	-
ρ Ophiucus	0.53	-	-
IC348	0.49	-	-
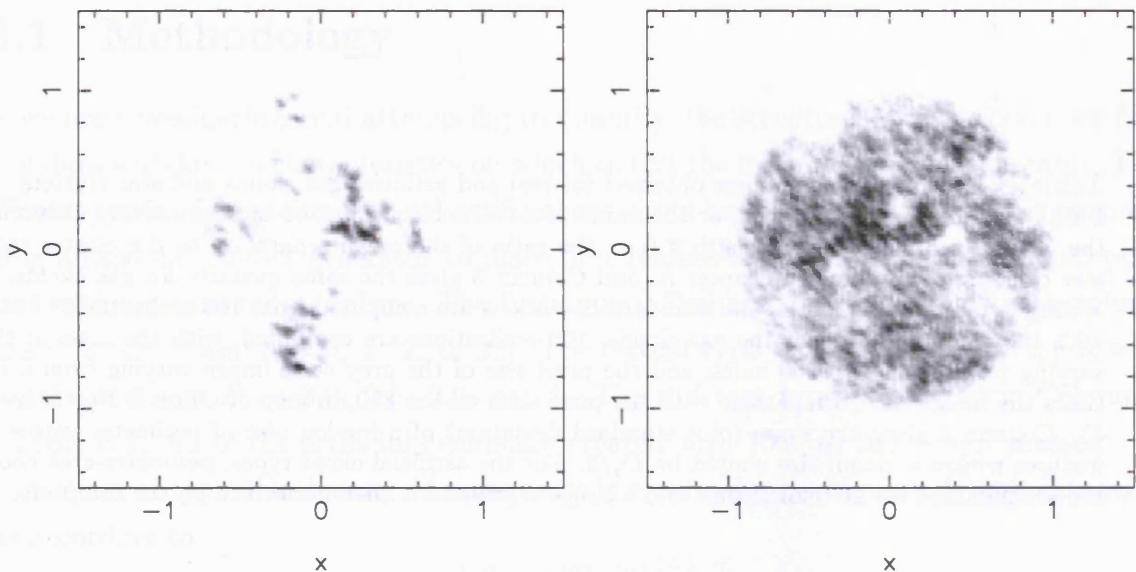
Figure B.1: 100×100 pixel images of artificial clouds. The grey-scale corresponds to ten equal linear column-density intervals between 0 and 2.5×10^3 mass units per unit area. The lefthand cloud has $D_3 = 1.5$, and the righthand one has $D_3 = 2.5$.

of children that we can remove all children lying *outside* the unit radius sphere within the ur-cube and still have $\geq \mathcal{N}$ children left *inside* the sphere. Any excess children are then culled randomly until the required number, $\mathcal{N}$, are left. Provided that there have been many generations, this cull does not significantly alter the fractal dimension. The surviving children are identified with the unit masses of the cloud. At each generation, the survival of a child is determined by generating a random number $\mathcal{R}$ in $(0,1)$; survival then requires that $\mathcal{R} < 2^{(D_3-3)}$.

Once the three-dimensional positions of the $\mathcal{N}$ unit masses have been determined, these positions are projected onto an arbitrary plane, and the masses are accumulated into an $\mathcal{I} \times \mathcal{I}$ array of square pixels. The number of unit masses in each pixel, $\mathcal{N}_i$, divided by the area of a pixel, δ^2, gives the column-density for that pixel, $N_i = \mathcal{N}_i/\delta^2$, and these column-densities can then be displayed as a grey-scale image. The linear size of a pixel, δ, is chosen so that, at least in regions of relatively high column-density, the number of unit masses in a pixel is large enough to keep statistical fluctuations to an acceptable level. A simple spreading algorithm is applied to the image, mimicking the point-spread function of the instrument used in the acquisition of real data. Finally, the image is centred on the centre of mass, and distances are normalised by setting the radius of the cloud (i.e. the distance from the centre of mass to the most distant occupied pixel) to unity. In the rest of this paper, all distances are normalised in this way. Correlation Lengths are calculated for 100 realisations of each cloud and cluster type, yielding means and standard deviations
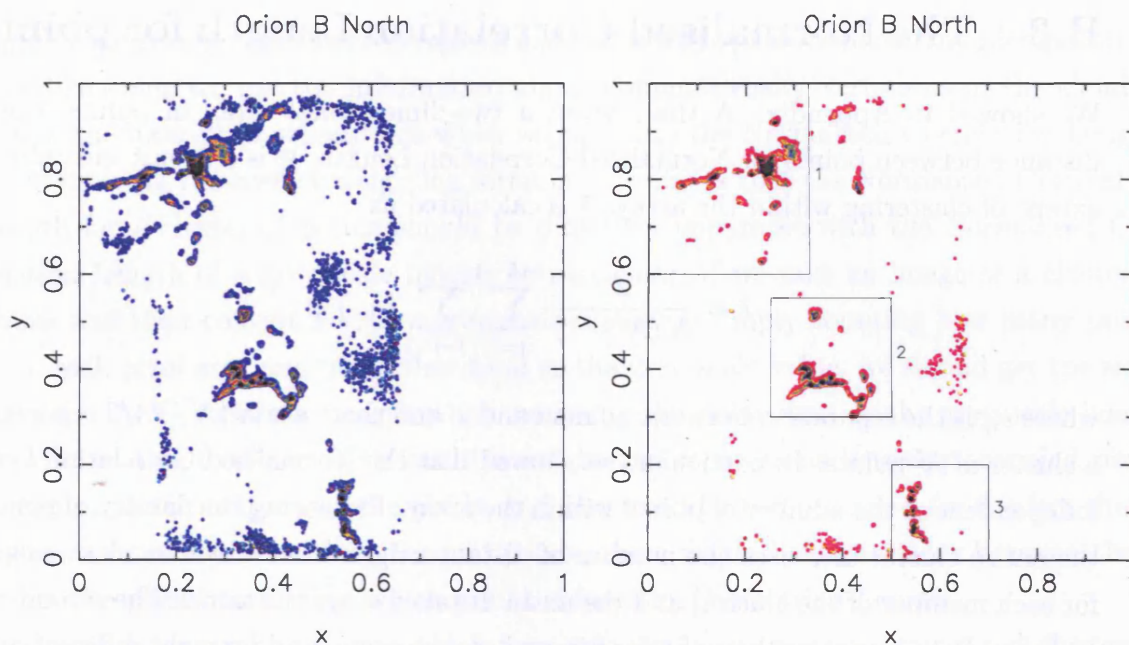
Figure B.2: 850μm maps of Orion B North. The lefthand map shows the raw data, including low level (< 0.1 Jy) noise. In the righthand map, the noise has been cleaned and the boxes identify the individual core-clusters – 1, 2 and 3 – as discussed in the text. The extent of the image is 5.25 pc from top to bottom, and the imaging sensor has 1024×1408 pixels. The dynamic range is 0 to 8.5 Jy per 14 arcsec beam and the grey-scale values are linear.

for $\bar{s}$. 20 realisations of each cloud type are used for perimeter-area analysis.

B.2   Submillimetre Maps of the Orion B North star forming region

850μm maps of the Orion B North star forming region were obtained using the Submillimetre Common User Bolometer Array (SCUBA) at the James Clerk Maxwell Telescope (JCMT). For details of the data acquisition and reduction, see Nutter & Ward-Thompson (2006). The mapped area contains the two optical nebulae NGC 2068 and NGC 2071. This region is known to be a site of ongoing star formation (Motte et al. 2001; Johnstone et al. 2001). The cloud is just over 5pc across. There are three distinct clusters of cores, which we have labelled 1, 2 and 3 (see Fig. B.2). These core-clusters each have an extent of 1 to 2 pc. The whole image is 1024×1408 pixels, while the regions containing the core-clusters are $\sim 300 \times 300$ pixels.

B.3   The Normalised Correlation Length for point data

We showed in Appendix A that, given a two-dimensional array of points, the mean distance between points, or Normalised Correlation Length, $\bar{s}$, is a robust indicator of the extent of clustering within the array. $\bar{s}$ is calculated as

$$\bar{s} = \frac{2}{\mathcal{N}(\mathcal{N}-1)} \sum_{i=1}^{i=\mathcal{N}-1} \sum_{j=i+1}^{\mathcal{N}} \{s_{ij}\} . \qquad (B.2)$$

where s_{ij} is the separation between points i and j, and there are $\mathcal{N}(\mathcal{N}-1)/2$ separations in a cluster of $\mathcal{N}$ points. In particular, we showed that the Normalised Correlation Length is independent of the number of points within the array. Increasing the density of points over the entire cluster increases the number of distant neighbours as well as close neighbours for each member of the cluster, and the mean distance stays the same. The second column of Table B.1 gives the values of $\bar{s}$ for five real star clusters, and for eight different artificial cluster types with known fractal dimension or centrally concentrated density gradient.

We showed in chapter A that, for point data, $\bar{s}$ decreases monotonically with increasing α, and can therefore be used to estimate α for star clusters which are presumed a priori to have radial density gradients. $\bar{s}$ was also found to increase monotonically with increasing D_3 and can therefore be used to estimate D_3 for star clusters which are presumed a priori to be fractally subclustered.

One advantage of using the Normalised Correlation Length to characterise the structure of a star cluster is that it explicitly incorporates edge effects and uses all the data. In contrast, the slope of the two point correlation function or the mean surface density of companions (e.g. Larson 1995; Simon 1997; Bate, Clarke and McCaughrean 1997; Klessen & Kroupa 2001) is severely affected by edge effects, and these can only be minimised by arbitrarily neglecting the large-scale data.

B.4   Adapting the Correlation Length for grey-scale images

A grey scale image of a cloud consists of position data (i.e. the two-dimensional coordinates of the pixels of the image) and a grey-scale value for each pixel (corresponding to the column density of the cloud at that point). If we calculate a Correlation Length simply from the position data, we are unable to discriminate between clouds of the same overall shape, whether they are perfectly uniform with constant column-density, or highly

variable with some concentrated regions and other very sparse regions. In order to correct this deficiency, we use the information about column-density variations in the cloud to weight the inter-pixel separations when we calculate the Normalised Correlation Length.

In deriving the correct weighting formula, our aim is that the Normalised Correlation Length for a cluster of points should be directly comparable with the Normalised Correlation Length of a grey scale image. In particular, if we take an image of a cluster of points and then convert it into a grey-scale image by simply counting how many points lie in each pixel area and using that total as the grey-scale value, we should get the same value for the Correlation Length when analysing the point data or the grey-scale image. To achieve this it is necessary both to weight the separations between occupied pixels according to the contents of the pixels, and also to add a term to allow for the fact that if the contents of a pixel were individual points, there would be separations between them, within the pixel boundaries, which would reduce the Correlation Length.

Consider an array of points which form two similarly sized well separated clusters, i and j, containing $\mathcal{N}_i$ and $\mathcal{N}_j$ points respectively. To calculate the value of $\bar{s}$ for the whole array, we must calculate a total of $(\mathcal{N}_i + \mathcal{N}_j)(\mathcal{N}_i + \mathcal{N}_j - 1)/2$ separations between all the possible pairings of points in the array. $\mathcal{N}_i(\mathcal{N}_i - 1)/2$ of these separations are between points in cluster i, and $\mathcal{N}_j(\mathcal{N}_j - 1)/2$ separations are between points in cluster j. These intra-cluster separations are less than the maximum dimensions of the individual clusters, and their means are the Correlation Lengths for the individual clusters. The number of possible pairs of points with one in cluster i and the other in cluster j is $\mathcal{N}_i\mathcal{N}_j$, and the mean separation between each of these pairs is approximately the distance between the centres of the two sub-clusters, s_{ij}. The Correlation Length for this array is therefore

$$\bar{s} = \frac{\mathcal{N}_i(\mathcal{N}_i - 1)\bar{s}_i + \mathcal{N}_j(\mathcal{N}_j - 1)\bar{s}_j + 2\mathcal{N}_i\mathcal{N}_j s_{ij}}{(\mathcal{N}_i + \mathcal{N}_j)(\mathcal{N}_i + \mathcal{N}_j - 1)} \qquad (B.3)$$

where $\bar{s}_i$ and $\bar{s}_j$ are the Normalised Correlation Lengths of the individual sub-clusters.

From Eqn B.3 we can derive an expression for the Normalised Correlation Length of a pixellated grey-scale image. Each pixel is treated as a small cluster. The number of points in pixel i is proportional to its column-density N_i, and we discuss in the succeeding paragraph the proportionality required. On the assumption that the points in a pixel are distributed uniformly over the area of the pixel, their Correlation Length is 0.52δ. Hence the Correlation Length of the total image, $\bar{s}$, is given by

$$\frac{N_{\mathrm{TOT}}(N_{\mathrm{TOT}} + 1)\bar{s}}{2} = \sum_{i=1}^{\mathcal{I}_0} \left\{ \frac{N_i(N_i + 1)\,0.52\,\delta}{2} \right\} + \sum_{i=1}^{\mathcal{I}_0 - 1} \sum_{j=i+1}^{\mathcal{I}_0} \left\{ N_i\,N_j\,s_{ij} \right\}, \qquad (B.4)$$

where $\mathcal{I}_o$ is the number of occupied pixels,

$$N_{\text{TOT}} = \sum_{i=0}^{i=\mathcal{I}_o} \{N_i\} \, , \tag{B.5}$$

and s_{ij} is the distance between the centres of pixels i and j.

The first summation on the righthand side of Eqn. B.4 accounts for separations between points in the same pixel, and the second summation accounts for separations between points in different pixels. The values of N_i must be scaled so that most of them are greater than unity, and those which are then still less than unity must be ignored in the summations in Eqn. B.4; otherwise the $(N_i - 1)$ terms will become negative.

Using this algorithm, we obtained $\bar{s}$ for the different artificial cloud types. The third column of Table B.1 gives the mean values of $\bar{s}$ and the standard deviations obtained on multiple realisations of each cloud type. The results obtained for the clouds match those for star clusters to within 5%.

This analysis was also applied to the 850μm map of Orion B North. $\bar{s}$ was calculated for the whole cloud, and then for the three individual core-clusters identified in Fig. B.2. The results are tabulated in Table B.1.

B.5   The Minimal Spanning Tree

The Minimal Spanning Tree (MST) is the unique network of straight lines joining a set of points, such that the total length of all the lines in the network (hereafter 'edges') is minimised and there are no closed loops. The construction of such a tree is described by Gower & Ross (1969). In chapter A we found that the mean edge length of the MST for a cluster of points, $\bar{\ell}$, varies monotonically with either radial concentration or fractal clustering. Combining $\bar{\ell}$ with the Normalised Correlation Length, $\bar{s}$, we defined a measure, $Q = \bar{s}/\bar{\ell}$, which could be used to distinguish between the two types of clustering. Despite considerable effort, we have been unable to devise a reliable MST edge length algorithm for grey scale data, and therefore it appears that Q is not applicable to pixellated grey-scale data.

B.6   The Perimeter-Area Method

Although the Q parameter is not adaptable for use with grey-scale images, the Normalised Correlation Length does provide a useful measure of the clustering in grey-scale maps or

clusters of points, as shown in Table B.1. It is therefore appropriate to establish whether the Correlation-Length method of measuring structure in clouds yields similar results to the established Perimeter-Area method.

The fractal dimension of a grey-scale map is normally estimated by measuring the perimeters, P, and areas, A, of iso-contour features, and plotting them on a log-log scale (Voss, 1988). The Perimeter-Area relation of the map is $P \propto A^{D_2/2}$. Hence the slope of the plot should yield the two-dimensional fractal dimension of the cloud, D_2. Using this method, Falgarone, Phillips & Walker (1991) found $D_2 \simeq 1.36$, and Williams, Blitz & McKee (2000) found $D_2 \simeq 1.4$, for clouds within our galaxy. Kim et al. (2003) found $D_2 = 1.47$ for HI clouds in the Large Magellanic Cloud, and most recently, Lee (2004) obtained $D_2 \simeq 1.34$ and $D_2 \simeq 1.4$, for slices of CO clouds in the Galactic Anticentre.

For each of the artificial cloud types, a Perimeter-Area plot was obtained, by calculating the perimeters and areas of contiguous features above 100 varying threshold values, from zero to the maximum pixel column-density, N_{MAX}. The perimeter of each feature was measured in numbers of pixel edges, and then divided by 4, the normalising factor for pixellated data (Voss, 1988). Twenty different realisations of each cloud type were analysed and the results for each superimposed. The results for single datasets are shown in Fig. B.3. Note that data for all of the features within the cloud, at all thresholds, are plotted, unless they are very small. Islands with an area of less than 30 pixels distort the relationship between perimeter and area because of 'rectangularisation' effects (Milne 1988), and are therefore omitted from the analysis. This cut-off also has the effect of removing areas of low-contrast noise in the empty areas of the image. The resulting data points are scattered around straight line trends, and the slope of the line and the scatter about the line increase with increasing fractal dimension, as shown in Fig. B.3. A least squares linear regression was performed on the data and the values of the slopes are recorded in Table B.1.

The Perimeter-Area analysis was then repeated for the $850\mu m$ map of the Orion B North molecular cloud (Fig. B.2). Perimeter-Area analyses have not, to our knowledge, been performed before on submillimetre data. The field of view and therefore the absolute sizes of the features being analysed here are much smaller than the features analysed by Falgarone et al. (1991), Williams et al. (2000), Kim et al. (2003) and Lee (2004). The Perimeter-Area relation is unaffected by the absolute scale of an image, but does depend on the dynamic range of resolved structure in the image. In the case of Orion, the Perimeter-Area plot was calculated for the whole cloud, and for the three core-clusters 1, 2 and 3 identified in Fig. B.2, and straight lines were then fitted to the data. The results are plotted in Fig. B.4, and the slopes of the lines are recorded in Table B.1.
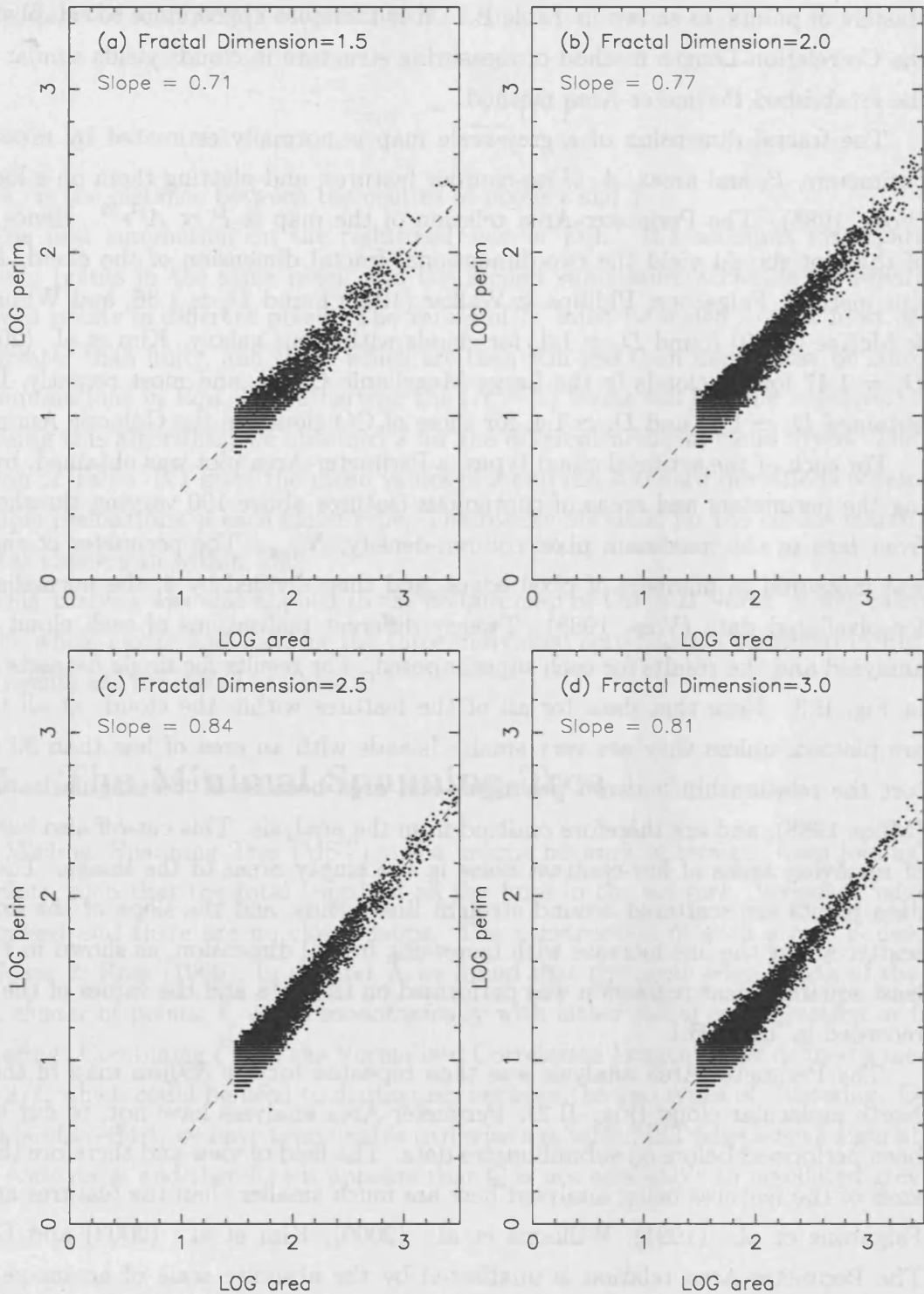
Figure B.3: Perimeter-Area plots for artificial clusters with different fractal dimensions: (a) $D_3 = 1.5$, (b) $D_3 = 2.0$, (c) $D_3 = 2.5$, and (d) $D_3 = 3.0$. The dashed lines and slopes are based on linear regression for multiple realisations of the given cluster type. However, data for only one realisation are plotted, to avoid saturation of the image.
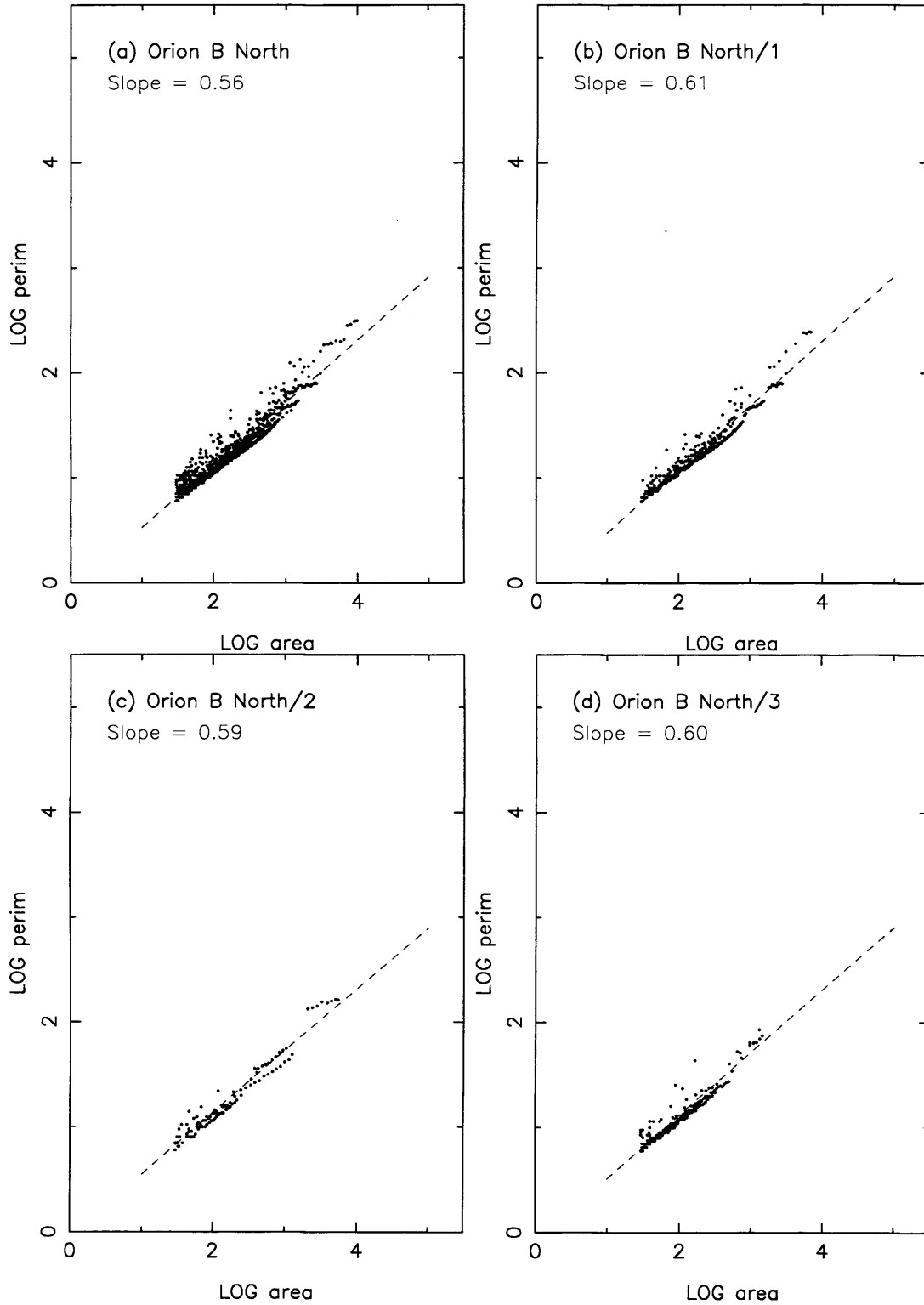
Figure B.4: Perimeter-Area plots for the 850μm map of the Orion B North cloud: (a) the whole cloud complex; (b), (c) and (d) the three individual core-clusters, 1, 2 and 3, identified on Fig. B.2. The dashed lines are the best linear fits to the data.

B.7 Discussion

B.7.1 The Correlation-Length Method

The Normalised Correlation Length, $\bar{s}$, can be adapted for use with grey-scale pixellated images, and gives results which are directly comparable with those for two-dimensional arrays of points. It is therefore potentially very useful as a means of comparing the internal structures of star clusters and gas clouds. Results are also comparable between fine and coarsely imaged data, indicating that the method is not very sensitive to the resolution of the measurement system. $\bar{s}$ decreases monotonically with increasing D_3 for values of D_3 up to 3.0 and can therefore be used without ambiguity as a diagnostic of fractal clustering in the range $D_3 = 1.5$ to 3.0.

The Normalised Correlation Length for the whole Orion B North Cloud (see Table B.1) suggests that the cloud is either highly fractally sub-clustered (with a $D_3 \lesssim 1.5$), or strongly radially concentrated about the centre of mass (with $\alpha \equiv -d\ell n[n]/d\ell n[r] \gtrsim 2$). However, breaking the cloud into three separate core-clusters and analysing them individually, we find that the Normalised Correlation length is much larger for core-clusters 2 and 3 than for core-cluster 1. This suggests that core-clusters 2 and 3 are fractal, whereas core-cluster 1 is more radially concentrated. The Normalised Correlation Length for the whole Orion B North Cloud is similar to those for the star clusters IC348 and ρ Ophiuchus, as reported in chapter A.

B.7.2 The Perimeter-Area Method

The slopes obtained from Perimeter-Area plots yield another indicator of fractal dimension. For a two dimensional slice, or Poincaré section, of a three dimensional object, the relationship between perimeter and area is given by $P = kA^{D_2/2}$, and so the slope of a log-log plot is $D_2/2$. (Voss 1988). D_2 is the two-dimensional fractal dimension, and measures the extent to which the perimeter of an area fills the two-dimensional space. Cloud data are not a slice but rather a projection of the three-dimensional density (at least in the ideal, optically thin, uniform-emissivity case), and the Perimeter-Area plot yields estimates of D_2 increasing from $D_2 \simeq 1.4$ for $D_3 = 1.5$ to $D_2 \simeq 1.7$ for $D_3 = 2.5$. Thus D_2 is not a very sensitive indicator of the fractal dimension D_3, particularly for high values of D_3. In fact, for values of $D_3 > 2.5$, the slope of the Perimeter-Area plot no longer increases with increasing D_3, but starts to decrease. The method is therefore inconclusive if the slope of the plot is greater than 0.8, which corresponds to $D_3 > 2.25$ in our simulations. This is to be expected, because such clouds are efficient at filling

the three-dimensional volume, and the details of the internal structure are therefore lost when viewing a projection, rather than a slice. On Fig. B.3 there is a large spread of points around the overall straight line trend. Thus, although the straight-line fit is good, with quite small standard deviation, it appears that simply selecting a few contours from a map and fitting a straight line to the resultant Perimeter-Area plot, will yield rather unreliable results.

If we now consider the Perimeter-Area data for Orion B North, as plotted on Fig. B.4, the slopes of the plots for the whole map, and for the individual core-clusters, are all in the range 0.59 ± 0.03, which yields $D_2 \simeq 1.2$, and – by comparison with the artificial clusters – suggests that $D_3 < 1.5$. At small scale, the Orion map is rather smooth and has little detail, whereas the artificial data, even after heavy smoothing, retains some small-scale detail, which increases the measured perimeters and hence reduces the derived fractal dimensions. The Perimeter-Area method is therefore sensitive to the spatial resolution of the image, and also to any noise in the pixel column-densities, N_i.

B.7.3 Comparison of Correlation-Length and Perimeter-Area Methods

We find that the results from the Correlation-Length and Perimeter-Area methods are comparable as indicators of the fractal dimension, D_3, of three-dimensional structures which have been projected onto two-dimensional arrays of pixels. The advantage of the Correlation-Length method is that it may be used to compare point data with grey-scale data, and can yield results even from images with little small-scale detail. It also gives useable results right up to $D_3 = 3.0$. The disadvantage is that it cannot be used on part of a cloud or cluster, unless, as in Orion B North, there are clearly self-contained structures within the image. It is also best used on data with a limited dynamic range, as a very large value in one pixel (or very large values in a few pixels) may distort the analysis.

The Perimeter-Area method is useful for values of $D_3 < 2.0$, but it is sensitive to the resolution of the image. Molecular clouds with clearly resolved features ranging from 100pc to 0.1pc are suitable for this type of analysis. The range of scales in the submillimetre data we have used is far smaller and therefore are less suitable for Perimeter-Area analysis. The Perimeter-Area method has the advantage that it can be used on incomplete data, where the whole structure has not been imaged. Care must be taken to analyse sufficient contours, so as to get a good estimate of the slope of the Perimeter-Area plot. Islands having an area of less than 30 pixels should be omitted from the analysis, to avoid rectangularisation problems. Lee (2004) correctly notes the inaccuracies introduced by

including small islands, but unfortunately about half his data points fall into this category.

When real data are compared using the two methods, similar results are obtained; the fractal dimension, D_3, for the Orion B North Cloud is estimated to be $D_3 < 1.5$ by both methods. However, when comparing the individual core-clusters, the Perimeter-Area method detects little difference, whereas the Correlation-Length method finds the northern core-cluster (core-cluster 1 on Fig. B.2) to be the most strongly centrally concentrated one, and the southern core-cluster (core-cluster 3 on Fig. B.2) to be the least strongly centrally concentrated one.

B.8 Conclusions

We have shown that the Normalised Correlation Length can be adapted for use with grey-scale images, thus allowing a direct comparison between point data from star clusters and grey-scale images of molecular clouds. Tests on artificial clouds containing small-scale sub-clustering show that this method can quantify the degree of fractal clustering quite accurately. However, the method has to be used on complete, isolated clouds or clusters.

We have been unable to adapt our Minimal Spanning Tree methodology for use with grey-scale images, and so the measure Q which we derived in chapter A for analysing star clusters cannot be applied to molecular clouds.

We find that the Perimeter-Area method is noise prone, particularly if only a few contours are selected for analysis. It has the advantage that it may be used on partial images of clouds, but the image must have quite large dynamic range, and islands of less than 30 pixels must be omitted from the analysis. It gives ambiguous results for fractal dimensions $D_3 \gtrsim 2$.

Bibliography

[1] Balsara D., 1989, PhD Thesis, Univ. Illinois

[2] Barnes J. and Hut P., 1986. A heirarchical O(N logN) force-calculation algorithm. *Nat.*, 324, 446

[3] Barrado y Navascues D., Stauffer J.R., Briceno C., Patten B., Hambly N.C., Adams J.D., 2001, Low-mass members of IC 2391. *Astrophys. J*, 134, 103

[4] Barrow J.D., Bhavsar S.P., Sonoda D.H., 1985, Minimal spanning trees, filaments and galaxy clustering. *Mon. Not. R. Astro. Soc*, 216, 17

[5] Bate M.R., Clarke C.J., McCaughrean M.J., 1997. Interpreting the mean surface density of companions in star-forming regions. *Mon. Not. R. Astro. Soc*, 297, 1163

[6] Bate M.R., 2000, Predicting the properties of binary stellar systems: the evolution of accreting protobinary systems. *Mon. Not. R. Astro. Soc*, 314, 33

[7] Bate M.R., Lubow S.H., Ogilvie G.I., Miller K.A., 2003, Three-dimensional calculations of high- and low-mass planets embedded in protoplanetary discs. *Mon. Not. R. Astro. Soc*, 341, 213

[8] Bate M.R., Burkett A., 1997, Resolution requirements for smoothed particle hydrodynamics calculations with self-gravity. *Mon. Not. R. Astron. Soc*, 288, 1060

[9] Batty C., Whitworth A.P., 2006, Density formulation in Smoothed Particle Hydronamics simulations of shear flow. In prep.

[10] Baugh C., 1993, Self-Avoiding Random Walks as a Probe of Largescale Structure in the Universe. *Mon. Not. R. Astro. Soc*, 264, 87

[11] Beckwith S.V.W., Sargent, A.I., Chini R.S., Guesten R. 1990, A survey for circumstellar disks around young stellar objects. *Astrophys. J* 99, 924

[12] Beckwith S.V.W., Sargent A.I., 1993, Molecular line emission from circumstellar disks. *Astrophys. J*, 402, 280

[13] Binney J., Tremaine S., 1987 Galactic Dynamics. *Princeton University Press*

[14] Boffin, H.M.J., Watkins, S.J., Bhattal, A.S., Francis,N., Whitworth,A.P., 1998, Numerical simulations of protostellar encounters - I. Star-disc encounters *Mon. Not. R. Astro. Soc*, 300, 1189

[15] Bontemps S., Nadre P., Kaas A.A., Nordh L., Olofsson G., Huldtgren M., Abergel A., Blommaert J., Boulanger F., Burgdorf M., Cesarsky C.J., Cesarsky D., Copet E., Davies J., Falgarone E., Lagache G., Montmerle T., Perau M., Persi P., Prusti T., Puget J.L., Sibille F., 1979, ISOCAM observations of the rho Ophiuchi cloud: Luminosity and mass functions of the pre-main sequence embedded cluster. *A&A*, 372, 173

[16] Boss A.P, 1993, Evolution of the Solar Nebula. II. Thermal Structure during Nebula Formation. *Astrophys. J*. 417, 351

[17] Boss A.P., Yorke H.W. 1996, Protoplanetary Disks, Mid-Infrared Dips, and Disk Gaps. *Astrophys J*. 469, 366

[18] Boss A.P, 1993, Evolution of the Solar Nebula. IV. Giant Gaseous Protoplanet Formation. *Astrophys. J*. 503, 923

[19] Boss A.P., 2000, Possible Rapid Gas Giant Planet Formation in the Solar Nebula and Other Protoplanetary Disks. *Astrophys J*. 536, 101

[20] Boss A.P. 2001, Gas Giant Protoplanet Formation: Disk Instability Models with Thermodynamics and Radiative Transfer. *Astrophys.J*. 563, 367

[21] Boss A.P., Hartmann A.P., 2001a, Protostellar Collapse in a Rotating, Self-gravitating Sheet. 2001 *Astrophys. J*. 562, 842

[22] Boss A.P. 2002, Evolution of the Solar Nebula. V. Disk Instabilities with Varied Thermodynamics. *Astrophys. J*. 576, 462

[23] Boss A.P., 2003, Rapid Formation of Outer Giant Planets by Disk Instability. *Astrophys. J*. 599, 577

[24] Brandner W., Köhler R., 1998, Star Formation Environments and the Distribution of Binary Separations. *Astrophys. J*, 499, 79

[25] Briceno C., Calvet N., Gomez M., Hartmann L., Kenyon S.J., Whitney B.A., 1993, First results of the CIDA Schmidt survey - Selected zones in Taurus-Auriga. *Pubs. Astr. Soc. Pac.*, 105, 686

[26] Cartwright A., Whitworth A.P., 2004, The Statistical Analysis of Star Clusters. *Mon. Not. R. Astro. Soc.*, 348, 589

[27] Cartwright A., Whitworth A.P., Nutter D., 2006. Methods for the analysis of structure in Molecular Clouds. *Mon. Not. R. Astro. Soc.*, 369, 1411

[28] Cartwright A., Cartwright J.A., 2006, Spatial analysis of submarine pockmarks indicates rapid sea level change. In Prep.

[29] Clarke C.J., Pringle J.E., 2004 Kinetic theory viscosity. *Mon. Not. R. Astro. Soc.*, 351, 1187

[30] Diggle P., 1983, Statistical Analysis of Spatial Point Patterns. *London Academic Press*

[31] Dussert C., Rasigni M., Palmari J., Rasigni G., Llebaria A., Marty F., 1987, Minimal Spanning Tree analysis of biological structures. *J Theor. Biol.*, 125, 317

[32] Eisner J.A., Carpenter J. M., 2006, Massive Protoplanetary Disks in the Trapezium Region. *Astrophys. J.* 641, 1162

[33] Falgarone E., Phillips T.G., Walker C.K., 1991, The edges of molecular clouds - Fractal boundaries and density structure. *Astrophys. J*, 378, 186

[34] Gammie C.F., 2001, Nonlinear Outcome of Gravitational Instability in Cooling, Gaseous Disks. *Astrophys. J.* 553, 174

[35] Ghez A.M., Neugebauer G., Matthews K., 1993, The multiplicity of T Tauri stars in the star forming regions Taurus-Auriga and Ophiuchus-Scorpius: A 2.2 micron speckle imaging survey. *Astron. J*, 106, 2005

[36] Gladwin P.P., Kitsionas S., Boffin H.M.J., Whitworth A.P., 1999, The structure of young star clusters. *Mon. Not. R. Astro. Soc*, 302, 305

[37] Gladwin P.P., 2000, Numerical Simulations of the Collapse of Dense Molecular Cores. *Ph. D. Thesis*,

[38] Goldreich p., Lynden-Bell D., 1964, Gravitational stability of uniformly rotating disks. *Mon. Not. R. Astro. Soc* 130, 97

[39] Gomez M., Jones B.F., Hartmann L., Kenyon S.J., Stauffer J.R., Hewett R., Reid I.N, 1992, On the ages of pre-main-sequence stars in Taurus. *Astron. J*, 104, 762

[40] Gower J.C., Ross G.J.S., 1969, Minimum Spanning Trees and Single Linkage Cluster Analysis. *J. Appl. Stat.*, 18, 54

[41] Graham M.J., Clowes R.G.,Campusano L.E., 1979, Finding Quasar Superstructures. *Mon. Not. R. Astro. Soc*, 275, 790

[42] Griffiths 1983 An introduction to Electrodynamics. *Prentice Hall, NJ*

[43] Hammersley J.M., Halton J.H., Beardwood J., 1959, The shortest path through many points. *Camb. Philos. Soc. Proceedings*, 55, 299

[44] Haisch K.E., Lada E.A., Lada C.J., 2001, Disk frequencies and lifetimes in young clusters. *Astrophys. J*, 553, 153

[45] Haisch K.E., Lada E.A., Lada C.J., 2001a, Circumstellar Disks in the IC 348 Cluster. *Astrophys. J*, 121, 2065

[46] Hartmann L., Stauffer J.R., Kenyon S.J., Jones B.F., 1991, A proper motion survey for pre-main-sequence stars in Taurus-Auriga *Astrophys. J.*, 101, 1050

[47] Hayashi, E., Matsuda, T., 2001, Is Angular Momentum in an Accretion Disk Transported Inwards? *Prog. Theo. Phys.* 105, 531

[48] Hennebelle, P., Whitworth, A. P., Gladwin, P. P., Andr, Ph. 2003, Protostellar collapse induced by compression.*Mon. Not. R. Astro. Soc* 340, 870

[49] Herbig G.H., Bell K.R., 1988, Catalog of emission line stars of the Orion population. *Lick Obs. Bull.*, 1111

[50] Hernquist, L., Katz, N., 1989, TREESPH - A unification of SPH with the hierarchical tree method. *Astrophys. J.* 70, 419

[51] Hoffman R.,Jain A. K., 1983, A test of randomness based on the minimal spanning tree. *Patt. Rec. Lett.* 1, 175

[52] Hubber D.A., Goodwin S.P., Whitworth A.P, 2006, Resolution requirements for simulating gravitational fragmentation using SPH. *A & A* 450, 881

[53] Imaeda Y., Inutsuka S., 2003, Shear Flows in Smoothed Particle Hydrodynamics. *Astrophys. J.* 569, 501

[54] Jang-Condell H., Sasselov D.D., 2003, Radiative Transfer on Perturbations in Protoplanetary Disks *Astrophys. J.* 593, 1116

[55] Johnstone D.; Fich M.; Mitchell G. F.; Moriarty-Schieven G. 2001, A Large Area Mapping at 850 Microns. III. Analysis of the Clump Distribution in the Orion B Molecular Cloud. *Astrophys. J.*, 559, 307

[56] Kim S., Stavely Smith L., Dopita MA., Sault R.J., Freeman K.C., Lee Y., Chu Y.H., 2003, A Neutral Hydrogen Survey of the Large Magellanic Cloud: Aperture Synthesis and Multibeam Data Combined. *Astrophys. J*, 148, 473

[57] Klein R.I., Fisher R., McKee C.F., 2004, Resolution Issues in the Collapse and Fragmentation of Turbulent Molecular Cloud Cores. *Revista Mexicana de Astronoma y Astrofsica (Serie de Conferencias)*22,3

[58] Klessen R.S., Kroupa P., 2001, The mean surface density of companions in a stellar-dynamical context. *A&A*, 372, 105

[59] Larson R.B., 1995, Star formation in groups. *Mon. Not. R. Astro. Soc*, 272, 213

[60] Larson R.B., 2001, Implications of Binary Properties for Theories of Star Formation. *The Formation of Binary Stars, Proceedings of IAU Symp. 200, held 10-15 April 2000, in Potsdam, Germany, Edited by Hans Zinnecker and Robert D. Mathieu* 93.

[61] Lawson W.A., Fiegelson E.D., Huenemoerder D.P., 1996, An improved HR diagram for Chamaeleon I pre-main-sequence stars. *Mon. Not. R. Astro. Soc*, 280, 1071

[62] Lecar M., Podolak M., Sasselov,D.,Chiang,E., 2006, On the Location of the Snow Line in a Protoplanetary Disk. *Astrophys. J.* 640, 1115

[63] Lee Y., 2004, Fractal Dimensions of Interstellar Medium : I. The Molecular Clouds in the Antigalactic Center. *J.Kor.As.Soc.*, 37, 137

[64] Leinert Ch., Zinnecker H., Weitzel N., Christou J., Ridgway S.T., Jameson R., Haas M., Lenzen R., 1993, A systematic approach for young binaries in Taurus. *A&A*, 278, 129

[65] Lo Curto G., Mayor M.,Clausen J.V., Benz W., Bouchy F., Lovis C., Moutou C., Naef D.,Pepe F., Queloz D., Santos N.C., Sivan J-P., Udry S., Bonfils X., Delfosse X., Mordasini C., Fouqu P., Olsen E.H., Pritchard J.D., 2006, The HARPS search for southern extra-solar planets. VII. A very hot Jupiter orbiting HD 212301. *A&A*, 451, 345

[66] Lodato G., Rice W.K.M., 2004, Testing the locality of transport in self-gravitating accretion discs. *Mon. Not. R. Astro. Soc*, 351, 630

[67] Lucy, L.B., 1977, A numerical Approach to the testing of the fission hypothesis. *Astrophys. J.*, 502, 342.

[68] Luhman K.L., Stauffer J.R., Muench A.A., Rieke G.H., Lada E.A., Bouvier J., Lada C.J., 2003, A Census of the Young Cluster IC 348. *Astrophys. J.*, 593, 1093

[69] Lynden-Bell D., Pringle J.E., 1974, The evolution of viscous discs and the origin of the nebular variables. *Mon. Not. R. Astr. Soc.*, 168, 603

[70] Maddison S.T., Murray J.R., Monaghan J.J., 1996, SPH Simulations of Accretion Disks and Narrow Rings. *Publ. Astron. Soc. Aust.*, 13, 66

[71] Marcy, G.; Butler, R.; Fischer, D.; et.al. 2005, Observed Properties of Exoplanets: Masses, Orbits and Metallicities. *Prog. Th. Phys. Supp.*, 158: 24 42.

[72] Masset and Papaloizou, 2003, Runaway Migration and the formation of Hot Jupiters. *Astrophys. J.*, 588, 494

[73] Mayer L., Quinn T., Wadsley J., Stadel J., 2004, The Evolution of Gravitationally Unstable Protoplanetary Disks: Fragmentation and Possible Giant Planet Formation. *Astrophys. J.*, 609, 1045

[74] Mayor, M.; Queloz, D., 1995 A Jupiter-Mass Companion to a Solar-Type Star. *Nature* 378, 355

[75] McCaughrean, M. J.; O'dell, C. R., 1996, Direct Imaging of Circumstellar Disks in the Orion Nebula. *Astron. J* 111, 1977

[76] Mestel L., 1963, On the galactic law of rotation. *Mon. Not. R. Astr. Soc.*, 126, 557

[77] Milne B.T. 1988, Spatial and Temporal Analysis of landscape patterns. *Appl. Math. Comp.* 27, 67

[78] Monaghan J.J. Gingold R.A., 1983, Shock Simulation by the particle method SPH. *J. Comput. Phys.* 52, 374

[79] Monaghan, J.J., Lattanzio, J.C., 1983, A refined particle method for astrophysical problems. *A & A* 149, 135

[80] Monaghan J.J., 1988, An Introduction to SPH. *Comp. Phys. Comm*, 48, 89

[81] Monaghan J.J., 1992, Smoothed Particle Hydrodynamics. *Annu. Rev. Astron. Astrophys.*, 30, 543

[82] Monaghan J.J., 2002, SPH compressible turbulence. *Mon. Not. R. Astro. Soc*, 335, 843

[83] Monaghan J.J., 2005, Smoothed Particle Hydrodynamics. *Rep. Prog. Phys.*, 68, 1703

[84] Monaghan J.J.,2006, Smoothed particle hydrodynamic simulations of shear flow. *Mon. Not. R. Astro. Soc*,365, 199

[85] Morris J.P., Monaghan J.J., 1997, A switch to reduce SPH Viscosity. *J. Comp. Phys.*, 136, 41

[86] Motte F., Andr, P., Ward-Thompson D., Bontemps S., 2001, The initial conditions of isolated star formation. *A. & A.*, 372, 41

[87] Najita J.R., Tiede G.P., Carr J.S., 2000, From Stars to Superplanets: The Low-Mass Initial Mass Function in the Young Cluster IC 348. *Astrophys. J.*, 541, 977

[88] Nakajima Y., Tachihara K., Hanawa T., Nakano M., 1998, Clustering of Pre-Main-Sequence Stars in the Orion, Ophiuchus, Chamaeleon, Vela, and Lupus Star-forming Regions. *Astrophys. J* 497, 721

[89] Nelson A.F., Benz W, Adams F.C., Arnett D., 1998, Dynamics of Circumstellar Disks. *Astrophys. J.*, 502, 342.

[90] Nelson A.F., 2003, On the Early Evolution of Forming Jovian Planets. I. Initial Conditions, Systematics, and Qualitative Comparisons to Theory. *Astrophys. J.*, 589, 556

[91] Nemiroff R.J., 2005, Can a Gravitational Lens magnify gravity? A possible solar system test. *Astrophys. J*, 628, 1081

[92] Nutter D., Ward-Thompson D., 2006, in prep.

[93] O'dell C.R., Disks and Outflows in the Orion Nebula as Determined by the HST. 1995. *Revista Mexicana de Astronomia y Astrofísica Serie de Conferencias, Vol. 1, Circumstellar Disks, Outflows and Star Formation, Cozumel, Mexico* p. 11

[94] O'dell C.R., Wong K., 1996, Hubble Space Telescope Mapping of the Orion Nebula. I. A Survey of Stars and Compact Objects. *Astron. J* 111, 846

[95] Oliveira J.M., Jeffries R.D., Kenyon M.J., Thompson S.A., NaylorT., 2002, No disks around low-mass stars and brown dwarfs in the young sigma Orionis cluster? *A & Astrophysics* 382, 22

[96] Papaloizou J.C.B., Disk Planet Interactions and early evolution in young planetary systems. *Celest. Mech. & Dyn. Astron.* 91, 33

[97] Pickett B.K., Durisen R.H., Cassen P., Mejia A.C.,2000, Protostellar Disk Instabilities and the Formation of Substellar Companions *Astrophys. J.*, 540, 95

[98] Press W.H., Teukolsky S.A., Vetterling W.T., Flannery B.P., 1992, *Numerical Recipes in Fortran. Cambridge University Press, Cambridge, 2nd Edition.*

[99] Rafikov R.R., 2004, Can Giant Planets Form by Direct Gravitational Instability? *Astrophys. J.*, 621, 69

[100] Rice W.K.M., Armitage P.J., Bonnell I.A., Bate M.R., Jeffers S.V., Vine S.G., 2003, Substellar companions and isolated planetary-mass objects from protostellar disc fragmentation. *Mon. Not. R. Astro. Soc*, 346, 36

[101] Rice W.K.M., Armitage P.J., Bate M.R., Bonnell I.A., 2003a, The effect of cooling on the global stability of self-gravitating protoplanetary discs. *Mon. Not. R. Astro. Soc*, 339, 1025

[102] Rice W.K.M., Lodato G., Pringle J.E., Armitage P.J., Bonnell I.A., 2004, Accelerated planetesimal growth in self-gravitating protoplanetary discs. *Mon. Not. R. Astro. Soc*, 355, 543

[103] Schaefer C., Speith R., Hipp M,. Kley W., 2004, Simulations of planet-disc interactions using Smoothed Particle Hydrodynamics. *astro-ph*, 0401425

[104] Schmeja S., Klessen R.S., 2005, Evolving structures of star-forming clusters. *A&A* 449, 151

[105] Simon M., Ghez A.M., Leinert Ch., Cassar L., Chen W.P., Howell R.R., Jameson R.F., Matthews K., Neugebauer G., Richichi A., 1995, A lunar occultation and direct imaging survey of multiplicity in the Ophiuchus and Taurus star-forming regions. *Astrophys. J.*, 443, 625

[106] Simon M., 1997, Clustering of Young Stars in Taurus, Ophiuchus, and the Orion Trapezium. *Astrophys. J.*, 482, L81

[107] Steele J.M., 1988, Growth rates of Euclidean minimal spanning trees with power weighted edges. *Ann. Prob.*, 16, 1767

[108] Tanaka H., Takeuchi T., Ward W.R., 2002, Three-Dimensional Interaction between a Planet and an Isothermal Gaseous Disk. I. Corotation and Lindblad Torques and Planet Migration. *Astrophys. J* 565, 1257

[109] Toomre A., 1964, On the gravitational stability of a disk of stars. *Astrophys. J.*, 139, 1217

[110] Voss R.F. 1988. Fractals in nature:from characterization to simulation. *Springer, New York; eds. Peitgen, H.-O. and D. Saupe* 21-70

[111] Walter F.M., Brown A., Mathieu R.D., Myers P.C., Vrba F.J., 1988, X-ray sources in regions of star formation. III - Naked T Tauri stars associated with the Taurus-Auriga complex. *Astron. J*, 96, 297

[112] Watkins S.J., Bhattal A.S., Boffin H.M.J., Francis N., Whitworth, A.P., 1998, Numerical simulations of protostellar encounters - III. Non-coplanar disc-disc encounters. *Mon. Not. R. Astro. Soc*, 300, 1214

[113] Williams J.P., Blitz L., McKee C.F., 2000, *Protostars and Planets, Vol. IV* (University of Arizona Press; eds Mannings V., Boss A.P, Russell S.S.) p.97

[114] Wiedenschilling S.J., 1977 The distribution of mass in the planetary system and solar nebula. *Astrophys. & Space Sci.*, 51, 153